

TECHNISCHE UNIVERSITÄT MÜNCHEN

Wissenschaftszentrum Weihenstephan für Ernährung, Landnutzung, Umwelt

Lehrstuhl für Entwicklungs-genetik

Establishment and cell biological analysis of neurodegeneration models in zebrafish  
based on Parkinson's disease-linked genes *LRRK2* and *PINK1*

Rosemarie Waltraud Söllner

Vollständiger Abdruck der von der Fakultät Wissenschaftszentrum Weihenstephan für  
Ernährung, Landnutzung und Umwelt der Technischen Universität München zur Erlangung  
des akademischen Grades eines

Doktors der Naturwissenschaften

genehmigten Dissertation.

Vorsitzende: Univ.-Prof. Dr. A. Kapurniotu  
Prüfer der Dissertation: 1. Univ.-Prof. Dr. W. Wurst  
2. Univ.-Prof. Dr. T. Misgeld

Die Dissertation wurde am 13.10.2014 bei der Technischen Universität München eingereicht  
und durch die Fakultät Wissenschaftszentrum Weihenstephan für Ernährung, Landnutzung  
und Umwelt am 26.01.2015 angenommen.

Biology is the greatest teacher.  
Die Biologie ist der größte Lehrmeister.

## Abstract

Parkinson's disease (PD) is a progressive incurable neurodegenerative disorder affecting seven to ten million people worldwide. The pathological hallmark of the disease is the selective loss of dopaminergic (DA) neurons in the *substantia nigra pars compacta*, and this is causative for the characteristic motor dysfunctions. Although it is considered a multifactorial disease and most cases are of unknown etiology, evidence has been accumulating that mitochondria are adversely affected by several mechanisms and insults, and mitochondrial dysfunction seems to be a major trigger for neuronal cell death. Recently, genetic mutations in several genes have been linked to PD. They account for about 10% of the cases. Among them are the two genes, *LRRK2* and *PINK1*, mutations in which are linked to autosomal dominant late-onset PD or a recessive early-onset form, respectively.

The *Leucine-Rich Repeat Kinase 2* gene encodes a large multidomain protein with GTPase and kinase activity that might function as a signalling hub with different and context-dependent output activities. So far, it has been implicated in diverse cellular processes, e.g. the cytoskeleton, vesicle trafficking and function (including autophagosomes and synaptic vesicles), protein synthesis and degradation. The most common mutation in *LRRK2* encodes the G2019S substitution in the kinase domain. However, how PD-linked point mutations alter *LRRK2* function and lead to the specific DA neurodegeneration still remains unknown. The second gene, *PTEN-Induced Kinase 1*, is a mitochondria-targeted kinase that has been linked to several aspects of mitochondrial homeostasis including mitophagy, respiratory chain function, mitochondrial fission-fusion dynamics and transport.

Based on these genes we generated and analyse two zebrafish disease models. Zebrafish has several advantages over other vertebrates. Its embryos and larvae are numerous, develop externally and are transparent. They can thus be used for *in vivo* microscopic observation of cellular and subcellular pathogenic processes. They can also be employed in high-content screening assays to identify novel disease-modifying compounds.

We used the Gal4/UAS expression system to generate a novel neuronal driver line that expresses an improved version of the Gal4 transcription factor in many central and peripheral neurons from early developmental stages onwards. We also compiled several tri-functional effector plasmids. These mediate Gal4-dependent, UAS-regulated expression of the mutant human *LRRK2(G2019S)* disease gene or a control allele. At the same time, expression of two fluorescent reporter proteins, mitoTagRFP to label mitochondria in red and Venus-LC3 to highlight autophagosomes in yellow, is achieved. Injecting effector constructs into one-cell

stage embryos of the neuronal driver line yielded a mosaic transgene expression in single or few neurons at larval stages. As a readout to detect a potential pathogenic effect of the disease gene, we established a standardized imaging procedure to observe mitochondrial axonal transport in long nerve fibres of the posterior lateral line (PLL) system. An influence of mutant LRRK2 on mitochondrial transport velocities and size distributions was not detected with our experimental system. However, this lack of a phenotype could be due to an insufficiently low expression of the transgene. A final conclusion about any interference of mutant LRRK2 with mitochondrial axonal transport can therefore not be drawn. Nevertheless, our system is well suited to analyse mitochondrial transport, and several novel insights about this fast intracellular logistics process could be gained. Within axons of the PLL nerve the percentage of mobile mitochondria clearly is higher than that of stationary mitochondria, and their movement is highly persistent in one transport direction. Anterograde and retrograde transport are mechanistically distinct and can be discriminated by their transport parameters. Although transport velocities are distributed over a wide range for both directions, retrograde transport on average is faster than anterograde transport. It is also more unsteady and discontinuous. Additionally, mitochondria travelling in the retrograde direction are slightly larger than mitochondria moving in the anterograde direction.

The second zebrafish disease model represents a loss of Pink1 function and was provided by a collaborating research group. We quantified the dopaminergic (DA) neuronal complement in brain tissue from 6-months-old animals by performing tyrosine hydroxylase immunohistochemistry on serial tissue sections. A reduction in neuron number could not be observed in characteristic DA cell clusters, which constitute a system homologous to the *substantia nigra pars compacta* in humans. However, a statistical evaluation of the data could not be achieved. On the other hand, when mitochondrial ultrastructure was analysed by electron microscopy in muscle tissue from larvae and adult animals of Pink1-deficient and wild-type lines, clear alterations could be detected. Mitochondrial sizes were enlarged in the mutant from early developmental stages onwards. Additionally, mitochondria in adult muscle had a heterogeneous appearance. Some mitochondria had a less electron-dense matrix with reduced and disorganized cristae membranes. And this phenotype clearly resembles other PD animal models.

## Zusammenfassung

Morbus Parkinson ist eine progressive, unheilbare, neurodegenerative Erkrankung, die geschätzt, weltweit sieben bis zehn Millionen Menschen betrifft. Der charakteristische pathologische Befund ist das selektive Absterben dopaminerger Neuronen in der Gehirnregion der *Substantia nigra, Pars compacta*. Dieser Zellverlust verursacht die typischen motorischen Symptome der Erkrankung. Obwohl multifaktorielle Ursachen angenommen werden, ist die Ätiologie in den meisten Fällen unbekannt. In letzter Zeit häufen sich Hinweise darauf, dass Mitochondrien durch verschiedene Einflüsse und Mechanismen in Mitleidenschaft gezogen werden. Die Fehlfunktion von Mitochondrien wird somit als Hauptauslöser der Apoptose von Nervenzellen vermutet. In jüngster Zeit konnten Mutationen in verschiedenen Genen ursächlich mit dem Auftreten der Parkinsonschen Erkrankung in Zusammenhang gebracht werden. Darunter sind die zwei Gene, *LRRK2* und *PINK1*. Mutationen im *LRRK2* Gen wurden in Fällen von autosomal-dominantem, spät auftretendem Morbus Parkinson gefunden, wohingegen Mutationen im *PINK1* Gen eine rezessiv-vererbte, in jungen Jahren auftretende Erkrankung auslösen.

Das *Leucine-Rich Repeat Kinase 2* Gen kodiert für ein großes Protein mit vielen funktionalen Domänen, das sowohl GTPase als auch Kinaseaktivität aufweist. Es könnte als übergeordnete Schaltstelle fungieren und, je nach Kontext, unterschiedliche Signale weiterleiten. Bisher wurde seine Beteiligung an verschiedenen zellulären Prozessen ausgemacht, darunter die Regulierung des Zytoskeletts, Transport und Funktion verschiedener Vesikeln (darunter Autophagosomen und synaptische Vesikel), Translation und Proteinabbau. Die häufigste Mutation des *LRRK2* Gens führt zur Aminosäuresubstitution G2019S in der Kinasedomäne. Es ist jedoch weiterhin unklar, welche Veränderungen in der Aktivität von *LRRK2* die Krankheits-assoziierten Mutationen hervorrufen und wie das mutierte Protein zur Degeneration dopaminerger Neuronen beiträgt. Das zweite Gen, *PTEN-Induced Kinase 1*, codiert für eine, an den Mitochondrien lokalisierte, Kinase, deren Funktion bereits mit verschiedenen Aspekten der Mitochondrienhomöostase assoziiert wurde, darunter Mitophagie, die Funktion der Atmungskette, Mitochondriendynamik (Teilung und Fusion) und Transport. Basierend auf diesen beiden Genen wurden zwei transgene Zebrafischmodelle generiert. Der Zebrafisch weist verschiedene Vorteile gegenüber anderen Vertebraten auf. Die Nachkommen sind zahlreich und ihre Entwicklung erfolgt extern im Ei. Aufgrund ihrer Transparenz können Embryonen und Larven für mikroskopische Lebendbeobachtungen von zellulären und subzellulären Prozessen herangezogen werden. Desweiteren können sie in

Hochdurchsatz-screening-assays eingesetzt werden, um neue Wirkstoffe für Medikamente zu identifizieren.

Unter Verwendung des Gal4/UAS Expressionssystems konnten wir eine neue neuronale Treiber-Fischlinie etablieren. Diese exprimiert eine verbesserte Version des Transkriptionsfaktors Gal4 in vielen Neuronen des zentralen und peripheren Nervensystems, und zwar beginnend in frühesten Entwicklungsstadien. Außerdem wurden mehrere tri-funktionale Effektor-plasmide konstruiert. Diese ermöglichen die Gal4-abhängige Expression des *LRRK2(G2019S)* Allels oder eines Kontrollallels. Gleichzeitig, und ebenfalls reguliert über UAS Sequenzen, wird die Expression zweier Fluoreszenz-Reporter ermöglicht. MitoTagRFP markiert Mitochondrien durch rote Fluoreszenz und Venus-LC3 läßt Autophagosomen in gelb aufleuchten. Durch DNS-Injektion der Effektorplasmide in einzellige Embryonen der neuronalen Treiberlinie wurde eine mosaikartige Transgenexpression in einzelnen oder wenigen Neuronen der Zebrafischlarven erreicht. Um einen potenziellen pathogenen Effekt des Krankheitsgens feststellen zu können, wurde eine standardisierte Mikroskopiermethode zur Beobachtung des Mitochondrientransports in den langen peripheren Axonen des posterioren Seitenlinienorgans etabliert. Ein Einfluss der G2019S Variante des LRRK2 Proteins auf die Transportgeschwindigkeiten und die Größenverteilung von Mitochondrien konnte mit unserem experimentellen System nicht entdeckt werden. Dieser unauffällige Phänotyp ist jedoch möglicherweise auf eine zu niedrige Transgenexpression zurückzuführen. Dadurch ist eine endgültige Aussage über den Einfluß von LRRK2(G2019S) auf den Mitochondrien-transport nicht möglich. Trotzdem ist unser experimentelles System sehr gut zur Analyse des Mitochondrientransports geeignet, und es konnten mehrere neue Erkenntnisse über diesen schnellen, intrazellulären Logistikprozess gewonnen werden. In den Axonen des posterioren Seitenliniennervs ist der Prozentsatz an mobilen Mitochondrien deutlich höher als der der stationären Mitochondrien. Auch ist der Mitochondrientransport äußerst persistent in die jeweilige Richtung – anterograd oder retrograd. Beide Transportprozesse basieren auf unterschiedlichen Mechanismen und lassen sich aufgrund ihrer Parameter unterscheiden. Obwohl die Geschwindigkeitswerte für beide Richtungen breit gestreut sind, ist der retrograde Transport im Durchschnitt schneller als der anterograde. Der retrograde Verkehr ist außerdem ungleichmäßiger und wird durch häufigere Pausen unterbrochen. Desweiteren sind Mitochondrien, die sich in retrograder Richtung bewegen, etwas größer als Mitochondrien mit anterograder Transportrichtung.

Das zweite Zebrafischmodell repräsentiert einen Verlust der Pink1 Proteinfunktion und wurde von einer kooperierenden Forschungsgruppe bereitgestellt. Wir quantifizierten dopaminerge

Neuronen im Gehirn von 6 Monate alten Fischen durch Immunfluoreszenzfärbung gegen Tyrosinhydroxylase auf seriellen Gewebeschnitten. Ein Verlust dopaminerger Neuronen in charakteristischen Zellgruppen, die als homologe Strukturen zur *Substantia nigra, Pars compacta* des menschlichen Gehirns beschrieben wurden, konnte nicht festgestellt werden. Allerdings war eine statistische Auswertung der Daten aufgrund des zu geringen Probenumfangs nicht möglich. Andererseits konnten bei der elektronenmikroskopischen Analyse von Mitochondrien im Muskelgewebe von Larven und adulten Tieren klare ultrastrukturelle Veränderungen in Tieren mit Pink1-Defekt im Vergleich zum Wildtyp erkannt werden. Im Muskelgewebe der Mutante waren die Mitochondrien bereits im Larvenstadium deutlich vergrößert, und in adulten Tieren zeigten sie ein heterogenes Erscheinungsbild. Die mitochondriale Matrix war in einigen Organellen weniger Elektronendicht, und wies verminderte und ungeordnete Cristaemembranen auf. Dieser Phänotyp erinnert sehr an den anderer Tiermodelle des Morbus Parkinson.

## Abbreviations

2A	viral self-processing peptide	MeOH	methanol
4OH	4-hydroxy group	MJFF	Michael J. Fox Foundation
aa	amino acids	Mw	molecular weight
bp	base pairs	NBT	neuronal beta-tubulin
CMV	cytomegalovirus promoter	ORF	open reading frame
CNS	central nervous system	P	parental generation (=F0)
COR	C-terminal of Roc domain	PD	Parkinson's disease
DA	dopaminergic or dopamine agonist (see context)	PLL	posterior lateral line
DAT	dopamine transporter	Roc	Ras of complex proteins domain
dpf	days post fertilization	ROS	reactive oxygen species
ENU	N-ethyl-N-nitrosourea	RT-PCR	reverse transcription-polymerase chain reaction
ER, ER <sup>T2</sup>	estrogen receptor	T2A	viral self-processing peptide
EtOH	ethanol	Tg	transgenic construct or animal
F0, F1	generations of transgenic animals	TH	tyrosine hydroxylase
FP	fluorescent protein	TILLING	targeting induced local lesions in genomes
Gal4	yeast transcriptional activator	UAS	upstream activating sequence
H2B	histone 2B	WISH	whole-mount <i>in situ</i> hybridization
hpf	hours post fertilization	wt	wild-type
IHC	immunohistochemistry		
ISH	<i>in situ</i> hybridization		
kb	kilo bases		
kd	kinase-dead		
kDa	kilo Dalton		
LC3	MAP1-LC3, a ubiquitin-like autophagy regulator		
LSM	laser scanning microscope		
MAP	microtubule-associated protein		
MCS	multiple cloning site		

## Acknowledgements

I would like to thank the people who have made the experiments of this thesis and the writing of it possible. Foremost are all the people of the Reinhard Köster lab, the colleagues at the Institute of Developmental Genetics and all co-workers at other institutes and core facilities at the Helmholtz Center Munich.

First, I want to thank Prof. Reinhard Köster who provided the research project and who supervised my progress in his lab. I am grateful that I could get to know the vertebrate model organism zebrafish and that I could learn many tricks of its genetic and experimental manipulation. Thank you for training me on the confocal microscope and for introducing me to *in vivo* time-lapse imaging.

Next I would like to thank Prof. Wolfgang Wurst who approved and supervised my research work in the context of a thesis committee and who represented this dissertation at the Technical University Munich.

At this point I want to thank the other members of my thesis committee, Dr. Daniela Vogt Weisenhorn (Helmholtz Center) and Dr. Johannes Gloeckner (University of Tübingen and Helmholtz Center Munich). Both shared their valuable insights about the Parkinson's disease genes *LRRK2* and *PINK1*. They provided many useful hints and guidance to the project. Johannes Gloeckner also supplied me with important research material.

I am happy to remember the warm and helpful environment in the Köster lab. Dr. Martin Distel, Dr. Niklas Senghaas and Enrico Kühn were the first to instruct me in zebrafish experimental techniques. With Drs. Kazuhiko Namikawa and Thomas Weber I could discuss their as well as my own research results on numerous occasions, and they offered many useful comments. Dr. Jennifer Hocking provided me with Tol2kit vectors and gave helpful information about their use. Dr. Changsheng Liu often shared his cells for cell culture experiments with me. Dr. Anna-Lena Kerner was of great support especially at the time when the lab had moved to Braunschweig, as she stayed in Munich with me. Her presence was encouraging and her tips about computer programs were very much appreciated. Christiane Lach contributed to the great atmosphere during every day's work and her friendship goes beyond the lab. Last but not least, Petra Hammerl and the animal caretakers Sylvie Böhme, Anni Sedlmeir, Vera Banjac, Heike Grunewald and Yvonne Riedel were experts in handling and maintaining our zebrafish populations. A big thank-you goes to all of you.

This work could not have been done without the help of many others. The art of cryopreservation, sectioning and immunohistochemistry of zebrafish brain tissue was brought to me by Anja Folchert. Dr. Mario Wullmann (Ludwig Maximilian University Munich) helped me to get oriented in the zebrafish brain and to identify the characteristic dopaminergic cell clusters. He and his doctoral student, Ms. Sigrid Kress, also generously shared their protocols on tissue fixation and immunostaining with me. I am also indebted to Dr. Prisca Chapouton as she shared her zebrafish knowledge with me on many occasions. She also supplied me with reagents and equipment.

I am thankful to my collaborators, Prof. Oliver Bandmann and his team in Sheffield, which were working with and provided the *pink1* mutant zebrafish, to Mrs. Luise Jennen, Helmholtz Center Munich, for expert knowledge in electron microscopy and to Prof. Andreas Reichert, now Heinrich Heine University Düsseldorf, for the quantitative evaluation of mitochondrial ultrastructure.

Dr. Karina Kloos introduced me to the use of kymographs and provided the necessary software tools. The mathematician Mrs. Theresa Faus-Keßler offered her expertise for the statistical analysis of mitochondrial transport data, for which I am very thankful.

I appreciated the opportunity to take part in the lab meetings of Prof. Wolfgang Wurst's group, respectively Dr. Daniela Vogt Weisenhorn's group, as their research focus is on the functional analysis of Parkinson's disease genes using different mouse models. I also drew inspiration from the seminars of the SFB596 'Molecular Mechanisms of Neurodegeneration' at the German Center for Neurodegenerative Diseases, headed by Prof. Christian Haass.

I am grateful to the Helmholtz Center to be able to finish my research here in Munich after Reinhard Köster's group moved to Braunschweig in Mai 2011.

Finally, and most important, I want to thank my family, especially my sister and my mother, for their continued encouragement, advice and support. Our motto "always forward, always upwards" keeps me going and I know that often babysteps are required – "passo per passo".

My memories are also with Simone Grassi, who will always be an example for endurance and courage to me.

# Table of Content

Abstract .....	I
Zusammenfassung .....	III
Abbreviations .....	VI
Acknowledgements .....	VII
Table of Content .....	IX
<b>1 Introduction .....</b>	<b>1</b>
<b>1.1. Parkinson's Disease .....</b>	<b>1</b>
1.1.1. Clinical symptoms and pathologies .....	1
1.1.2. Treatment options in Parkinson's disease .....	3
1.1.3. Disease etiology .....	5
1.1.4. Environmental factors related to PD .....	6
1.1.5. The genetics of Parkinson's disease .....	9
<b>1.2. PINK1 .....</b>	<b>11</b>
<b>1.3. Leucine-Rich Repeat Kinase 2 .....</b>	<b>15</b>
1.3.1. Identification and characterization of LRRK2 .....	15
1.3.2. Enzymatic activities of wild-type and mutant LRRK2 .....	16
1.3.3. Additional hints on physiological and pathogenic functions .....	17
<b>1.4. Mitochondrial Transport .....</b>	<b>20</b>
<b>1.5. Autophagy .....</b>	<b>22</b>
<b>1.6. Zebrafish as a Model for PD Research .....</b>	<b>24</b>
1.6.1. A vertebrate model organism with many advantages .....	24
1.6.2. The zebrafish genome contains orthologs of PD genes .....	26
1.6.3. The zebrafish dopaminergic system .....	27
1.6.4. Our sophisticated experimental toolbox to generate PD models .....	29
<b>1.7. Aim of the Study .....</b>	<b>31</b>
<b>2 Materials and Methods .....</b>	<b>33</b>
<b>2.1. Reagents and Equipment .....</b>	<b>33</b>
2.1.1. Bacterial strains .....	33
2.1.2. Mammalian and zebrafish cell lines .....	33
2.1.3. Zebrafish strains .....	33
<u>2.1.3.1. Wild-type lines .....</u>	<u>33</u>
<u>2.1.3.2. Transgenic lines .....</u>	<u>33</u>
2.1.4. Chemicals and consumables .....	34
2.1.5. Enzymes and kits for molecular biology .....	34
2.1.6. Equipment .....	34
2.1.7. Software for image processing .....	35
2.1.8. Solutions, buffers and media .....	36
<u>2.1.8.1. E.coli and cell culture media .....</u>	<u>36</u>
<u>2.1.8.2. Zebrafish husbandry .....</u>	<u>36</u>
<u>2.1.8.3. In situ hybridization .....</u>	<u>36</u>

---

2.1.8.4. Cryosectioning and immunohistochemistry .....	37
2.1.8.5. Protein biochemistry .....	37
2.1.9. Antibodies .....	38
2.1.10. Plasmid vectors .....	39
2.1.11. Oligonucleotides for sequencing and cloning .....	43
<b>2.2. Experimental Procedures .....</b>	<b>44</b>
2.2.1. DNA and RNA manipulation and cloning .....	44
2.2.1.1. Plasmid transformation .....	44
2.2.1.2. Mini preparation of plasmid DNA .....	44
2.2.1.3. Maxi preparation of plasmid DNA .....	45
2.2.1.4. Restriction digest of plasmid DNA .....	45
2.2.1.5. DNA and RNA agarose gel electrophoresis .....	46
2.2.1.6. Extraction of DNA fragments from agarose gels .....	46
2.2.1.7. Purification of DNA from enzymatic reactions .....	46
2.2.1.8. Dephosphorylation of DNA fragments .....	46
2.2.1.9. DNA ligation .....	47
2.2.1.10. Removal of 5' DNA overhangs .....	47
2.2.1.11. PCR .....	47
2.2.1.12. RNA extraction from zebrafish embryos .....	48
2.2.1.13. cDNA synthesis .....	48
2.2.1.14. Synthesis of capped mRNA for microinjection into embryos .....	48
2.2.2. Zebrafish maintenance and genetic manipulation .....	49
2.2.2.1. Zebrafish maintenance .....	49
2.2.2.2. Zygotic microinjection of DNA and RNA .....	49
2.2.2.3. Embedding of embryos for microscopic observation .....	50
2.2.3. Histological techniques .....	50
2.2.3.1. Whole-mount <i>in situ</i> hybridisation (WISH) .....	50
2.2.3.2. Preparation of tissue cryosections .....	52
2.2.3.3. Immunohistochemistry (IHC) of tissue sections .....	53
2.2.4. Cell culture techniques .....	54
2.2.4.1. Maintenance and transfection of zebrafish Pac2 cells .....	54
2.2.4.2. Induction of autophagy in Pac2 cells .....	54
2.2.4.3. Maintenance and transfection of mammalian cells .....	55
2.2.5. Biochemical methods .....	56
2.2.5.1. Protein extraction from cultured cells .....	56
2.2.5.2. SDS-PAGE .....	56
2.2.5.3. Western blotting .....	57
2.2.6. Confocal microscopy .....	58
2.2.7. Transmission electron microscopy .....	59
2.2.7.1. Tissue preparation and image acquisition .....	59
2.2.7.2. Quantitative analysis of electron micrographs .....	59
<b>2.3. Mitochondrial Transport Analysis .....</b>	<b>59</b>
2.3.1. Generation of kymographs .....	59
2.3.2. Statistical evaluation of mitochondrial velocity and size data .....	60

<b>3 Results</b> .....	<b>61</b>
<b>3.1. Zebrafish <i>lrrk2</i> expression</b> .....	<b>61</b>
3.1.1. Human and zebrafish <i>lrrk2</i> transcripts .....	61
3.1.2. Expression analysis of zebrafish <i>lrrk2</i> .....	61
<b>3.2. Generation of a Neurodegeneration Model in Zebrafish based on Expression of Human LRRK2(G2019S)</b> .....	<b>64</b>
3.2.1. Generation of a neuron-specific KalTA3-expressing transgenic driver line ...	64
<u>3.2.1.1. Characterization of the 3.8 kb NBT promoter from <i>Xenopus laevis</i></u> ....	64
<u>3.2.1.2. The driver construct is bicistronic and co-expresses a nuclear-targeted blue fluorescent reporter</u> .....	66
<u>3.2.1.3. Cloning and analysis of a potentially ligand-inducible estrogen receptor-KalTA4 fusion protein</u> .....	71
<u>3.2.1.4. Establishing the transgenic driver line</u> .....	75
3.2.2. Generation of LRRK2-expressing effector constructs .....	82
<u>3.2.2.1. Modification and use of the Tol2kit Gateway-based cloning system</u> ...	82
<u>3.2.2.2. Evaluation of the fluorescent reporter cassette to label subcellular structures</u> .....	84
<u>3.2.2.3. Human <i>LRRK2</i> alleles are expressed as CFP-tagged fusion proteins</u> ...	89
<u>3.2.2.4. Combining fluorescent markers and disease gene in the final destination vectors</u> .....	91
<u>3.2.2.5. Detection of expression of the three transgenes in cell culture and <i>in vivo</i></u> .....	92
<u>3.2.2.6. Initiating the generation of transgenic effector lines</u> .....	97
<b>3.3. Imaging Mitochondrial Axonal Transport <i>in vivo</i> in the Posterior Lateral Line Nerve</b> .....	<b>98</b>
3.3.1. Choosing a driver line to label suitable neurons for axonal imaging .....	98
3.3.2. Optimizing parameters for reproducible image and data acquisition .....	101
3.3.3. General observations about mitochondrial transport in PLL axons .....	102
3.3.4. Establishing a method to quantify mitochondrial mobility .....	104
3.3.5. LRRK2(G2019S) does not affect mitochondrial transport <i>in vivo</i> .....	107
<b>3.4. Characterization of a Pink1 deficiency zebrafish disease model</b> .....	<b>116</b>
3.4.1. DA neuron numbers are not altered in adult brain of <i>pink1</i> mutant animals ...	116
3.4.2. Mitochondrial ultrastructure is altered in muscle tissue of <i>pink1</i> mutants ....	121
<b>4 Discussion</b> .....	<b>129</b>
<b>4.1. Zebrafish Swims into Focus as a New Parkinson's Disease Model</b> .....	<b>129</b>
<b>4.2. Mapping <i>LRRK2</i> Gene Expression</b> .....	<b>130</b>
<b>4.3. Setting the Stage for <i>in vivo</i> Imaging of Mitochondrial Axonal Transport</b>	<b>131</b>
4.3.1. A novel neuronal driver line with advantages and handicaps .....	131
4.3.2. Alternative zebrafish lines for neuron-specific gene expression .....	133
4.3.3. Reaching the limit with tri-functional effector constructs .....	134
4.3.4. Simplify your cloning and start with a transient transgenic approach first ...	136
<b>4.4. Mitochondrial Speed Dating in the Posterior Lateral Line Nerve</b> .....	<b>137</b>
4.4.1. Our standard operating procedure for mitochondrial transport imaging .....	137

4.4.2. Obtaining the bigger picture with extensive data collection and evaluation ..	139
4.4.3. The lack of a phenotype .....	139
4.4.4. Moving our understanding of mitochondrial trafficking forward .....	140
<b>4.5. The Pink1 Loss-of-function Mutant .....</b>	<b>143</b>
4.5.1. Mitochondrial form follows function in homeostasis and disease .....	143
4.5.2. Are DA neurons in zebrafish brain in the pink? .....	145
<b>4.6. A Final Glance at Pink1 and Lrrk2 Function, and future perspectives .....</b>	<b>147</b>
<b>5 Supplementary Movies .....</b>	<b>149</b>
<b>6 References .....</b>	<b>150</b>
<b>7 Appendix .....</b>	<b>171</b>
7.1. Eidesstattliche Erklärung .....	171
7.2. Publications .....	172
7.3. Curriculum Vitae .....	173

# 1 Introduction

## 1.1. Parkinson's Disease

Parkinson's disease (PD) is the second most common neurodegenerative disease after Alzheimer's disease and is a profound movement disorder. The typical age at onset is over 60 years and a sharp rise in incidence is seen with advancing age. About 1% of the general population older than 60 is affected, and this rises to about 5% within the population over 85 years of age (Samii *et al.*, 2004; Wood-Kaczmar *et al.*, 2006).

### 1.1.1. Clinical symptoms and pathologies

First described as 'shaking palsy' by the English surgeon James Parkinson in 1817, the clinical diagnosis nowadays, too, is connected to the appearance of the characteristic motor symptoms: resting tremor, bradykinesia (slowing of movement), rigidity and postural instability (Fahn, 2003; Jankovic, 2008; Lees *et al.*, 2009). The well-known appearance of a PD patient shows gait disturbances with rapid shuffling steps and posture problems with a forward-flexed posture when walking. Freezing of gait and falls are quite common at advanced stages of the disease. It is now known that in addition to the cardinal motor symptoms, non-motor brain functions are also affected. These include cognitive and autonomic dysfunctions, like loss of assertiveness, passivity, loss of motivation, anxiety, depression, sleep problems, constipation, bladder disturbances, olfactory and other sensory impairments (Fahn, 2003; Jankovic, 2008; Pedrosa and Timmermann, 2013). Additionally, there is a high risk of developing dementia. For this, age clearly is a risk factor and patients typically develop dementia in their 70s, including those with a young age at onset of PD (Fahn, 2010). PD has a long preclinical period before the manifestation of the typical motor symptoms and many of the non-motor dysfunctions are prodromal features of the disease, e.g. olfactory impairment, dysfunction of the autonomic nervous system, depression, cognitive impairment and sleep disturbance. These can be used as early diagnostic markers for the disease.

The motor symptoms of PD are associated with the pathological hallmark of the disease, which is the loss of pigmented dopaminergic (DA) neurons in the *substantia nigra pars compacta* (SNpc), a brain structure located in the midbrain (Fahn, 2003; Lees *et al.*, 2009). The substantia nigra provides dopaminergic input to the striatum and plays an important role in the control of the execution of movement via the neuronal circuits of the basal ganglia

(Figure 1). It is known from research conducted in animals in the 1950s and 60s that a lack of dopamine in the striatum is causative for the motor dysfunctions (Carlsson *et al.*, 1957; Ehringer and Hornykiewicz, 1960; Cotzias *et al.*, 1967). However, when first motor symptoms occur in patients about 60% of DA neurons in the SNpc have already degenerated and are lost (Fahn, 2003). Other brain areas are also affected by neuronal loss and this is accompanied by a second characteristic histopathological finding in PD brains, which is the presence of proteinaceous cytoplasmic inclusions called Lewy bodies (LB) and Lewy neurites, the latter being located in neuronal processes (Lees *et al.*, 2009). Lewy bodies are abnormal protein aggregates consisting mainly of  $\alpha$ -synuclein and of many other proteins, albeit in low abundance, e.g. ubiquitin, neurofilament, Tau and other microtubule-associated proteins, heat shock proteins and proteasomal subunits (Shults, 2006; Wakabayashi *et al.*, 2013). LBs can be found in brains of most Parkinson patients, as well as in dementia with Lewy bodies, Alzheimer's disease and several other neurological disorders. They are distributed over the whole central nervous system, including the olfactory bulb, hypothalamus, substantia nigra, locus ceruleus, nucleus basalis of Meynert, dorsal vagal nucleus, raphe nuclei and cerebral

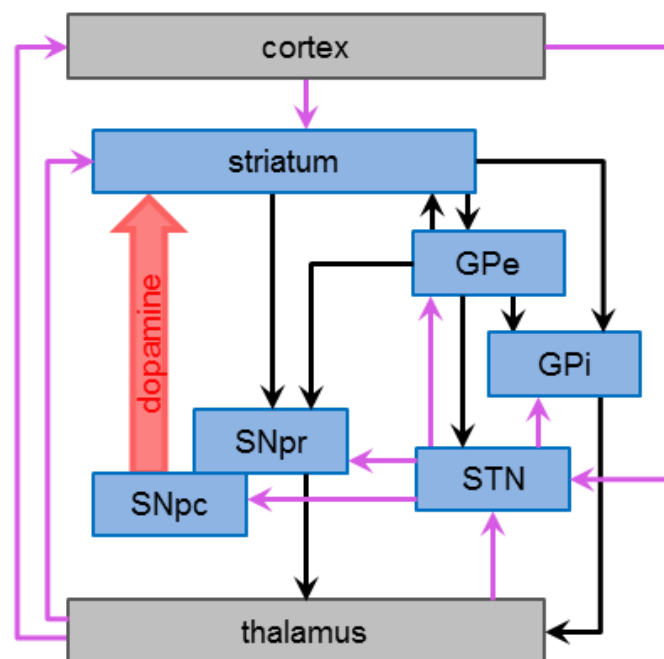


**Figure 1. The circuitry of the basal ganglia.** The neuroanatomical components of the basal ganglia, also called basal nuclei, are labelled in blue. Their interconnectivity, as well as pathways to and from the thalamus and cortex, is depicted. Black pathways indicate inhibitory connections and pink pathways indicate excitatory connections. The dopaminergic projections from the SNpc to the striatum are highlighted in red. This input is severely compromised in Parkinson's disease. Abbreviations are: GPe, external part of the *globus pallidus*; GPi, internal part of the *globus pallidus*; SNpr, *substantia nigra pars reticulata*; SNpc, *substantia nigra pars compacta*; STN, subthalamic nucleus. Drawing adapted from Gillies *et al.*, 2002.

cortex. They can also be detected in cells of the peripheral autonomic nervous system, and this widespread distribution of LB pathology may be responsible for the variety of non-motor symptoms of the disease. Braak *et al.*, in 2003 and 2004, proposed a staging schema for the spread of LB pathology in the progression of PD, in which early  $\alpha$ -synuclein aggregates are detectable in the olfactory bulb and the brainstem (stage 1). Pathology progresses from the brainstem in an antero-dorsal direction through the caudal raphe nuclei and the locus ceruleus (stage 2) to the substantia nigra and neostriatum (stage 3). Later, the mesocortex and thalamus become involved (stage 4) and finally pathology spreads through the neocortex (stages 5 and 6). However, the Braak staging system is discussed controversially as the severity of clinical symptoms is not always correlated with the distribution of LB pathology, and some cases of familial PD linked to mutations in *parkin* or *LRRK2* do not show LB pathology (Wood-Kaczmar *et al.*, 2006; Biskup and West, 2009; Fahn, 2010). Finally, more recent molecular biological research about the pathogenic mechanisms of  $\alpha$ -synuclein indicates that LBs are not the cytotoxic species and likely represent a detoxification response of cells via the aggresome pathway. Thereby, cells are eliminating the cytotoxic soluble  $\alpha$ -synuclein oligomers and protofibrils by depositing them in cytoplasmic inclusions (Tanaka *et al.*, 2004; Olanow *et al.*, 2004; Shults, 2006; Wakabayashi *et al.*, 2013).

### 1.1.2. Treatment options in Parkinson's disease

PD is still a relentlessly progressive incurable disease. A plethora of symptomatic treatment options from different medical fields are available today, and these substantially improve motor and non-motor symptoms, delay the progressive course – at least of the symptoms – and improve the quality of life for the patients and their families (reviewed by Pedrosa and Timmermann, 2013).

Dopamine replacement therapy has been used for over 30 years and is still the major medical approach. Drug treatment starts when the patient is functionally impaired. Depending on the patient's age and severity of motor symptoms the first drugs used are either levodopa or a dopamine agonist (Samii *et al.*, 2004; Pedrosa and Timmermann, 2013). Levodopa, a precursor of dopamine, is given in combination with a peripheral decarboxylase inhibitor (e.g. carbidopa) to reduce the adverse side effects from elevated dopamine levels in peripheral tissues. However, patients treated with levodopa tend to develop motor complications, fluctuations and/or dyskinesias, after 4-6 years. An alternative medication is the use of dopamine agonists (DAs), which bind and activate postsynaptic dopaminergic receptors in the striatum. Dopamine agonists, like pramipexole, ropinirole, rotigotine and priribedil are

considered safe and efficacious, and are recommended for treatment in younger patients and in patients with milder symptoms, either as monotherapy or in combination with L-dopa. However, dopamine agonists, too, cause psychiatric and nonmotor side effects, which have to be monitored closely (Pedrosa and Timmermann, 2013). Another approach to elevate endogenous dopamine levels in the brain or to prolong the plasma half-life of levodopa is to inhibit its metabolization by monoamine oxidase type B (MAO-B). Available MAO-B inhibitors are selegiline or rasagiline. These can be used as monotherapy to improve motor symptoms and delay the need for levodopa in early stages of the disease. They can also be used in combination with levodopa or with DAs. Selegiline and rasagiline, as well as pramipexole and coenzyme Q10 have also been found to delay the disease progress in animal models of PD. To date, however, few results were reproducible in humans. Rasagiline possibly delays clinical progression in early stages of the disease and is therefore considered a good treatment choice in younger patients (Fahn, 2010; Pedrosa and Timmermann, 2013).

Another surgical approach for symptomatic therapy is deep brain stimulation (DBS). Here, an electronic pacemaker is placed into the brain, which electrically stimulates the desired target structure. Several structures of the basal ganglia circuitry can be selected, with the internal globus pallidus and the subthalamic nucleus (Figure 1) being the most common targets for DBS (Pedrosa and Timmermann, 2013). Deep brain stimulation is typically practiced in severe PD cases and in patients who are no longer responding to medication.

In summary, several treatment options are available today, which can ameliorate most symptoms. But it has to be kept in mind that all therapies have long-term side effects and cannot stop the progressive neuronal loss. Not only to reduce the enormous treatment costs but also to further improve the quality of life of the patients, more effective therapies are needed. Especially, neuroprotective therapies, which can halt disease progression, need to be developed urgently. To achieve this, a clear understanding of the causes of PD and the underlying neuropathological mechanisms is required. Secondly, suitable animal models have to be generated, which recapitulate major disease processes and which can be used to screen for disease-modifying active compounds.

### 1.1.3. Disease etiology

Through numerous epidemiological and genetic studies important insights into the factors contributing to the disease have been gained over the last years. PD is considered a multifactorial disease, with environmental influences and the genetic background of the individual contributing to the demise of the specifically vulnerable dopaminergic neurons (Figure 2). Aging is the greatest risk factor and it goes along with a reduced capacity of cells to deal with stress (Collier *et al.*, 2011; Green *et al.*, 2011). The ‘multiple hit hypothesis’ proposes that neurodegenerative conditions are caused by the summation of several unrelated insults/hits experienced over the lifetime, including genetic mutations and epigenetic changes, environmental factors (e.g. infections, inflammation, toxin exposure) and an age-related decline in cellular homeostasis (Carvey *et al.*, 2006; Sulzer, 2007). Each hit compromise the regenerative potential of the cell and, finally, the homeostatic balance is tilted towards cell death. In addition, evidence is accumulating that many insults converge on mitochondria, and mitochondrial dysfunction may be one of the major pathogenic and cytotoxic mechanisms in PD.

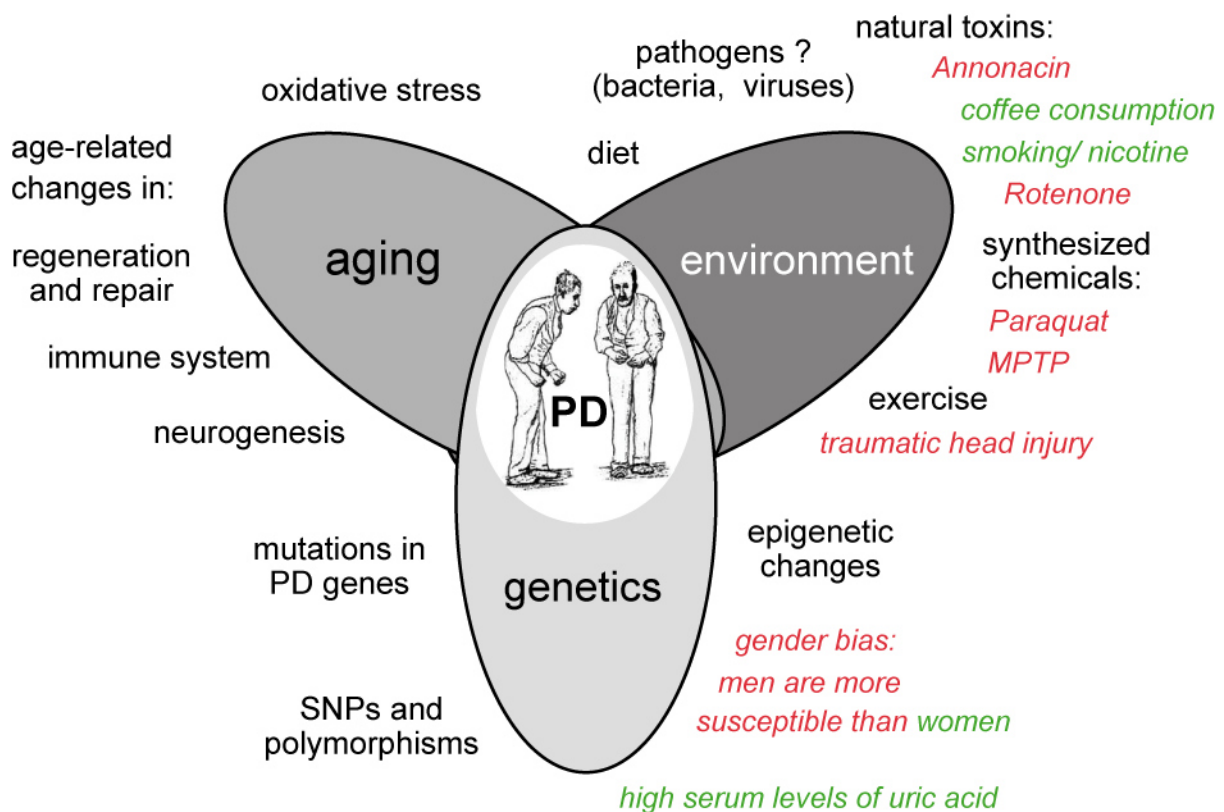


**Figure 2. Many factors can contribute to the development of PD.** Most cases of PD are sporadic with unknown etiology. It is suspected that several factors including environmental influences and genetic susceptibilities contribute to the disease. Aging is a high-risk factor probably due to adverse changes in homeostatic and regenerative processes, as well as in immune function. Through epidemiological studies some factors have been associated with a protective effect (indicated in green), while other factors seem to enhance the risk for PD (indicated in red) (genuine drawing).

#### 1.1.4. Environmental factors related to PD

What roles do environmental factors play in the pathogenesis of PD? In 1983, Langston and colleagues reported several cases of drug users in Northern California, who developed acute parkinsonian symptoms after accidental intake of MPTP (1-methyl-4-phenyl-1,2,3,6-tetrahydropyridine), which was identified as the toxic byproduct in the synthesis of an illicit opioid analogue (Langston *et al.*, 1983). From experimental studies in animals it is now known that MPTP freely crosses the blood-brain barrier and is converted to the neurotoxic metabolite MPP<sup>+</sup> (1-methyl-4-phenylpyridinium) by astrocytes (Figure 3). MPP<sup>+</sup> has a high affinity for the dopamine transporter (DAT) in the plasma membrane of dopaminergic neurons and is selectively taken up by this neuronal type. It is a potent inhibitor of respiratory complex I of mitochondria, which causes mitochondrial dysfunction (Samii *et al.*, 2004; Drechsel and Patel 2008; Bové and Perier, 2012). Neuropathological analysis of individuals, who had been exposed to MPTP, as well as in animal models revealed a selective degeneration of dopaminergic neurons of the nigrostriatal pathway. MPTP, respectively its metabolite MPP<sup>+</sup>, was the first exogenous toxin that has been directly linked to the development of an acute and irreversible parkinsonism in humans, which is clinically indistinguishable from sporadic PD. With this discovery it was evident that substances in the environment can contribute to this neurodegenerative disease. Additionally, attention was focussed on complex I inhibitors and other mitochondrial toxins.

In the following years, numerous epidemiological studies were conducted to identify environmental risk factors for PD, but these studies were often performed with limited resources (e.g. exposure to a specific toxin is difficult to evaluate in humans) and are therefore of questionable quality (Berry *et al.*, 2010). Identified risk factors include herbicides and pesticides (e.g. rotenone, paraquat, maneb) and living in rural areas (in industrialized countries), exposure to metals (manganese and lead) and drinking well water (Samii *et al.*, 2004; Lees *et al.*, 2009). Interestingly, coffee/caffeine consumption and smoking are associated with a reduced risk of developing PD (Ross *et al.*, 2000; Ascherio *et al.*, 2001; Hernán *et al.*, 2001; Thacker *et al.*, 2007).

Rotenone, a naturally occurring compound extracted from the roots of certain plants, is used as an insecticide and piscicide to kill fish populations in lakes and reservoirs. Its mode of action is well characterized and it, too, is a specific inhibitor of complex I of the electron transport chain of mitochondria (Drechsel and Patel 2008; Bové and Perier, 2012). Rotenone is lipophilic and easily passes biological membranes (Figure 3). When infused continuously over several days or weeks into rats, it acts as a systemic inhibitor of complex I. Interestingly,

treated animals selectively present with the typical neuropathology of PD, namely nigrostriatal dopaminergic degeneration and cytoplasmic inclusions similar to Lewy bodies (Betarbet *et al.*, 2000). However, the role of rotenone in the development of the human disease is unclear as only few people, farmworkers and people handling the compound, are exposed.

Paraquat is an herbicide that was used worldwide and was banned in the European Union in 2007. It is known that it exerts its cytotoxic effects through induction of oxidative stress (Figure 3). It attracted attention in the PD field because it has a similar chemical structure to MPP<sup>+</sup> (Drechsel and Patel 2008; Bové and Perier, 2012). However, its mode of action is different from that of MPP<sup>+</sup>. Paraquat is not an inhibitor of complex I, instead it induces a process of redox cycling together with a cellular enzyme, e.g. nitric oxide synthase, which leads to the subsequent production of reactive oxygen species (ROS). Several studies in rodents suggest that paraquat can cause lesions in the *substantia nigra pars compacta*. The role of paraquat in the context of PD in humans has been reevaluated recently, and the evidence that this compound favors the onset of PD was found to be inconclusive and based on insufficient epidemiological data (Berry *et al.*, 2010).

Nevertheless, MPTP, rotenone and paraquat (as well as 6-hydroxydopamine, as shown in Figure 3) have been used to generate toxin-based animal models of PD, which have been useful to recapitulate and elucidate some aspects of the specific neurodegeneration (Drechsel and Patel 2008; Berry *et al.*, 2010; Bové and Perier, 2012). Why are DA neurons especially susceptible to these compounds? It is known that the toxins increase the oxidative stress in neurons either directly or indirectly by inflicting mitochondrial dysfunction. Currently, the hypothesis is that DA neurons due to their physiology (DA metabolism, interaction of cytosolic DA with  $\alpha$ -synuclein, high intracellular Ca<sup>2+</sup> used to generate action potentials) are already under a high level of endogenous stress and therefore specifically susceptible to increased oxidative stress (Fahn, 2010; Exner *et al.*, 2012).

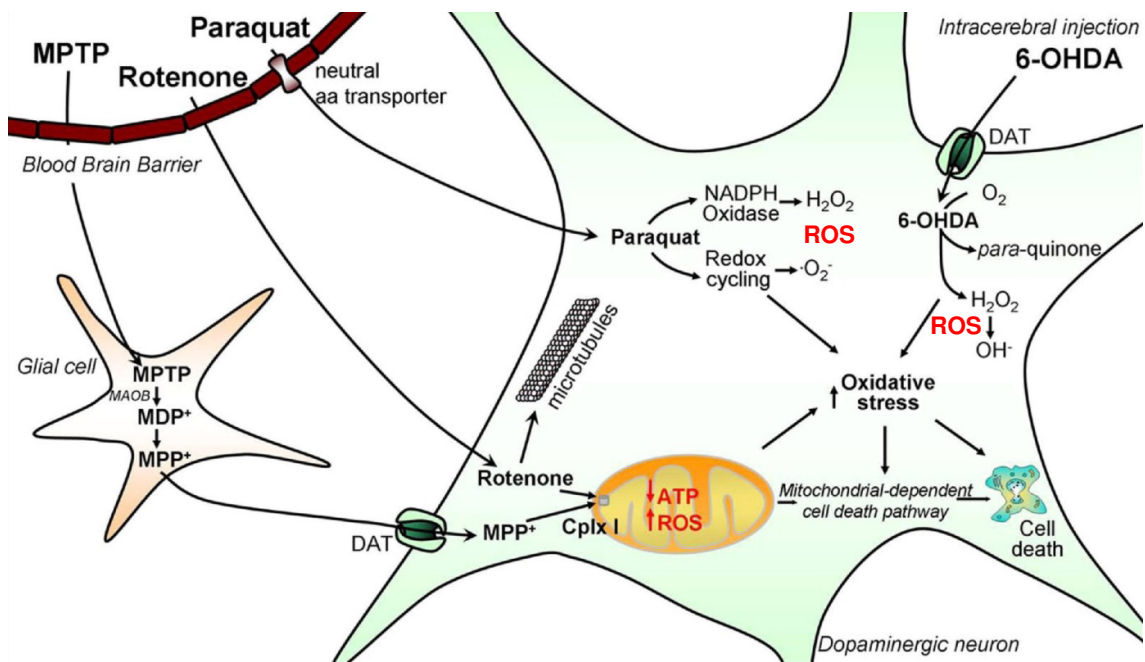


**Figure 3. Toxic mechanisms of synthetic and environmental compounds used to produce Parkinson's disease animal models.** The production of reactive oxygen species (ROS) and the induction of oxidative stress in DA neurons are the main mechanisms of action of various toxins implicated in PD pathology. Following stereotactic injection into the brain of rodents, 6-hydroxydopamine is specifically taken up by DA neurons via the dopamine transporter (DAT). It is oxidized in a stepwise reaction with the concomitant production of ROS, and para- and semiquinone products. MPTP and rotenone are highly lipophilic compounds and can cross the blood-brain barrier. MPTP is converted to its toxic product MPP<sup>+</sup> by the enzyme monoamine oxidase B (MAOB) in astrocytes. MPP<sup>+</sup> is released from astrocytes and specifically enters DA neurons via the DAT, where complex I of the mitochondrial respiratory chain is its primary target of inhibition. The disruption of electron transport in mitochondria triggers ROS production and causes dissipation of the mitochondrial membrane potential with subsequent inhibition ATP synthesis. This can trigger a mitochondria-dependent cell death pathway. The pesticide rotenone is a known complex I inhibitor. Additionally, it affects and destabilizes microtubules, which contributes to the cell death process. Paraquat is a quick-acting and non-selective herbicide that destroys green plant tissue on contact. Its mechanism of action is different to that of the aforementioned compounds. It induces ROS production and oxidative damage via the process of redox cycling together with a cellular enzyme. The superoxide radical is a key mediator of its toxicity. Paraquat can also activate ROS-generating enzymes, such as NADPH oxidases, that contribute to toxicity. Drawing adapted from Bové and Perier, 2012.

### 1.1.5. The genetics of Parkinson's disease

Historically, PD was considered a sporadic disorder. But during the last two decades intensive research has revealed an important genetic contribution to the disease. Linkage analysis in families with Mendelian inheritance of the disease allowed mapping of 18 genetic loci, called *PARK1* to *18*, which are associated with dominantly or recessively inherited PD. Most of the affected genes could subsequently be identified by positional cloning (Gasser, 2009; Lesage and Brice, 2009; Klein and Westenberger, 2012). Table 1 provides a description of the genes. Although most PD cases are of unknown etiology, up to 10% of patients represent a monogenic familial form of the disease. More recently, genome-wide association studies (GWAS) have shown that mutations or common genetic variants at some of the identified loci correspond to several cases of sporadic PD (Satake *et al.*, 2009; Simón-Sánchez *et al.*, 2009). These polymorphisms or gene variants can therefore be considered genetic risk factors of the disease (Figure 2). They also support the idea that inherited and sporadic cases have common pathological mechanisms.

A detailed analysis of the identified genes and their products ensued immediately after their discovery and is still ongoing. Research is performed with cellular systems and by genetic manipulation of the classical model organisms, *Drosophila*, *C. elegans* and mice, allowing the dissection of molecular pathways implicated in the pathogenesis. The results obtained have greatly expanded our understanding of the underlying pathogenic molecular mechanisms. Again, defects in mitochondrial biology, oxidative stress, and impaired clearance of misfolded proteins and dysfunctional organelles by proteasomal and autophagy pathways were identified as the root cause leading to neuronal dysfunction (reviewed by Dawson *et al.*, 2010; Corti *et al.*, 2011, Martin *et al.*, 2011; Exner *et al.*, 2012).

The molecular era of PD research started in 1997 with the identification of the first gene encoding  $\alpha$ -synuclein by Polymeropoulos and colleagues. So far three missense mutations in *SNCA*, as well as duplications and triplications of the genomic locus segregate with autosomal dominant PD. Soon after,  $\alpha$ -synuclein was found to be the main protein component of Lewy bodies, and this was an immediate hint that the proteasomal protein degradation pathway might be impaired, leading to aberrant protein accumulation and possibly cell death (Martin *et al.*, 2011; Exner *et al.*, 2012).  $\alpha$ -synuclein appears to be a natively unfolded protein in aqueous solutions *in vitro* and has a high propensity to aggregate. It is now known that it can bind to synaptic vesicles and the plasma membrane and is likely involved in synaptic vesicle membrane fusion and neurotransmission, and these processes could be disrupted early in the pathogenic process.

<b>Table 1 Summary of Parkinson's disease-associated genes and loci</b>					
<b>PARK locus</b>	<b>Gene name/ gene symbol</b>	<b>Inheritance</b>	<b>Pathogenic mutations</b>	<b>Clinical features</b>	<b>First description</b>
<b>PARK1 = PARK4</b>	$\alpha$ -synuclein/ <i>SNCA</i>	dominant, rarely sporadic	missense, duplication, triplication	A30P: late onset, L-dopa responsive; E46K: dementia with Lewy bodies-like symptoms; A53T: typical parkinsonism with rapid progression; duplication: typical parkinsonism; triplication: early onset parkinsonism with rapid progression	Polymeropoulos, et al., 1997; Singleton et al., 2003
<b>PARK2</b>	<i>parkin/ PRKN</i>	recessive, sporadic	missense, nonsense, frameshift	juvenile, early onset, slow progression with spasticity and sleep benefits, dyskinesia, dystonia	Kitada et al., 1998
<b>PARK3</b>	sepiapterin reductase/ <i>SPR</i>	dominant	not identified	late onset, dementia	Gasser et al., 1998
<b>PARK5</b>	<i>ubiquitin carboxyl- terminal esterase L1/ UCHL1</i>	dominant	missense	late onset, similar to sporadic PD	Leroy et al., 1998
<b>PARK6</b>	<i>PTEN-induced kinase1/ PINK1</i>	recessive	missense, nonsense, frameshift, rare large deletions	early onset typical parkinsonism with psychiatric symptoms and L-dopa associated dyskinesia, slow progression	Valente et al., 2004
<b>PARK7</b>	<i>DJ-1</i>	recessive	missense, large deletions	early onset parkinsonism with psychiatric symptoms, dystonia	Bonifati et al., 2003
<b>PARK8</b>	leucine-rich repeat kinase 2/ <i>LRRK2</i>	dominant, sporadic	missense, 5 pathogenic mutations including the common G2019S	middle to late onset typical parkinsonism with response to L-dopa	Paisan-Ruiz et al., 2004; Zimprich et al., 2004
<b>PARK9</b>	<i>ATPase type 13A2/ ATP13A2</i>	recessive	missense	early onset, rapid progression, pyramidal signs, dementia	Ramirez et al., 2006
<b>PARK10</b>	unknown	unclear	not identified	late onset, not well characterized	Hicks et al., 2002
<b>PARK11</b>	<i>GRB10 inter- acting GYF protein 2/ GIGYF2</i>	dominant	missense	late onset, not well characterized	Pankratz et al., 2002 and 2003
<b>PARK12</b>	unknown	unclear	not identified	late onset, not well characterized	Pankratz et al., 2003
<b>PARK13</b>	<i>HtrA serine peptidase 2/ HTRA2</i>	dominant	missense	late onset, typical parkinsonism	Strauss et al., 2005
<b>PARK14</b>	phospholipase A2 groupVI/ <i>PLA2G6</i>	recessive	missense	juvenile, early onset, rapid progression, cognitive decline and brain atrophy (cerebellum and cerebrum), L-dopa responsive dystonia-parkinsonism	Paisan-Ruiz et al., 2009
<b>PARK15</b>	F-box protein 7/ <i>FBXO7</i>	recessive	missense, frameshift	early onset parkinsonism with spasticity, pyramidal signs	Shojaee et al., 2008
<b>PARK16</b>	unknown	unclear, sporadic	not identified	not characterized	Satake et al., 2009
<b>PARK17</b>	vacuolar protein sorting 35 homolog/ <i>VPS35</i>	dominant	missense	late onset, typical parkinsonism	Vilariño-Güell et al., 2011; Zimprich et al., 2011
<b>PARK18</b>	eukaryotic translation initiation factor 4 gamma 1/ <i>EIF4G1</i>	dominant	missense	late onset, typical parkinsonism	Chartier-Harlin et al., 2011

The table is adapted from Wirdefeldt et al., 2011, and includes information from Chartier-Harlin et al., 2011; Corti et al., 2011, Vilariño-Güell et al., 2011; Zimprich et al., 2011, Saiki et al., 2012. For information about references not cited in this thesis see Wirdefeldt et al., 2011. Genes analysed in this study are highlighted in yellow.

Mutations in three genes – *parkin*, *PINK1* and *DJ-1* – were identified as the cause of recessive early-onset PD, with an occurrence of clinical symptoms before the age of 40. *PINK1* encodes a mitochondria-targeted kinase (Valente *et al.*, 2004) that can also be found in the cytoplasm. It has since been implicated in several aspects of mitochondrial biology including mitochondrial dynamics (fission and fusion) and transport (Exner *et al.*, 2012; de Vries and Przedborski, 2013), as will be outlined in more detail in the next chapter. Parkin is an E3 ubiquitin ligase, and these enzymes are commonly responsible to tag dysfunctional proteins for degradation by the ubiquitin-proteasome system. More recent studies suggest that PINK1 and Parkin function in a mitochondrial quality control pathway that goes awry in PD, again with the suspected consequences of mitochondrial dysfunction and oxidative damage (Narendra *et al.*, 2008; Jin and Youle, 2012). DJ-1, too, seems to play a role in the protection against oxidative stress and its specific function might be the detoxification of mitochondrial H<sub>2</sub>O<sub>2</sub> (Andres-Mateos *et al.*, 2007; Martin *et al.*, 2011; Exner *et al.*, 2012).

Mutations in other genes could disrupt cellular homeostasis in several ways. Mutant ATP13A2, a lysosomal ATPase, may cause lysosomal dysfunction with subsequent inhibition of autophagy. Mutations in the *LRRK2* gene segregate with autosomal dominant late-onset parkinsonism and are the most common genetic cause of PD, accounting for up to 4% of familial cases. The gene encodes a large protein composed of multiple functional domains, which supported the idea that it may play a role in several different cellular signalling pathways, as will be outlined in Chapter 1.3.

## 1.2. PINK1

When *PTEN-induced kinase 1* (*PINK1*) was identified in 2004 as the gene responsible for *PARK6*-linked autosomal recessive, early-onset PD, its sequence containing a mitochondrial targeting motif immediately implied that this kinase is associated with mitochondria and likely affects their function (Valente *et al.*, 2004) (Figure 4). In this initial study and later analyses, PINK1 has been shown to exert a protective effect in the context of diverse cellular stressors and in a kinase dependent manner (reviewed by Exner *et al.*, 2012). PD-associated missense or nonsense mutations in PINK1 (Figure 4; list of mutations in Deas *et al.*, 2009) abrogate its protective effect, and several mutations have been shown to impair kinase activity or to reduce the stability of the protein, in accordance with a loss-of-function mechanism.

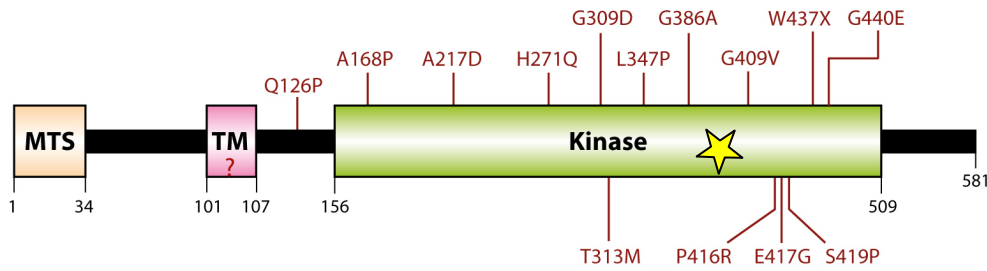


**Figure 4. PINK1 protein domains and pathogenic mutations.** PINK1 is a cytosolic and mitochondria-localized serine/threonine kinase of 581 amino acids. 30 pathogenic *PINK1* mutations have been identified and positions of some of the amino acid substitutions or a deletion (W437X) are indicated. Enzymatic activity is marked by a yellow star. The graph is adapted from Martin *et al.*, 2011. Abbreviations: MTS, mitochondrial targeting sequence; TM, putative transmembrane domain.

Experiments of PINK1 deficiency conducted in *Drosophila* produced a strong phenotype with reduced life span, impaired locomotor activity and flight muscle degeneration, male sterility and clear mitochondrial ultrastructural abnormalities (Clark *et al.*, 2006; Park *et al.*, 2006; Yang *et al.*, 2006). These studies also revealed that loss of PINK1 leads to a very similar phenotype to loss of Parkin function, which is an indication that both gene products act in a common pathway. And indeed, Parkin expression could rescue the PINK1 mutant phenotype in flies and also in cell culture experiments but not *vice versa*, thereby placing Parkin downstream of PINK1 in the same pathway (Clark *et al.*, 2006; Park *et al.*, 2006; Yang *et al.*, 2006; Exner *et al.*, 2007; Lutz *et al.*, 2009). Research conducted by Richard Youle's laboratory provided the first evidence – and more details later – that both proteins act together in a mitochondrial quality control pathway whereby dysfunctional mitochondria are sorted out for degradation by a special form of autophagy, called mitophagy (Narendra *et al.*, 2008; Narendra *et al.*, 2010). These observations could be reproduced and extended by other labs, and the following scenario emerged: PINK1 is a short-lived mitochondrial protein under normal conditions. It is targeted to mitochondria, where it is quickly processed by mitochondrial proteases, released back into the cytosol and degraded (Jin *et al.*, 2010; Deas *et al.*, 2011; Meissner *et al.*, 2011). Mitochondrial damage followed by dissipation of the mitochondrial membrane potential blocks PINK1 processing and leads to an accumulation of full-length PINK1 at the outer mitochondrial membrane, with the kinase domain facing the cytoplasm (Jin *et al.*, 2010; Matsuda *et al.*, 2010; Narendra *et al.*, 2010). This step is followed by Parkin activation and translocation to damaged mitochondria, and subsequent ubiquitination of substrate proteins (Geisler *et al.*, 2010; Lee *et al.*, 2010b; Vives-Bauza *et al.*, 2010; Chan *et al.*, 2011; Seibler *et al.*, 2011; Lazarou *et al.*, 2012; Sarraf *et al.*, 2013). Some of these ubiquitinated proteins are degraded by the proteasome. Others may act as molecular

flags to attract ubiquitin-binding adaptor proteins to the damaged mitochondria, which in turn recruit the autophagic machinery. Several of the molecular details of this process are still incompletely understood; e.g. do PINK1 and Parkin interact by direct binding; which substrates does PINK1 phosphorylate on mitochondria; what are the genuine Parkin substrates and how are autophagic membranes recruited. Additionally, experiments so far have mainly been performed with tumor cell lines (e.g. HeLa cells) or with murine embryonic fibroblasts (MEFs), in the presence of overexpressed Parkin and by treating cells with the mitochondrial uncoupling agent CCCP (carbonyl cyanide 3-chlorophenylhydrazone) to trigger mitochondrial dysfunction. So, it is not clear to what extent this quality control pathway is relevant in neurons *in vivo* and if it is activated under physiological stress conditions.

PINK1 also affects other mitochondrial processes and functions. Mitochondria form highly dynamic tubular networks in cells that constantly undergo fission and fusion, and this exchange of material is required to maintain a healthy and functional mitochondrial pool by facilitating replacement of damaged components, including mitochondrial DNA (Campello and Scorrano, 2010; Palmer *et al.*, 2011; Pilsl and Winklhofer, 2012). Additionally, mitochondria are moved around inside cells through active transport processes along microtubule tracks and the actin cytoskeleton (Cai *et al.*, 2011; Saxton and Hollenbeck, 2012; Sheng and Cai, 2012) (see Chapter 1.4).

Alterations in mitochondrial morphology due to changes in the fission-fusion dynamics have been reported in several PINK1 PD models, albeit with conflicting observations depending on the experimental system used. While PINK1- and Parkin-deficient flies show a phenotype with elongated mitochondria, supposedly as a result of excess fusion, the opposite is true for cultured mammalian cells (reviewed by Exner *et al.*, 2012; de Vries and Przedborski, 2013). Here, acute loss of PINK1 or Parkin causes mitochondrial fragmentation, which is dependent on the fission-promoting factor Drp1. However, cells from *PINK1* knock-out mice show no characteristic mitochondrial phenotype, indicating that compensatory mechanisms are taking place. In this regard, the fly phenotype can be interpreted as an overshooting compensation leading to hyperfusion of mitochondria.

Recently, human PINK1 was found to interact with the mitochondrial outer membrane Rho-like GTPase Miro2 and the adaptor protein Milton, which links mitochondria to kinesin motor proteins (Weihofen *et al.*, 2009). This observation indicated that PINK1 might affect mitochondrial transport. Later, Miro1 was shown to be phosphorylated by PINK1 and subsequently degraded in a Parkin-dependent manner. This observation fits to a model

whereby degradation of Miro on damaged mitochondria by the PINK1/Parkin pathway stops mitochondrial transport and facilitates their clearance by mitophagy.

Last but not least, PINK1 (and not Parkin) seems to have a direct influence on respiratory complex I activity and mitochondrial energy production. Loss of PINK1 in flies leads to defects in complex I activity and reduced ATP levels, and this deficiency can be rescued by expression of Ndi1p, the yeast NADH dehydrogenase that can bypass electron transport in complex I (Morais *et al.*, 2009; Vilain *et al.*, 2012). Recently, the gene *heixuedian* (*heix*) was identified as a suppressor of the *Drosophila* PINK1-mutant energy-depletion phenotype and its protein product is involved in the synthesis of vitamin K2, another electron carrier of the electron transport chain (Vos *et al.*, 2012).

In general, data on PINK1 function are multifarious and seem to depend on the specific experimental set-up. It has also to be kept in mind that all mitochondrial molecular processes (fission-fusion, transport, ATP synthesis) are interdependent, and an effect on one process will influence the others. Finally, most experiments have either been conducted in *Drosophila* or in cell culture systems in the context of protein knock-down or overexpression and using harsh mitochondrial stressors, like CCCP. More physiological experiments clearly have to be conducted. In addition, important animal models – mice with targeted null mutations in *PINK1* – do not recapitulate the dopaminergic neurodegeneration of the human pathology (Kitada *et al.*, 2007; Zhou *et al.*, 2007; Gautier *et al.*, 2008; Gispert *et al.*, 2009). Better animal models are therefore required to study pathogenic processes on the cellular level *in vivo*.

### 1.3. Leucine-Rich Repeat Kinase 2

#### 1.3.1. Identification and characterization of LRRK2

By genetic analysis of patients from several families with dominantly inherited *PARK8*-linked PD, two research groups could identify point mutations in coding exons of the *leucine-rich repeat kinase 2* gene (Paisán-Ruíz *et al.*, 2004; Zimprich *et al.*, 2004). The *LRRK2* gene consists of 51 exons and encodes a large protein of 2527 aa with a molecular weight of 280 kDa. Sequence analysis identified several functional domains including protein-protein interaction domains, as well as two enzymatic domains, as depicted in Figure 5. LRRK2 belongs to the ROCO protein family, characterized by the Roc (Ras of complex proteins) domain with GTPase activity followed by the COR (C-terminal of Roc) linker domain. A kinase domain, which has sequence similarity to receptor-interacting protein kinases (RIPKs) and mixed-lineage kinases (MLKs), a subclass of the mitogen-activated protein kinase kinase kinase (MAPKKK) family, follows C-terminal to the COR domain. The Roc-COR-kinase module constitutes the catalytic core of the protein. It is flanked by a LRRK2-specific N-terminal repeat domain, ankyrin and leucine-rich repeats, and a C-terminal WD40 domain, that likely mediates protein-protein or protein-membrane interactions (Marín, 2006; Mata *et al.*, 2006; Marín, 2008; Martin *et al.*, 2011). It should be considered that vertebrate genomes contain one paralogous gene, called *LRRK1*. The LRRK1 protein, composed of 2015 aa, is slightly smaller than LRRK2 and is missing the N-terminal repeat domain, but otherwise has an identical domain organisation to that of LRRK2 (Marín, 2006; Mata *et al.*, 2006). Both genes are widely expressed in many organs and tissues, including the brain, and have partially overlapping expression, as detected on the mRNA level in rodent and human tissues (Biskup *et al.*, 2007; Westerlund *et al.*, 2008).

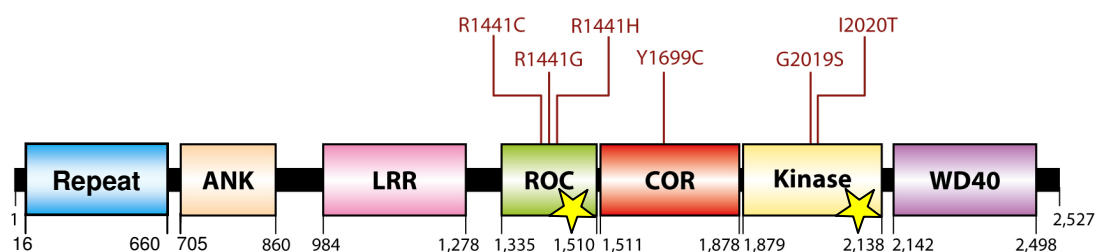


**Figure 5. LRRK2 protein domains and pathogenic mutations.** LRRK2 is a large protein of 2527 amino acids. It consists of multiple protein-protein interaction domains, as well as two enzymatic domains, the Roc GTPase and the kinase domain. Positions of pathogenic amino acid substitutions are indicated. Enzymatic activities are marked by yellow stars. The graph is adapted from Martin *et al.*, 2011. Abbreviations: ANK, ankyrin repeats; COR, C-terminal of ROC; LRR, leucine-rich repeats; ROC, Ras of complex proteins.

Among numerous putative pathogenic sequence variants of *LRRK2* identified to date, six mutations clearly segregate with familial PD cases and these are all located in or between the two enzymatic domains of the protein (Figure 5) (Mata *et al.*, 2006; Biskup and West, 2009). One amino acid position in the Roc domain can have multiple mutations (R1441C/G/H). Two missense mutations (G2019S and I2020T) lie in the activation loop of the kinase domain, and one mutation (Y1699C) is located in the COR region. The G2019S mutation is the most common *LRRK2* mutation and the most common genetic cause of familial PD. In certain ethnical groups, e.g. North African Arabs and Ashkenazi Jewish populations, up to 40% of PD cases are linked to this mutation. It can also be stated that the penetrance of disease in G2019S carriers is not complete but varies with age and reaches up to 80% in people older than 80 years of age (Mata *et al.*, 2006).

### 1.3.2. Enzymatic activities of wild-type and mutant *LRRK2*

The location of disease-causing mutations directly implied that alterations in enzymatic functions might be involved in the disease process. Indeed, *in vitro* enzymatic assays with purified protein and studies performed in cell culture have shown that mutations in the Roc GTPase and COR domain lead to decreased GTPase activity (Guo *et al.*, 2007; Lewis *et al.*, 2007; Li *et al.*, 2007), while the G2019S *LRRK2* mutation increases kinase activity (by about 3-fold *in vitro*; West *et al.*, 2005; Jaleel *et al.*, 2007). However, it should be noted that both GTPase and kinase activities of *LRRK2* are weak, which can be explained by the fact that cofactors or stimulators of the GTPase (e.g. GTPase activating proteins) were potentially missing in experimental set-ups in the first case and only generic substrates and no true physiological substrates were analysed in kinase assays. It was also shown that *LRRK2* forms dimers under physiological conditions, and dimer formation seems to be required for full catalytic activity (Deng *et al.*, 2008; Greggio *et al.*, 2008; Sen *et al.*, 2009). The two enzymatic domains located in the same protein might be an indication that the two activities are functionally linked. Is *LRRK2* a GTPase-regulated kinase or a kinase-regulated GTPase? While the first scenario attained much attention and some experimental proof in the beginning, later several groups observed that the kinase domain phosphorylates sequences within the GTP-binding Roc domain, thereby possibly modulating its function (Mata *et al.*, 2006; Greggio *et al.*, 2008; Greggio *et al.*, 2009; Kamikawaji *et al.*, 2009; Gloeckner *et al.*, 2010; Webber *et al.*, 2011). However, it is still not completely clear how the interaction of the two domains is regulated and what the enzymatic output of *LRRK2* is. In addition and due to the presence of multiple protein interaction domains *LRRK2* might function as a scaffold for

assembly of a multiprotein signalling complex or complexes (Lewis and Manzoni, 2012; Tsika and Moore, 2012). On the other hand, it was shown that kinase activity is required for the cytotoxic effects of overexpressed wild-type or mutant LRRK2, observed in cell culture and primary neurons (Greggio *et al.*, 2006; Smith *et al.*, 2006; West *et al.*, 2007), and later also in a rodent model (Dusonchet *et al.*, 2011). And inhibition of kinase activity by genetic or pharmacological means has a protective effect in these LRRK2-induced toxicity models (Lee *et al.*, 2010a). Selective and potent LRRK2 kinase inhibitors could be a potential novel therapeutic approach in the treatment of PD, and the identification and development of such inhibitors gained attention in recent years and is followed by several research groups (Anand *et al.*, 2009; Covy and Giasson, 2009; Lee *et al.*, 2010a; Deng *et al.*, 2011). However, it is still not resolved what the authentic cellular substrates of LRRK2 are. A list of candidate substrates has emerged over the years, these include members of the ERM protein family (ezrin/radixin/moesin) that anchor the actin cytoskeleton to the plasma membrane (Jaleel *et al.*, 2007; Parisiadou *et al.*, 2009);  $\beta$ -tubulin, one subunit of the microtubule cytoskeleton (Gillardon, 2009); MAPs (microtubule associated proteins) like Futsch in *Drosophila* or Tau (Lee *et al.*, 2010c; Lin *et al.*, 2010; Kawakami *et al.*, 2012); 4E-BP, the eukaryotic translation initiation factor 4E-binding protein was identified as a substrate in a *Drosophila* model (Imai *et al.*, 2008); and finally MKKs (MAP kinase kinases) (Gloeckner *et al.*, 2009) – to mention a few. But it should be kept in mind that most of these substrates were identified *in vitro* or in *Drosophila*, and their physiological relevance has to be verified in mammalian cells and in more relevant *in vivo* models. At this juncture, the most reliable LRRK2 substrate is LRRK2 itself and autophosphorylation occurs at numerous sites throughout the protein (West *et al.*, 2005; Gloeckner *et al.*, 2006; Greggio *et al.*, 2009; Kamikawaji *et al.*, 2009; Gloeckner *et al.*, 2010; Li *et al.*, 2010; Pungaliya *et al.*, 2010).

### 1.3.3. Additional hints on physiological and pathogenic functions

Which other information about LRRK2 was available at the beginning of this project that could provide clues to the normal cellular and disease-causing functions of LRRK2? As mentioned before, LRRK2 is expressed in many organs and tissues throughout the body in humans and rodents. Specific antibodies allow detection of the endogenous protein in many different neuronal types in the brain, including DA neurons of the *substantia nigra pars compacta* (Higashi *et al.*, 2007). In neuronal perikarya and processes an intracytoplasmic punctate structure was observed, which partially colocalized with Mitotracker and Lyso-tracker dyes (Biskup *et al.*, 2006). Further studies on the subcellular localization of LRRK2

revealed that a significant proportion of the protein is associated with various intracellular membranes and vesicular structures as revealed by confocal and electron microscopy, as well as by subcellular fractionation experiments (Biskup *et al.*, 2006; Gloeckner *et al.*, 2006). LRRK2 localizes to lysosomes, endosomes, transport vesicles from the Golgi, synaptic vesicles, autophagic vacuoles and multivesicular bodies (Biskup *et al.*, 2006; Hatano *et al.*, 2007; Alegre-Abarrategui *et al.*, 2009). About 10% of the protein can be found at the outer mitochondrial membrane upon overexpression. Additionally, endogenous protein was detected on mouse brain mitochondria (West *et al.*, 2005; Biskup *et al.*, 2006). LRRK2 can also interact with microtubules (Gandhi *et al.*, 2008; Gillardon, 2009). These observations suggest that LRRK2 might play a role in cytoskeletal organization and vesicular transport (Figure 6). In support of this, overexpression of G2019S LRRK2 in a neuronal cell line and cultured primary neurons reduces neurite outgrowth and branching pattern. Additionally, phospho-Tau-positive inclusions and an accumulation of autophagic vesicles were observed in axons of these mutant LRRK2-expressing cells. On the contrary, knock-down of endogenous LRRK2 increases neurite length and complexity in these cells (MacLeod *et al.*, 2006; Plowey *et al.*, 2008). In this regard it is interesting to know that some PD patients with the G2019S mutation show Tau pathology in the brain. This can be another hint how LRRK2 could interfere with microtubule network function and axonal maintenance by regulating proteins involved in cytoskeletal organization (e.g. Tau; ERM family proteins) (Figure 6). Finally, LRRK2 might modulate protein translation by phosphorylating 4E-BP. Evidence therefore comes from studies in *Drosophila*, where gain- and loss-of-function of the *Drosophila* homolog dLRRK leads to either increased or decreased 4E-BP phosphorylation, respectively (Imai *et al.*, 2008). 4E-BP normally sequesters the eukaryotic translation initiation factor 4E (eIF-4E). Phosphorylation of 4E-BP disrupts this interaction, and eIF-4E is set free to initiate cap-dependent mRNA translation. 4E-BP is also a target of mammalian target of rapamycin (mTor) and this signalling pathway is known to regulate autophagy in response of nutrient limitation (Figure 6).

In the course of this project, LRRK2 has been implicated in several other, remarkably diverse pathways, including microRNA-mediated translational repression, mitochondrial function, synaptic vesicle function, protein degradation pathways, autophagy and regulation of immune responses (reviewed by Cookson, 2010; Martin *et al.*, 2011; Tsika and Moore, 2012; Exner *et al.*, 2012).

As described before, the focus in the PD field recently turned on mitochondrial function and maintenance. LRRK2 has been found associated with mitochondria as well as with

cytoskeletal structures, including microtubules in neurons. Additionally, abnormalities in autophagic activity have been observed in several LRRK2-based experimental set-ups. Mutant LRRK2 could therefore interfere with mitochondrial trafficking and/or turn over. This warrants further investigation and will be approached in this study.

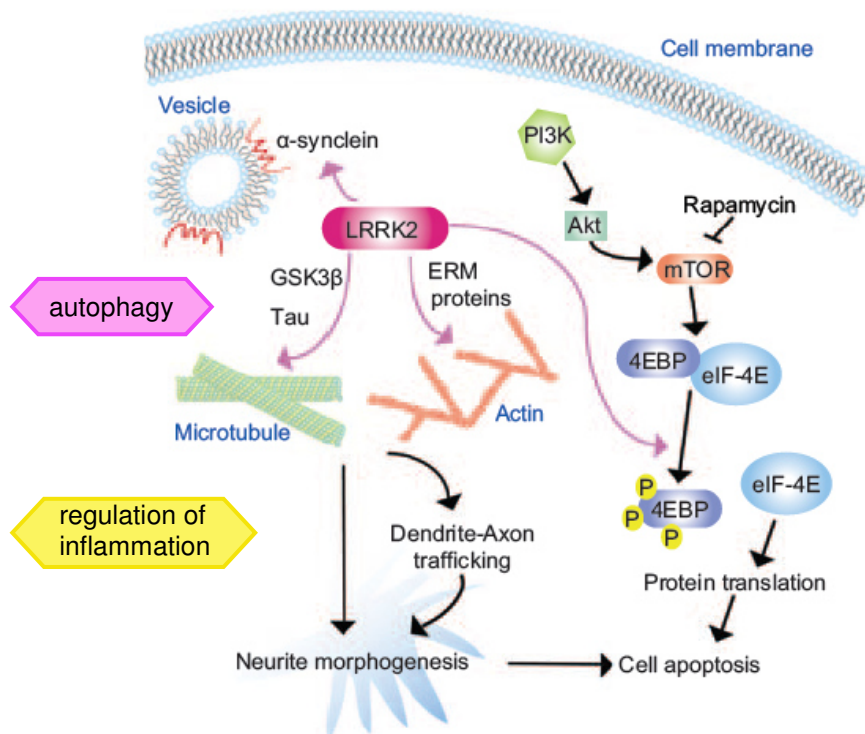


**Figure 6. LRRK2 has been implicated in diverse cellular processes and signalling pathways.** Observations from cell culture and animal models of LRRK2 loss and gain of function demonstrate that LRRK2 plays a role in regulating actin and microtubule cytoskeleton dynamics and neurite outgrowth. LRRK2 has been found associated with diverse intracellular membranes and can affect vesicle trafficking and regulation of the synaptic vesicle recycling pool. A pathophysiological interaction between LRRK2 and  $\alpha$ -synuclein has been suggested by Lin *et al.*, 2009, in their study with G2019S LRRK2 and mutant  $\alpha$ -synuclein double transgenic mice. The results could not be confirmed by Daher *et al.*, 2012, in a similar experimental approach. The eukaryotic translation initiation factor 4E-binding protein (4E-BP) is a target of the mTOR signalling pathway. Phosphorylated 4E-BP dissociates from eIF-4E and thus permits mRNA translation. LRRK2 has been shown to directly phosphorylate 4E-BP in a *Drosophila* model. Kidney pathology and a defect in the autophagic-lysosomal pathway in LRRK2 knock-out mice were reported by Tong *et al.*, 2010 and 2012. Recently, it has been uncovered that mutant LRRK2 inhibits its own degradation as well as degradation of other proteins via chaperone-mediated autophagy (Orenstein *et al.*, 2013). Finally, a role of LRRK2 in regulating inflammatory reactions has emerged (reviewed by Greggio *et al.*, 2012). LRRK2 is expressed in several cell types of the immune system, e.g. monocytes, macrophages, dendritic cells and B lymphocytes. It inhibits nuclear translocation of the transcription factor NFAT, a transcription factor involved in immune responses. Drawing adapted from Lin *et al.*, 2011.

## 1.4. Mitochondrial Transport

Mitochondria are essential for neuronal function and survival. Through the process of oxidative phosphorylation, they provide the energy required for key neuronal functions, like action potential propagation and synaptic transmission. In addition, they have a high  $\text{Ca}^{2+}$ -buffering capacity, which is required during neuronal activity, especially at the synapse, where  $\text{Ca}^{2+}$  influx triggers neurotransmitter release through synaptic vesicle exocytosis. To distribute mitochondria within the highly polarized neurons, they are actively transported by molecular motor proteins along microtubule tracks in dendrites and axons, and along the actin

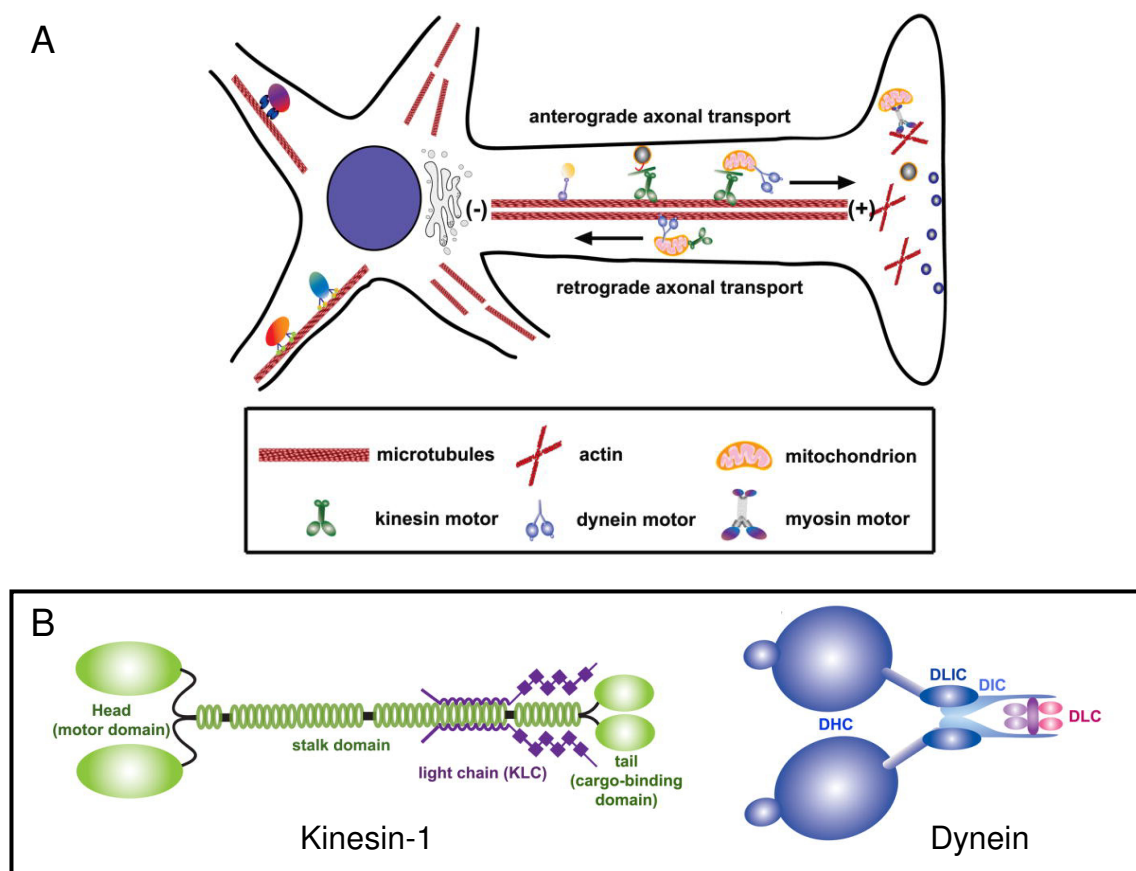


**Figure 7. Mitochondrial axonal transport.** **A** Long-range transport of mitochondria is mediated by molecular motors which move along microtubule tracks, while short range movement in the synapse or in dendritic spines passes along actin filaments. Microtubules in axons are uniformly oriented with their plus ends towards the distal tip and the minus ends towards the soma. Kinesins are plus end-directed motor proteins. They bind to mitochondria via adaptor proteins and mitochondrial outer membrane proteins and are responsible for anterograde transport towards the synapse. Cytoplasmic dynein motors move towards microtubule minus ends and mediate retrograde transport towards the soma. **B** The structure of the two main microtubule-based motor proteins is shown. Members of the kinesin-1 family (also known as KIF5) play a key role in anterograde mitochondrial transport in neurons. They contain two kinesin heavy chains with motor activity, shown in green, and two kinesin light chains with regulatory function, depicted in purple. Cytoplasmic dynein is a huge complex composed of multiple polypeptide chains: two dynein heavy chains (DHC) and several dynein intermediate chains (DLIC), dynein light intermediate chains (DLIC) and dynein light chains (DLC). Drawing adapted from Cai *et al.*, 2011.

cytoskeleton for short-range transport (Figure 7). Mitochondrial axonal transport toward the synapse is called anterograde transport and is mediated by kinesin motor proteins (reviewed by Hirokawa *et al.*, 2010; Cai *et al.*, 2011; Sheng and Cai, 2012). These attach to mitochondria via the adaptor Milton (identified in *Drosophila*, the mammalian homologs are called TRAK 1 and 2), and Milton in turn binds to the mitochondrial integral membrane Rho-family GTPases Miro (two mammalian homologs Miro1 and 2). Several alternative adaptor proteins have been identified (Sheng and Cai, 2012). Dynein is responsible for microtubule minus end-directed transport, which is oriented in the retrograde direction within axons. How cytoplasmic dynein attaches to mitochondria is less well described but many proteins seem to be involved as dynein is a huge multiprotein complex.

As mentioned before, PINK1 has been found in a complex with Miro and Milton (Weihofen *et al.*, 2009), and cessation of mitochondrial transport in the context of mitophagy was reported recently to occur in a PINK1 and Parkin-dependent manner, involving Miro phosphorylation, ubiquitination and its subsequent proteasomal degradation (Chan *et al.*, 2011; Wang *et al.*, 2011).

LRRK2 has been described to modulate microtubule stability by phosphorylating brain beta-tubulin (Gillardon, 2009). It also seems to be able to interact with microtubules directly via its Roc domain (Gandhi *et al.*, 2008), and Dauer and coworkers reported that PD mutations in LRRK2 enhance its association with microtubules (Kett *et al.*, 2012). In addition, several groups have observed that LRRK2 interferes with the phosphorylation status and function of Tau, an important microtubule associated protein (MAP) that is required for the stabilization of axonal microtubules (Lin *et al.*, 2010; Melrose *et al.*, 2010; Kawakami *et al.*, 2012). These results indicate that wild-type LRRK2 or the PD G2019S mutant might interfere with mitochondrial axonal transport.

## 1.5. Autophagy

Autophagy is one of the two major degradation pathways inside cells beside the ubiquitin-proteasome system (Wong and Cuervo, 2010). During autophagy whole organelles or portions of the cytoplasm are typically enwrapped by a double membrane structure called the phagophore, which enlarges and fuses to form the double-membraned autophagosome (Figure 8). After fusion of the autophagosome with lysosomes, lysosomal enzymes gain access to the autophagosome inner membrane and the enclosed material, which are subsequently hydrolytically degraded. Small molecule degradation products are then released back into the cytosol for recycling. This form of autophagy, more precisely termed macroautophagy, is the main and best studied process of self-degradation of bulk cellular material. Depending on the type of the degraded substrate and the mechanism of cargo sequestration two other types of autophagy are known: chaperone-mediated autophagy, for the specific removal of individual proteins, and microautophagy (Figure 8). The latter was mainly described in yeast where certain organelles, e.g. peroxisomes, are directly taken up at the surface of the vacuole (the yeast equivalent of the lysosome) (reviewed by Xie and Klionsky, 2007; He and Klionsky, 2009; Todde *et al.*, 2009; Wong and Cuervo, 2010; Yang and Klionsky, 2010; Lynch-Day *et al.*, 2012; Rubinsztein *et al.*, 2012).

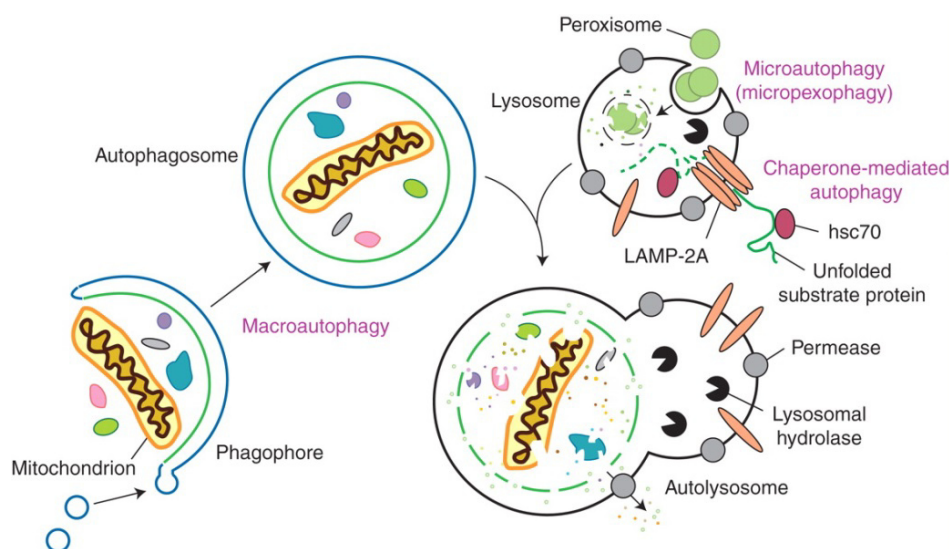


**Figure 8. Schematic drawing of the three main types of autophagy.** In chaperone-mediated autophagy, proteins that contain a KFERQ-consensus motif in their sequence (e.g.  $\alpha$ -synuclein) are unfolded by HSC70 chaperones. Then they translocate directly across the lysosomal membrane through interaction with a LAMP-2A oligomer. During microautophagy, bulk material or small organelles, like peroxisomes, are directly taken up into lysosomes by interaction with and invagination of the lysosomal membrane. Macroautophagy, often referred to by the term autophagy, involves sequestration of bulk material or portions of the cytoplasm by formation of a double-membraned autophagosome. Autophagosome fusion with lysosomes leads to degradation of the inner autophagosomal membrane and its enclosed content. Small molecule breakdown products are released back into the cytosol for recycling. Drawing adapted from Lynch-Day *et al.*, 2012.

Macroautophagy, more generally called autophagy, is required for normal cellular homeostasis and is constantly taking place in every cell at a low basal level. It can be upregulated by various stress conditions. For example, it ensures cell survival under starvation conditions when nutrients, and especially amino acids, are in short supply by recycling some of the cytosolic components and proteins. Additionally, autophagy is required for the specific elimination of intracellular pathogens (e.g. bacteria) or the removal of cytotoxic protein aggregates. Abnormalities in autophagy, therefore, may contribute to pathologies, such as cancer, myopathies, heart disease and various neurodegenerative diseases (Mizushima *et al.*, 2008; Ravikumar *et al.*, 2010; Mizushima and Komatsu, 2011).

Autophagy is a tightly controlled process and more than 30 autophagy (*ATG*) genes have been identified mainly through genetic screens in yeast (*Saccharomyces cerevisiae*). Mammalian cells contain homologs of most of the yeast *ATG* genes, plus additional regulators and interacting proteins. These regulatory proteins participate in one of four major steps of the autophagic process (reviewed by Xie and Klionsky, 2007; Yang and Klionsky, 2010; Florey and Overholtzer, 2012; Rubinsztein *et al.*, 2012). Two protein complexes regulate the induction of autophagy and the initiation of phagophore formation. The class III phosphatidylinositol 3-kinase complex composed of Vps34, Beclin-1 (the mammalian Atg6 homolog), Atg14 and Vps15 determines the site of phagophore formation through the local synthesis of phosphatidylinositol 3-phosphate, which mediates recruitment of other Atg proteins. The activity of this complex is regulated by the upstream kinase complex containing the mammalian Atg1-homologs ULK1 and ULK2, plus Atg13, Fip200 and Atg101. Several Atg proteins are involved in two ubiquitin-like conjugation systems that regulate phagophore enlargement and autophagosome completion. First, the ubiquitin-like molecule Atg12 is conjugated to Atg5 through the enzymatic activity of Atg7 and Atg10. Atg12-Atg5 forms a ternary complex by binding to Atg16, and the whole complex is associated with the phagophore outer membrane. In a second reaction, the mammalian Atg8 homolog MAP1-LC3 (also called LC3), another ubiquitin-like molecule, is conjugated to phosphatidylethanolamine (PE) and LC3-PE is located at the outer and inner autophagosomal membrane. LC3-PE can be detected as punctate structures inside cells by antibody staining or when using LC3-GFP fusion proteins. It is used as a marker for autophagy, as it decorates autophagosomes (Fleming and Rubinsztein, 2011). Finally, the fourth regulatory protein complex is required for membrane trafficking events to the expanding phagophore and involves the integral membrane protein Atg9 plus many additional factors.

The mTOR kinase complex (mTORC1, mammalian target of rapamycin complex I) is the master upstream regulator of autophagy. Several signalling pathways induced by extracellular growth factors and their transmembrane receptors, as well as intracellular pathways integrate information about the nutritional status of the cell and converge on this negative regulator of autophagy. Consequently, inhibition of mTOR by pharmacological means, for example with rapamycin, can be used as an experimental strategy to induce autophagy (Soulard and Hall, 2007; He and Klionsky, 2009; Yang and Klionsky, 2010).

In the context of PD and other neurodegenerative diseases an insufficient autophagic clearance of aggregation-prone proteins, like  $\alpha$ -synuclein, or damaged mitochondria may lead to neuronal dysfunction, oxidative damage and ultimately cell death. A special focus was recently cast on mitophagy (autophagy of mitochondria) by the discovery of the PD-linked genes *PINK1* and *parkin*, which play a role in the recognition and tagging of damaged mitochondria (see Chapter 1.2). However, it is still not clear how the autophagic machinery and autophagic membranes are subsequently recruited to mitochondria. Specific adaptor proteins, which bind ubiquitinated proteins and which have yet to be identified, are probably involved in this selective form of autophagy.

So far, experiments to unravel these intracellular trafficking and homeostatic processes involving mitochondria have mainly been conducted with established cell lines or differentiated neurons *in vitro*. To study the influence of PD-linked genes on the precise subcellular control and regulation of these motile processes in highly polarized neurons, an observation within functional neuronal networks is required. This can only be achieved *in vivo*. The model organism zebrafish, especially its embryos and larvae, offers such an *in situ* analysis of its nervous system through advanced microscopic techniques.

## **1.6. Zebrafish as a Model for PD Research**

### **1.6.1. A vertebrate model organism with many advantages**

The teleost *Danio rerio*, a small tropical fresh water fish (adults are about 3 cm long), is robust, relatively cheap and easy to maintain and has several advantages over other vertebrate models. These include its high fecundity (several hundred eggs per spawning), transparent embryos and their external embryonal development. Additionally, development proceeds rapidly, and many tissues and organs are functional by 2-3 days post fertilization (dpf), the time when larvae hatch from the chorion. They start to swim at about 5 dpf. Finally, the generation time of this animal is short, being 2 to 3 months. These features were previously mainly found in invertebrate models, like *Drosophila* and *C. elegans*, and allow zebrafish

embryos and larvae to be used for large-scale genetic screens, high-throughput functional studies and for *in vivo* imaging.

Experimental work with zebrafish as a model for vertebrate development started more than 30 years ago, in the late 1970s and early 80s with research conducted by Charles B. Kimmel, George Streisinger and, a bit later, Christiane Nüsslein-Volhard (first zebrafish publications by these researchers: Kimmel, 1972; Streisinger *et al.*, 1981; Culp *et al.*, 1991). Over the following years an impressive set of tools and techniques for the experimental manipulation and analysis of this organism has been developed. Besides the classical forward genetic approach of random chemical mutagenesis with the compound ENU (N-ethyl-N-nitrosourea) and the subsequent identification of specific mutant phenotypes, several reverse genetic techniques have been established (reviewed by Lawson and Wolfe, 2011). Gene expression can be temporarily knocked-down in the first days of development by antisense Morpholino oligonucleotides that are injected into fertilized eggs (Nasevicius and Ekker, 2000; Bill *et al.*, 2009). A method to identify stable mutants for a specific gene is via the Targeting Induced Local Lesions In Genomes (TILLING) approach. Here, large libraries of ENU-mutagenized zebrafish are screened by sequencing the gene of interest in individual animals (Wienholds *et al.*, 2003; Sood *et al.*, 2006). Lately, techniques for targeted gene inactivation have been established by directing DNA nucleases to the desired genomic site via sequence-specific DNA-binding proteins and thereby inducing targeted mutations in the genome. So-called zinc finger nucleases (ZFNs) were applied first and now transcription activator-like effector nucleases (TALENs) are more commonly used (Doyon *et al.*, 2008; Meng *et al.*, 2008; Huang *et al.*, 2011; Sander *et al.*, 2011). The latest improvement is the CRISPR-Cas system for genome editing whereby guide RNAs direct DNases to modify endogenous genes (Hwang *et al.*, 2013). For transgenesis, genes of interest can be efficiently introduced into the genome by Tol2 transposon-mediated random integration and their expression is regulated by an ever growing list of tissue or cell type-specific promoter fragments, which have been isolated and characterized over the last years. As zebrafish embryos and larvae are nearly completely transparent, they are ideally suited for live microscopy. For this purpose, certain cell types or subcellular structures (e.g. organelles, cytoskeleton) can be stained in living animals by specific dyes or by expression of fluorescent reporter proteins. Many fluorescent proteins with different physical properties and over the full spectral range are now available, allowing for multi-colour *in vivo* imaging (Shaner *et al.*, 2007; Davidson and Campbell, 2009; Day and Davidson, 2009; Stepanenko *et al.*, 2011; Weber and Köster, 2013). Finally, all the classical experimental staining approaches for fixed tissue are, of course, applicable, like

immunohistochemistry with a constantly growing list of zebrafish-specific antibodies, and *in situ* hybridization to analyse gene expression and to determine cell identity. The Zebrafish Model Organism Database at [www.zfin.org](http://www.zfin.org) offers a wealth of data on gene expression and anatomy; additionally, it provides information about tools (transgenic constructs, transgenic lines, antibodies), protocols and other useful links.

### 1.6.2. The zebrafish genome contains orthologs of PD genes

Recently, the completed zebrafish genome sequence was annotated and could be compared to the human genome (Howe *et al.*, 2013). It became evident that approximately 70% of human genes have at least one zebrafish ortholog. Due to an additional round of whole-genome duplication, which took place during evolution of the teleost lineage, orthologs of some human genes are duplicated in the zebrafish genome (Amores *et al.*, 1998; Postlethwait *et al.*, 2004; Postlethwait, 2007; Howe *et al.*, 2013). When specifically looking for zebrafish orthologs of human disease-related genes, 82% of the 3,176 human disease genes that are listed in the Online Mendelian Inheritance in Man (OMIM) database have at least one zebrafish ortholog (Howe *et al.*, 2013).

Concerning PD, single zebrafish orthologs have been identified for human *PINK1*, *parkin*, *DJ-1* and *UCH-L1* (Son *et al.*, 2003; Bretau *et al.*, 2007; Flinn *et al.*, 2009; Fett *et al.*, 2010; Sager *et al.*, 2010; Xi *et al.*, 2010). The situation is more complex for  $\alpha$ -synuclein, where zebrafish has no ortholog but three paralogous genes: *sncb*, *sncg1* and *sncg2* encoding  $\beta$ -,  $\gamma 1$ - and  $\gamma 2$ -synuclein (humans have  $\alpha$ -,  $\beta$ - and  $\gamma$ -synuclein) (Sun and Gitler, 2008; Milanese *et al.*, 2012). A detailed phylogenetic analysis by Ignacio Marín in 2008 confirmed that single orthologs for each of human *LRRK1* and *LRRK2* can be found in zebrafish and other vertebrate genomes. Additionally, a remark of caution was made by the author about the use of protostome model organisms for the study of *LRRK2* gene function. The insect *Drosophila* and the nematode *C. elegans* only contain a single *LRRK* gene, which seems to be no true ortholog of the human Parkinson's disease gene *LRRK2*. Researchers, who try to elucidate *LRRK2* function in these organisms, should be cautious in extrapolating their results to the human situation (Marín, 2008). Vertebrate genomes contain a true ortholog of *LRRK2* and are therefore better suited to study the physiological and pathological functions of this gene. Zebrafish *lrrk2* (ZFIN ID: ZDB-GENE-071218-6) is located on chromosome 25 in a region showing synteny to the human *LRRK2* locus on chromosome 12q12. And syntenic gene order is a hint for orthology of genes.

In summary, the striking degree of phylogenetic conservation suggests that the molecular processes regulated by these gene products are of fundamental importance to the function of neurons and cells in all vertebrates. It also implies that interfering with gene function in zebrafish might provoke neuronal dysfunction or loss through molecular processes similar to those involved in the human condition. Besides the molecular level, also higher order structural and functional features – cell types, neuronal structures and circuits– are conserved and can be identified in the zebrafish central nervous system.

### **1.6.3. The zebrafish dopaminergic system**

Dopaminergic neuron development during embryogenesis and larval stages is well documented in zebrafish (Guo *et al.*, 1999; Holzschuh *et al.*, 2001; Rink and Wullimann 2002b), and the DA system has been analysed and described in detail in the adult brain (Rink and Wullimann, 2001, 2002a, 2002b; Ma, 2003; Yamamoto *et al.*, 2010). DA neurons can be identified by expression of tyrosine hydroxylase (TH), the enzyme catalysing the rate-limiting first step in dopamine synthesis. TH-expressing neurons are detectable from 22 hpf onwards (Guo *et al.*, 1999). Between 2 and 5 dpf the spatial organization of characteristic DA cell clusters is established, and these clusters can be identified and have a similar arrangement in the adult brain – albeit with higher cell numbers (Rink and Wullimann 2001, 2002a, 2002b). In contrast to the mammalian brain, no DA neurons could be detected in the midbrain of teleosts. However, by carefully studying development, gene expression and anatomical location of DA neurons and their processes, Rink and Wullimann argue that a system homologous to the midbrain dopaminergic system of mammals exists in fish and is located in the ventral diencephalon – the caudal part of the forebrain. The authors identified and characterized twelve DA cell populations in the adult zebrafish diencephalon (Rink and Wullimann, 2001, 2002b). The TH-immunoreactive cell populations, designated Cluster 0 to Cluster 11, are shown in Figure 9B. Their location with respect to anatomical landmarks was detailed and three characteristic cellular morphologies were described (Figure 9C). By retrograde labelling with tracer dye injection into the ventral telencephalon (subpallium) and identification of double-labelled neurons (labelled by the tracer as well as by anti-TH immunostaining), ascending dopaminergic neurons could be identified. Cells from three populations located in the posterior tuberculum of the ventral diencephalon, namely Cluster 1, 2 and 4, send processes to the ventral telencephalon (indicated in Figure 9B). These clusters constitute an ascending dopaminergic system homologous to the *substantia nigra pars*

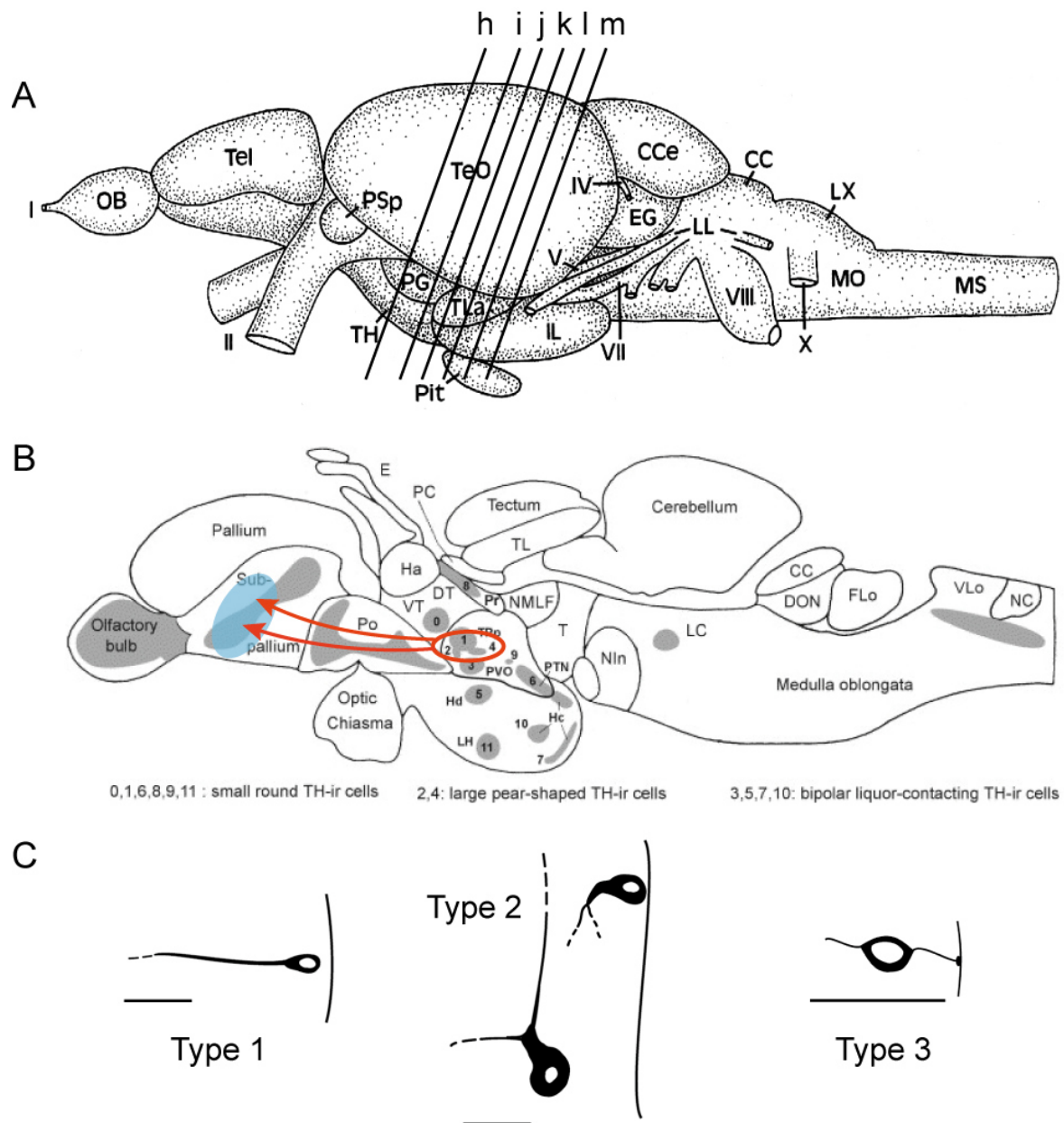


**Figure 9.** An ascending dopaminergic system homologous to the mammalian midbrain dopaminergic system exists in zebrafish and is located in the basal diencephalon of the forebrain. **A** A lateral view of an adult zebrafish brain is shown. Section levels (h to m) are according to Rink and Wullimann, 2001. Corresponding cross sections are shown in the results part of this thesis. Abbreviations: CC, cerebellar crest; CCe, corpus cerebelli; EG, eminentia granularis; IL, inferior lobe; I-X, cranial nerves; LL, lateral line nerve; LX, vagal lobe; MO, medulla oblongata; MS, medulla spinalis; OB, olfactory bulb; PG, preglomerular region; Pit, pituitary; PSp, parvocellular superficial pretectal nucleus; Tel, telencephalon; TeO, optic tectum; TH, tuberal hypothalamus; TLa, torus longitudinalis. **B** Cells projecting to the subpallium (striatum) have been identified by retrograde labelling experiments with tracer injection (blue colour) into the ventral telencephalon. Concomitant immunochemical detection of TH identified three double-labelled cell groups. Cells of Cluster 1, 2 and 4 are located in the posterior tuberculum of the ventral diencephalon (encircled in red, ascending tracts indicated as red arrows). Locations of dopaminergic cells are indicated in grey; drawing adapted from Rink and Wullimann, 2002b; see therein for abbreviations. **C** Three cytological types of diencephalic dopaminergic neurons have been observed: small round Type 1 cells, large pear-shaped Type 2 cells, and small bipolar, cerebrospinal fluid-contacting Type 3 cells. Vertical lines mark the ventricle, horizontal lines indicate relative dimension; drawings from Rink and Wullimann, 2001.

*compacta* in mammals. As mentioned before, cells belonging to these three clusters can be detected from 2 dpf onwards. An impact of mutant gene products on DA neuron development and function can therefore be analysed from early developmental stages onward in zebrafish disease models.

#### **1.6.4. Our sophisticated experimental toolbox to generate PD models**

In order to generate a dominant *LRRK2*-based PD model we wanted to make use of several newly-established and improved techniques for efficient transgenesis, for cell type-specific gene expression and to allow co-expression of two or more transgenes.

Transgenesis in zebrafish was dramatically advanced by the discovery of the Tol2 transposable element of medaka fish and its modification as a gene transfer tool for zebrafish (Koga *et al.*, 1996; Kawakami *et al.*, 1998; Kawakami *et al.*, 2000; Kawakami, 2007). A transfer vector was constructed, which contains the minimal 5'- and 3'-cis-active transposon terminal sequences (200 and 150 bp) required for transposition. The desired transgenic construct has to be cloned between these terminal sequences. After co-injection of the construct into fertilized zebrafish eggs together with mRNA encoding the Tol2 transposase, the transgene is excised from the plasmid and randomly integrated into the genome of dividing cells of the embryo by a cut-and-paste transposition mechanism. If transposition occurs in cells of the germ line, the transgenic construct is stably inherited to the next generation.

To improve gene expression, the *Drosophila* Gal4/UAS expression system (Brand and Perrimon, 1993) has been adapted for use in zebrafish (Scheer and Campos-Ortega, 1999; Köster and Fraser, 2001). Together with Tol2-mediated transgenesis, the Gal4/UAS system can be employed in a similar way as in *Drosophila* for the generation of stable transgenic driver and effector lines (Asakawa and Kawakami, 2008). The transgenic driver or activator line expresses the transcriptional activator Gal4 under the control of an isolated promoter fragment or an endogenous promoter, captured by the enhancer trap approach. This line can be crossed to the transgenic effector line, which contains a desired transgene (for example a fluorescent reporter) under the control of Gal4-binding sites, known as upstream activating sequences (UAS). The target gene is not expressed in the effector line as Gal4 is not present endogenously in zebrafish. Only in double-transgenic offspring of a cross between driver and effector fish, Gal4 is expressed and induces expression of the transgene.

The Gal4/UAS system has recently been optimized in our laboratory (Distel *et al.*, 2009). Köster and Fraser (2001) had cloned the strong Gal4-VP16 transcriptional activator. Later,

attenuated versions of the VP16 transactivation domain, called TA2, TA3 and TA4, were used (Baron *et al.*, 1997). Translation of the protein was improved by adapting the gene sequence to the codon usage in zebrafish, by adding a Kozak ribosome recognition sequence at the translation start site, and by including the rabbit *beta-globin* intron at the 3'-end of the gene (Distel *et al.*, 2009). These modified versions of Gal4, called KalTA3 and KalTA4, were used in the course of this project.

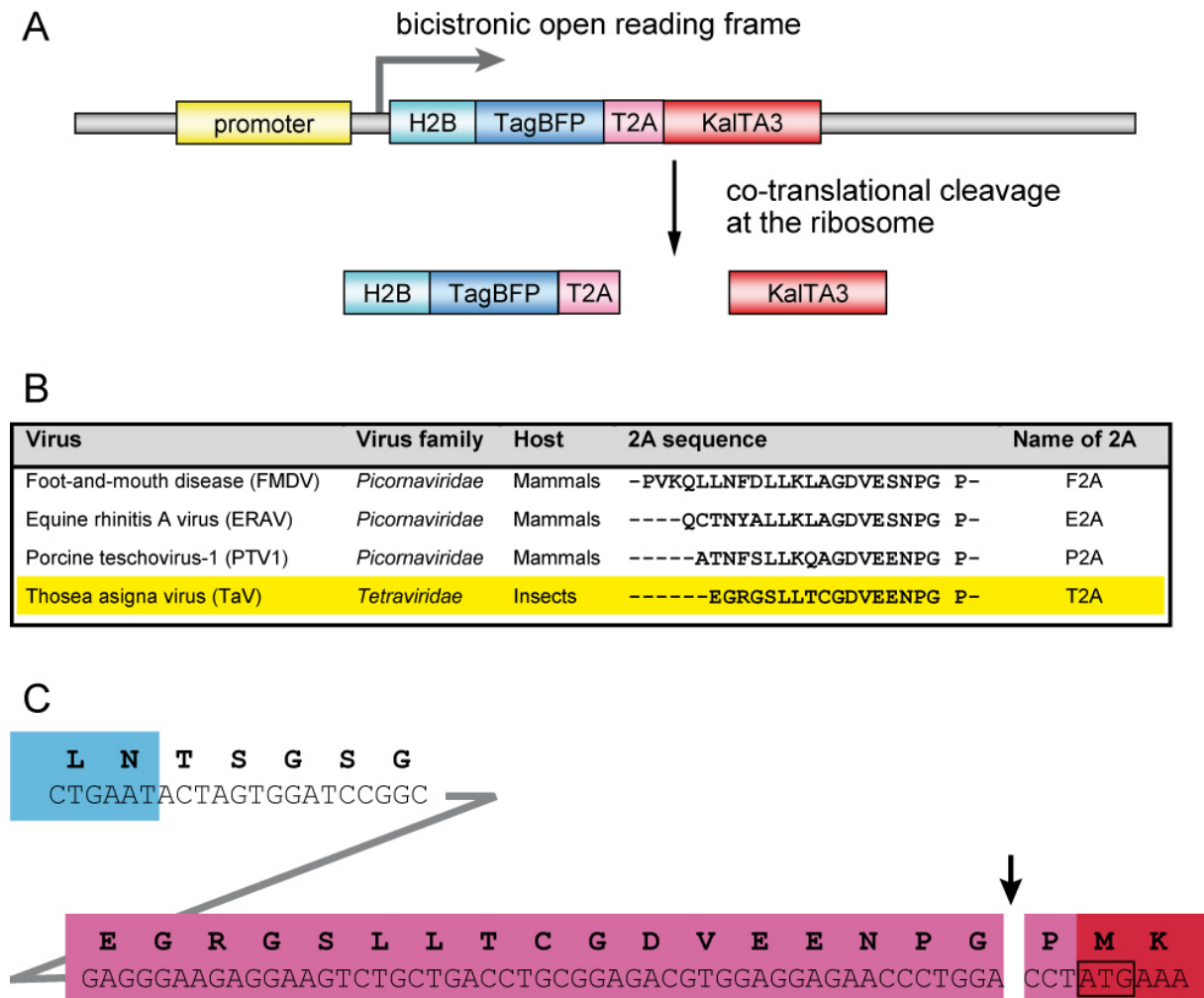


**Figure 10. The viral T2A peptide mediates reliable and stoichiometric co-expression of a fluorescent reporter and the transcriptional activator KalTA3.** **A** The open reading frames of the fluorescent reporter and the transcriptional activator are fused with the intervening T2A sequence into one long ORF. A single mRNA is transcribed from the promoter. During translation the nascent T2A peptide induces a ribosomal-skip event, leading to hydrolytic release of the first protein. Translation of the second protein continues. Thereby, two separate proteins are produced in equimolar amounts. **B** T2A is derived from the insect virus, *Thosea asigna* virus, and is the shortest peptide of four well-characterized and highly functional 2A-like sequences (table adapted from de Felipe *et al.*, 2006). **C** The T2A sequence remains as a C-terminal extension of the upstream protein. The sequence of blue fluorescent protein TagBFP (last two aa are in blue) continues with a 5 aa long linker and is then followed by the T2A peptide (in pink). The skipping event occurs after the glycine (indicated by an arrow), while the proline of the T2A sequence is fused to the first methionine of KalTA3 (in red).

Direct detection of transgenes can be achieved by co-expression of a fluorescent reporter together with the protein of interest (e.g. Gal4). Recent advance in the co-expression of several proteins from the same polycistronic construct and under control of a single promoter came with the identification and characterization of viral “self-cleaving” 2A peptide sequences (Ryan and Drew, 1994; de Felipe *et al.*, 2006) (Figure 10). These sequences of 18-23 aa contain a conserved D(V/I)EXNPGP motif at the C-terminus that mediates a “ribosome skipping” event during translation, where a specific glycyl-prolyl peptide bond is not formed and the upstream protein is released (Doronina *et al.*, 2008). Translation of the continuous ORF and the following protein sequence resumes. Thereby, two or more proteins are synthesized at equimolar concentrations. As observed by our group and by Kim *et al.*, 2011, the 2A peptide sequence functions efficiently in zebrafish.

Finally, 2A-mediated coexpression of different fluorescent proteins can be used for labelling several subcellular structures at the same time. For multi-colour imaging, the choice of proteins depends on the one hand on the microscopic setup and on the other hand the physical properties of the FPs should have minimal overlap in excitation and emission.

## 1.7. Aim of the Study

Mutations in several genes have been identified as causative for dominantly or recessively inherited Parkinson’s disease. Additionally, recent experimental results have highlighted mitochondrial dysfunction as a major cause of neurotoxicity in PD. Two genes, *LRRK2* and *PINK1*, will be the focus of this study. A role of PINK1 in several aspects of mitochondrial biology and maintenance has been revealed. However, if and how LRRK2 could also affect mitochondrial function and the pathogenic consequences of PD-linked mutations in LRRK2 are still unresolved and warrant further investigation. In this study, we want to generate a transgenic neurodegeneration model in zebrafish based on expression of mutant human LRRK2(G2019S). At the same time, our disease model should allow imaging of two dynamic subcellular processes in neurons *in vivo*, which are fundamentally important for neuronal function and survival. These are mitochondrial transport and autophagy. In more detail, the following experimental strategy will be pursued:

We want to make use of the Gal4/UAS system to generate an independent neuron-specific transgenic driver fish line. A driver construct, which facilitates its own detection and which expresses Gal4 under the control of the *neuronal beta-tubulin* promoter, will be compiled. The functionality of this construct has to be evaluated *in vitro* and *in vivo*. Subsequently, a

transgenic zebrafish line will be established by Tol2-mediated transgenesis, selection of transgene carriers and outcrossing to *wt* animals.

Second, several effector constructs will be assembled. Each construct should facilitate Gal4-dependent, UAS-regulated expression of the disease gene *LRRK2(G2019S)* or one of two control alleles, *LRRK2 wt* or the kinase-dead *LRRK2(K1906M)*. One construct will be without *LRRK2* sequence. At the same time, expression of the two fluorescent reporter proteins, the red fluorescent protein mitoTagRFP, to label mitochondria and the yellow FP Venus-LC3, to highlight autophagosomes, is mediated. T2A peptide-regulated coexpression is used to obtain two independent reporter functions from one single open reading frame. Effector protein expression from the final construct and the correct subcellular targeting of the proteins has to be tested in cell culture by confocal microscopy and through biochemical means.

Due to time limitations, a transient-transgenic disease model will subsequently be generated. Effector constructs will be injected into one-cell stage embryos of the established transgenic neuronal driver line. In order to address a pathogenic influence of mutant LRRK2 on mitochondrial transport in neurons, confocal imaging of this dynamic process will be established in axons of a suitable neuronal type. Mitochondrial motility will be recorded in the presence and absence of *LRRK2(G2019S)*. Sufficient data will be collected, quantified and statistically evaluated.

A second disease model for *PINK1*-linked recessive PD requires identification of a loss-of-function mutation in the zebrafish *pink1* gene. Such a *pink1* mutant fish line was identified and provided by the research group of Prof. Oliver Bandmann through a TILLING approach. In this study, we want to analyse this line for a PD-related neurodegeneration phenotype. Specifically, we want to determine if dopaminergic neurons are lost in adult mutant zebrafish in brain structures that are homologous to the *substantia nigra pars compacta* of mammals. For this, serial sections of brain tissue from 6-months-old animals will be cut and will be processed by anti-tyrosine hydroxylase immunohistochemistry to reveal DA neurons. Subsequently, specific DA neuron clusters have to be identified and confocal image stacks will be recorded. Then, cell numbers will be quantified within image stacks and will be compared between *pink1* mutant and wild-type tissue.

Second, we want to look for and possibly quantify mitochondrial ultrastructural abnormalities and dysfunction by electron microscopic analysis of mitochondria in muscle tissue from larval stages and from adults of *pink1* mutant and wild-type zebrafish lines.

## 2 Materials and Methods

### 2.1. Reagents and Equipment

#### 2.1.1. Bacterial strains

The following *E. coli* strains were used in the course of this study:

XL1-Blue	(Stratagene, Waldbronn, Germany)
StrataClone SoloPack Competent Cells	(Stratagene, Waldbronn, Germany)
Stbl3 <i>E. coli</i>	(Invitrogen, Darmstadt, Germany)
TOP10 <i>E. coli</i>	(Invitrogen, Darmstadt, Germany)

#### 2.1.2. Mammalian and zebrafish cell lines

HEK293T human embryonic kidney cells (Graham *et al.*, 1977)  
 Pac2 zebrafish embryonic fibroblast cells originating from Patricia Ann Culp (Culp, 1994)

#### 2.1.3. Zebrafish strains

##### 2.1.3.1. Wild-type lines

AB	(Zebrafish International Resource Center)
Brass	This strain is of AB background with a mutation in the brass gene ( $brs^{b2/b2}$ ). It has a reduced melanin pigmentation phenotype.

##### 2.1.3.2. Transgenic lines

<i>Tg(her3:KalTA4)</i>	A. Babaryka, Köster lab
<i>Tg(zic4:KalTA4, UAS:mCherry)</i>	M. Distel, Köster lab (Distel <i>et al.</i> , 2009)
<i>Tg(UAS:GFP)hzm3</i>	M. Distel, Köster lab (Distel <i>et al.</i> , 2009)
<i>Tg(UAS:Lyn-Venus-T2A-NLS-CFP)</i>	K. Namikawa, Köster lab
<i>Tg(NBT:DsRed)</i>	F. Peri, EMBL, Heidelberg (Peri and Nüsslein-Volhard, 2008)

This strain contains the promoter of the *Xenopus laevis* neuronal beta-tubulin gene (NBT) driving expression of DsRed. The correct nomenclature of this strain, according to ZFIN nomenclature guidelines, would be *Tg(Xla.tubb2b:DsRed)*. This promoter was used to generate a new transgenic line in the course of this study. For simplicity, the promoter will be called NBT throughout this work.

Transgenic line constructed in the course of this work:

*Tg(NBT:H2B-TagBFP-T2A-KalTA3)*

Additionally, the following effector constructs were constructed and injected into wild-type embryos in the course of this project. However, screening and out-crossing could not be performed due to time limitations:

*Tg(4xUAS-E1b:mito-TagRFP-T2A-Venus-LC3, 4xUAS-E1b:Hsa.LRRK2-Strep-CFP)*

Three different alleles of the human LRRK2 gene have been used and three different constructs have been made, containing either wild-type LRRK2, the Parkinson's disease-linked G2019S allele or the kinase-dead point mutation K1906M. Additionally, one construct has no LRRK2 sequence: *Tg(4xUAS-E1b:mito-TagRFP-T2A-Venus-LC3)*

#### 2.1.4. Chemicals and consumables

Standard chemicals were obtained from Sigma-Aldrich and Fluka (both Taufkirchen, Germany), Merck (Darmstadt, Germany), Roth (Karlsruhe, Germany), Serva (Heidelberg, Germany) and Biozym (Hessisch Oldendorf, Germany). Enzymes for molecular biology were obtained from Fermentas (St. Leon-Rot, Germany), Invitrogen (Darmstadt, Germany), New England Biolabs (Frankfurt/ Main, Germany), Promega (Mannheim, Germany), Roche (Mannheim, Germany) and Stratagene (Waldbronn, Germany). Components for Western blotting were bought from Invitrogen, Biorad (München, Germany), Kodak (Stuttgart, Germany) and Amersham (Freiburg, Germany). Cell culture media and supplements were from Gibco (Darmstadt, Germany). Plastic ware was obtained from Falcon (Heidelberg, Germany), Nunc (Langenselbold, Germany), Eppendorf (Wesseling-Berzdorf, Germany) and Greiner (Solingen, Germany), and glassware was purchased from Schott (Mainz, Germany).

#### 2.1.5. Enzymes and kits for molecular biology

Alkaline phosphatase (1 U/ $\mu$ l)	Roche Diagnostics, Mannheim, Germany
Complete Ultra tablets, protease inhibitors	Roche Diagnostics, Mannheim, Germany
DIG RNA labeling mix	Roche Diagnostics, Mannheim, Germany
DNaseI (RNase free, 1 U/ $\mu$ l)	Roche Diagnostics, Mannheim, Germany
ECL detection kit	GE Lifescience, Upsala, Sweden
FuGENE <sup>®</sup> HD transfection reagent	Roche Diagnostics, Mannheim, Germany
Geneclean Turbo kit	MP Biomedicals, Illkrich, France
GeneRuler <sup>™</sup> 1kb DNA ladder	Invitrogen, Darmstadt, Germany
mMessage mMachin <sup>®</sup> Kit	Ambion, Darmstadt, Germany
NucleoBond <sup>®</sup> PC500 maxi prep kit	Macherey-Nagel, Düren, Germany
PageRuler <sup>™</sup> prestained protein ladder	Fermentas, St. Leon-Rot, Germany
Pfu Ultra II fusion DNA polymerase	Stratagene, Waldbronn, Germany
Pronase	Roche Diagnostics, Mannheim, Germany
Proteinase K solution	Roche Diagnostics, Mannheim, Germany
QIAquick gel extraction kit	Qiagen, Hilden, Germany
QIAquick nucleotide removal kit	Qiagen, Hilden, Germany
QIAquick PCR purification kit	Qiagen, Hilden, Germany
QIAshredder	Qiagen, Hilden, Germany
Restriction endonucleases	Fermentas, St. Leon-Rot, Germany; New England Biolabs, Frankfurt/ Main, Germany; Roche Diagnostics, Mannheim, Germany
RNasin <sup>®</sup> ribonuclease inhibitors (40 U/ $\mu$ l)	Promega, Mannheim, Germany
RNeasy mini kit	Qiagen, Hilden, Germany
RNA polymerases SP6, T3, T7 (20 U/ $\mu$ l)	Fermentas, St. Leon-Rot, Germany; Roche Diagnostics, Mannheim, Germany
StrataClone PCR cloning kits	Stratagene, Waldbronn, Germany
SuperScript <sup>®</sup> II, RT (200 U/ml)	Invitrogen, Darmstadt, Germany

#### 2.1.6. Equipment

Binocular	Stemi SV11 (Zeiss, Jena, Germany)
Centrifuges	Sorvall Evolution (Kendro Laboratory Products, München, Germany), Tabletop Centrifuge 5415D and 5415R, (Eppendorf, Hamburg, Germany)

Confocal laser scanning microscopes	LSM510 equipped with Diode (405 nm), Argon/2 laser (458, 477, 488, 514 nm), DPSS (561 nm) and two Helium-Neon lasers (594 and 633 nm); Zeiss LSM510 Meta equipped with Argon laser (451, 477, 488, 514 nm) and two Helium-Neon lasers (543 and 633 nm), (Zeiss, Jena, Germany)
Cryostat with microtome	CM1950 (Leica, Wetzlar, Germany)
Developing machine	Curix60 (AGFA, Köln, Germany)
Electrophoresis power supplies	Electron EC105 (Thermo Fisher Scientific, Rockford, USA); Power Pac 3000, (BioRad, München, Germany)
Fluorescent Stereomicroscope	MZ 16FA equipped with filters for UV, GFP, FITC/Cy-3, YFP, Rhodamine and Texas Red, (Leica, Wetzlar, Germany)
Gel documentation system	(Herolab, Wiesloch, Germany)
Microinjection needle puller	Model PC-10 (Narishige, Tokyo, Japan)
Microinjector	FemtoJet Express (Eppendorf, Hamburg, Germany)
Microscope (upright compound)	Axioplan 2 (Zeiss, Jena, Germany)
Microscope camera	Axiocam HRC digital camera (Zeiss, Jena, Germany)
Objectives (Zeiss)	C-Apochromat 40x/NA1.20 water immersion C-Apochromat 63x/NA1.20 water immersion Plan-NeoFluar 5x/NA0.15 Plan-NeoFluar 10x/NA0.3 Plan-NeoFluar 20x/NA0.5 Plan-NeoFluar 40x/NA0.75 DIC Plan-NeoFluar 100x/NA1.3 Ph3 Plan-Apochromat 63x/NA1.4 DIC (Zeiss, Jena, Germany)
PAGE electrophoresis and blotting	Mini-Protean 3 Cell (Biorad, München, Germany); XCell II blot module (Invitrogen, Life Technologies, Darmstadt Germany)
PCR machines	PTC 100 (MJ Research Inc., Waltham, MA, USA), Mastercycler gradient (Eppendorf, Hamburg, Germany)
Photometer	Biophotometer (Eppendorf, Hamburg, Germany)
Rotators and shakers	Rotamax 120 and Polymax 1040 (Heidolph, Schwabach, Germany);
Thermomixer	Thermomixer Comfort (Eppendorf, Hamburg, Germany)

### **2.1.7. Software for image processing**

Adobe Illustrator CS3 Version 10.0.2 (Adobe, San Jose, CA, USA)  
 Adobe Photoshop CS3 Extended Version 10.0.1 (Adobe, San Jose, CA, USA)  
 Axio Vision Software 4.5 SP1 (Zeiss, Jena, Germany)  
 ImageJ 1.37v + macros (NIH, Bethesda, MD, USA)  
 LSM 510 Release Version 4.0 SP2 (Zeiss, Jena, Germany)  
 QuickTime Player Pro Version 7.1.6 (Apple, Cupertino, CA, USA)

## 2.1.8. Solutions, buffers and media

### 2.1.8.1. *E.coli* and cell culture media

<b>LB medium:</b> 10 g bacto tryptone 5 g yeast extract 10 g NaCl  add H <sub>2</sub> O dest. <i>ad</i> 1 l, pH 7.0	<b>LB agar:</b> 10 g bacto tryptone 5 g yeast extract 10 g NaCl 15 g agar add H <sub>2</sub> O dest. <i>ad</i> 1 l, pH 7.0
<b>1000x Ampicillin stock solution</b> 100 mg/ml in H <sub>2</sub> O dest., filter sterilized, store at -20°C	<b>1000x Kanamycin stock solution</b> 50 mg/ml in H <sub>2</sub> O dest., filter sterilized, store at -20°C
<b>Mammalian cell culture medium:</b> Dulbecco's modified Eagle medium (DMEM, #21969, Gibco) 10% fetal bovine serum 1% penicillin-streptomycin, (#15140-163, Gibco) 1% GlutaMAX, (#35050-061, Invitrogen)	<b>Zebrafish PAC2 cell culture medium:</b> Leibovitz's L-15 medium (#11415 or #21083, Gibco) 10% fetal bovine serum 1% penicillin-streptomycin, (Gibco) 1% GlutaMAX, (#35050-061, Gibco)
<b>Dulbecco's phosphate buffered saline</b> (D-PBS, w/o CaCl <sub>2</sub> , w/o MgCl <sub>2</sub> , #14190, Gibco)	<b>1x Trypsin</b> 0.05% in PBS, #L11-002, PAA Laboratories
<b>Opti-MEM I reduced serum medium</b> (#31985-070, Gibco)	

### 2.1.8.2. Zebrafish husbandry

Embryo solutions and standard zebrafish protocols were derived from Kimmel *et al.*, 1995, and Westerfield, 2000.

<b>300% Danieau buffer (aka 10x Danieau):</b> 174 mM NaCl 2.1 mM KCl 1.2 mM MgSO <sub>4</sub> 1.8 mM Ca(NO <sub>3</sub> ) <sub>2</sub> 15 mM HEPES (pH 7.2)  dilute 1:10 for working solution; add PTU anti-pigmentation solution if required	<b>100x PTU anti-pigmentation solution:</b> 0.3% (w/v) 1-phenyl-2-thiourea (PTU); heat before each use to dissolve precipitate
	<b>Salt water to collect eggs:</b> 0.3 g/l instant ocean salt mix
	<b>1x Tricaine buffer to anaesthetize larvae:</b> 0.013-0.02% (w/v) Tricaine in 30 % Danieau

### 2.1.8.3. *In situ* hybridization

<b>PBS</b> 137 mM NaCl 2.7 mM KCl 4.3 mM Na <sub>2</sub> HPO <sub>4</sub> x 7H <sub>2</sub> O 1.4 mM KH <sub>2</sub> PO <sub>4</sub> pH 7.2 – 7.4, adjust with NaOH	<b>PTW:</b> 0.1% Tween 20 in PBS (v/v)
--	---

<b>Fixation buffer:</b> 4% PFA in PTW (v/v) to dissolve PFA the solution has to be heated to not more than 60°C; aliquots are stored for several month frozen at -20°C	<b>NGS blocking buffer:</b> 10% normal goat serum in PTW (v/v)
<b>Hybridization buffer:</b> 50% Formamide (v/v) 25% 20x SSC (v/v) 150 µg/ml Heparin 5 mg/ml Torula-RNA 0.1% Tween 20 (v/v)	<b>20x SSC:</b> 3 M NaCl 0.3 M NaCitrate tribasic pH 7.0, adjusted with NaOH
<b>NBT stock:</b> 75 mg/ml in 70% DMF	<b>BCIP stock:</b> 50 mg/ml in 100% DMF store both stocks at -20°C
<b>Staining buffer:</b> 0.1 M NaCl 0.1 M Tris HCl pH 9.5 50 mM MgCl <sub>2</sub> 0.1% Tween 20	<b>Staining solution:</b> add to staining buffer: 3.75 µl/ml BCIP stock 5 µl/ml NBT stock

#### 2.1.8.4. Cryosectioning and immunohistochemistry

<b>2x Phosphate buffer</b> 192.3 mM Na <sub>2</sub> HPO <sub>4</sub> 46 mM NaH <sub>2</sub> PO <sub>4</sub> pH 7.3	<b>Sucrose buffer</b> 15% sucrose in 1x phosphate buffer
<b>Gelatin-sucrose buffer</b> 7.5% gelatin 15% sucrose in 1x phosphate buffer	Alternatively, these buffers for cryoprotection and cryosectioning can be prepared with 1x PBS instead of phosphate buffer
<b>PBST:</b> 0.5% Triton X100 in PBS (v/v)	<b>NGS Blocking buffer:</b> 10% normal goat serum in PBST

#### 2.1.8.5. Protein biochemistry

<b>IP lysis buffer (S.J. Martin lab):</b> 150 mM NaCl 50 mM Tris-HCl, pH 8.0 1% NP-40 (or TX-100)  add freshly 1x Complete protease inhibitors 1mM PMSF	<b>IPN<sub>150</sub> lysis buffer (M. Üffing lab):</b> 150 mM NaCl 50 mM Tris-HCl (pH 7.6) 5 mM MgCl <sub>2</sub> 0.1% Nonidet P40 (v/v) add freshly: 1x Complete protease inhibitor mix (Roche) 1 mM DTT 1 mM PMSF
--	---

<b>2x SDS loading buffer:</b> 125 mM Tris-HCl, pH 6.8 20% glycerol 4% SDS 0.02% bromophenol blue 5% $\beta$ -mercaptoethanol, added freshly	<b>5x SDS running buffer:</b> 125 mM Tris-HCl, pH 8.3 1.25 M glycine 0.5% SDS
<b>25x Novex Tris-glycine stock solution:</b> 300 mM Tris base 2.4 M glycine pH 8.3 no adjustment of pH necessary	<b>1x Novex Tris-glycine transfer buffer:</b> dilute 25x Novex Tris-glycine buffer, add 20% methanol
<b>10x TBST:</b> 100 mM Tris-HCl, pH 8.0 1.5 M NaCl 0.5% Tween20	<b>Non-fat dried milk blocking buffer:</b> 2% (up to 5 %) non-fat dried milk in 1x TBST; for reuse of primary antibody in blocking buffer add 0.05% sodium azide; do not add $\text{NaN}_3$ to the secondary antibody

### 2.1.9. Antibodies

Primary Antibodies for IHC and Western blotting	Host Species and Clonality	Immunogen	Dilution	Supplier	Order-No.
$\alpha$ -human LRRK2	rabbit, monoclonal	aa970-2527 of human LRRK2	1:1000	Michael. J. Fox Foundation, Epitomics	MJFF2 (c41-2); #3514-1
$\alpha$ -human LRRK2	rat	NN	1:1000	gift from Dr. M. Üffing lab	custom made
$\alpha$ - $\beta$ actin	rabbit, polyclonal	N-terminal peptide	1:1000	Cell signaling; NEB	4967
$\alpha$ -tyrosine hydroxylase	rabbit, polyclonal	rat TH	1:400	Millipore	AB152
$\alpha$ -digoxigenin-AP	sheep, polyclonal Fab	digoxigenin	1:2000	Roche	11093274910
$\alpha$ -GFP	chicken, polyclonal	GFP	1:1000	Aves	1020
<b>Secondary Antibodies</b>					
$\alpha$ -rabbit Alexa Fluor 488	goat	rabbit IgG	1:1000	Invitrogen	A-11034
$\alpha$ -rabbit Alexa Fluor 555	goat	rabbit IgG	1:1000	Invitrogen	A-21428
$\alpha$ -rabbit Cy3	donkey, polyclonal	rabbit IgG	1:400	Jackson Immuno Research	711-166-152
$\alpha$ -chicken HRP	rabbit, polyclonal	chicken IgY	1:10000	Upstate	12-341
$\alpha$ -rabbit HRP	goat, polyclonal	rabbit IgG	1:10000	Jackson Immuno Research	111-036-045
$\alpha$ -rat HRP	goat, polyclonal	rat IgG	1:10000	Jackson Immuno Research	112-035-063

### 2.1.10. Plasmid vectors

#### #1 pCS2+

This is a multipurpose expression vector that functions in *Xenopus* or zebrafish embryos as well as in a wide variety of mammalian cells. It contains the strong CMV promoter. For further information see:

[www.biology.kyushu-u.ac.jp/~hassei/sagata/lab\\_only/protocols/cs2\\_polylinker\\_descriptio%202.htm](http://www.biology.kyushu-u.ac.jp/~hassei/sagata/lab_only/protocols/cs2_polylinker_descriptio%202.htm)

#### #753 pCS-Tol transposase

The ORF of medaka Tol2 transposase is cloned in pCS. The *NotI* linearized vector was used for Tol2 mRNA synthesis. This plasmid was originally obtained from the K. Kawakami lab; see: <http://kawakami.lab.nig.ac.jp/>

#### #884 pCS-KalTA4

This plasmid encodes an optimized version of the Gal4 transcriptional activator with a Kozak sequence in front of the ATG Start condon and a humanized codon usage. It was from the Köster lab plasmid collection.

#### #895 pCS-H2B-CFP

This plasmid contains the enhanced CFP1 from Clontech (Clontech, Mountain View, CA, USA) with the N-terminal histone 2B nuclear targeting sequence added. The plasmid was constructed by Martin Distel, R. Köster lab.

#### #1234 pCS-H2BCFP-GI

This plasmid was used for nuclear CFP staining and was obtained from R. Köster

#### #1439 pBTolRG-2xSce

This plasmid contains the 200 bp TolR and 150 bp TolG inverted repeats with a MCS containing *SceI* sites in the middle. It was obtained from R. Köster

#### #1768 pBlueskriptSK-4xUAS-GFP

This reporter plasmid contains four Gal4-binding sites (called UAS sites) followed by the minimal E1b promoter. These regulatory sequences activate GFP expression only in the presence of Gal4 or one of its variants. The plasmid was from the Köster lab plasmid collection.

#### #1943 pDestTol2pA2 Tol2kit vector

This is the destination vector for the Gateway-based recombination cloning from the Tol2kit. It contains the recombination sites attR4-attR3. These are flanked by Tol2 inverted repeats for Tol2-mediated transgenesis of the construct. This plasmid was originally provided by the L. Bally-Cuif lab (CNRS, Gif-sur-Yvette, France). To amplify it the *E. coli* strain *ccdB* Survival (Invitrogen) is required.

#### #2079 pNBTtauGFP

This plasmid was constructed by D. Gilmour and F. Peri (EMBL, Heidelberg). It contains a 3.8 kb promoter fragment of the *neuronal beta-tubulin* gene from *Xenopus laevis* including the transcription start site (isolated by Rebecca Beach and Paul A. Krieg; see plasmid #17146 at [www.addgene.org](http://www.addgene.org)). This promoter fragment was cloned as *Sall-HindIII* fragment.

#2230 p5E-MCS Tol2kit vector

For more information about this plasmid see the web site of the C. B. Chien lab: <http://chien.neuro.utah.edu/>. Tol2kit vectors were obtained from the L. Bally-Cuif lab. As they are prone to rearrangements they were amplified in Stb13 *E. coli* and cultures were grown at 30°C.

#2231 p3E-polyA Tol2kit vector#2232 p3E-Myc tag-polyA Tol2kit vector#2233 p5E-attL4-attL2 modified Tol2kit vector

Plasmid #2230 p5E-MCS was modified by exchanging the Gateway recombination site attR1 against attL2. The attL2 site was obtained as a custom-synthesized and cloned 150bp oligonucleotide from Entelechon. This 150 bp oligo was excised as a *XhoI-EcoRV* fragment from the Entelechon vector and was cloned into the *XhoI-EcoRV* cleaved p5E-MCS. Sequencing confirmed the correct attL2 sequence.

#2389 pCS-H2BTagBFP-T2A-KalTA3-GIpA

This plasmid contains a bicistronic ORF that mediates expression of the nuclear-localized TagBFP and a version of the Gal4 transcriptional activator (KalTA3). The sequence encoding human histone 2B can be found at Genbank, accession number AK311849. The plasmid was provided by R. Köster.

#2434 p3E-linker-polyA

This is the modified vector p3E-polyA. Plasmid #2231 has been cleaved with *Bam*HI and a 41 bp linker oligonucleotide was inserted. This linker has restriction sites for *Bam*HI-*Acc*65I-*Hind*III-*Sma*I-*Bgl*II and *Xho*I. Correct integration and orientation of the linker has been confirmed by sequencing.

#2436 pcDNA3-hLRRK2 wt-Strep-CFP

The plasmid contains the human LRRK2 wild type coding sequence fused to the Strep-tag for protein purification and to CFP for visualization. The plasmid was provided by J. Gloeckner (M. Üffing lab, Tübingen). For amplification of LRRK2-encoding plasmids use Stb13 *E. coli* and grow cultures at 30°C.

# 2437 pcDNA3-hLRRK2(G2019S)-Strep-CFP

This plasmid encodes the Parkinson disease-linked human LRRK2 allele with the G2019S missense mutation. The plasmid was provided by J. Gloeckner.

#2438 pcDNA3-hLRRK2 kd-Strep-CFP

This plasmid encodes a kinase-dead version of human LRRK2 containing the K1906M missense mutation. The plasmid was provided by J. Gloeckner.

#2441 pBTolRG-NBTpr-H2B-TagBFP-T2A-KalTA3-GIpA

This plasmid was used to generate the transgenic driver fish line described in this work. It was constructed by inserting the H2B-TagBFP-T2A-KalTA3-GIpA sequence as an *Eco*RI-*Not*I fragment into the *Eco*RI-*Not*I cleaved #1439, pBTolRG. Subsequently the 3.8 kb NBT promoter fragment was isolated from plasmid #2079 as *Sal*I(blunt)-*Hind*III fragment. It was inserted in front of the H2BBFP of the cloning intermediate pBTol-H2BBFP-T2A-KalTA3, which had been cleaved with *Cl*aI(blunt)-*Hind*III.

#2484 pCS-mitoTagRFP-T2A-Venus-LC3

The plasmid contains the bicistronic cassette encoding two fluorescent reporter proteins: mitoTagRFP and Venus-LC3, regulated by the strong CMV promoter in the vertebrate multipurpose expression vector. The zebrafish LC3 (*map1-lc3b*) coding sequence was obtained from T. Yabu and M. Yamashita. This plasmid was provided by R. Köster.

#2487 pBTol-4xUASshuffleE1b-mitoTagRFP-T2A-Venus-LC3

This vector is a cloning intermediate and contains 4 shuffled (with opposite orientation) UAS enhancer sequences plus a minimal promoter in front of the fluorescent reporter cassette, which was retrieved from plasmid #2484 by *EcoRI-NotI* digest. The plasmid was cloned by R. Köster.

#2534 p5E-attL4-4xUASshuffleE1b-mitoTagRFP-T2A-VenusLC3-attL2

This is the final and modified 5' entry plasmid containing the fluorescent protein reporter cassette. It was used in the final Gateway recombination reaction to generate the effector construct. Plasmid #2534 was generated by cloning the 4xUAS-mitoTagRFP-T2A-VenusLC3 cassette as an *XhoI-NotI* fragment (isolated from plasmid #2487) in between the recombination sites attL4-attL2 of plasmid #2233 cleaved with the same enzymes.

#2544 p3E-modifiedMCS-polyA

The MCS of plasmid #2231 was modified with a 347 bp PCR product generated with primers #1098 and #1099 (see 1.1.11) from the same plasmid. Thereby three additional restriction enzyme sites *SacII-BamHI-Asp718/Acc65I/KpnI* are inserted after the original *BamHI* site (which is destroyed) of #2231. The PCR product was digested with *BglIII-NotI* and inserted into the *BamHI-NotI* cleaved plasmid #2231.

#2644 p3E-modMCS-4xUASshuffle-hLRRK2 wt-Strep-CFP

This is the final 3' entry plasmid containing the human LRRK2 wild-type allele under control of the 4xUASshuffle sequence. This 4xUASshuffle-hLRRK2 cassette was excised from a cloning intermediate, plasmid #2555, by *SmaI-Asp718* digest. It was cloned into plasmid #2544 cleaved with *BamHI*(blunt)-*Asp718*. This plasmid can be used for the final Gateway recombination reaction to create the effector construct.

#2645 p3E-modMCS-hLRRK2(G2019S)-Strep-CFP

This is the final 3' entry plasmid containing the human LRRK2 (G2019S) allele under control of the 4xUASshuffle sequence. Cloning was performed as mentioned for #2644. The cloning intermediate for the LRRK2 cassette was plasmid #2556.

#2646 p3E-modMCS-hLRRK2 kd-Strep-CFP

This is the final 3' entry plasmid containing the human LRRK2 kinase-dead allele under control of the 4xUASshuffle sequence. Cloning was done as mentioned for #2644. The cloning intermediate for isolating the LRRK2 cassette was #2557.

#2677 pCS-ER<sup>T2</sup>-KalTA4

This should be a tamoxifen-inducible KalTA4. It is N-terminally fused to the estrogen receptor ligand binding domain T2 variant. Inducibility was tested in the course of this study. However, it could not be detected. The plasmid was constructed by R. Köster.

#2707 pBTol-NBTpr-H2B-TagBFP-T2A-ERT2-KalTA4

This is a potentially tamoxifen-inducible KalTA4. It is N-terminally fused to the estrogen receptor ligand binding domain T2 variant. Inducibility was tested in the course of this study but could not be validated. This plasmid was cloned by exchanging the T2A-KalTA3-GIpA *SpeI-NotI* fragment of plasmid #2441 against the *SpeI-NotI* fragment T2A-ER<sup>T2</sup>-KalTA4-GIpA of the cloning intermediate #2676, which was provided by R. Köster.

#2760 and #2761 pSC-B-hLRRK2 C-term

These plasmids contain two orientations of a 1343 bp PCR product of the C-terminus of hLRRK2-Strep-CFP used to generate an in situ probe. PCR was performed with primers hLRRK2+6486 for and CFP rev (see 1.1.11) and the blunt product was cloned into StrataClone Blunt PCR cloning vector.

#2781 pDest-hLRRK2 wt

This is the final destination plasmid containing the 4xUAS-mitoTagRFP-T2A-VenusLC3 cassette as well as the 4xUAS-hLRRK2 wild-type-Strep-CFP cassette. It is the product of the LR recombination reaction between plasmids #2534, #2644 and #1943. The hLRRK2 wt ORF was confirmed by sequencing it completely.

#2782 pDest-hLRRK2(G2019S)

This is the final destination plasmid containing the 4xUAS-mitoTagRFP-T2A-VenusLC3 cassette as well as the 4xUAS-hLRRK2(G2019S)-Strep-CFP cassette. It is the product of the LR recombination reaction between plasmids #2534, #2645 and #1943. The hLRRK2(G2019S) ORF was completely sequenced and confirmed.

#2783 pDest-hLRRK2 (kinase-dead)

This is the final destination plasmid containing the 4xUAS-mitoTagRFP-T2A-VenusLC3 cassette as well as the 4xUAS-hLRRK2(kinase dead)-Strep-CFP cassette. It is the product of the LR recombination reaction between plasmids #2534, #2646 and #1943. The hLRRK2 kd ORF was confirmed by sequencing.

#2784 pDest-4xUAS-mitoTagRFP-T2A-VenusLC3

This is the final destination plasmid containing the 4xUAS-mitoTagRFP-T2A-VenusLC3 cassette only and no human LRRK2. It is the product of the LR Gateway recombination reaction between plasmids #2534, #2544 and #1943.

## 2.1.11. Oligonucleotides for sequencing and cloning

Stock number	name	Sequence 5' → 3'
custom-synthesized by Entelechon; not in stock	pEN08H-XhoI-NotI-BglIII-PstI-EcoRI-attL2-EcoRV; cloned 150 bp oligo	CTCGAGTGTGCGGCCGCACCAGATCTGTTCTGCAGGGTGAATTCACC CAGCTTTCCTGTACAAAGTTGGCATTATAAGAAAGCATTGCTTATCA ATTTGTTGCAACGAACAGGTCACTATCAGTCAAATAAAATCATTAT TTGGATATC
Üffing lab	Linker for	GATCCGGTACCAAGCTTAACCCGGGAAAGATCTCTCGAGAA
Üffing lab	Linker rev	GATCTTCTCGAGAGATCTTCCCGGGTTAAGCTTGGTACCG
#334	Kal-Nseq	GAGTGGACTTCGCTTGGTTTTGG
#510	Globin intron rev seq	AGAAAGAACAATCAAGGGTC
#877	zflRRK2(+3534) for	GAGAACTCATCGGGTTCAAGATCCAGG
#878	zflRRK2(+4860) rev	AGTATATGTGGGTTACAACCAGCAGCC
#1025	M13 (-29) rev	CAGGAAACAGCTATGACC
#1026	M13 (-21) universal	TGTAAAACGACGGCCAGT
#1098	p3Entry up Bgl	ATAAGATCTCCGCGGATCCGGTACCAGACATGATAAGATACATTGATG AGT
#1099	p3Entry lo Not	TATCGCGGCCGCGTTAACGCTACCATGGAGCTCCA
Üffing lab	hLRRK2(+41) for	AAACTCTGAAGAAGTTGATAGTCAG
#1164	hLRRK2 5' rev	CGACTCTCATATAGGAGTCC
Üffing lab	hLRRK2(+446) for	CCTTGCTGATACTGGATGAAG
Üffing lab	hLRRK2(+852) for	TATCCTGGTATTAACGAAG
Üffing lab	hLRRK2(+1254) for	TGCGAATGCATTGTCAACTC
Üffing lab	hLRRK2(+1655) for	GGTTCATTGGAATCCTGGG
Üffing lab	hLRRK2(+2051) for	TGGAACAAAAGGATCAACAG
Üffing lab	hLRRK2(+2451) for	GCTTGGTCCTTTATTTCCAG
Üffing lab	hLRRK2(+2931) for	GGCTTCTGAGAGAGAATATATTAC
Üffing lab	hLRRK2(+3354) for	AATATCAGGGATATGCTCC
Üffing lab	hLRRK2(+3731) for	GGTCTAGAGTAGAGAACTGCATC
Üffing lab	hLRRK2(+4148) for	AAAGAAAGAGAGATCTCGTCC
Üffing lab	hLRRK2(+4559) for	GACAGCTGATTCCAGACTGC
Üffing lab	hLRRK2(+4937) for	TGTCACAGTATTTTAAGCTCCTAG
Üffing lab	hLRRK2(+5358) for	TCTCATGGAAGAATGGTTTCC
Üffing lab	hLRRK2(+5538) for	AAGGCTCACCATTCCAATATC
Üffing lab	hLRRK2(+6006) for	TTTCACTGTATCCCAATGC
Üffing lab	hLRRK2(+6674) for	TGGTCATCAATACCGAAGATG
Üffing lab	hLRRK2(+7105) for	AATAGCCCTGTTGTGGAAGTG
#1184	CFP internal forward	TGACCCTGAAGTTCATCTGC
	hLRRK2 +6486 for	CAGGAATGCAAGCATTGGC
	CFP rev	AGATGAACTTCAGGGTCAGC
	N-term(+326) for	GACTCCTATATGAGAGTCGC
	N-term(+1188) rev	GCTTTGTAACAGGCTTCCAG
	LRR(+2756) for	CCTGACTCTTCTATGGACAG
	LRR(+3575) rev	AAGCCTCAAGAAAGTTCTCTG
	COR-kinase(+5132) for	AGCAGTTTGTCTGACCACAG
	COR-kinase(+5976) rev	TTGGAGGCTAACTCCATCAC

## 2.2. Experimental Procedures

### 2.2.1. DNA and RNA manipulation and cloning

#### 2.2.1.1. Plasmid transformation

Competent bacteria, stored in aliquots of 100 µl at -80°C, were thawed on ice. Up to 1 µg of plasmid DNA was added to one vial of bacteria and mixed by flicking the tube. Bacteria were incubated for 30 min on ice. They were heat shocked at 42°C for 45 sec to induce plasmid uptake and immediately placed on ice for 2 min. 0.5 ml LB medium was added and bacteria were incubated for 1 h at 37°C on a shaking incubator. Aliquots and dilutions of the transformation mixture were plated onto LB agar containing the appropriate antibiotic for plasmid selection. Plates were incubated overnight at 37°C. Unstable DNA sequences were cloned using Stbl3 *E. coli*. In this case plated bacteria were incubated overnight at 30°C.

#### 2.2.1.2. Mini preparation of plasmid DNA

A bacterial mini-prep culture was set up with 5 ml LB medium containing the appropriate antibiotic for plasmid selection (usually Ampicillin or Kanamycin). A bacterial colony was picked with a sterile pipette tip from the agar plate and added to the LB-medium. Cultures were incubated overnight at 37°C (in case Stbl3 *E. coli* had been used at 30°C) on a shaking incubator. In order to isolate plasmid DNA bacterial cultures were transferred into 1.5 ml tubes and pelleted by centrifugation at top speed for 4 min in a microcentrifuge. Pellets were resuspended in 200 µl buffer S1 by vortexing the tubes. 200 µl of lysis buffer S2 was added and the suspension was mixed by inverting the tube several times. Tubes were left on the bench for 5 min. Subsequently, 200 µl of neutralization buffer S3 was added to precipitate genomic DNA and bacterial debris. The suspension was mixed by inverting the tube several times. Precipitated material was removed by centrifugation at top speed for 10 min and the supernatant, which contains the plasmid DNA, was transferred to a new 1.5 ml tube. Plasmid DNA was then precipitated by adding 400 µl isopropanol, mixing and incubating on the bench for 20 min. Precipitated DNA was pelleted by centrifugation at top speed for 10 min. The supernatant was discarded and the pellet was washed with 70% ice-cold ethanol, followed by centrifugation for 10 min. All remaining liquid was removed and the DNA was air-dried for 10 min on the bench. Finally, DNA was resuspended in 35 µl ddH<sub>2</sub>O.

The buffers mentioned above were from the NucleoBond Plasmid DNA Purification Kit (Macherey-Nagel) and have the following composition:

Resuspension buffer S1: 50 mM Tris-HCl, pH 8.0  
10 mM EDTA  
100 µg/ml RNaseA

Lysis buffer S2: 0.2 M NaOH  
1% SDS

Neutralization buffer S3: 2.8 M KAc, pH 5.1

#### 2.2.1.3. Maxi preparation of plasmid DNA

For large scale purification of plasmid DNA an individual *E. coli* colony was picked from an agar plate and inoculated in 200 or 2x 200 ml (for weakly growing clones) LB-medium supplemented with the appropriate antibiotic. Cultures were incubated overnight at 37°C (or 30°C for unstable inserts) on a shaking incubator at 200 rpm. Bacteria were harvested by centrifugation at 5000 rpm for 15 min at 4°C in the Sorval GSA rotor. All subsequent steps were performed using the NucleoBond PC500 plasmid isolation kit (Macherey-Nagel) as described by the manufacturer. Plasmid DNA was eluted from the affinity columns and was subsequently precipitated at room temperature by addition of 0.7 volumes isopropanol and standing on the bench for 20-30 min. Precipitated DNA was pelleted in round bottom plastic tubes by centrifugation at  $\geq 12,000$  g for 30 min at 4°C in a Sorvall SS-34 rotor. The DNA pellet was washed once with 5 ml of ice-cold 70% ethanol followed by centrifugation. All liquid was removed and DNA was air-dried for 10 min on the bench. The DNA pellet was resuspended in 350 µl ddH<sub>2</sub>O by incubating on a shaker for 10 min at 37°C. The DNA concentration of a 1:50 dilution was determined with a spectrophotometer (BioPhotometer, Eppendorf). The concentration of plasmid DNA was adjusted to 1 µg/µl. Commonly, this preparation yielded between 0.5 to 1 mg of plasmid DNA.

#### 2.2.1.4. Restriction digest of plasmid DNA

Restriction endonucleases cut double stranded DNA at specific recognition sites. For analytical purposes 2-3 µl of a mini-prep or 1 µg plasmid from a maxi-prep were digested with 1-5 units of restriction enzyme in a 20 µl reaction volume. For cloning and linearization, 12 µg of DNA and 20-30 units of enzyme were used in a 50 µl reaction volume. Reactions were incubated at 37°C for several hours or overnight. Digests were analysed by agarose gel electrophoresis.

#### 2.2.1.5. DNA and RNA agarose gel electrophoresis

DNA and RNA fragments can be separated according to their molecular weight by agarose gel electrophoresis. 6x DNA loading buffer was added to the sample and the DNA was loaded together with a 1 kb DNA ladder (Invitrogen) as a size standard onto 0.8% agarose gels in 1x TAE buffer. Voltage during separation was set to 120 V. DNA or RNA fragments were detected by ethidium bromide staining which was done after electrophoresis by incubating the gels in 1 µg/ml ethidium bromide solution for 15-30 min.

RNA gel electrophoresis was performed similar to DNA electrophoresis. To avoid RNase activity, gel chamber and combs were washed before use with desalted water and soap and were rinsed with 70% ethanol. The gel was pre-run for 10 min before applying the samples. 2 µl of the RNA sample were mixed with 8 µl 5x Gel-loading Buffer II (Ambion). RNA was denatured at 90°C for 10 min to break up secondary structures before loading onto the gel.

50x TAE stock:                    2 M Tris-acetate, pH 8.0  
    50 mM EDTA  
    adjust pH with 100% acetic acid

#### 2.2.1.6. Extraction of DNA fragments from agarose gels

DNA bands were excised from agarose gels and gel pieces were transferred into 2 ml tubes. DNA was extracted using the QIAquick Gel Extraction Kit (Qiagen) according to the manufacturer's protocol. DNA was eluted in 40 µl ddH<sub>2</sub>O.

#### 2.2.1.7. Purification of DNA from enzymatic reactions

Purification of DNA fragments from restriction digests, PCR reactions or other enzymatic reactions was performed with the QIAquick Nucleotide Removal Kit or the QIAquick PCR Purification Kit (Qiagen) according to the manufacturer's recommendations. DNA was eluted in 40 µl ddH<sub>2</sub>O.

#### 2.2.1.8. Dephosphorylation of DNA fragments

In order to prevent linearized, blunt-ended or single enzyme digested vectors from re-ligation DNA was dephosphorylated using shrimp alkaline phosphatase (SAP) or calf intestinal alkaline phosphatase (CIP). 1.5 µl of SAP or CIP were added directly to the restriction digest and the reaction was incubated for 1 h at 37°C. SAP was heat-inactivated at 65°C for 15 min. DNA was then purified or subjected to agarose gel electrophoresis.

#### 2.2.1.9. DNA ligation

Vector and insert DNA were mixed at a molar ratio of 1:2 to 1:3. For a typical 15 µl ligation reaction 1.5 µl 10 x ligation buffer and 1.5 µl of T4 DNA ligase were added. Reactions were incubated at room temperature for 20 min or at 16°C overnight. 5 µl of the ligation reaction were used to transform competent bacteria.

#### 2.2.1.10. Removal of 5' DNA overhangs

Ligation of non-complementary DNA termini created by restriction digests can be accomplished by blunt end cloning. 5' DNA overhangs are filled up using the Klenow fragment of *E. coli* DNA polymerase I. 50 µM each of dNTPs and 1 µl Klenow enzyme were added to the reaction. The reaction was incubated at 37°C for 10 min. Subsequently the polymerase was heat-inactivated at 75°C for 10 min. DNA was then purified with the QIAquick Kit for further enzymatic manipulation.

#### 2.2.1.11. PCR

A typical 100 µl PCR reaction contained the following constituents:

- 2 µl plasmid DNA (50-250 ng/µl) or 10 µl cDNA
- 10 µl 10x PCR buffer containing MgCl<sub>2</sub>
- 10 µl dNTP mix (2 mM each)
- 1 µl forward primer (10 µM)
- 1 µl reverse primer (10 µM)
- 1 µl DNA polymerase (Taq or proof-reading enzyme)
- add ddH<sub>2</sub>O to a total volume of 100 µl

Cycling conditions were chosen according to the annealing temperatures of the primers and the length of the PCR product. A common PCR program was as follows:

initial denaturation:	94°C	3 min
35 cycles of the following		
denaturation:	94°C	30 sec
annealing:	55-68°C	30 sec
elongation:	72°C	1 min per 1 kb
final extension:	72°C	10 min

The proof-reading polymerase Pfu UltraII (Stratagene) was used in the course of this project. Most proof-reading enzymes produce blunt-ended PCR products. For cloning into the pSC-A-amp/kan vector using the StrataClone PCR Cloning Kit (Stratagene) 3' overhangs had to be added using Taq polymerase. 1 Unit Taq polymerase plus dNTPs (e.g. 7 µM dATP is

sufficient) were added directly after the PCR and the reaction was incubated for 10 min at 72°C. Cloning of PCR fragments could then be done with the StrataClone PCR cloning Kit. Alternatively, blunt-ended PCR products were cloned using the StrataClone Blunt PCR Cloning Kit (Stratagene).

#### 2.2.1.12. RNA extraction from zebrafish embryos

For total RNA extraction from zebrafish embryos the RNeasy Mini Kit and QIAshredder columns (Qiagen) were used. 25 and 50 embryos were homogenized in 50 µl RLT buffer with a pestle in a 1.5 ml reaction tube. 300 µl or 600 µl of RLT buffer, respectively, were added before transferring the lysate to the QIAshredder columns. All subsequent steps were performed according to the manufacturer's protocol. RNA was eluted from the column with 43 µl ddH<sub>2</sub>O. For lysates from 50 embryos elution was repeated once with 43 µl of ddH<sub>2</sub>O. Residual DNA was removed by DNaseI digest of the eluates. In a total volume of 50 µl, 43 µl eluted RNA, 5 µl 10x transcription buffer (Roche), 2 µl RNAsin (Promega) were incubated with 2 µl DNaseI (Roche) for 20 min at 37°C. RNA was purified after this enzymatic reaction using the RNeasy kit.

#### 2.2.1.13. cDNA synthesis

11 µl of extracted total RNA and 1 µl random hexamer primers (Promega) were incubated at 70°C for 5 min.

In the meantime the following reagents were mixed and heated to 25°C:

- 10 µl 5x first strand buffer (Invitrogen)
- 17 µl RNase-free water
- 1 µl RNAsin (Promega)
- 5 µl dNTPs (2mM each)
- 5 µl DTT (100µM)

The mixture was added to the RNA and primer followed by a 5 min incubation at 25°C. Subsequently, 1 µl Superscript II reverse transcriptase was added and the reaction was incubated at the following temperatures:

- 25°C 10 min
- 42°C 60 min
- 70°C 10 min

4-8 µl of the cDNA were used for PCR amplification.

#### 2.2.1.14. Synthesis of capped mRNA for microinjection into zebrafish embryos

For mRNA synthesis from pCS2+ plasmids, 12 µg plasmid DNA was cleaved 3' to the polyA sequence to generate a template for run-off transcription (usually by a *NotI* digest).

Subsequently, DNA was purified using the QIAquick Nucleotide Removal Kit and eluted in 40  $\mu$ l RNase free water. Complete linearization of the plasmid was confirmed by gel electrophoresis. *In vitro* synthesis of capped mRNA was performed with the mMESSAGE mMACHINE SP6 Kit (Ambion) according to the manufacturer's protocol. Briefly, 5  $\mu$ l linearized plasmid, 10  $\mu$ l 2x dNTP Cap mix, 2  $\mu$ l 10x reaction buffer, 2  $\mu$ l Sp6 enzyme mix and 1  $\mu$ l ddH<sub>2</sub>O were mixed. The reaction was incubated for 2-4 hours at 37°C. To remove the DNA template 1  $\mu$ l DNaseI was then added and the reaction was incubated for 20 min at 37°C. Capped mRNA was purified using the RNeasy Mini Kit and eluted with 50  $\mu$ l RNase-free water. Quality and quantity of the mRNA were analysed by agarose gel electrophoresis and UV spectrophotometry. In the course of this project mRNA for Tol2 transposase was synthesized in this way. When coinjected with plasmid DNA, transposase enzyme expressed from the mRNA mediates genomic integration of plasmid sequences flanked by Tol2 inverted repeats. This is the most common transgenesis technique for zebrafish.

## **2.2.2. Zebrafish maintenance and genetic manipulation**

### 2.2.2.1. Zebrafish maintenance

Spawning, raising and general husbandry of zebrafish lines was performed as described by Kimmel *et al.*, 1995, and Westerfield, 2000.

### 2.2.2.2. Zygotic microinjection of DNA and RNA

The standard method for genetic manipulation of zebrafish embryos is microinjection of nucleic acids into the cytoplasm of one-cell stage embryos. For transient mosaic expression plasmid DNA from maxi preparations was additionally purified using the GeneClean Turbo Kit (MP Biomedicals) and was injected at concentrations of 30-50 ng/ $\mu$ l. Messenger RNA can also be used for transient transgene experiments and is injected at concentration of 50-250 ng/ $\mu$ l. For stable transgenesis, plasmid DNA containing Tol2 inverted repeat-flanked sequences was coinjected together with mRNA encoding transposase – both at concentrations of 25 ng/ $\mu$ l. A phenol red solution (0.5%, Sigma) was added at 1/10 of the injection solution as a staining agent. The mix was centrifuged at 700 rpm, 4°C and loaded into a glass needle. These glass needles were pulled from 1.0 mm glass capillaries (Harvard Apparatus, #30-0019) using a Narishige needle puller at 65°C, step1 melting program. Injection into the cytoplasm of one-cell-stage embryos was achieved with a micromanipulator (Eppendorf) and using a binocular. To immobilize the eggs during injection they were placed into grooves formed by 1.5% agarose in 30% Danieau buffer. These agarose dishes were kept at 4°C to

slow down the first zygotic cleavage divisions. After injection embryos were removed from the grooves and transferred into a Petri dish. Embryos were incubated at 28.5°C in Danieau buffer containing 0.003% PTU until they reached the desired developmental stage for further investigation.

#### 2.2.2.3. Embedding of embryos for microscopic observation

For *in vivo* imaging zebrafish embryos were anaesthetized with 0.013% Tricaine in 30% Danieau buffer containing 0.003% (w/v) PTU. Self-made imaging chambers with a glass bottom were used. For this purpose, a glass cover slip was sealed with silicone underneath a 14 mm hole cut in the bottom of a 5 cm cell culture dish. Fish were embedded and oriented in a drop of 1.2% low melting agarose (agarose, type IX-A, Sigma) in 30% Danieau, which was placed on top of the glass bottom. Agarose was solidified by placing the imaging dish for 1-2 min on ice. The embedded embryos were covered with 30% Danieau buffer containing Tricaine and PTU. The Specimen is now ready for imaging. PFA-fixed embryos can be embedded in the same way.

To reduce variation between experiments for live imaging of mitochondrial axonal transport, imaging chambers were treated in a standardized way. In this case, embedded embryos were covered with 14 ml Danieau buffer and dishes were incubated at 28.5°C for one hour before imaging to adjust the temperature.

### **2.2.3. Histological techniques**

#### 2.2.3.1. Whole-mount *in situ* hybridisation (WISH)

To detect the spatio-temporal pattern of gene expression by means of mRNA detection, embryos and young larvae can be PFA-fixed and processed as whole-mount preparations. Antisense probes are either labelled by incorporation of radioactive nucleotides or non-radioactively by use of digoxigenin-labelled nucleotides – as used here. The probe is hybridized to endogenous mRNA and subsequently detected with an anti-digoxigenin antibody coupled to alkaline phosphatase (AP). A colorimetric reaction catalyzed by AP with two colorless substrates, BCIP and NBT, is performed to detect the hybridized probe.

#### *In vitro* transcription of antisense RNA probes:

Digoxigenin (DIG)-labelled, single-stranded RNA probes were generated by *in vitro* transcription using linearized plasmid DNA. DIG-11-UTP was incorporated into the transcript by Sp6, T3 or T7 RNA polymerase using the DIG RNA-Labeling Mix (Roche).

Briefly, 1-2 µg linearized plasmid, 4 µl 5x transcription buffer, 2 µl Labeling Mix, 1 µl DTT (100 mM), 1 µl RNAsin and 2 µl RNA polymerase were mixed in a total volume of 20 µl and incubated at 37°C. After 1 h an additional 1 µl of polymerase was added and the reaction was incubated for another 1.5 h. The template DNA was subsequently removed by DNaseI treatment. For this, 1.5 µl DNaseI was added and the reaction was incubated for 20 min at 37°C. The RNA probe was purified using the RNeasy Mini Kit following the product manual.

Fixation and storage of zebrafish embryos:

Dechorionated zebrafish embryos were fixed overnight in 4% PFA in PTW at 4°C or for 4 h at RT on a shaker. They were washed 3x 10 min each in PTW, dehydrated by incubation for 10 min each in 25%, 50%, 75% MetOH in PTW and 2x in 100% MetOH. Storage was in MetOH at -20°C overnight or up to several weeks. For ISH embryos were transferred to a 6-well plate and rehydrated by washing for 5 min each in 75%, 50%, 25% MetOH in PTW followed by washing two times with PTW.

Proteinase K treatment of embryos:

To permeabilize the tissue for RNA probe and antibody penetration, rehydrated embryos were treated with proteinase K (Roche). Embryos were incubated in proteinase K solution in PTW (final conc. 10-16 µg/ml) for the following time period depending on the developmental stage of the embryos:

24 hpf	7-10 min
36 hpf	20-25 min
48 hpf	25-28 min
72 hpf	30 min

The digest was stopped by washing twice quickly with 2 mg/ml glycine in PTW and by subsequent refixation in 4% PFA for 20 min. Embryos were washed 5x 5 min in PTW.

Hybridization:

Embryos were transferred into 2 ml reaction tubes and prehybridized in 1-2 ml hybridization buffer at 60°C in a water bath for 1 h. The 50 µl QIAquick-purified RNA probe had been diluted with 200 µl hybridization buffer. 8 µl of this diluted probe plus 200 µl hybridization buffer were mixed and denatured at 90°C for 10 min to break up secondary structures. After removal of the prehybridization buffer the probe was quickly transferred onto the embryos. Hybridization was performed overnight at 60°C. The next day, embryos were washed 2x 45

min at 60°C with 2 ml 50% formamide in 2x SSCT, once for 45 min in 2x SSCT and 2x 45 min using 0.2x SSCT.

#### Antibody detection

Unspecific binding sites were blocked by incubating the embryos in 2 ml 10% NGS in PTW for 1 h at room temperature on a rotator. The embryos were then incubated overnight at 4°C in a 1:2000 dilution of anti-digoxigenin-AP Fab fragments (Roche) in 10% NGS in PTW on a rotor. The next day, embryos were transferred to a six-well plate and rinsed 5x 15 min with 5 ml PTW at room temperature on a shaker in order to remove unbound antibody. The staining buffer was mixed freshly from stock solutions and sterile filtered to remove any precipitate. Embryos were equilibrated in this staining buffer twice for 5 min. The buffer was removed and staining solution containing BCIP (187.5 µg/ml) and NBT (375 µg/ml) was added. Embryos were put on a shaker for 1 min. The staining reaction was then performed in the dark at RT without shaking or at 4°C overnight. During this time the staining solution was exchanged several times and the reaction was monitored. Once staining had reached sufficient intensity, the reaction was stopped by washing embryos 3x 15 min with PTW. For long term storage and to record images, embryos were transferred into 90% glycerol.

#### 2.2.3.2. Preparation of tissue cryosections

##### Fixation and embedding of brain tissue for cryosectioning:

For preparation of adult brain, fish were sacrificed with an overdose of tricaine solution (at least 500 µg/ml). They were decapitated and the roof of the skull was removed quickly with forceps to expose the brain to the fixative. Heads were fixed in cold 4% PFA in PBS overnight at 4°C. The next day brains were dissected out of the skull with forceps by removing the eyes first and then the rest of the skull. Special care has to be taken to save the olfactory bulbes. Brains were then rinsed 3x 10 min with PTW. They can be transferred into 100% MetOH for long-term storage at -20°C by successive incubation for 10 min each in 25%, 50%, 75% and 2x 100% MetOH. However, the best option for freshly fixed tissue is to proceed immediately with cryoprotection in 15% sucrose. Fish brains stored in 100% methanol had to be rehydrated by inverting the dehydration steps described before. Each brain was placed in a 2 ml tube and covered with 1.5 ml 15% sucrose in 1x phosphate buffer (or 1x PBS). Brains were allowed to settle on ice. The sucrose solution was exchanged once with fresh solution and brains were incubated overnight at 4°C. Brains were then embedded in 7.5% gelatine in 15% sucrose solution. Gelatine had to be heated to 60°C to dissolve. Then a thin layer of 4

mm gelatine was cast in a small plastic weighing boat and allowed to harden. Brains were removed from the 15% sucrose solution, placed on top the solidified gelatine and remaining liquid was removed carefully with tissue paper. Another layer of gelatine was cast on top. Brains were mixed with the gelatine by moving them back and forth with forceps. Subsequently, they had to be fixed in the desired orientation until the gelatine became solid. Afterwards, brains could be excised as small transparent gelatine blocks. These blocks were placed on top of a small piece of cork support in a drop of tissue freezing medium (NEG 50, Thermo Scientific or Tissue-Tek, Sakura) and were subsequently shock frozen by immersing them for 1 min with long forceps in a  $\beta$ -methylbutane bath cooled in liquid N<sub>2</sub>. Blocks were immediately transferred to -80°C for long-term storage.

#### Cryosectioning of tissue:

Frozen brains were removed from -80°C and acclimatized in the cryostat at the sectioning temperature of -24°C for at least 30 min. The sample block was frozen onto a specimen disk with tissue freezing medium and the disk was inserted into the object head set at -24°C. Knife temperature was -23°C. After trimming away excess material with a blade by hand and by cutting at 70  $\mu$ m trim thickness on the microtome, tissue sections of 25  $\mu$ m thickness were cut and immediately positioned onto pre-warmed microscope slides. Tissue sections sticking on slides were stored at -80°C until processed for IHC.

#### 2.2.3.3. Immunohistochemistry (IHC) of tissue sections

Slides were removed from the -80°C storage and were incubated for 5 min on a 55°C heated plate. Then they were immersed briefly in PBS at RT. Blocking was done by adding 150  $\mu$ l blocking buffer (10% NGS, 0.5% Triton X-100 in PBS) onto each slide and covering it with a pre-cut piece of parafilm. Slides were incubated for a minimum of 1 hour at RT in a wet chamber. After removing the blocking buffer, 150  $\mu$ l of the primary antibody diluted in blocking buffer were pipetted onto the slide. Slides were again covered with parafilm. Binding of the first antibody was allowed to proceed overnight at 4°C. The next day, the primary antibody was removed. It can be preserved for reuse in 0.05% NaN<sub>3</sub>. Slides were washed 4x for 10-15 min by submerging them in PTW. Subsequently, samples were incubated with the secondary antibody diluted in blocking buffer for 45 min to 1 h at RT and in the dark. Secondary antibodies are conjugated to fluorophores such as Alexa dyes (e.g. Alexa488, Alexa555) or Cy3, Cy5 or FITC. After incubation, slides were washed 4x 10-15 min in PTW. They were blot-dried on tissue paper and then sections were covered with Aqua

Poly/Mount (Polysciences Inc., Warrington, PA, USA) containing DAPI (1 µg/ml) to stain nuclei. A large glass cover slip was placed on top. Samples are now ready for inspection by fluorescence or confocal microscopy.

## **2.2.4. Cell culture techniques**

### 2.2.4.1. Maintenance and transfection of zebrafish Pac2 cells

The zebrafish Pac2 fibroblast cell line is well suited for imaging applications because these cells are large and have a spread-out morphology. They can be cultured at RT. Therefore, they do not need a temperature-controlled environment during live microscopy. Pac2 cells were cultured in 10 cm dishes with 12 ml of Leibovitz L15 medium containing 1% Penicillin/Streptomycin, 1% Glutamax and 10% fetal calf serum in an incubator at RT. Cells were passaged every 3-4 days. For this purpose the medium was aspirated and cells were washed twice with 5 ml DPBS (Gibco). They were removed from the plate by incubation with 1 ml of 0.05% trypsin for 3 min at RT. Detachment of cells was monitored by microscopic observation. The digest was stopped by adding 10 ml of complete medium and cells were split 1:2 and transferred to a new 10 cm dish. For transfection experiments cells from one 10 cm dish can be transferred and distributed to 7-10 imaging dishes (Ø 3.5 cm). Cells were allowed to attach to the new dish and were grown for at least 6 h or overnight. Pac2 cells were transfected using the FuGENE HD Transfection Reagent from Roche (see paragraph 2.2.4.3.).

### 2.2.4.2. Induction of autophagy in Pac2 cells

Autophagy was induced by several treatment regimes in Pac2 cells 24 hours after transfection with plasmid pCS-mitoTagRFP-T2A-Venus-LC3 encoding the fluorescent Venus-LC3 autophagy reporter protein. In some cases, cells were cotransfected with plasmid pCS-H2B-CFP to stain nuclei in blue with cyan fluorescent protein. For amino acid starvation, cells were rinsed four times with sterile PBS and then incubated in Dulbecco's PBS buffer supplemented with CaCl<sub>2</sub> at 0.9 mM final concentration, MgCl<sub>2</sub> at 0.493 mM final conc. and 11 mM D-(+)-glucose for the indicated periods (1 to 6 hours). For rapamycin-induced autophagy, Pac 2 cells were incubated in full Leibovitz medium in the presence of 1 µM rapamycin. Rapamycin was obtained from Tocris (Tocris Bioscience, Bristol, UK) and was stored in aliquots of a 1 mM stock solution in DMSO at -80°C. A dilution of the stock solution was prepared with culture medium and added directly to the cells. Ammonium chloride treatments were done by directly adding the appropriate amount of a 2 M stock

solution to the culture medium to achieve a final concentration 50 mM NH<sub>4</sub>Cl, as described by Bampton *et al.*, 2005.

#### 2.2.4.3. Maintenance and transfection of mammalian cells

In the course of this work HEK293 T human embryonic kidney cells were used. This cell line is easy to maintain, has high transfection efficiency and can express high levels of exogenous proteins. However, as cells are small and not contact-inhibited they are not optimal for imaging applications. HEK293 T cells were maintained at 37°C and 5% CO<sub>2</sub> in DMEM supplemented with 1% Penicillin/Streptomycin, 1% Glutamax and 10% fetal calf serum (FCS). Cells were passaged 1:10 onto new plates twice a week. Trypsinization was done at RT and as described for Pac2 cells. For transfection experiments cells were counted after trypsinization with an improved Neubauer chamber (Marienfeld GmbH, Germany) and 1.2x 10<sup>6</sup> cells were seeded onto a 6 cm dish in 5 ml medium, or 3-6x 10<sup>5</sup> cells were transferred onto 3.5 cm imaging chambers with 2-3 ml of medium. This was usually performed one day prior to transfection to allow cells to attach and to re-enter into the growth phase. Transfection was performed with the FuGENE HD transfection reagent from Roche.

The transfection complex was set up for different culture volumes as follows:

<b>culture vessel</b>	<b>3.5 cm imaging dish</b>	<b>6 cm dish</b>
<b>culture volume</b>	<b>2-3 ml</b>	<b>5 ml</b>
plasmid DNA	2 µg	5 µg
serum-free medium	100 µl	250 µl
Fugene reagent	4 µl	8 µl

Plasmid DNA and serum-free medium (e.g. Opti-MEM medium, Gibco) were mixed in a reaction tube by pipetting. The Fugene transfection reagent was added and the solution was mixed by vortexing for 2 seconds. The mixture was then incubated for 15-30 min on the bench to allow formation of the DNA-lipid transfection complex. The solution was added drop-wise to the cells and the dish was moved back and forth to ensure distribution of the transfection reagent over the entire plate surface. Cells were then incubated for growth and there is no need to exchange the medium. 48 h after transfection protein expression could be analysed by confocal microscopy, if cells were grown in imaging chambers, or cell lysates were prepared for Western blotting.

## **2.2.5. Biochemical methods**

### 2.2.5.1. Protein extraction from cultured cells

In order to extract proteins from cultured cells for biochemical analysis such as Western blotting, cells were lysed using non-ionic detergents. This condition is suitable to solubilize most proteins. Only some nuclear proteins and structural proteins require harsh lysis conditions where the lysis buffer contains SDS. For the experiments described here, cells were grown in 6 cm dishes. First, cells were washed with PBS. They were harvested directly by addition of 400  $\mu$ l IPN lysis buffer containing protease inhibitors and the plates were placed on ice. Cells were removed from the plastic surface with a cell scraper and the suspension was transferred to a 1.5 ml reaction tube. Cell lysis was allowed to proceed for 1 hour at 4°C and by inverting the tubes on a rotor. After lysis the cell debris was removed by centrifugation for 10 min at 4°C and maximum speed. The supernatant was transferred to a new tube and the pellet containing the membrane, organelle and insoluble protein fraction was discarded. For SDS-PAGE an aliquot of the protein lysate was mixed 1:1 with 2x SDS loading buffer (125 mM Tris-HCl, pH 6.8, 20% glycerol, 4% SDS, 0.02% bromophenol blue, 10%  $\beta$ -mercaptoethanol) and denatured for 2 min at 90°C prior to use. It has to be noted that LRRK2-containing samples were denatured at 60°C for 10 min because LRRK2 is a large and degradation-prone protein. It is also recommended to load and run LRRK2-containing samples immediately after lysate preparation as repeated freeze-thawing also causes LRRK2 degradation. Lysates were shock-frozen in liquid nitrogen and kept at -80°C for long-term storage.

### 2.2.5.2. SDS-PAGE

SDS polyacrylamide gel electrophoresis is used to separate protein mixtures in an electrical field according to their molecular mass. SDS is a strong ionic detergent that will denature proteins and decorate them with negative charge. Protein lysates were mixed with 2x SDS loading buffer and denatured by heating the samples as described before. They were then loaded onto polyacrylamide gels. These consist of an upper stacking gel part of 3% acrylamide and the lower and higher concentrated separating gel. Depending on the  $M_w$  of the proteins to be separated, gels of 6% to 10% were used in this work. Gels were prepared immediately before use from stock solutions. Volumes of stock solutions, required to cast one gel of the indicated concentration, are given here:

<b>3% stacking gel (4 ml)</b>	
H <sub>2</sub> O	2.52 ml
30% acrylamide mix	0.4 ml
0.5 M Tris, pH 6.8	1 ml
10% SDS	40 µl
10% ammonium persulfate	40 µl
TEMED	4 µl

<b>separating gel (10 ml)</b>	<b>6%</b>	<b>8%</b>	<b>10%</b>
H <sub>2</sub> O	5.3 ml	4.6 ml	4 ml
30% acrylamide mix	2.0 ml	2.7 ml	3.3 ml
1.5 M Tris, pH 8.8	2.5 ml	2.5 ml	2.5 ml
10% SDS	100 µl	100 µl	100 µl
10% ammonium persulfate	100 µl	100 µl	100 µl
TEMED	10 µl	10 µl	10 µl

First, the resolving gel mix was poured between the glass plates of the assembled gel mould and was allowed to polymerize. Then the stacking gel mix was poured on top, a comb was inserted and the gel was allowed to solidify. Gels were inserted into the Mini-PROTEAN 3 chamber from Biorad which was filled with SDS running buffer (25 mM Tris, 250 mM glycine, 0.1% SDS, pH 8.3). Samples were loaded and the gel was run at 140 V for 15 min until the dye front had moved into the resolving gel. Then the voltage was increased to 180 V and gels were run until the bromophenol blue reached the bottom of the gel (approximately 50 min). After electrophoresis the module was disassembled and the gel was carefully removed.

#### 2.2.5.3. Western blotting

Polyacrylamide gels were blotted onto PVDF membranes using the XCell II Blot Module from Invitrogen. One or two gels can be transferred at the same time. All steps were performed as described for Tris-glycine gels by the manufacturer. Briefly, pre-cut pieces of filter paper and the blotting pads were pre-soaked in 1x Novex Tris-glycine transfer buffer containing methanol. The pre-cut PVDF membrane was soaked in 100% methanol for 30 s prior to use. The blotting sandwich consisting of blotting pads, filter paper, gel and transfer membrane was assembled between cathode and anode core plates. Care has to be taken not to trap any air bubbles between filter paper, gel and membrane, which would hinder protein transfer. The blot module was inserted into the buffer chamber and filled with transfer buffer. The outside was cooled with water. Transfer was driven at 25 V for 1 h 45 min. Afterwards, the module was disassembled and the membrane was labelled for orientation of loaded

samples. The efficiency of the protein transfer can be verified by staining with Ponceau solution, which can be removed easily by rinsing the blot with water or 1x TBS buffer. For subsequent immuno-probing, unspecific binding sites were blocked by placing the membrane in blocking buffer (TBST, 2% non-fat dried milk) for 30 min to 1 h at room temperature. The blocking solution was removed and the membrane was transferred into a 15 ml plastic culture tube. Then, the primary antibody diluted 1:1000 (if not recommended otherwise) in 2-3 ml blocking buffer was added. Incubation of the primary antibody was performed on a rotor at 4°C overnight. The next day, the primary antibody solution was removed and the blot was washed three times with TBST for a total time of 20 min. The primary antibody can be preserved for re-use in 0.05% sodium azide. Incubation with the peroxidase-conjugated secondary antibody diluted in blocking buffer (without sodium azide) followed. Binding was allowed by incubating for 1 h at room temperature. The membrane was washed again 3x 10 min with TBST buffer at RT.

For detection a chemiluminescence-based detection reagent, the Amersham ECL Western Blotting Detection Reagent, was used. The reagent consists of two components, enhanced luminol reagent and oxidizing reagent, that are mixed in a 1:1 ratio shortly before use. The membrane was lightly blotted against tissue paper after washing to remove excess liquid and then incubated with 1 ml detection agent for 1 min. Excess detection solution was removed with tissue paper. The membrane was transferred into a film cassette, covered with plastic foil and exposed to an X-ray film (Hyperfilm, Kodak) in a darkroom. The film was exposed for a few seconds up to 30 min or longer depending on the amount of protein to be detected. Films were developed in a Curix 60 developing machine from AGFA.

#### **2.2.6. Confocal microscopy**

The microscope settings of the Zeiss LSM510 used for mitochondrial axonal transport imaging are reported here. In order to keep photobleaching of the mitochondrial fluorescent reporter mitoTagRFP and phototoxicity during repeated confocal recordings at a minimum, transmission of the DPSS laser (561 nm) was set to 3%. The scan time for a defined region of interest (ROI) was 424 ms, with a cycle delay of 1.576 seconds between frames. According to this, images were recorded every 2 seconds over an interval of 10 min. Microscope settings have been optimized to obtain best-quality recordings and were as follows: C-Apochromat 40x water immersion objective; pinhole maximal open (12.4 Airy units); 4x zoom; frame size: x=1024, y=1024; scan speed: 9; scan mode: line; number of scans: 1.

## **2.2.7. Transmission electron microscopy**

### 2.2.7.1. Tissue preparation and image acquisition

5-days-old larvae or muscle tissue from 6-months-old, adult zebrafish were fixed in 2% PFA/2% glutaraldehyde in 1x PBS for several days. Sample processing for EM analysis was performed by Ms. Luise Jennen (Helmholtz Center, Munich) as follows. Tissue was Epon-embedded. For orientation, semi-thin sections (1  $\mu$ m) were cut and stained with toluidine blue. Areas of interest were selected using a light microscope. Subsequently, ultra-thin sections were cut, mounted on copper grids and contrasted with uranyl acetate and lead citrate. The tissue was observed and images were taken with an electron microscope (Zeiss EM10 at 60 kV).

### 2.2.7.2. Quantitative analysis of electron micrographs

The quantitative evaluation of mitochondrial ultrastructure within muscle tissue was done by Prof. Andreas Reichert (Frankfurt, Germany) as described here. The average area per mitochondrial section in muscle fibres from zebrafish 5-days-old larvae or adults was determined using a stereology approach (Griffiths, 1993). In brief, a grid with known distance ( $d=2.5$  mm, 5 mm, or 10 mm) was randomly placed on individual electron micrographs and the number of grid intersections located within a mitochondrial section were counted, the enlargement factor was taken into account, and the mitochondrial area was calculated. For each sample the cumulative areas of 174 to 231 mitochondrial sections were determined and the average area per mitochondrial section was deduced. The density of mitochondria was determined by additionally determining the area between myofibrils that in theory is accessible to mitochondria; the area covered by myofibrils was consequently excluded from the analysis.

## **2.3. Mitochondrial Transport Analysis**

### **2.3.1. Generation of kymographs**

Kymographs of mitochondrial axonal transport were generated with ImageJ (NIH, Bethesda, MD, USA). Several macros and plug-ins were required. The macro tsp050706.txt was written by Dr. Karina Kloos and had to be installed anew each time ImageJ was started (Plugins> Macros>install>go to the file tsp050706.txt and open it). LSM510 image files can be directly opened with ImageJ. If it is required contrast can be enhanced (Process>Enhance Contrast). The axon was tracked with a segmented line of adjustable width (Segmented Line button in the task bar), and the corresponding kymograph was then generated (Plugins>

Macros>kymograph). Each line on a kymograph represents a single mitochondrion. To extract numerical data about mitochondrial movement, each line on the kymograph has again to be traced by a segmented line. Distances travelled and velocities can then be obtained (Plugins>Macros>read velocities from tsp). Note that data is in pixel or pixel/pixel and has to be converted to  $\mu\text{m}$  and  $\mu\text{m/s}$ .

### **2.3.2. Statistical evaluation of mitochondrial velocity and size data**

Classical statistics assumes that observations are independent. However, mitochondrial velocity data have a clustered structure with measurements from the same animal representing dependent data. Applying classical statistics to clustered data may lead to false results. The mixed-effects model is a statistical model that treats clustered data adequately and allows two sources of variation, within clusters/groups and between clusters.

The statistical evaluation of mitochondrial velocities and size distributions presented in this thesis were performed by the mathematician Ms. Faus-Keßler and come from a process with double sampling: animals were sampled and then cells/movies within animals. The statistical analysis takes this double-grouping into account by using mixed effects models (Reference 1; see below).

Many classical statistical methods assume normal distribution, which means symmetrically distributed data. However, velocity values determined in this work were not distributed symmetrically but values were skewed to the left. In this case values were transformed to the logarithmic scale (of the natural logarithm) and statistical analysis was performed with logarithmic values.

For two-group comparisons, modified t-tests for grouped data were calculated, and for two-factorial comparisons, two-way ANOVAs for grouped data were performed. Calculations were done with the open-source statistics program and computer language R (Reference 2).

#### 1. Linear mixed-effects models:

Jose Pinheiro, Douglas Bates, Saikat DebRoy, Deepayan Sarkar and the R Development Core Team (2012). nlme: Linear and Nonlinear Mixed Effects Models. R package version 3.1-103.

#### 2. Statistics software and computer environment:

R Development Core Team (2011). R: A language and environment for statistical computing. R Foundation for Statistical Computing, Vienna, Austria. ISBN 3-900051-07-0, URL <http://www.R-project.org/>.

## 3 Results

### 3.1. Zebrafish *lrrk2* Expression

#### 3.1.1. Human and zebrafish *lrrk2* transcripts

The major human *LRRK2* transcript consists of 51 exons and encodes the 2527 aa full-length protein (Genbank accession number NM\_198578.3). In order to search for zebrafish *lrrk2* transcripts, the nucleotide sequences encoding either the Roc-COR-kinase domain or solely the kinase domain of human *LRRK2* were used to perform tblastx queries of all available RNA sequences from zebrafish (query performed in July 2012). With both sequences the hit with the highest score and the only *lrrk2* transcript retrieved was *lrrk2-001*. This transcript is available at the NCBI genome server with accession numbers HM143897 and NM\_001201456. The exon-intron structure of zebrafish *lrrk2* seems to be conserved. It consists of 51 exons and encodes a full-length protein of 2532 aa – nearly identical in size to human LRRK2.

It can be stated that at the moment there is only one functional transcript annotated in public databases for each of human and zebrafish *LRRK2*, and up to now research in the LRRK2 field has been performed based on this full-length sequence. However, this situation might change in the near future as the search for alternative tissue- and cell-type specific transcripts gained recent interest (Lewis and Manzoni, 2012; webcast by N. Wood, 2012, on [www.youtube.com](http://www.youtube.com)).

#### 3.1.2. Expression analysis of zebrafish *lrrk2*

In the publications from 2004, where human *LRRK2* was identified as a Parkinson's disease-linked gene, it was described that this gene is expressed ubiquitously in many human tissues and brain regions (Paisán-Ruíz *et al.*, 2004; Zimprich *et al.*, 2004). We wanted to know if the expression pattern of zebrafish *lrrk2* is similar to the human mRNA as this could be an indication that the functions and signalling pathways of the two proteins are conserved. At the beginning of this study, the only recorded zebrafish transcript, XM\_682700, was an incomplete sequence encoding a 1985 aa protein. This sequence has been removed from the database since and has been replaced by the aforementioned full-length *lrrk2* transcript.

To study expression of *lrrk2*, a 1327 bp sequence encompassing the COR and kinase domain of the transcript was amplified by RT-PCR with total RNA extracted from 55 hpf wild-type embryos as a template. A fragment of the right size and with the correct sequence could be cloned, which is an indication that *lrrk2* is expressed at this early larval stage. The cloned

sequence was used to generate anti-sense and sense RNA probes, and whole-mount *in situ* hybridization (WISH) experiments of embryonic and larval stages between 24 hpf and 3 dpf were performed. As shown in Figure 1, a very weak staining could be detected with the antisense probe after a prolonged staining reaction of larvae at 2 and 3 dpf. But control larvae were completely unstained. *Lrrk2* seemed to be expressed mostly in the brain at 55 hpf, while muscle tissue was less stained (Figure 1A). However, with this weak antisense signal a

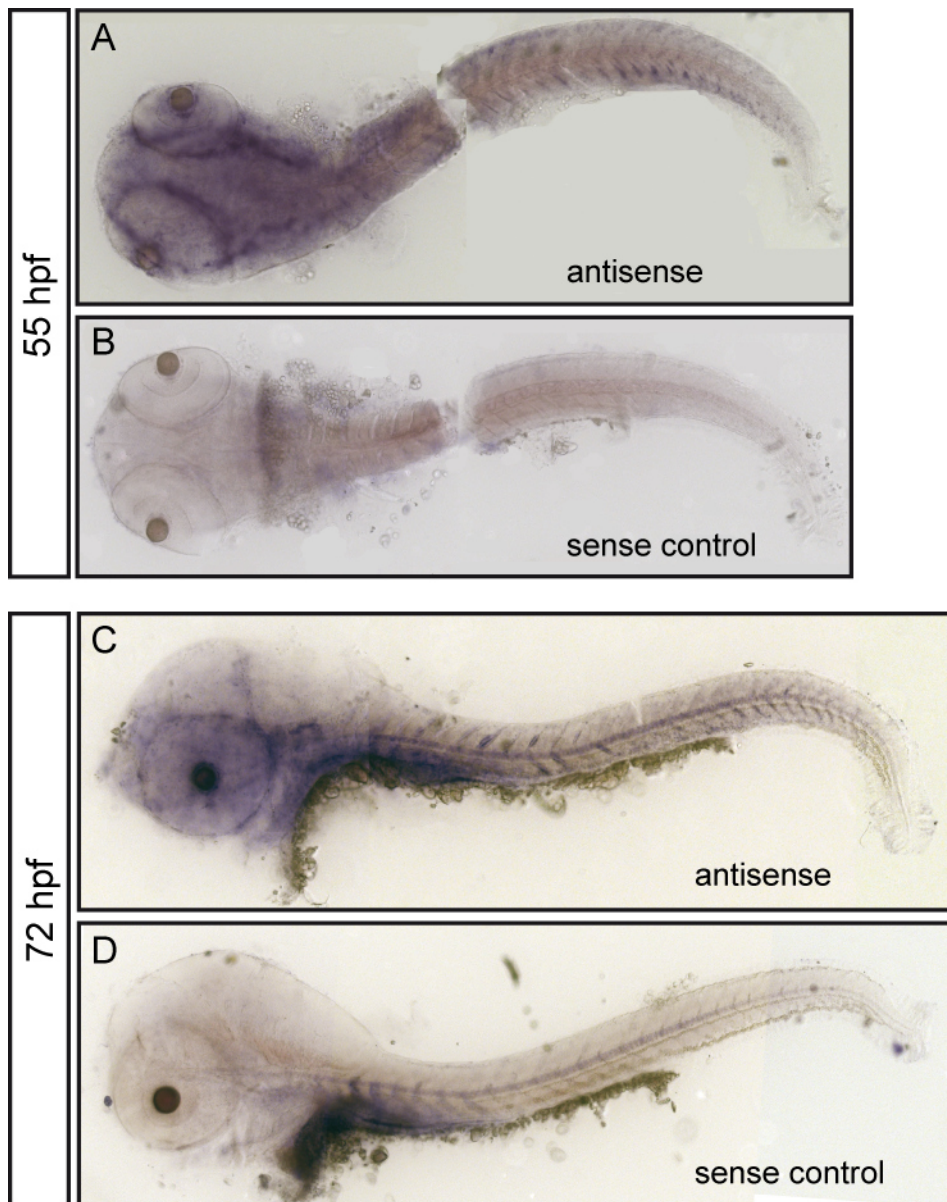


**Figure 1. The *lrrk2* gene is weakly expressed during early larval stages.** Whole-mount *in situ* hybridization to detect *lrrk2* gene expression was performed on zebrafish embryos and larvae with a 1327 bp antisense probe or the corresponding sense control. Brightfield images show dorsal (A and B) or lateral views (C and D) of larvae. **A** and **B** *Lrrk2* expression is weakly detectable in the brain and in muscle tissue at 55 hpf. **C** and **D** Larvae at 3 dpf show a very weak expression signal.

precise localization of the transcript to certain tissues or cell-types was hardly possible. Instead *lrrk2* seemed to be expressed quite ubiquitously and at very low levels.

In the course of this study, another research group analysed *lrrk2* expression during embryonic and larval development, as well as in different adult tissues (Sheng *et al.*, 2010). The authors could detect maternal and zygotic *lrrk2* mRNA by quantitative RT-PCR from the earliest developmental stages onward, with a steady and relative increase of expression during larval development up to 10 dpf. In their study, a strong expression signal was localized mainly to the brain, where it was distributed ubiquitously, at 24 hpf and at 6 dpf as detected by WISH. Up to now, this expression analysis could not be repeated and confirmed by our group or others.

With the knowledge of this highly conserved *lrrk2* ortholog in zebrafish we wanted to establish a neurodegeneration disease model based on expression of the human Parkinson's disease-linked allele *LRRK2(G2019S)*. This mutation is considered a gain-of-function mutation and is inherited in a dominant way in humans. It seems to have enhanced kinase activity due to the missense mutation in the kinase domain, or it might have an otherwise aberrant and possibly novel function (Cookson, 2010; Tsika and Moore, 2012). Such dominant disease models can be established easily in zebrafish by Tol2-mediated genomic integration of expression constructs.

## 3.2. Generation of a Neurodegeneration Model in Zebrafish based on Expression of Human LRRK2(G2019S)

We wanted to make use of the Gal4/UAS system to generate two transgenic zebrafish lines. The activator line should drive expression of an improved version of the Gal4 transcriptional activator under the control of a neuronal promoter, and the effector line should contain the integrated target genes – the *LRRK2* disease gene and two fluorescent reporter genes – under the control of UAS sites, which are bound and activated by Gal4.

### 3.2.1. Generation of a neuron-specific KalTA3-expressing transgenic driver line

#### 3.2.1.1. Characterization of the 3.8 kb NBT promoter from *Xenopus laevis*

In search for a neuron-specific promoter to drive expression of the disease gene we made use of a previously characterized 3.8 kb fragment encompassing the *neuronal beta tubulin* (NBT) promoter from *Xenopus laevis* (obtained from Dr. D. Gilmour, EMBL, Heidelberg). This promoter has been used to label neurons in the transgenic zebrafish line *Tg(NBT:DsRed)* (Peri and Nüsslein-Volhard, 2008), which was available in our laboratory. To document expression of the DsRed fluorescent protein in this transgenic line, live confocal microscopy recordings were acquired at various embryonic and larval stages (Figure 2). DsRed expression could be detected from early developmental stages onwards when the first differentiated neurons are appearing (Ross *et al.*, 1992; Kimmel, 1993). Especially neurons of the central nervous system (CNS), in the brain and spinal cord, were clearly visible in embryos from 24 hpf onwards (Figure 2B, B', C). The fluorescent signal intensity increased with advancing development of the CNS (Figure 2A-A", C, D). Additionally, neurons of the peripheral nervous system were stained. These were motoneurons, sensory neurons innervating the skin and neurons of the lateral line system (not shown here). As no DsRed signal was detectable in other tissues, it could be assumed that the NBT promoter is restricting expression to neuronal cell types.

In the following, the NBT promoter fragment had to be tested in the context of the Gal4/UAS system. A vector was constructed in which the promoter was driving expression of the transcriptional activator KalTA4, an optimized version of Gal4 (Distel *et al.*, 2009). The construct was tested by injection into fertilized eggs of the reporter line *Tg(UAS:GFP)*, which can express GFP only in the presence of Gal4. Injected embryos were analysed by confocal microscopy at 24 hpf. Mosaic GFP expression could be observed in tissues of the CNS:

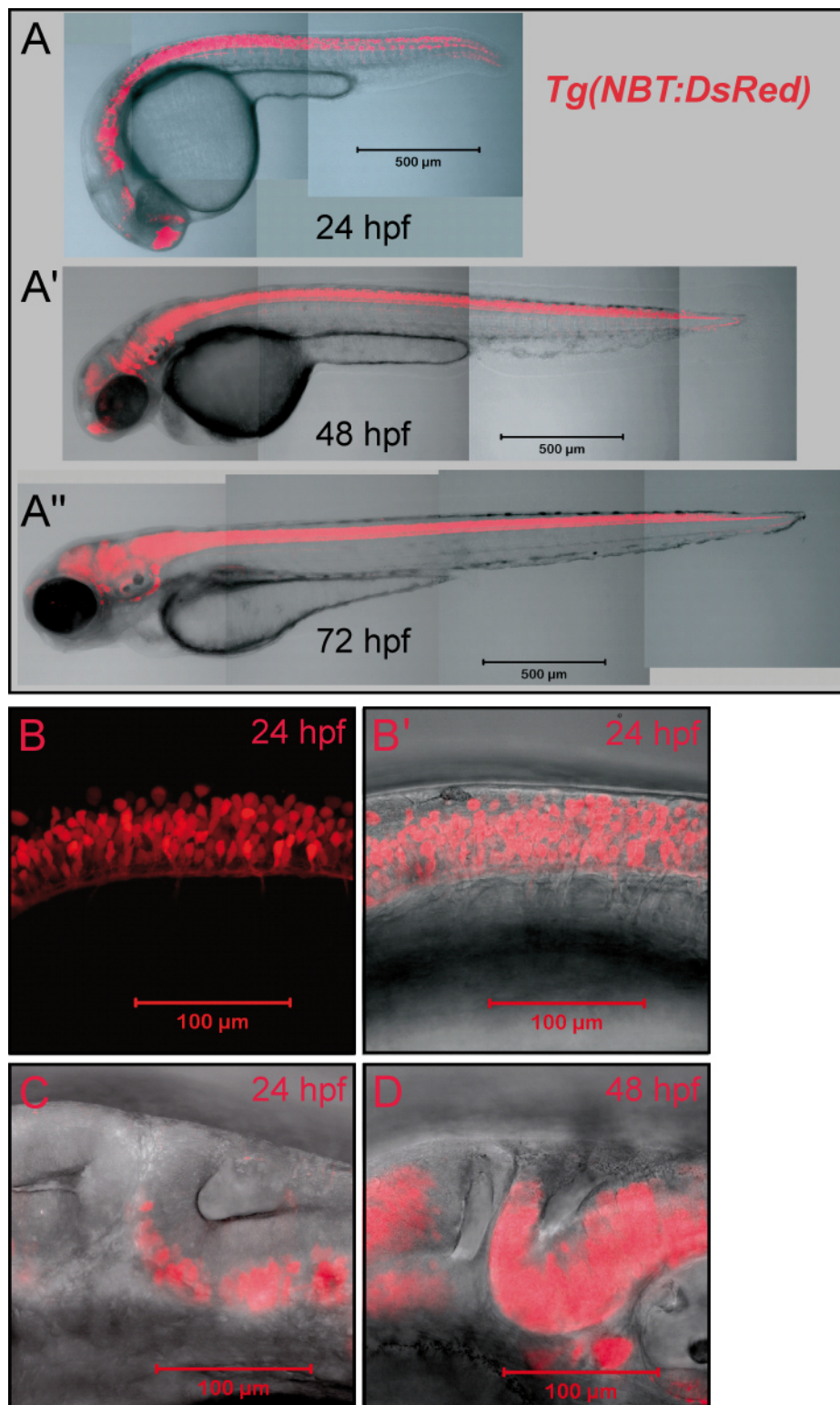


**Figure 2. *Tg(NBT:DsRed)* exhibits strong neuronal expression of the red fluorescent protein.**

Lateral view images of *Tg(NBT:DsRed)* embryos and larvae were recorded by confocal microscopy at the indicated developmental stages. **A-A''** The assembled images show a strong DsRed signal in the central nervous system from early developmental stages onwards. **B** and **B'** Spinal cord neurons expressing DsRed at 24 hpf. **C** At 24 hpf only few ventrally located neurons express the reporter in the brain. In this confocal projection part of the midbrain, the midbrain-hindbrain boundary, the cerebellum and part of the hindbrain are visible. **D** Expression has increased at 48 hpf when neuronal differentiation is further advanced. The same region as in (C) is shown. Rostral is always to the left.

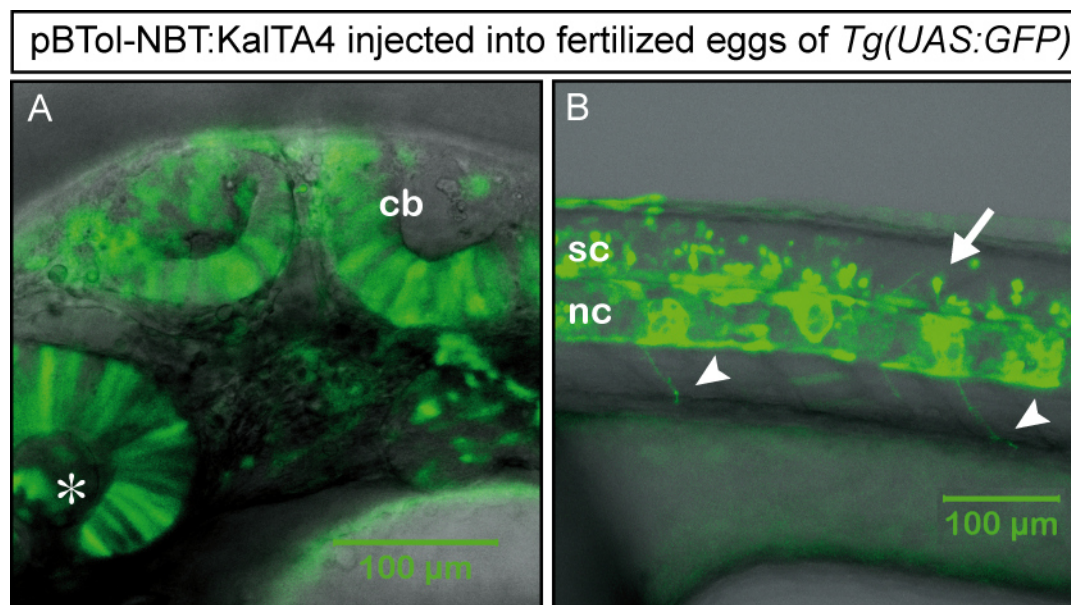


**Figure 3. The 3.8 kb NBT promoter combined with the Gal4/UAS system induces GFP expression in neuronal tissues.** Lateral view images were recorded by confocal microscopy of 24 hpf *Tg(UAS:GFP)* embryos, injected with plasmid pBTol-NBT:KalTA4 at the one-cell stage. **A** The fluorescent reporter is expressed in neuronal precursor cells of the eye (indicated by an asterisk), in the midbrain, cerebellum and hindbrain. **B** GFP-expressing neuronal somata in the spinal cord (arrow) and motoraxons (indicated by arrowheads) are stained. Unspecific expression is detectable in the notochord. Abbreviations: cb, cerebellum; nc, notochord; sc, spinal cord. Rostral is to the left.

in different regions of the brain, the developing eye and in the spinal cord (Figure 3). Individual neuronal somata were visible in the spinal cord and axons from motoneurons could be identified. Some unspecific expression in the notochord and in muscle cells was observed in embryos with strong GFP signal, and this might be connected to a high concentration of injected plasmid.

From these observations it can be concluded that the *neuronal beta-tubulin* promoter from *Xenopus laevis* is suited to drive neuron-specific expression of target genes in zebrafish, and expression is also achieved when it is regulated indirectly, via synthesis of Gal4 and its binding to UAS sequences.

### 3.2.1.2. The driver construct is bicistronic and co-expresses a nuclear-targeted blue fluorescent reporter

In our disease model we wanted to perform multi-colour fluorescence microscopy to study different subcellular structures and biological processes. At the same time, transgenic integration of the Gal4 driver construct should be monitored by co-expression of a fluorescent reporter protein (FP). To employ spectrally divergent FPs, we decided to label mitochondria with the red fluorescent protein, TagRFP (Merzlyak *et al.*, 2007), and autophagosomes with the yellow FP, Venus (Nagai *et al.*, 2002). LRRK2 should be tagged with the cyan

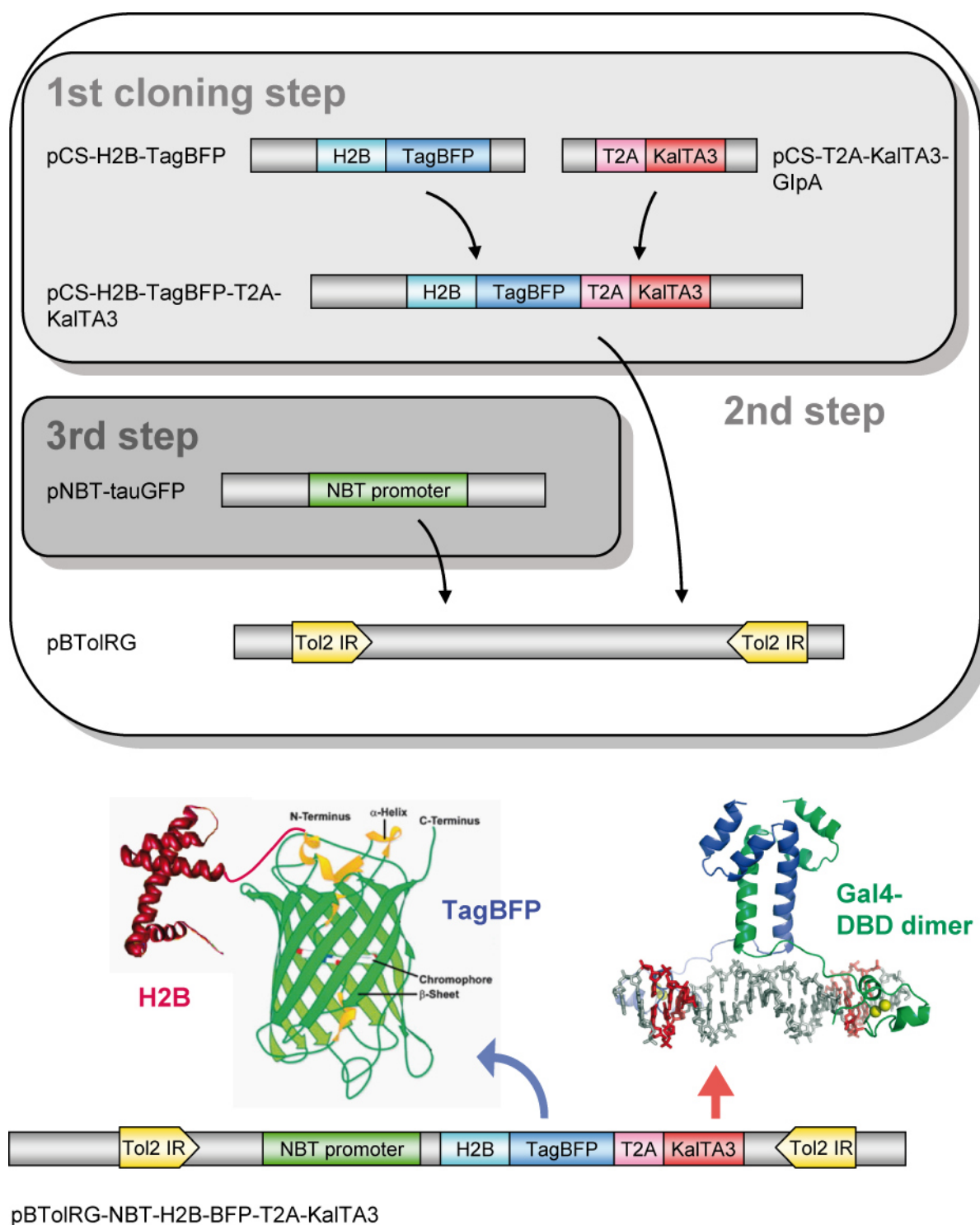


**Figure 4. Cloning strategy for the driver construct.** The driver construct was compiled from several separately cloned and assembled sequences in three major cloning steps. The final construct mediates expression of an improved version of the transcription factor Gal4, called KalTA3. At the same time the nuclear-targeted blue fluorescent protein, H2B-TagBFP, is synthesized. Expression of both proteins is restricted to neuronal cells by the neuronal beta-tubulin promoter (NBT). The sequence between the Tol2 recognition sites can be integrated into the zebrafish genome by Tol2-mediated transposition. Protein structures of the human histone 2B, the fluorescent protein GFP (TagBFP has a similar conserved  $\beta$ -barrel architecture) and the Gal4 DNA-binding domain dimer bound to DNA are depicted as ribbon models and were adapted from Tsunaka *et al.*, 2005, Day and Davidson, 2009, and Hong *et al.*, 2008, respectively.

fluorescent protein, ECFP (Tsien, 1998). Finally, the driver construct should encode TagBFP, a monomeric bright blue FP that is excited at the low nm range of the visible spectrum (excitation peak at 399 nm, emission peak at 456 nm, Subach *et al.*, 2008). To enhance the signal and spatially separate it from the other FPs, which are targeted to proteins and organelles in the cytoplasm, we aimed to direct TagBFP to the nucleus. For this purpose the sequence encoding human histone 2B was fused to its N-terminus (Kanda *et al.*, 1998).

We wanted to co-express the transcriptional activator KalTA3 (an improved version of Gal4; Distel *et al.*, 2009) together with the H2B-TagBFP reporter from the final driver construct. As outlined in Figure 4, several cloning steps were required. First, sequences encoding the two proteins were fused in one open reading frame via the coding sequence of the T2A peptide. Both proteins will thereby be produced at equal stoichiometric amounts. The

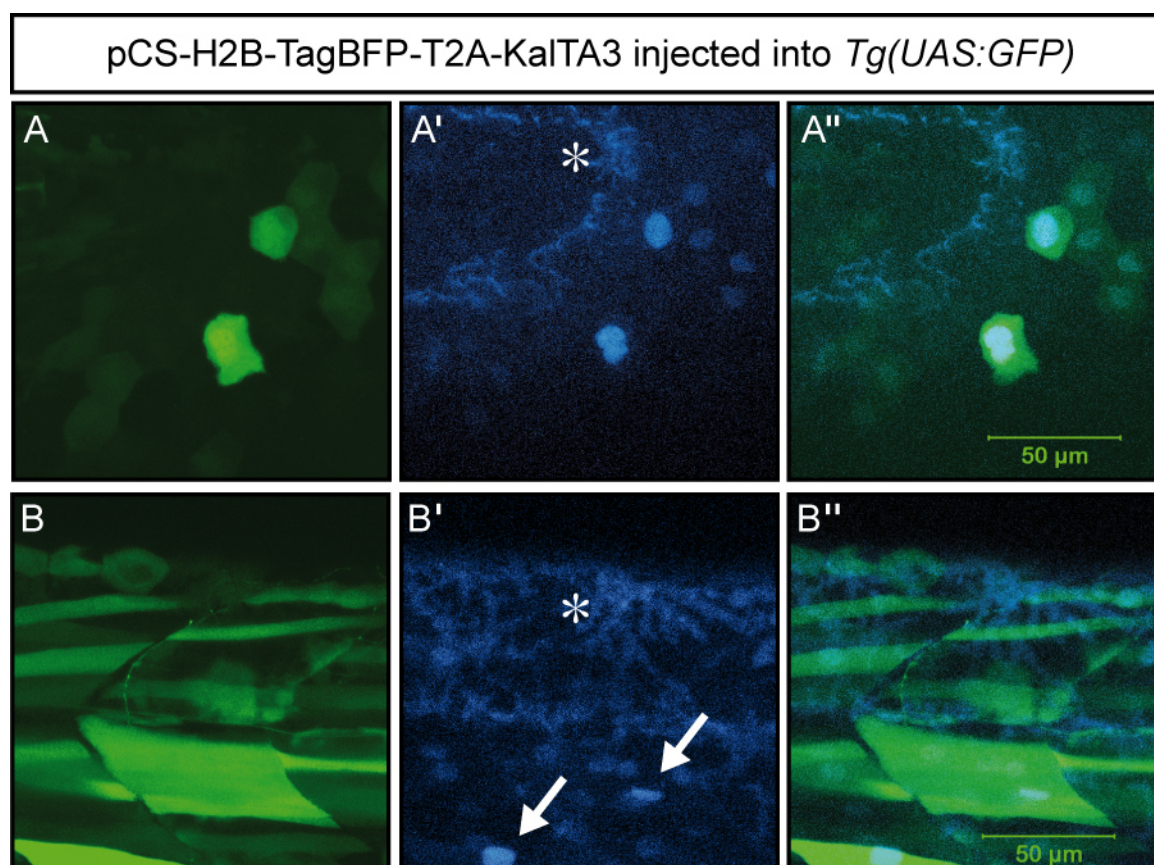


**Figure 5. The bicistronic cassette encoding H2B-TagBFP and KalTA3 is functional.** Plasmid pCS-H2B-TagBFP-T2A-KalTA3 was injected into one-cell stage embryos of *Tg(UAS:GFP)*. Images of FP-expressing cells were recorded by confocal microscopy of embryos at 24 hpf. Mosaic expression of nuclear TagBFP is visible in some cells, and cytoplasmic GFP is expressed in the same cells. **A-A''** Two skin fibroblasts show coexpression of both FPs. **B-B''** Muscle fibres have their characteristic shape revealed by GFP expression. Nuclei are stained in blue by H2B-TagBFP and are indicated by arrows. Autofluorescence of the skin is marked with an asterisk.

functionality of the bicistronic cassette was tested after the first cloning step by injection of plasmid pCS-H2B-TagBFP-T2A-KalTA3 into eggs of the reporter line *Tg(UAS:GFP)*. The pCS vector contains the strong eukaryotic CMV promoter. Injected embryos were analysed at 24 hpf by confocal microscopy. TagBFP fluorescence could be observed in nuclei of skin fibro-blasts (Figure 5A') and in muscle cells (Figure 5B'). The same cells expressed KalTA3 as detected by induction of the UAS:GFP transgene (Figures 5A, B and merged images). This was an indication that the coexpression strategy with the T2A sequence was functional. In the next two cloning steps, the expression cassette is flanked by recognition sites for Tol2 transposase, and the NBT promoter is cloned upstream of the ORF (Figure 4). The final construct can become randomly integrated into the zebrafish genome after injection into one-cell stage embryos together with mRNA encoding Tol2 transposase.

This construct was again tested by injection into the UAS-GFP reporter line. A mosaic neuronal GFP expression was visible in many of the injected larvae, as shown in Figure 6 for 2 dpf and 5 dpf larvae. Due to the transient transgenic approach via plasmid injection the expression pattern did vary between embryos (data not shown). Some unspecific staining of muscle cells could often be observed (Figure 6A, arrowhead). This can possibly be explained by a high copy number of injected plasmid and by binding of muscle-specific transcription factors of the MyoD family to the NBT promoter sequence as it is known that these transcription factors bind to similar DNA-sequences as NeuroD transcription factors (Fong *et al.*, 2012).

Additionally, the construct was injected into eggs of wild-type animals to test if NBT-driven expression of H2B-TagBFP could be observed and could possibly be used for screening of transgene carriers. A weak BFP signal was detectable in spinal cord neuronal nuclei by confocal microscopy only, as shown in Figure 7. The signal intensity of TagBFP was not strong enough to allow its detection with a fluorescence stereo microscope. This means that screening for transgenic embryos by eye on a fluorescence stereo microscope might not be feasible in subsequent experiments. Nevertheless, the construct was used to generate a transgenic driver line (see Chapter 3.2.1.4).

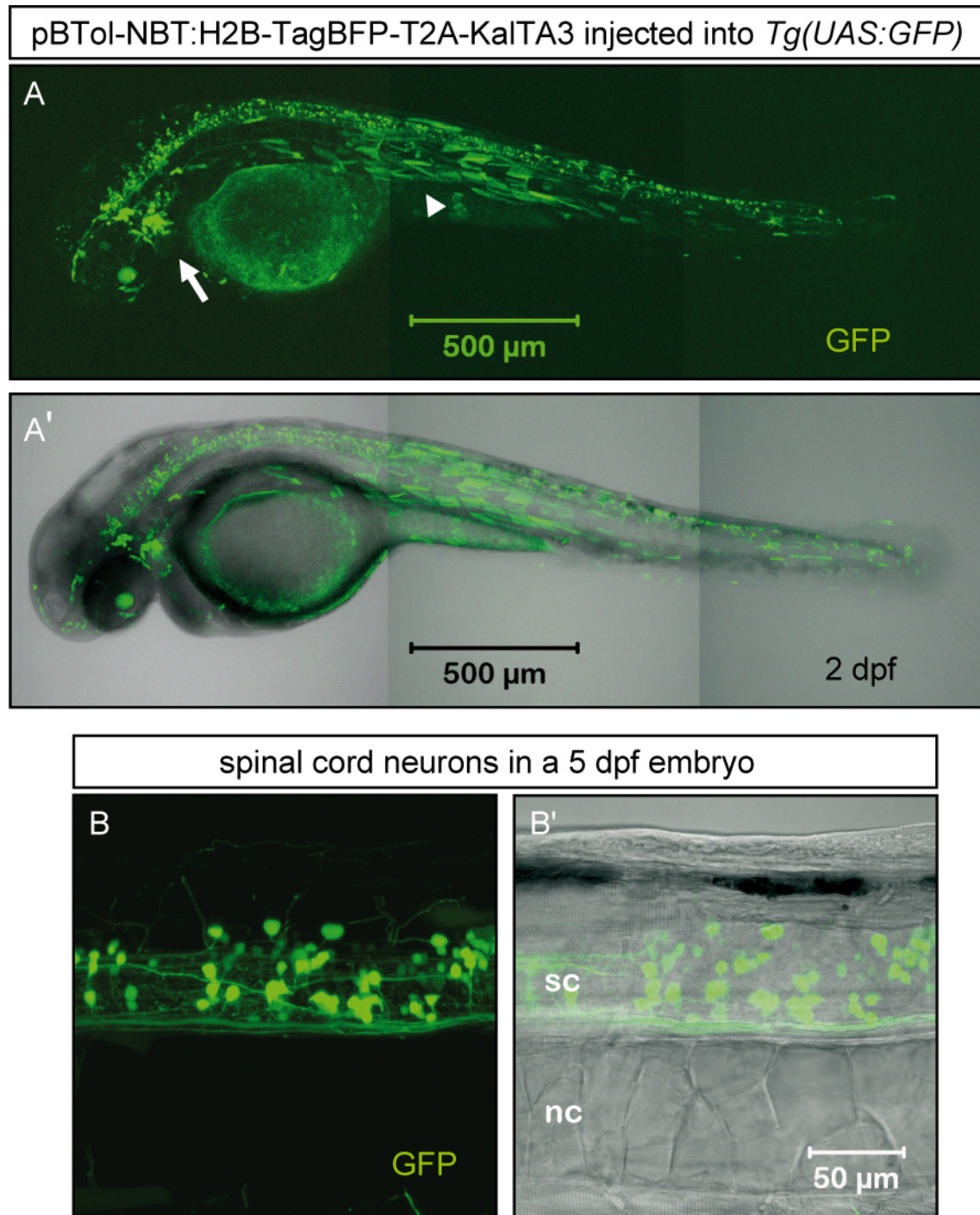


**Figure 6.** The driver construct directs GFP expression in neurons when injected into *Tg(UAS:GFP)*. The driver construct was injected into one-cell stage embryos of the UAS-GFP reporter line, followed by confocal microscopy at the indicated developmental stages. **A, A'** The assembled image of a larva at 2 dpf shows GFP fluorescence in ventral neurons of the brain and in the spinal cord. The trigeminal ganglion is visible (arrow). Some unspecific expression occurs in muscle fibres (arrowhead). **B, B'** Close-up view of neuronal somata and nerve fibres in the spinal cord. Abbreviations: nc, notochord; sc, spinal cord.

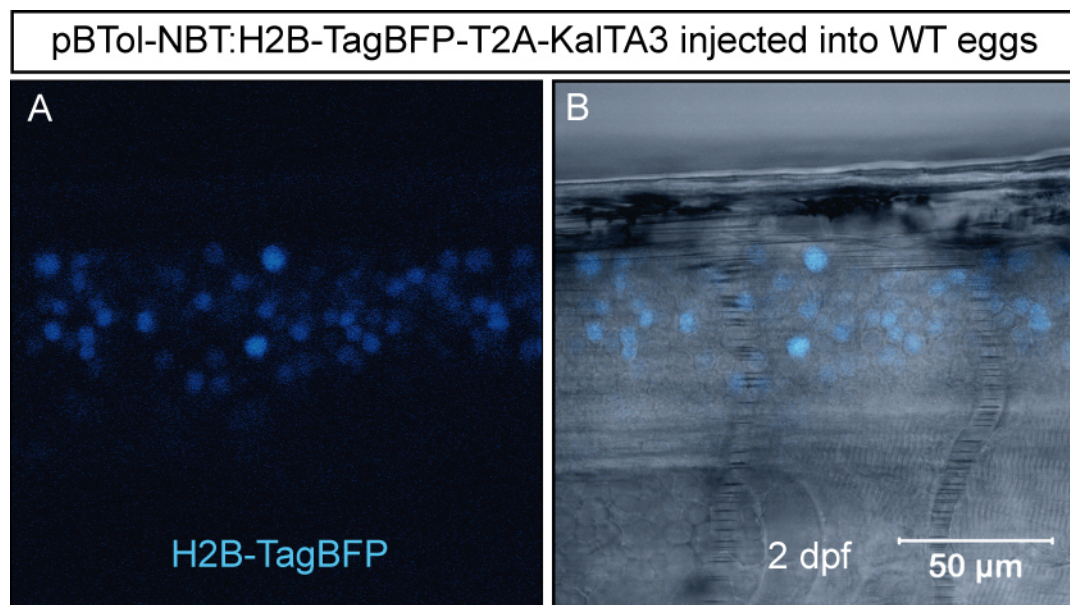


**Figure 7. Nuclear TagBFP expression in spinal cord neurons is induced by the driver construct.** The driver construct was injected into one-cell stage wild-type embryos, followed by confocal microscopy. **A** and **B** TagBFP is detectable in neuronal nuclei in the spinal cord. Lateral view images of a larval fish at 2 dpf are shown.

In order to have a more precise control on the timing of expression of the disease gene at any time of choice, which is for example required to study acute effects of the mutant gene product, we next tried to generate a compound-inducible Gal4 variant.

### 3.2.1.3. Cloning and analysis of a potentially ligand-inducible estrogen receptor-KalTA4 fusion protein

Unconditional expression of a potentially harmful or toxic transgene over a prolonged period of time – as for example *LRRK2(G2019S)* – might interfere with the normal differentiation or function of cells. In extreme cases this can be lethal to the organism. Alternatively, it is likely to elicit compensatory adaptations of the cells, and these might obscure a phenotype. In order to circumvent these problems it is useful to have a temporally-controlled, inducible system for transgene expression. One commonly used approach to regulate protein function on the posttranslational level is the Tamoxifen-induced system. This relies on the fact that fusion of the hormone-binding domain of the human estrogen receptor (ER) to another protein might render the function of the protein dependant on the ligand of the ER (Picard, 1994; Feil *et al.*, 1997) (Figure 8).

We obtained the coding sequence of ER<sup>T2</sup>, a mutated version of the ligand binding domain with a high affinity for the synthetic antagonists Tamoxifen and 4-Hydroxy-tamoxifen (Chu *et al.*, 2008), from Prof. Ralf Kühn (Helmholtz Center Munich). Two expression constructs

were generated, where the ER<sup>T2</sup> sequence is fused to the N-terminus of KalTA4, as depicted in Figure 8. Plasmid pCS-ER<sup>T2</sup>-KalTA4 expresses the fusion protein under the control of the CMV promoter. The second construct is similar to the driver construct described in the previous paragraph, with the non-inducible KalTA3 replaced by ER<sup>T2</sup>-KalTA4. Plasmid pCS-ER<sup>T2</sup>-KalTA4 was tested in transfection experiments with the zebrafish Pac2 fibroblast cell line (Senghaas and Köster, 2009). A reporter plasmid containing 4xUAS:GFP was cotransfected, which will initiate GFP expression in case an active ER<sup>T2</sup>-KalTA4 is present. 24 hours after transfection cells were treated with 100 nM or 1  $\mu$ M 4OH-Tamoxifen or with vehicle alone and were analysed 24 hours later for GFP expression by fluorescence and confocal microscopy. Green fluorescent cells could be observed in the Tamoxifen-treated

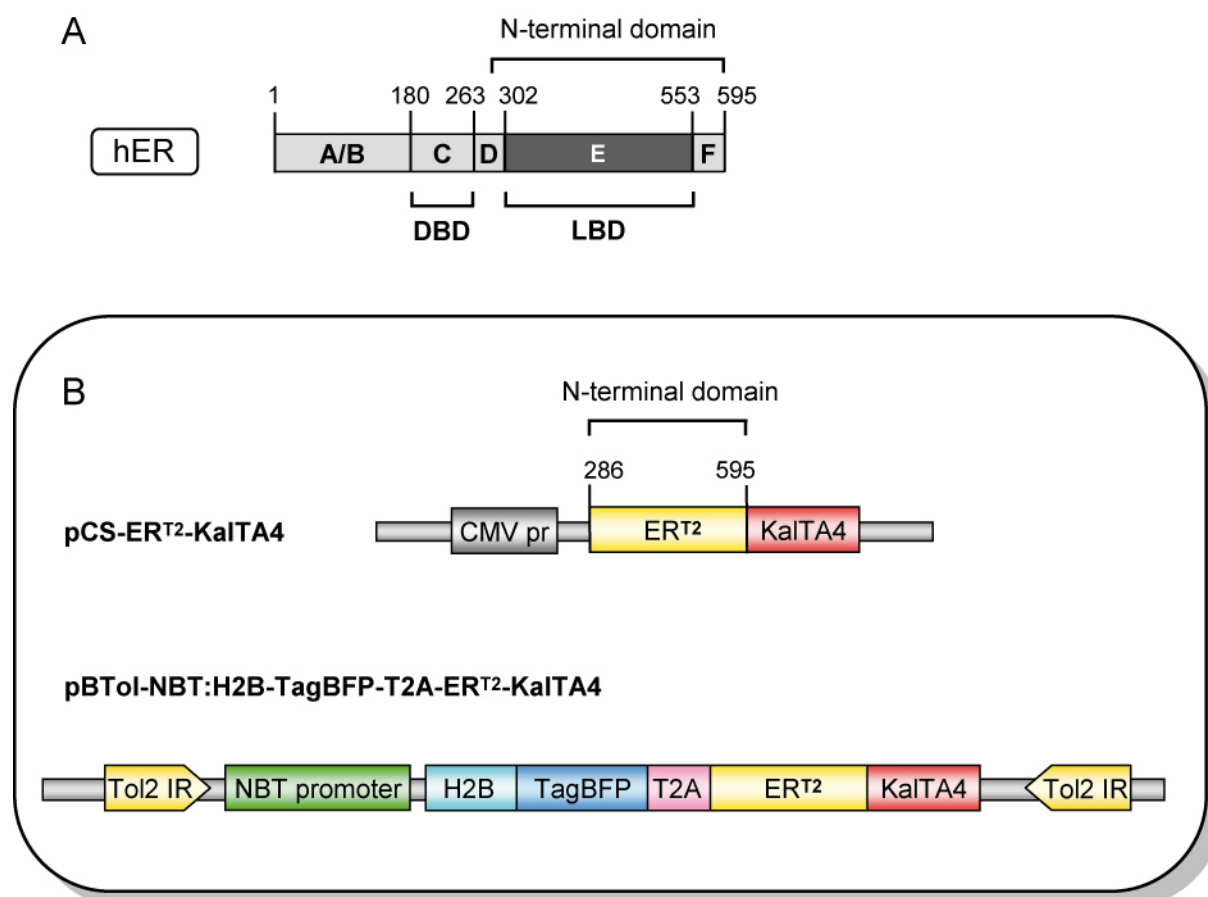


**Figure 8. Cloning of expression constructs encoding the ER<sup>T2</sup>-KalTA4 fusion protein.**

**A** Amino acid positions and homology regions A/B, C, D, E and F of the human estrogen receptor (ER) are depicted schematically. The ligand-binding domain (LBD) within the 310 aa-encompassing fragment used as N-terminal fusion construct are indicated, as well as the DNA-binding domain (DBD) (adapted from Metzger *et al.*, 1995). **B** Two constructs were cloned which contain a mutated ligand-binding domain of human ER (aa 286-595) with the triple mutation G400V/M543A/L544A fused to the N-terminus of KalTA4. This mutant version of the LBD, called ER<sup>T2</sup>, is characterized by its insensitivity to the endogenous steroid 17 $\beta$ -estradiol and a high affinity to the synthetic estrogen antagonist 4-Hydroxy-tamoxifen.

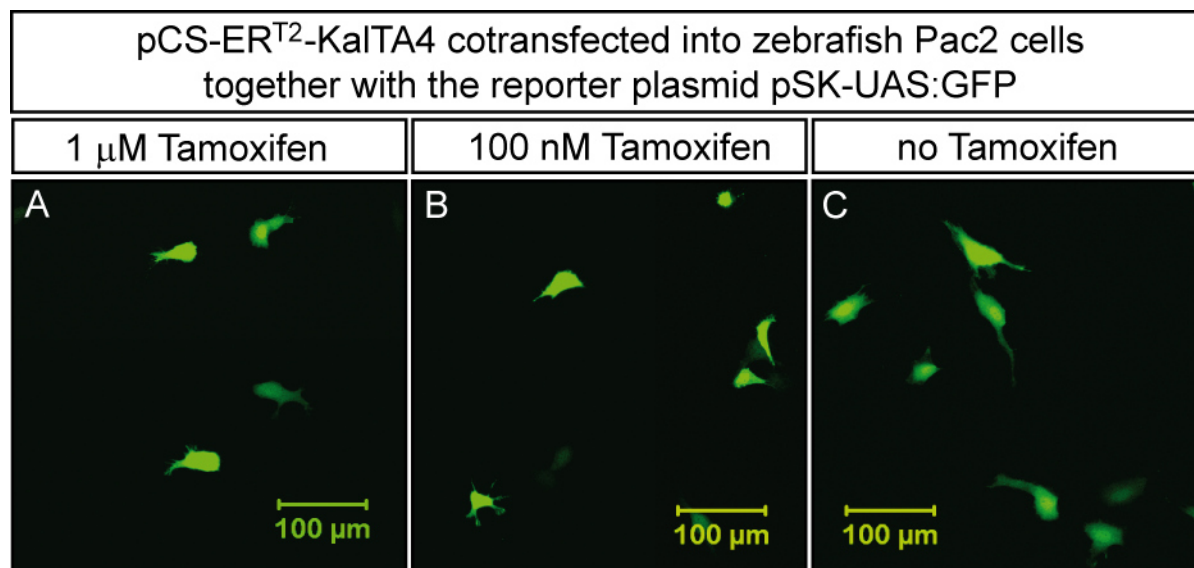


**Figure 9. ER<sup>T2</sup>-KalTA4 fusion proteins are constitutively active in cell culture.** Zebrafish Pac2 fibroblast cells were transiently transfected with pCS-ER<sup>T2</sup>-KalTA4 and the reporter plasmid pSK-4xUAS-GFP. 24 hours after transfection 4OH-Tamoxifen was added at the concentrations indicated in **A** and **B**, or cells were treated with vehicle alone, as shown in **C**. GFP expression was recorded by confocal microscopy 24 hours after treatment. Strong GFP expression can be detected in some of the Tamoxifen-treated cells as well as in cells after vehicle treatment. Additional control experiments were performed to preclude that the reporter plasmid induces leaky GFP expression in the absence of KalTA4 (data not shown).

conditions, as well as in the control culture, as visible in the images of Figure 9. The number of GFP expressing cells was similar in all three conditions analysed. Cells in the vehicle-control experiment contained less apoptotic cells and did look healthier than the Tamoxifen-treated cells (cells in Figure 9C are slightly larger than in A or B), indicating that Tamoxifen had some cytotoxic effects in cell culture at the concentrations used. To preclude the possibility that the UAS-GFP reporter plasmid induces leaky GFP expression in the absence of KalTA4, control experiments were performed by co-transfecting the reporter plasmid with an empty vector. In this case, no GFP expression was detectable (data not shown). These experiments indicate that KalTA4 is not repressed by fusion to ER<sup>T2</sup> and is not rendered Tamoxifen-inducible – at least in cell culture. However, the constitutive activity might also be connected to a high plasmid copy number in transfected cells.

Regulation and inducibility of the fusion protein might still be achieved *in vivo*. Both ER<sup>T2</sup>-KalTA4 expression plasmids were therefore tested by injection into eggs of the reporter line *Tg(UAS:Lyn-Venus-T2A-NLS-CFP)*. One day post injection, embryos were treated for at least 20 hours with 5  $\mu$ M or 10  $\mu$ M Tamoxifen or were treated with vehicle alone. Concentrations in this range had previously been shown to induce cell ablation in zebrafish larvae expressing a caspase8-ER<sup>T2</sup> construct in cerebellar Purkinje neurons (Dr. Thomas Weber, this laboratory, personal communication). This was an indication that 4OH-

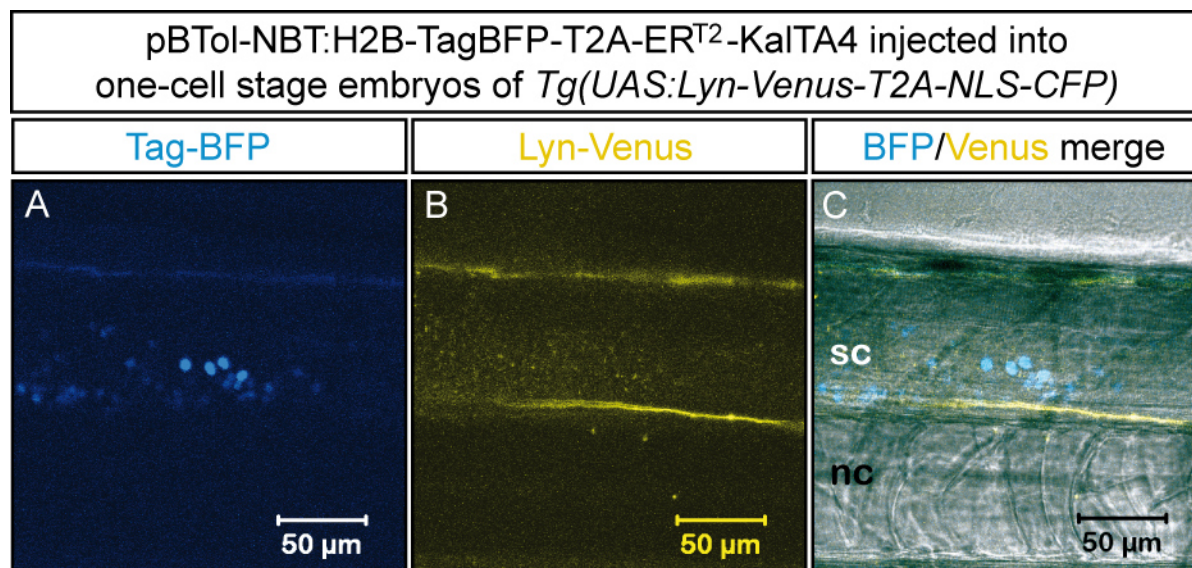


**Figure 10. ER<sup>T2</sup>-KalTA4 is not Tamoxifen-inducible *in vivo*.** Plasmid pBTol-NBT:H2B-TagBFP-T2A-ER<sup>T2</sup>-KalTA4 was injected into one-cell stage embryos of the reporter line *Tg(UAS:Lyn-Venus-T2A-NLS-CFP)*. At 30 hpf embryos were dechorionated and treated with 10  $\mu$ M 4OH-Tamoxifen or with vehicle alone for a minimum of 20 hours. Lateral view images of the trunk recorded by confocal microscopy are shown. **A** A weak nuclear TagBFP signal indicates neuronal somata in the spinal cord that express the injected plasmid. **B** No induction of Venus expression can be detected in the Tamoxifen-treated embryos. The unspecific autofluorescence is due to the strongly enhanced detection mode of the microscope. **C** A merge of A and B indicates locations of spinal cord, sc, and notochord, nc.

Tamoxifen is taken up by the embryos when added to the rearing water, it can reach target cells within the organism and can induce an effect via the ER<sup>T2</sup> domain. Embryos were observed by confocal microscopy after compound treatment. The ER<sup>T2</sup>-KalTA4 fusion protein expressed from each of the two plasmids was not constitutively active *in vivo* as no Venus fluorescence could be observed. However, an induction of Lyn-Venus reporter expression could not be achieved at any of the Tamoxifen concentrations tested, as shown in Figure 10 for 10  $\mu$ M Tamoxifen. Taken together, the results from the cell culture and the *in vivo* experiments of the fusion constructs indicate that the desired compound-inducible regulation of KalTA4 could not be achieved by fusing the ER<sup>T2</sup> domain to its N-terminus. As the fusion protein is able to constitutively activate transcription in cell culture a sterical hindrance of KalTA4's binding to its UAS sequences by the ER<sup>T2</sup> domain seems not to be the reason.

#### 3.2.1.4. Establishing the transgenic driver line

In order to generate a stable, *KalTA3*-expressing transgenic line, the driver construct, described in Chapter 3.2.1.2., was injected into one-cell stage wild-type embryos together with mRNA encoding Tol2 transposase. As anticipated from the experiments described before, the signal of the H2B-TagBFP reporter was too weak to allow for direct selection of transgene-expressing larvae with a fluorescence stereo-microscope. Instead, larvae were raised to adulthood. Then, fish of this injected parental generation (P or F0 generation) were crossed one by one to fish of the reporter line *Tg(UAS:GFP)* to reveal germline transmission of the driver construct by neuronal GFP expression in the offspring of this screening cross (F1 screening clutches). Typically, larvae were screened on a fluorescent stereomicroscope at 2 dpf and 7 dpf. It could be observed that in many of the analysed clutches only few larvae did show GFP expression, suggesting that only few germline cells did contain the transgene in the P generation. Second, GFP expression in F1 larvae was sometimes very weak and difficult to observe.

In total, 56 adult animals of the injected P generation were screened in this way. In each of 15 screening clutches a spectrum of neuronal GFP expression from weak to quite strong could be observed. In 10 F1 clutches only a weak neuronal expression was observable, and the remaining 31 clutches were either GFP-negative, had completely unspecific staining in notochord, muscle and fins, or parental fish did not lay (enough) eggs at all. It has to be noted that GFP expression in clutches with a strong CNS-specific signal never was pan-neuronal. This was clearly evident in the brain, where only ventral areas were GFP-positive (see Figures 13, 14 of the outcrossed line). Two of the P fish with strong GFP expression in F1 screening clutches were selected and outcrossed against wt animals to obtain the transgenic F1 generation. Then again, 22 F1 fish were screened as described before and F2 offspring in screening clutches did again show variable phenotypes. Some clutches only contained weakly expressing larvae while others did show a spectrum of GFP expression from weak to strong. Finally, one transgenic F1 fish with the latter phenotype was outcrossed in a second round against wild-type to obtain the F2 generation of the driver line. F2 transgene carriers were later used for transient-transgenic experiments with the effector constructs of our disease model. For this purpose they were crossed to wild-type fish and imaging experiments were performed with injected F3 larvae (see Chapters 3.3.1. and 3.3.2.).

F2 animals were also used to characterize the driver line *Tg(NBT:H2B-TagBFP-T2A-KalTA3)* by crossing them to the UAS-GFP reporter line. Larvae were analysed by fluorescence and confocal microscopy. One clearly visible and striking observation, as shown in Figure 11,

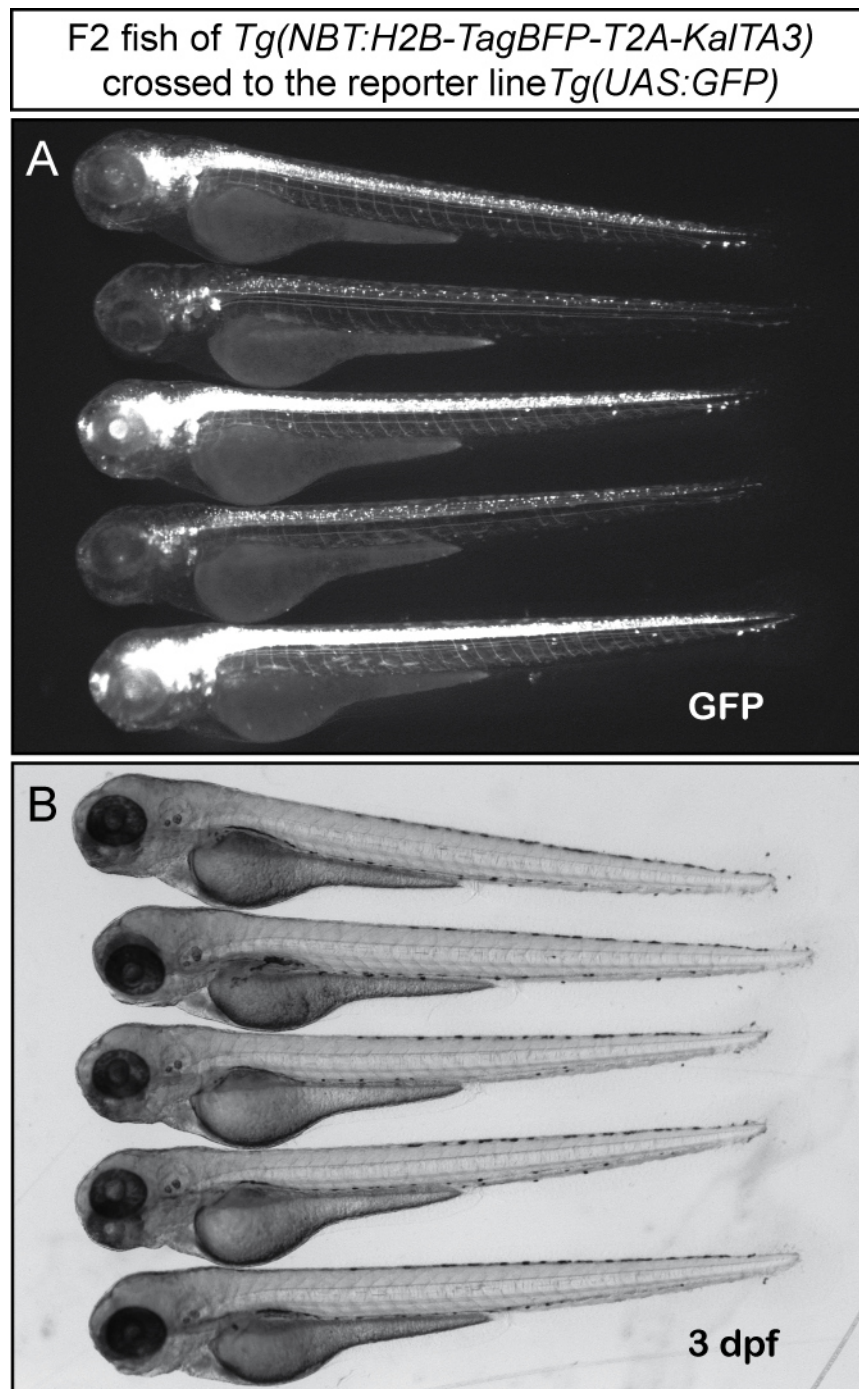


**Figure 11. Heterogeneity of the transgenic driver line.** F2 fish of *Tg(NBT:H2B-TagBFP-T2A-KalTA3)* were crossed to the reporter line *Tg(UAS:GFP)*. Images of 3 dpf larvae were recorded with a fluorescence stereomicroscope. **A** Double-transgenic larvae within one clutch show variable levels of GFP expression from a very weak signal and sparse distribution to a strong signal in many neurons. Identical results were obtained for clutches from several transgenic F2 fish analysed. **B** A bright field image of the same embryos as in (A) is shown.

was that double-transgenic larvae from this cross did show heterogeneous GFP expression within one clutch: from a very weak green fluorescence and quite mosaic staining of only few neurons in some animals to a strong GFP signal in many neurons in others. This was one hint that the selected F2 driver fish might contain several copies of the transgene integrated at

different sites of the genome, which would segregate in the next generation. Indeed, this could be confirmed when inheritance of the transgene was quantified in F3 screening clutches and compared to expected values for monogenic Mendelian inheritance. For 9 crosses between F2 animals of the driver line with heterozygous animals of *Tg(UAS:GFP)* the following percentages for double-transgenic animals were obtained: 29, 16, 35, 27, 51, 34, 59, 25, 37. All but one value are higher than the expected 25% if both fish were truly heterozygous. In case homozygous fish of the reporter line were used for crossing, values obtained were in 8 out of 10 cases higher than the expected 50% (values in percent: 84, 76, 72, 50, 76, 69, 74, 50, 61, 80). This indicates that the selected F2 fish of the driver line, which had been chosen because of their strong GFP signal under screening conditions (actually with a spectrum from weak to strong signal intensity) were likely to contain two or more copies of the transgene integrated at different sites in the genome to allow free segregation in the next generation. This discovery was not problematic for the usefulness of this line in the experiments described later. However, it was an indication that the *neuronal beta-tubulin* promoter was not a strong promoter in the context of our transgenic construct, and this was in contrast to *Tg(NBT:DsRed)*, described before (Figure 2), where expression of DsRed was strong and pan-neuronal.

Next GFP expression regulated by the driver construct in double-transgenic animals was characterized in more detail by confocal microscopy with a special focus on neuronal subtypes. As documented in Figure 12, the NBT promoter did activate transcription in the first differentiating neurons generated during embryogenesis (see also Figure 25 in Chapter 3.3.1). Neurogenesis starts as early as 15 hpf in the spinal cord of zebrafish embryos with the appearance of the first primary motoneurons (Myers *et al.*, 1986; Hanneman *et al.*, 1988). The first neurons in the presumptive fore- and midbrain appear at around 16 hpf in three characteristic clusters: the dorso-rostral, ventro-rostral and ventro-caudal cluster (Ross *et al.*, 1992). These CNS clusters were visible in 24 hpf embryos (Figure 12A). The most prominent cluster is the dorso-rostral cluster, while the ventro-caudal cluster is small and located close to the midbrain-hindbrain boundary (Figure 12A, indicated by a yellow arrowhead). Motoneurons with their ventrally growing axons and many other GFP-positive neurons in the spinal cord were visible at this early developmental stage (Figure 12B, B').

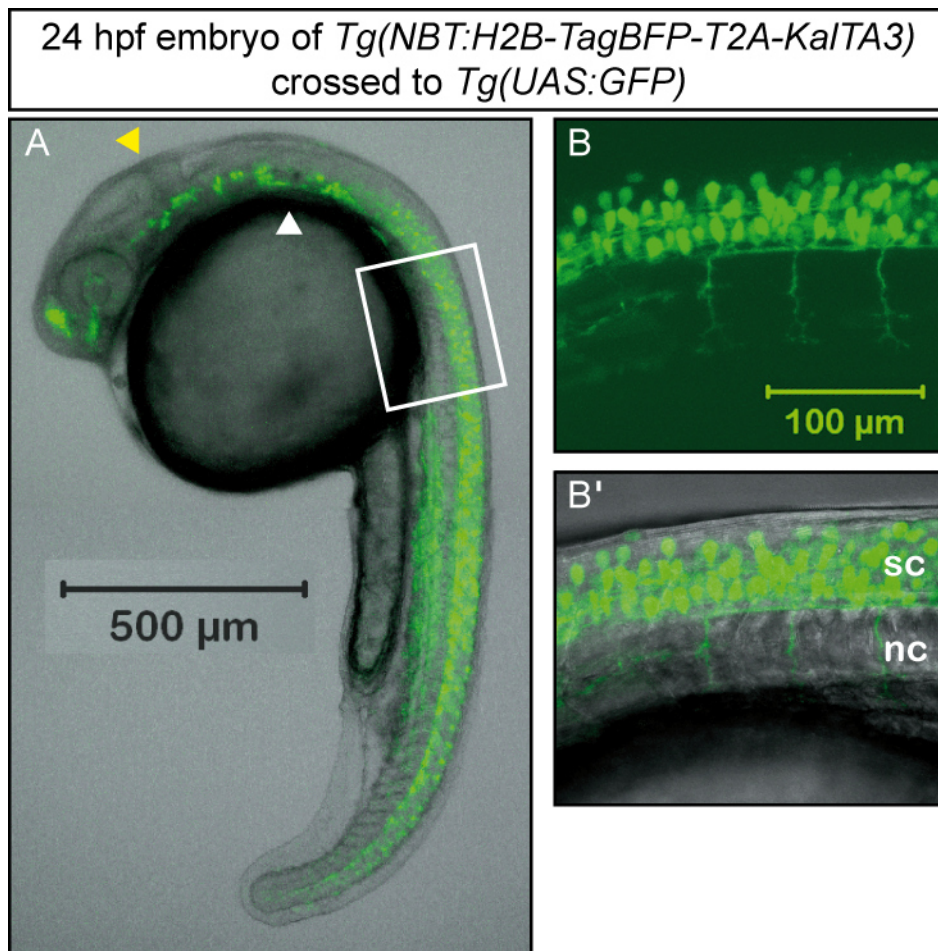


**Figure 12. The NBT promoter is transcriptionally active in the earliest differentiating neurons.** F2 fish of transgenic line *Tg(NBT:H2B-TagBFP-T2A-KalTA3)* were crossed to the reporter line *Tg(UAS:GFP)*. GFP expression was analysed by confocal microscopy in embryos at 24 hpf. **A** Overview of a typical embryo at 24 hpf. GFP-expressing cell clusters in the forebrain are the dorsorostral and ventrorostral cluster located anterior to the eye. Only few neurons are labelled in the midbrain. The midbrain-hindbrain boundary is indicated by a yellow arrowhead and the location of the otic vesicle by a white arrowhead. Several neuronal clusters are GFP-positive in the hindbrain, while many neurons are labelled in the spinal cord. **B** and **B'** A close-up image projection of GFP-expressing neurons in the spinal cord is shown (location indicated by white box in A). Outgrowing axons of motoneurons are visible. Abbreviations: nc, notochord; sc, spinal cord.

The expression pattern did not change much at later stages as shown for a 2 dpf embryo in Figure 13. It clearly is evident in Figure 13C that only few ventrally located neurons were GFP-positive in the forebrain and midbrain of double-transgenic embryos. This ventral staining pattern was also true for the hindbrain where the segmented organization of neurons into so-called rhombomers was visible. One characteristic of this transgenic line is the mosaic GFP expression in only some but not all neurons of the spinal cord (see Figure 13D and Figure 14). It is not clear how to explain this phenotype but it might be due to genomic silencing of the transgene in some neurons.

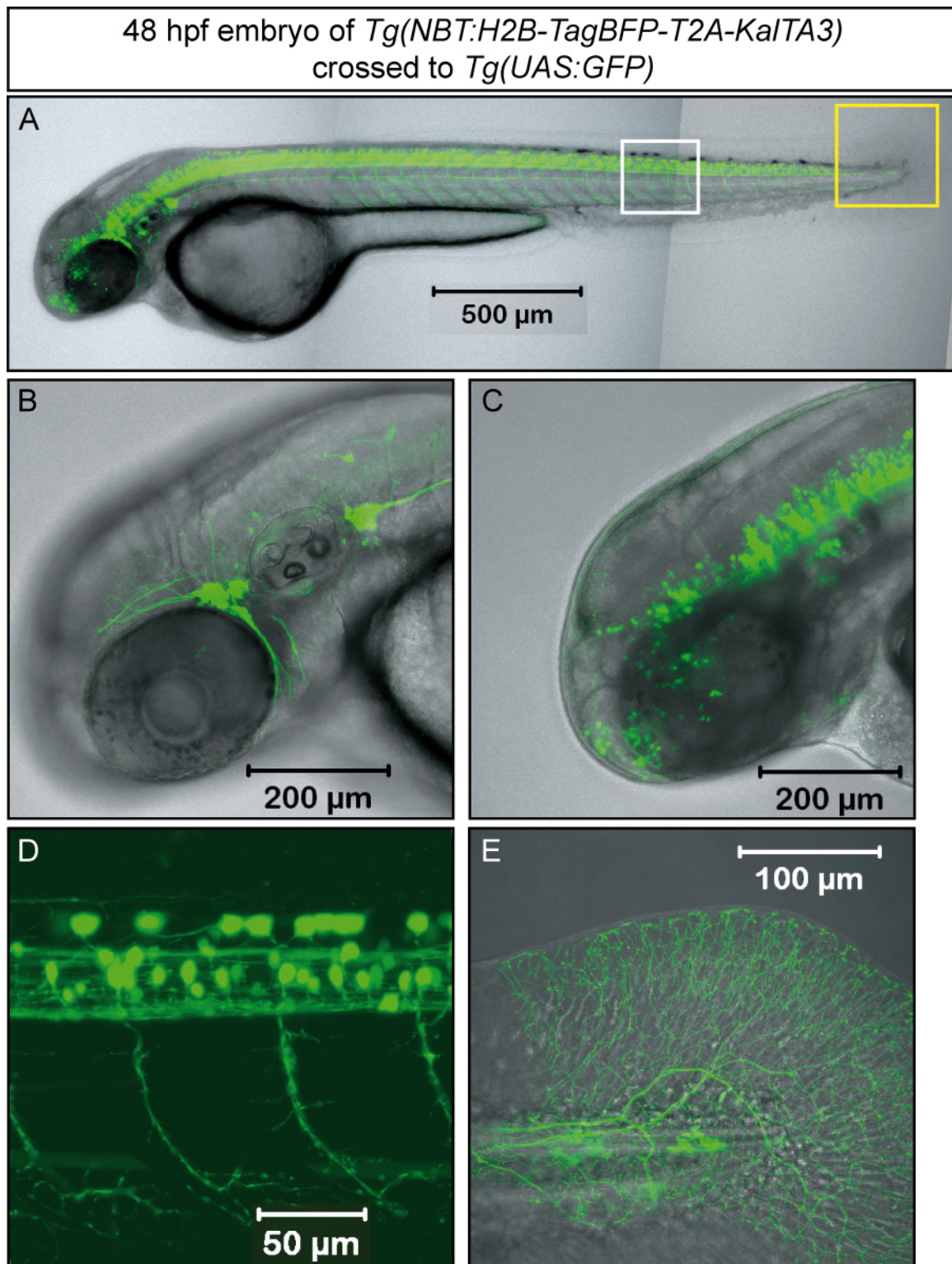


**Figure 13. Different central and peripheral neurons express the GFP reporter at early larval stages.** F2 fish of transgenic line *Tg(NBT:H2B-TagBFP-T2A-KalTA3)* were crossed to the reporter line *Tg(UAS:GFP)* and double-transgenic larvae were analysed by confocal microscopy at 48 hpf. **A** An overview of a typical larva with a strong GFP signal is shown. Many neurons in the hindbrain and spinal cord are labelled. **B** The close up view is focussed on the trigeminal ganglion, a cluster of sensory neurons located in the periphery at the caudal edge of the eye. Their axons project around the eye and innervate the skin of the head. The ganglion of the posterior lateral line system is visible posterior to the otic vesicle. Its peripheral axons project caudally. **C** Only few neurons express the reporter in the fore- and midbrain. GFP-positive neurons can be detected in the hindbrain and their segmental organization is visible. **D** A high-magnification image shows neuronal somata and axon

tracks in the spinal cord (location is indicated by the white box in A). Motoneurons with their ventrally projecting axons are labelled. **E** Rohon-Beard sensory neurons located in the dorso-lateral spinal cord innervate the skin of the trunk and the tail with elaborate networks of peripheral axons. The axon arbor innervating the tail fin is shown (yellow box in A).

Concerning the peripheral nervous system, the driver construct activated strong and reliable expression in motoneurons (Figure 13D) and sensory neurons innervating the skin of the head, trunk and tail. Cell bodies of sensory neurons innervating the head are located in the cranial ganglion, which is positioned between the eye and the otic capsule, as shown in Figure 13B. Their nerve fibres were clearly visible. Somata of sensory neurons innervating the skin of the trunk, tail and fins are located in the spinal cord. These are called Rohon-Beard neurons and their complex peripheral axonal trees were strongly GFP-stained (Figure 13E). Another sensory system specific to fish is the lateral line system composed of clusters of sensory hair cells and their innervating neurons. This system is used to detect changes in water current and thereby to determine the swimming speed and orientation of the fish. Especially neurons of the posterior lateral line system were strongly labelled, mediated by the driver construct, as documented in Figure 14. The cells bodies of these afferent neurons are located close to the otic capsule in the posterior lateral line ganglion (PLLg) (Figure 13B and 14; yellow arrow in Fig. 14B). Their axons are closely fasciculated into one bundle running along the lateral side of the fish and innervating clusters of sensory cells, called neuromasts (these are not neurons and they are not GFP-expressing). Neurons of the PLL system were used in the course of this study to image mitochondrial axonal transport. Differentiation and development of this sensory system will therefore be described in more detail in Chapter 3.3.1. In Figure 14 the heterogeneity of reporter gene expression induced by the transgenic driver line is again documented by two embryos from the same clutch showing different GFP expression levels.

3 dpf zebrafish larvae from a cross between *Tg(NBT:H2B-TagBFP-T2A-KalTA3)* and *Tg(UAS:GFP)*

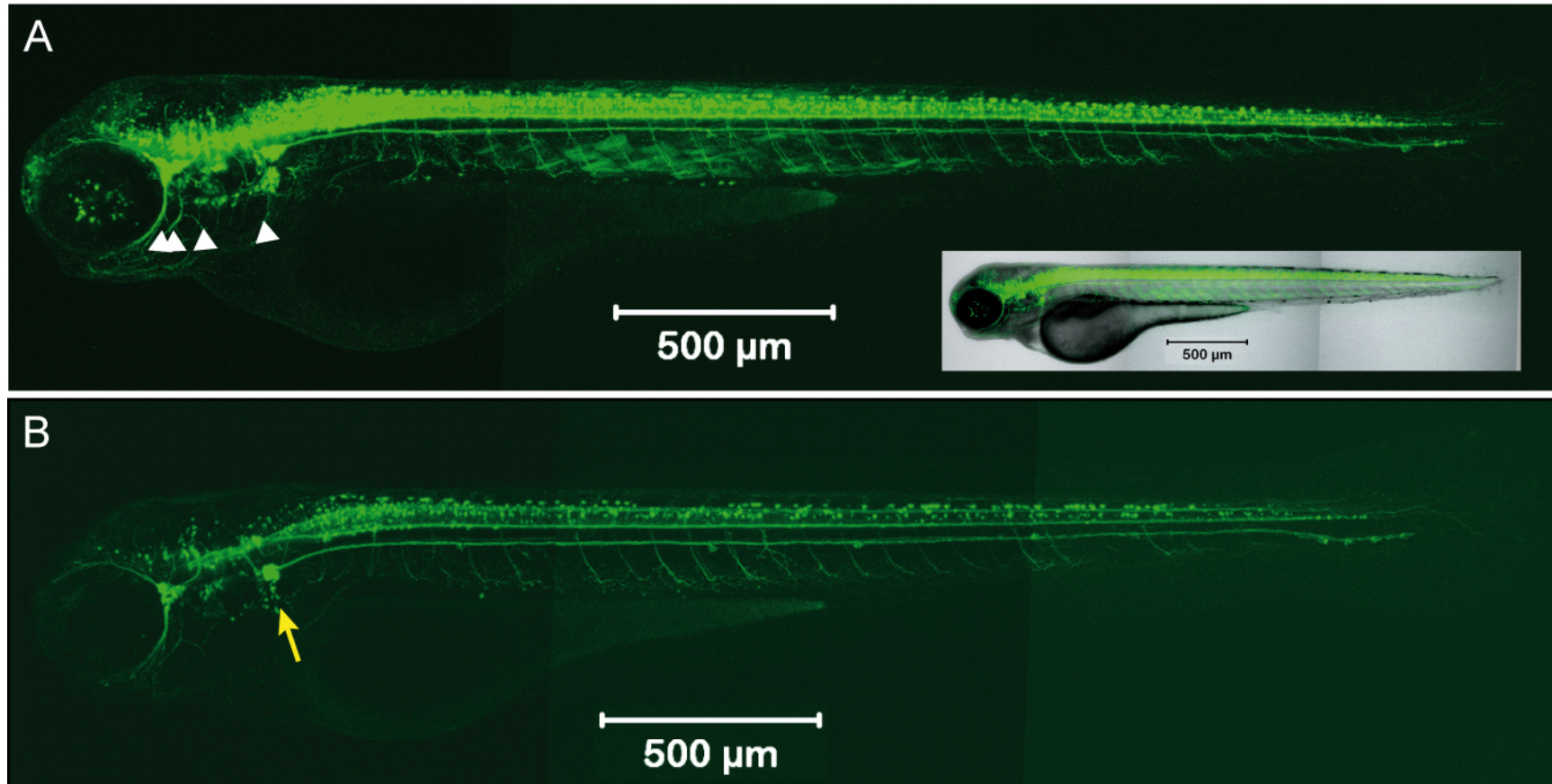


**Figure 14. Neuronal populations and heterogeneity of GFP expression driven by the newly generated transgenic line.** F2 fish of the driver line were crossed to the reporter line. Projections of confocal image stacks were assembled to show two larvae from the same clutch at 3 dpf. **A** A larva with strong GFP expression in many neurons is shown. The cranial sensory ganglia – trigeminal, facial, glossopharyngeal and vagal ganglion – of the peripheral nervous system (white arrowheads) are clearly visible at the posterior end of the eye and ventral to the otic vesicle. **B** This larva has a weaker GFP expression and less neurons are stained. The posterior lateral line ganglion (yellow arrow) and nerve are well visible. Other prominently stained neurons are primary motoneurons of the trunk and tail.

### 3.2.2. Generation of LRRK2-expressing effector constructs

The next step in generating our disease model was the construction of four different effector constructs. These should contain one of three version of the disease gene: either (1) human *LRRK2(G2019S)*, which is the most common missense mutation in familial Parkinson's disease (Biskup and West, 2009); or (2) the *LRRK2* wild-type allele; or (3) *LRRK2(K1906M)* with a mutation in the kinase domain, which abolishes kinase activity (Gloeckner *et al.*, 2006). One control vector should be constructed without *LRRK2*. Additionally, each of the constructs should contain two fluorescent reporters to label mitochondria and autophagosomes. We were planning to use the Tol2kit vector system developed by the Chien lab (Kwan *et al.*, 2007) to combine these transgenes into one plasmid.

#### 3.2.2.1. Modification and use of the Tol2kit Gateway-based cloning system

The Tol2kit is a three-partite cloning system, whereby DNA sequences cloned into three different entry vectors are combined in one recombination reaction into the final destination vector (Figure 15) (Kwan *et al.*, 2007). This destination vector contains recognition sites for Tol2 transposase-mediated genomic integration of the final construct. We wanted to take advantage of the highly efficient Gateway recombination reaction of this system (see product manual: MultiSite Gateway Three-Fragment Vector Construction Kit, Invitrogen), which should facilitate cloning of large DNA fragments like the 7584 bp ORF of LKRR2.

We planned to combine the subcellular markers for mitochondria and autophagosomes into one bicistronic cassette and fuse both fluorescent proteins via the T2A peptide into one ORF (see Figure 16). The second expression cassette would encode the disease gene. For this cloning strategy, we planned to adjust the 3-partite kit into a 2-partite system, as shown in Figure 15. The attachment R1 site of plasmid p5E-MCS site was exchanged against an *in vitro* synthesized attachment L2 site, to obtain plasmid p5E-attL4-attL2. Additionally, the multiple cloning site of p3E-polyA was adjusted by insertion of suitable restriction sites to simplify the subsequent cloning of the disease gene. Two modified plasmids, p3E-linker-pA and p3E-modifiedMCS-pA, were generated (see Materials and Methods).

After inserting the two transgene cassettes into the modified entry plasmids, these could be combined in the final recombination reaction into one destination or effector plasmid (outlined in Chapter 3.2.2.4.).

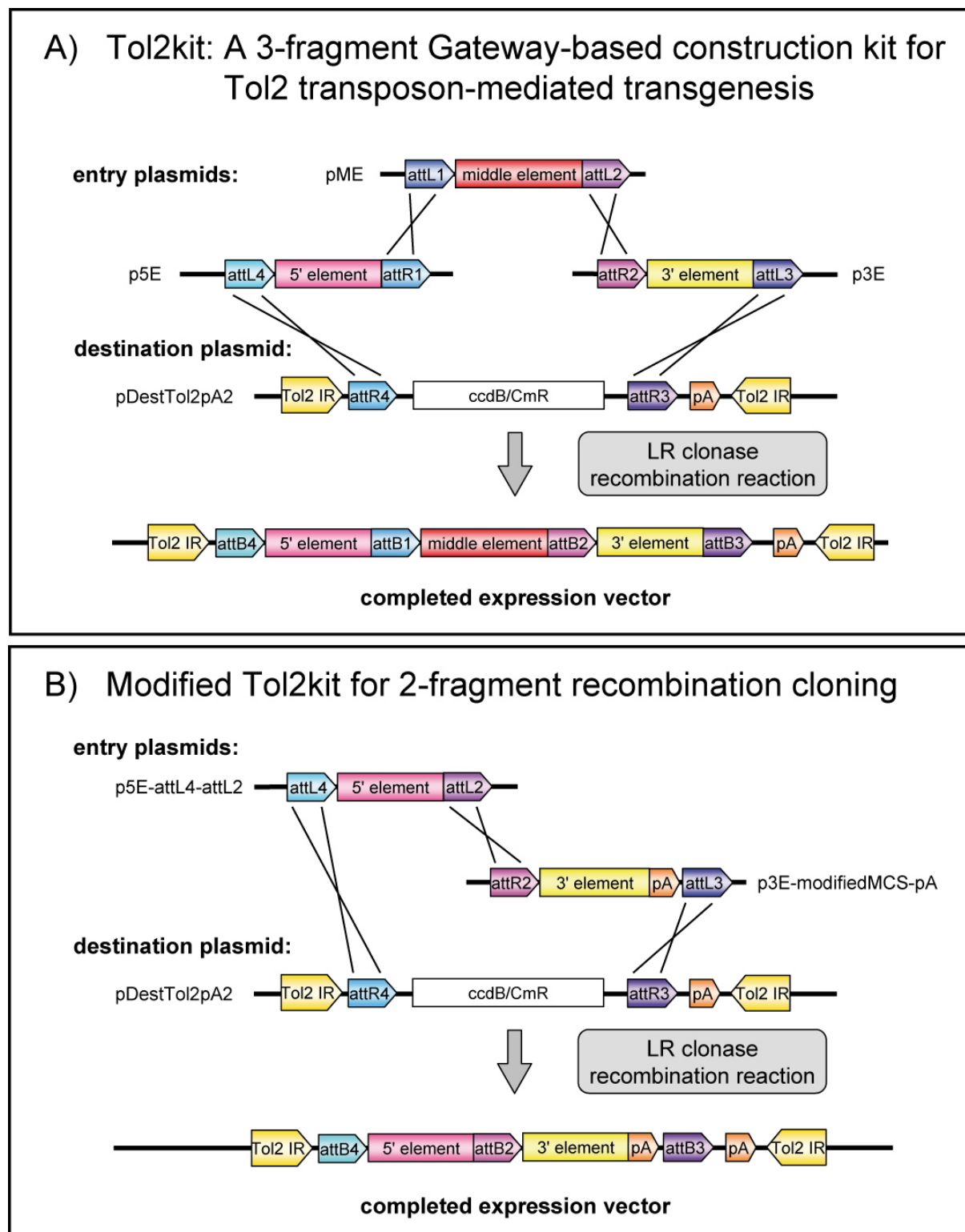


**Figure 15. Modification of the Tol2kit cloning system.** **A** The original Tol2kit is a 3-fragment cloning system based on the Gateway site-specific recombination technology (Kwan *et al.*, 2007). Recombination between attL- and attR-flanked sequences of the three different entry vectors and the destination vector is catalysed by the LR clonase enzyme mix in a single reaction. **B** The kit was modified here to obtain a 2-fragment cloning system. The 157 bp attR1 recombination site of the p5E vector was exchanged against an *in vitro* synthesized 100 bp attL2 site. Additionally, the multiple cloning site (MCS) of p3E-polyA was optimized to facilitate cloning of the disease gene. Drawing adapted from Kwan *et al.*, 2007.

### 3.2.2.2. Evaluation of the fluorescent reporter cassette to label subcellular structures

We wanted to be able to observe concomitantly two highly dynamic organelles within neurons *in vivo* – mitochondria and autophagosomes. The red fluorescent protein TagRFP was targeted to mitochondria by the N-terminal addition of the sequence encoding human cytochrome c oxidase subunit VIII A (COX8A), a small mitochondrial protein of 69 aa. The bright-yellow fluorescent protein Venus was modified to decorate autophagosomes by its C-terminal fusion to the sequence encoding the 122 aa of zebrafish microtubule-associated protein 1-light chain 3B (Map1-1c3b; in the following called: LC3). This fusion protein is cytoplasmic but will be incorporated into autophagosomal membranes due to cleavage and ubiquitin-like conjugation of LC3 to phosphatidyl-ethanolamine during autophagy (Kabeya *et al.*, 2000; Klionsky *et al.*, 2008; He *et al.*, 2009; Fleming and Rubinsztein, 2011). Both fluorescent markers were combined into one ORF via the T2A viral peptide sequence. Plasmid pCS-mitoTagRFP-T2A-Venus-LC3 (Figure 16) could be obtained from colleagues in our laboratory.

The functionality of the reporter cassette was tested by transient transfection of plasmid pCS-mitoTagRFP-T2A-Venus-LC3 into zebrafish Pac2 cells. Mitochondria were easily detected by fluorescence and confocal microscopy as a tubular network in transfected cells, as can be observed in Figures 17, 18 and 19. But how can autophagy be induced and visualized to test

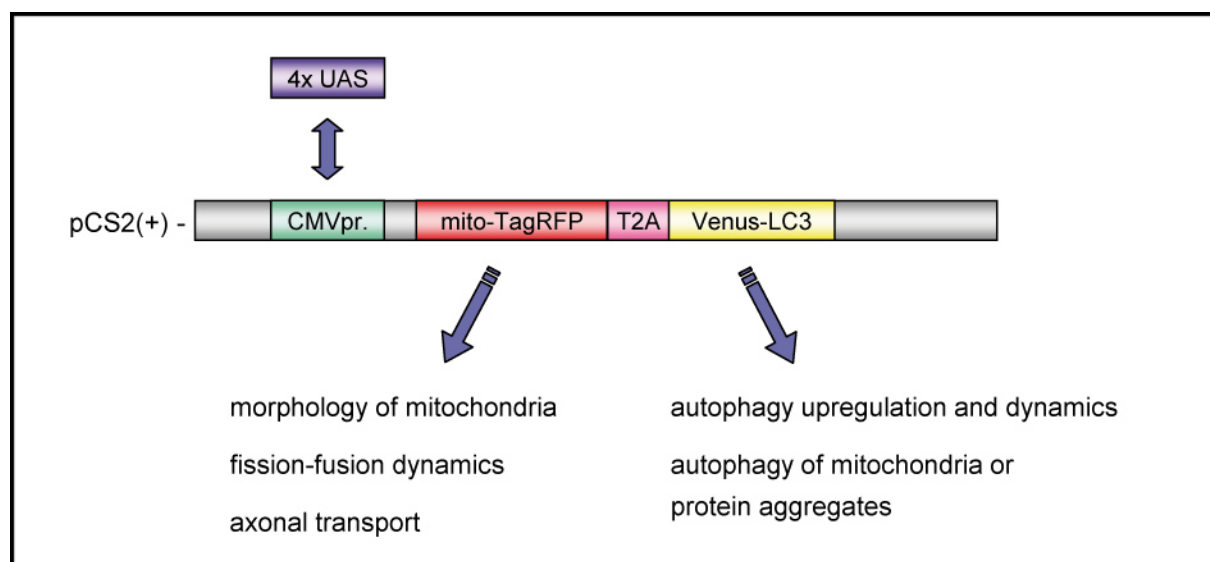


**Figure 16. The fluorescent reporter cassette labels mitochondria and autophagosomes.** TagRFP is targeted to mitochondria via the N-terminally-fused sequence of human COX8A, and the fluorescent protein Venus, will decorate autophagosomes after processing of LC3. ORFs for both fluorescent proteins were assembled into one bicistronic expression cassette. The CMV promoter of plasmid pCS2 is later replaced by 4xUAS Gal4-binding sites. Mitochondria are dynamic organelles, which constantly undergo fission and fusion, and which are moved around inside a cell and along neuronal processes. Autophagy is an intracellular catabolic process by which dysfunctional organelles and other bulky unwanted material in the cytoplasm are degraded.

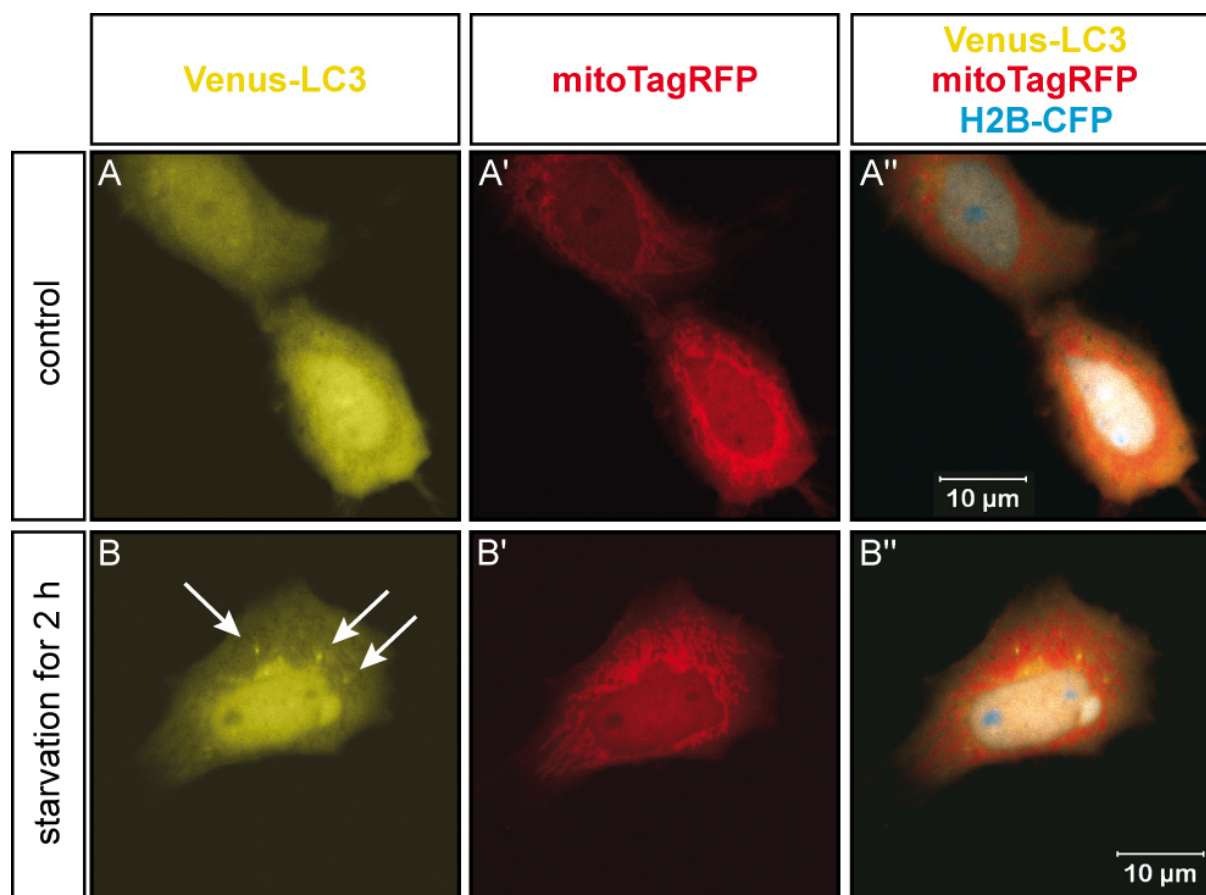


**Figure 17. Starvation-induced autophagy.** Zebrafish Pac2 cells were co-transfected with a plasmid expressing the [mitoTagRFP-T2A-Venus-LC3] cassette and with a plasmid expressing nuclear-localized CFP. 24 hours after transfection the growth medium was replaced by glucose-supplemented phosphate buffer to induce amino acid starvation. Control cells were kept in full medium. Images were recorded by confocal microscopy. **A-A''** No Venus-LC3 puncta representing autophagosomes are visible in these two cells, which were kept at normal growth conditions. **B-B''** After 2 hours of starvation few Venus-LC3-labelled autophagosomes (white arrows) can be detected in this cell.

the functionality of the Venus-LC3 reporter? Autophagy is an important homeostatic pathway and is constantly taking place at a low basal level in every cell. It can be induced or upregulated by various stress conditions, and one prominent physiological stress is nutrient starvation. Transfected Pac2 cells were subjected to amino acid starvation by replacing the normal growth medium with a glucose-supplemented buffer and incubation for 2 hours (Balgi *et al.*, 2009). Upon observation by fluorescence and confocal microscopy, the majority of Venus-LC3 was detected diffusely in the cytoplasm of cells subjected to starvation, as well as in control cells. Few Venus-LC3 puncta could be seen in cells at 2 hours of starvation (Figure 17). However, some small Venus-LC3 dots could also be observed in cells of the control cultures, incubated in normal medium (not shown). A strong stimulation of autophagy as evident by a drastic increase in punctate Venus-LC3 fluorescence was not achieved by this treatment regime. This is in contrast to what has been reported by others (Bampton *et al.*,

2005; Klionsky *et al.*, 2008) but it might be connected to the different cell types and experimental conditions. Another explanation can be that an upregulation of this highly dynamic process might lead to an increased autophagic flux and a fast lysosomal degradation of autophagosomes. Thereby, no changes in steady-state autophagosome numbers will be detectable. An attempt to quantify Venus-LC3 puncta within cells or the percentage of cells containing autophagosomes was not made.

Instead, we tried to achieve a better stimulation and visualization of autophagy by treatment with the mTor inhibitor Rapamycin. Mammalian target of rapamycin (mTor), a serine-threonine kinase, is the main functional component of the TORC1 signalling complex, which is an upstream regulator and inhibitor of autophagy. Rapamycin concentrations in the range of 50 nM to 1  $\mu$ M have been used in the past to induce autophagy in different mammalian cell culture systems and using different detection methods for autophagy (Bampton *et al.*, 2005; Sarkar *et al.*, 2005; Criollo *et al.*, 2010). Here, transfected Pac2 cells were treated with 1  $\mu$ M

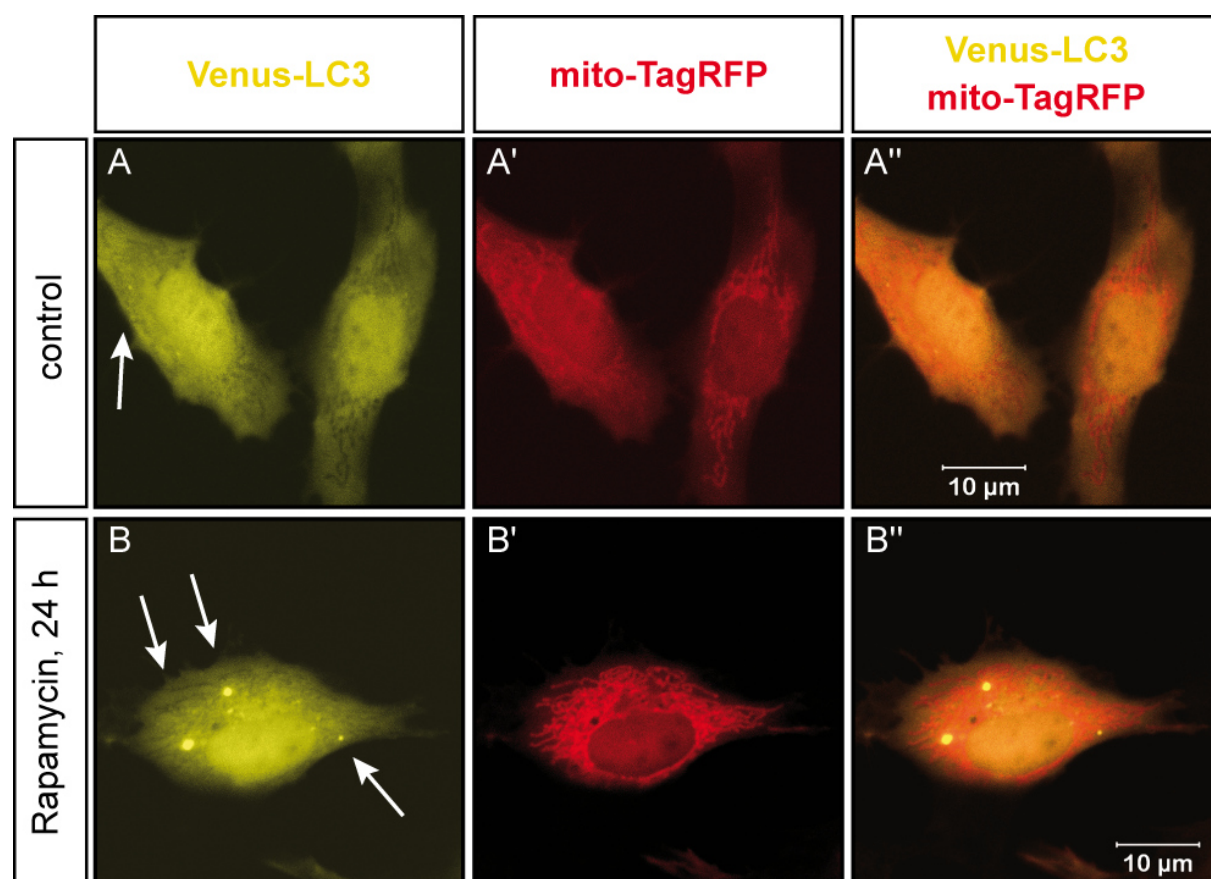


**Figure 18. Rapamycin-induced autophagy.** Pac2 cells were transfected with plasmid pCS-mito-TagRFP-T2A-Venus-LC3. 24 hours post transfection cells were treated with 1  $\mu$ M Rapamycin in DMSO or with vehicle alone for 24 hours, followed by live confocal microscopic observation. **A-A''** A few small Venus-LC3 puncta (i.e. autophagosomes) are visible in non-treated cells (indicated by an arrow). **B-B''** Several autophagosomes are visible in a Rapamycin-treated cell (indicated by arrows).

Rapamycin for at least 3 hours and up to 24 hours and analysed by confocal microscopy. Several Venus-LC3-stained dots representing autophagosomes were visible in cells following Rapamycin treatment, as shown in Figure 18, and these appear to be slightly larger than autophagosomes detected in vehicle-treated cells. But again, a strong increase in autophagosome numbers in treated versus non-treated cultures was not observed, and a quantification was not attempted. Nevertheless, the Venus-LC3-stained punctate structures seemed to be autophagosomes, and another approach was made to prove this.

The number of autophagosomes can be increased by treatment with lysosomal inhibitors such as ammonium chloride, which increases the pH of the acidic lysosomes and thereby inhibits autophagosome-lysosome fusion and autophagosome clearance (Seglen and Gordon, 1980; Bampton *et al.*, 2005). Indeed, application of 50 mM NH<sub>4</sub>Cl to transiently-transfected Pac2 cells expressing the reporter cassette caused a rapid reorganization of Venus-LC3 into compact perinuclear clusters of accumulated autophagosomes within one hour. The typical phenotype of a cell after 2 hours of NH<sub>4</sub>Cl treatment is shown in Figure 19. Besides the aggregated autophagosomes, vacuolar structures were visible as unstained, FP-free spots and were characteristic for this treatment regime. These vacuoles are probably osmotically swollen lysosomes because ammonium chloride has a lysosomotropic effect. This compound becomes protonated within the acidic environment of the lysosomes, and its intralysosomal accumulation leads to osmotic swelling – besides neutralization of the lysosomal pH (Seglen and Gordon, 1980). The effect of NH<sub>4</sub>Cl treatment was rapid and intense and was clear proof that Venus-LC3 expressed from the bicistronic ORF of the effector cassette is an efficient marker for autophagosomes.

Taken together, we were able to show that both fluorescent proteins mitoTagRFP and Venus-LC3 target their respective subcellular structures when co-expressed via the T2A peptide. Venus-LC3 did not localize to the mitochondrial network but was mainly cytosolic and did decorate autophagosomes. *Vice versa*, mitoTagRFP could not be observed in contact with autophagosomes but nicely highlighted mitochondria. Although the induction of autophagy in Pac2 cells by starvation or Rapamycin treatment was not very strong under the experimental conditions used here, several Venus-LC3 puncta could be observed. Finally, inhibition of the autophagic flux by NH<sub>4</sub>Cl did provide proof that these puncta indeed were autophagosomes.

Next several cloning steps were performed to generate the 5'-entry plasmid. The CMV promoter was replaced by 4xUAS sites, which have a shuffled consensus sequence to avoid

epigenetic silencing common to repetitive DNA. Then, the [4xUAS-mitoTagRFP-T2A-Venus-LC3] module was cloned into the 5'-entry vector (see Figure 15 and 21).

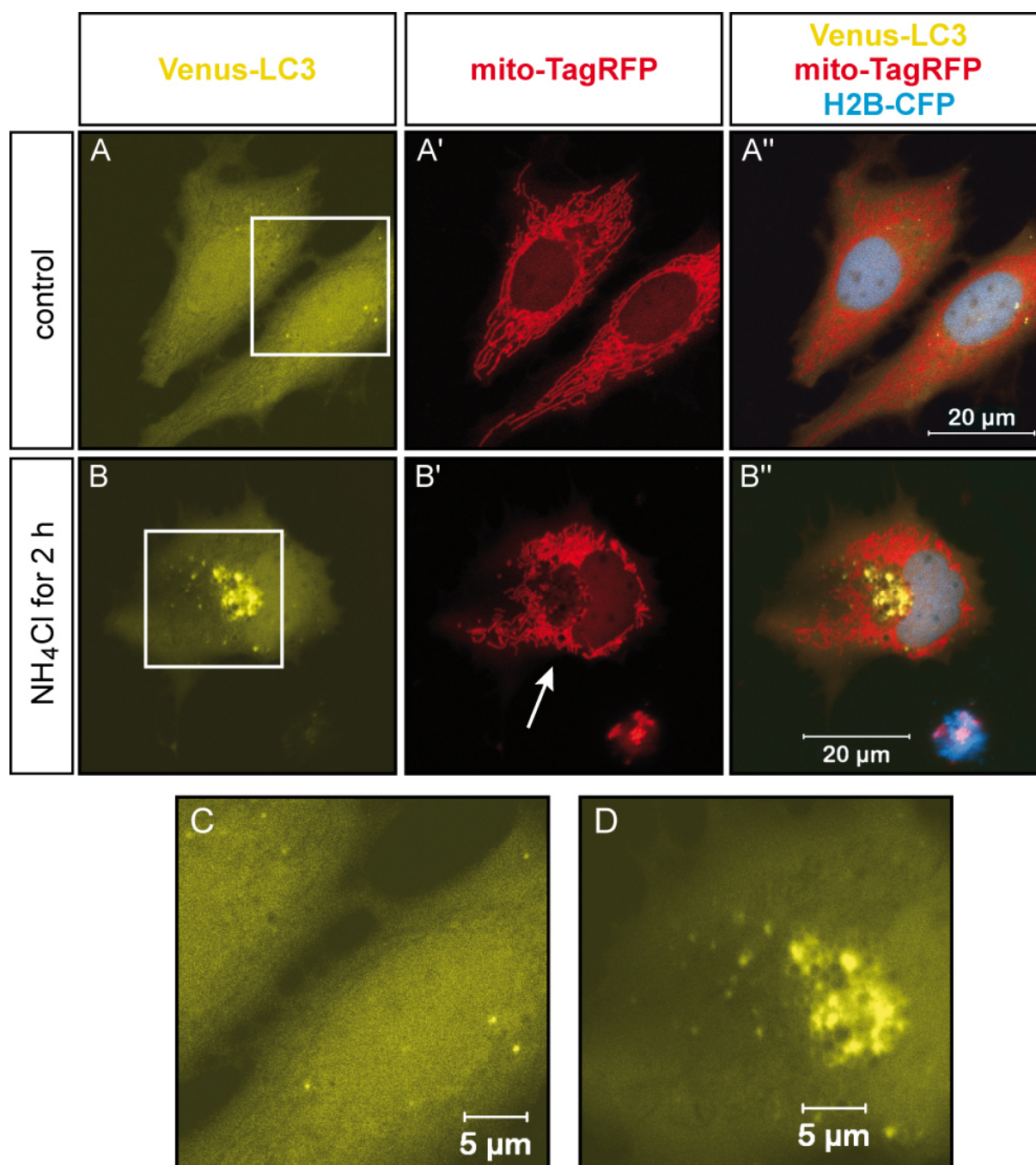


**Figure 19. The lysosomal inhibitor ammonium chloride halts the autophagic flow, which leads to an accumulation of autophagosomes.** Pac2 cells transfected with the mito-TagRFP-T2A-Venus-LC3-encoding expression plasmid and a vector expressing H2B-CFP were treated with 50 mM  $\text{NH}_4\text{Cl}$  or left untreated. Images of the fluorescent reporters were recorded by confocal microscopy. **A-A''** A few small Venus-LC3 puncta (i.e. autophagosomes) are visible in untreated cells. **B-B''** A massive accumulation of autophagosomes close to the nucleus is evident 2 hours after addition of ammonium chloride to the medium. Vacuolization of the cytoplasm as evident by fluorescent protein-free spots (“holes”), indicated by an arrow in (B'), is characteristic for this treatment. **C** and **D** Close-up views of the same cells as shown in A and B (white boxes), respectively, highlight the autophagosomal phenotypes.

### 3.2.2.3. Human *LRRK2* alleles are expressed as CFP-tagged fusion proteins

Three human *LRRK2* sequences, encoding wild-type LRRK2, the PD-linked G2019S mutant and the kinase-dead mutant K1906M, were provided by Dr. Johannes Gloeckner as Strep-tagged and CFP-tagged ORFs in eukaryotic expression vectors, depicted in Figure 20A. The tandem Strep tag II allows purification of the fusion protein together with possible interaction partners via streptavidin affinity chromatography (Skerra, 2003). This strategy could be used to further dissect LRRK2-containing multi-protein complexes in future experiments.

It should be noted that *LRRK2* sequences are prone to rearrangements when amplified in a normal DH5 $\alpha$  *E. coli* strain (information provided by J. Gloeckner and personal observation). To avoid these problems a recombination-defective *E. coli* strain (Stbl3, Invitrogen) was used for all *LRRK2* cloning steps and bacterial cultures were grown at a lower temperature of 30°C, a condition which additionally reduces the recombination activity of *E. coli*.

When Pac2 cells were transfected with the LRRK2-encoding expression vectors, cytoplasmic CFP staining could be detected by confocal microscopy in transfected cells (Figure 20B). LRRK2 protein synthesis was additionally analysed in transfected HEK293T cells by Western blotting of cell lysates, as shown in Figure 20C. The antibody used was a custom-made polyclonal anti-human LRRK2 antibody provided by the M. Üffing lab (Helmholtz Center; Gloeckner *et al.*, 2009). It specifically detected a protein band with a molecular weight of over 250 kDa (calculated molecular weight of LRRK2 is 286 kDa), which clearly was visible in LRRK2-expressing cell lysates only. Some unspecific binding to proteins of lower molecular weight could be observed. The human embryonic kidney cell line used for this analysis does not express endogenous LRRK2 protein (Biskup and West, 2009), and the faint band in the non-transfected control lane might represent carry-over of sample from the LRRK2-expressing lysate or might represent unspecific binding.

Next these ORFs encoding LRRK2-Strep-CFP fusion proteins were brought under control of 4xUAS(shuffled) regulatory sequences, and were subsequently cloned into the modified 3'-entry vector, p3E-modifiedMCS-polyA (see Figures 15 and 21).

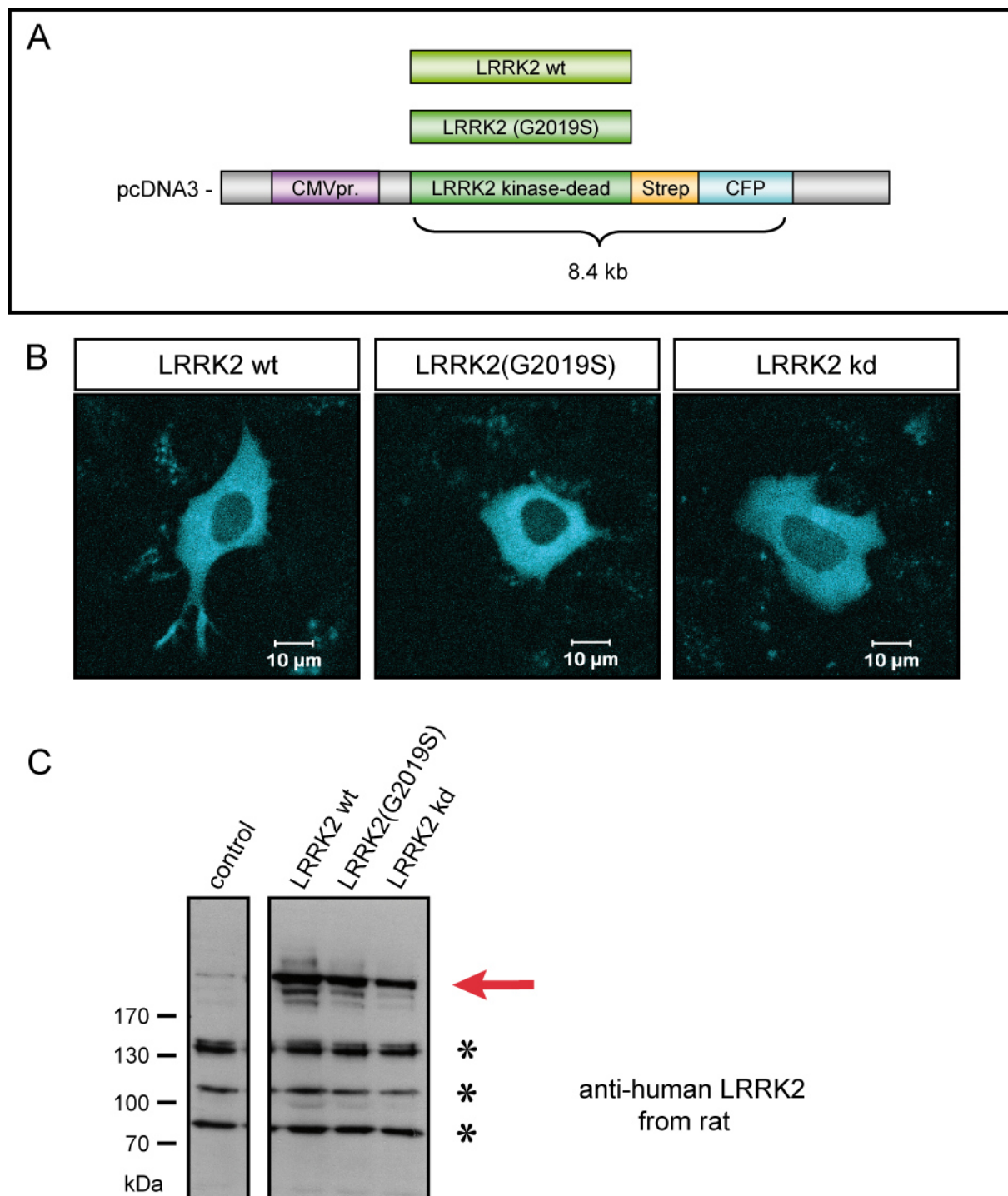
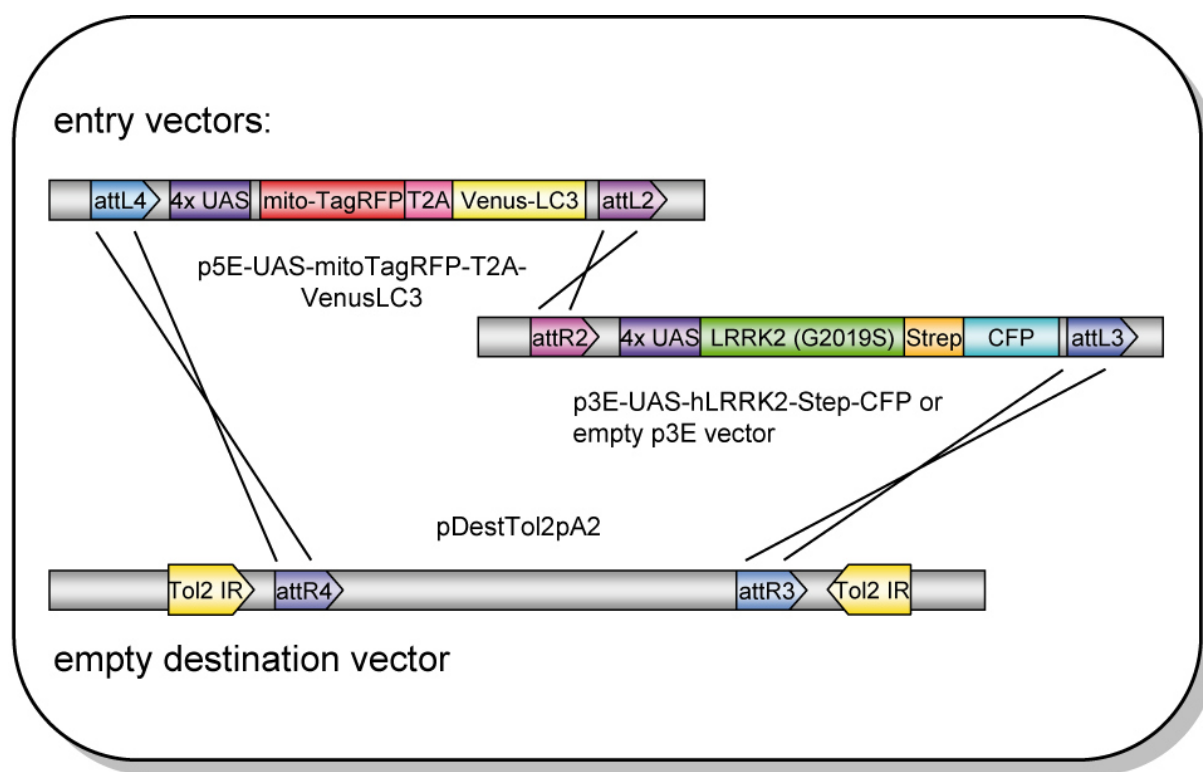


**Figure 20. LRRK2 is tagged with the Strep-tag for protein purification and with CFP for fluorescent detection.** **A** Expression constructs for three human LRRK2 variants, wild-type, PD-linked G2019S and the kinase-dead mutant K1906M, were provided by Dr. J. Gloeckner. Proteins are C-terminally fused to the tandem Strep-tag II peptide sequence (2x WSHPQFEK) to facilitate purification. Additionally, they are fused to CFP. **B** A cytoplasmic CFP signal is visible in transfected Pac2 cells for each of the three expression vectors. **C** Expression of the fusion proteins is also detectable by Western blotting with cell lysates from transfected HEK293T cells; the LRRK2 band is marked by a red arrow. The control culture was non-transfected. A polyclonal rat anti-human LRRK2 antibody was used (provided by the M. Üffing lab). Unspecific bands of lower molecular weight are indicated by asterisks and demonstrate equal loading of lysates. Abbreviations: kb, kilo bases; kd, kinase-dead; wt, wild-type.

### 3.2.2.4. Combining fluorescent markers and disease gene in the final destination vectors

With the 5'- and 3'-entry vectors ready and containing the two effector functions: subcellular fluorescent tags and the disease gene *LRRK2*, these could now be combined into one expression vector. The LR clonase enzyme (Invitrogen) was used to catalyse the site-specific recombination between all three pairs of compatible attL and attR sites of the two entry vectors and the empty destination vector in a one-step reaction. The two transgene cassettes were thereby combined in the final destination or effector plasmids (Figure 21).



one of four completed effector constructs:

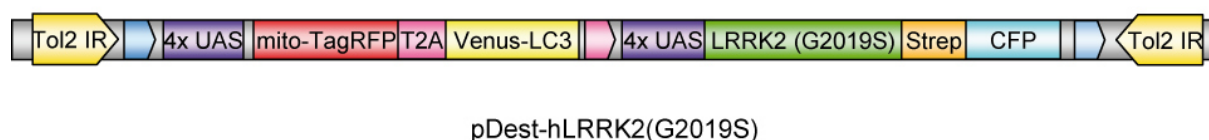


**Figure 21. Generation of the final effector constructs.** Four different effector plasmids were created by site-specific recombination reactions of the Gateway system, whereby DNA sequences inserted into two entry plasmids are combined in a defined order and orientation in the target destination vector. The resulting effector constructs allow expression of fluorescent markers to label mitochondria and autophagosomes, as well as the disease-linked gene *LRRK2* (one of three different alleles: wt, G2019S, and kinase-dead); another control vector is without *LRRK2* sequence. Only one vector is depicted here. Expression of the two ORFs is controlled by 4xUAS Gal4-binding sites. The sequence between Tol2-recognition sites (Tol2 IR) can become integrated into the zebrafish genome.

Four different effector plasmids were generated containing one of three different *LRRK2* sequences or the fluorescent reporter cassette only. Tol2 recognition sites flanking the effector cassette allow for its genomic integration in the presence of transposase activity.

As it is known that *LRRK2* sequences are prone to rearrangements during amplification, the 7581 bp ORFs of all three *LRRK2* alleles were verified by sequence analysis with a set of 19 primers (see Material and Methods). Indeed, a sequence rearrangement was identified in one of the clones, and the correct sequence had to be retrieved and confirmed by re-sequencing.

#### 3.2.2.5. Detection of expression of the three transgenes in cell culture and *in vivo*

The two reporter proteins to label subcellular structures were expressed from these four destination constructs as determined by confocal microscopy of transfected Pac2 cells. This is shown in Figure 22. Mitochondria appeared as highly interconnected network of uniform tubular structures. Venus-LC3 is a cytoplasmic protein and also seems to enter the nucleus. During autophagy LC3 is attached to the lipid phosphatidyl-ethanolamine and associates with autophagosomal membranes. A few autophagosomes were visible as bright-yellow spots in most of the transfected cells in these cultures at three days after plating and change of medium. Expression of human *LRRK2*-Strep-CFP was too weak to be detectable by fluorescence microscopy, where faint autofluorescence of cells in the blue to cyan spectral range was visible (data not shown). Its expression could also not be detected by confocal microscopy. The “CFP signal” shown in Fig. 22I-L was recorded with a highly amplified detection mode of the confocal microscope and seems to represent bleach-through of Venus fluorescence in the CFP channel because cells in Fig. 22L, which do not express *LRRK2*-CFP, seem to have a similar “CFP expression” level as the other *LRRK2*-expressing cells – compare images in Figure 22I-L. As an alternative method to detect *LRRK2* protein, Western blots were prepared with cell lysates from transfected HEK293T cells – a cell line well-suited for high-level expression of heterologous proteins. Western blots from two independent experiments are shown in Figure 23. The newly-available anti-human *LRRK2* antibody, MJFF#2 (developed by the Michael J. Fox foundation), was used, which at the moment is the most efficient antibody to detect human and mouse *LRRK2*. *LRRK2*-Strep-CFP was again efficiently expressed from the pcDNA3 vectors, as has been observed previously (Figure 20C). Expression from pDest plasmids clearly was detectable but was much weaker than from pcDNA3 vectors, as shown in Figure 23A and C. One reason for the different expression levels can be the indirect expression mode via Gal4 and UAS sites in the first

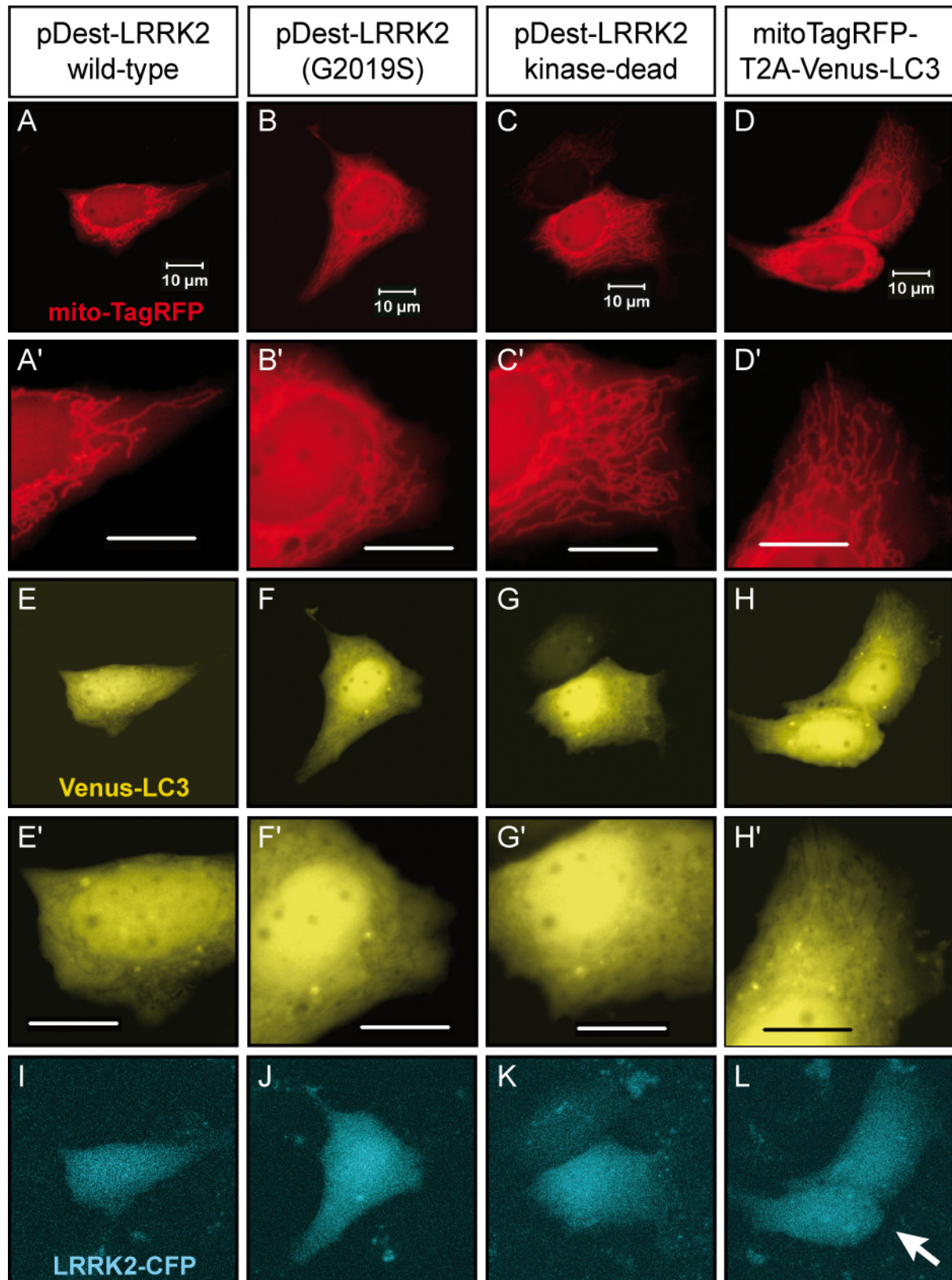


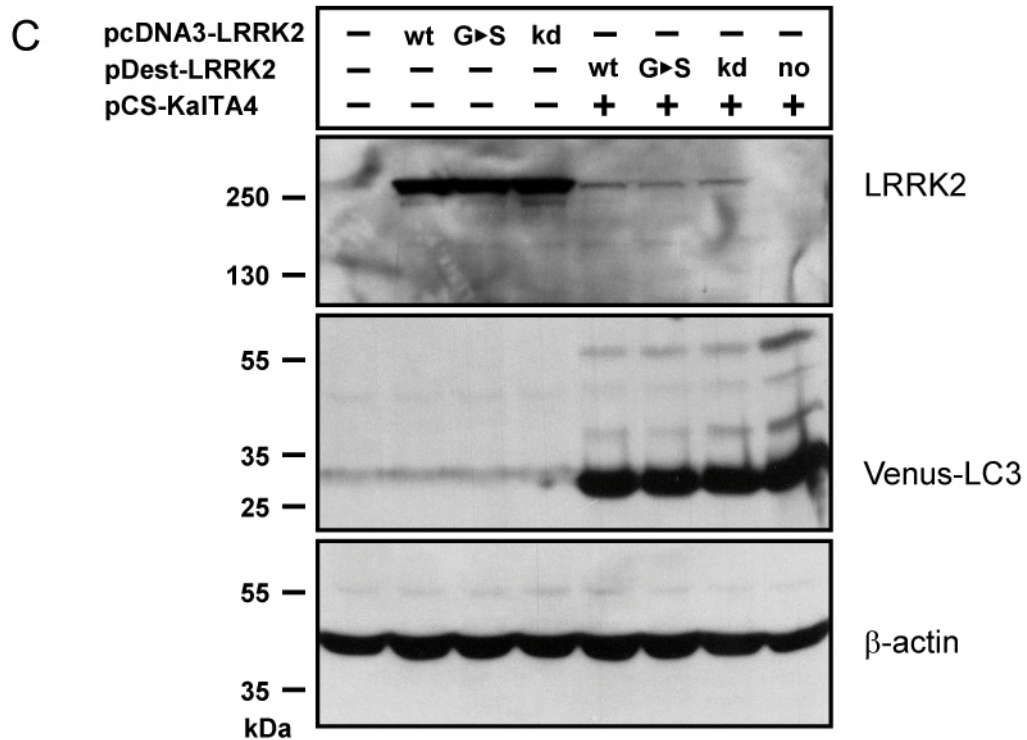
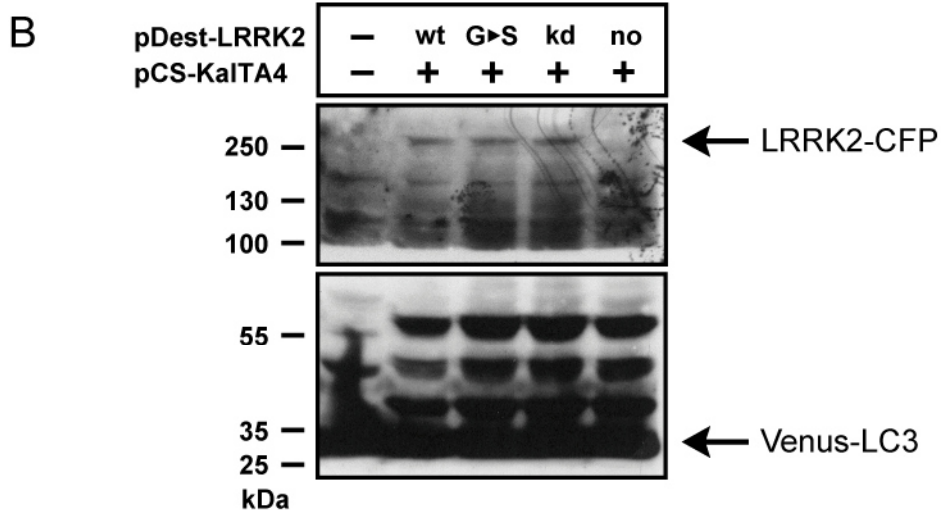
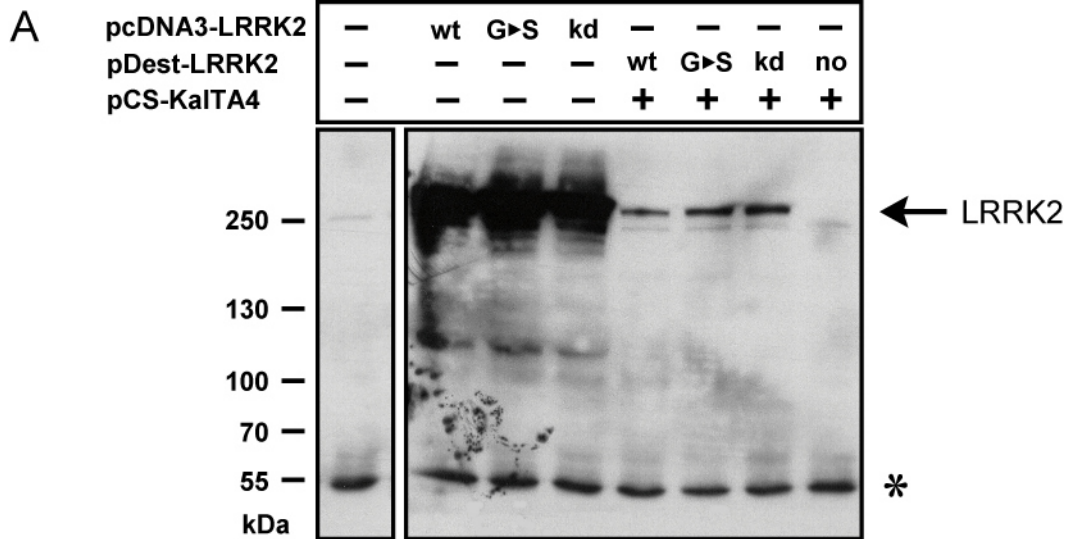
**Figure 22.** Mito-TagRFP and Venus-LC3 are expressed from the tri-functional effector constructs, while LRRK2-CFP cannot be detected by confocal microscopy. Pac2 cells were co-transfected with the destination plasmid, as indicated, plus the Gal4-expressing plasmid pCS-KalTA4 to activate transcription of UAS-regulated genes. **A-D'** Mito-TagRFP is targeted to mitochondria, which appear as a highly-interconnected and uniformly-tubular network. **E-H'** Venus-LC3 shows diffuse cytoplasmic staining and is not excluded from the nucleus. A few autophagosomes are visible as small, bright-yellow dots in the cytoplasm under normal growth conditions. **I-L** CFP was recorded

with strongly-enhanced detection mode, which was kept constant for all recordings. The arrow in (L) points to a “CFP signal” in the absence of LRRK2-CFP expression and might represent bleed-through of Venus fluorescence in the CFP channel or autofluorescence. I-K. Scale bars, 10  $\mu$ m.

**Figure 23 (next page). LRRK2 protein is expressed from the three destination vectors in cell culture.** HEK293T cells were transfected with the indicated plasmids and cell lysates were analysed by immunoblotting. **A** LRRK2 is expressed at low levels from the pDest vectors compared to the pcDNA3 expression vectors, as detected by the MJFF#2 anti-LRRK2 antibody. The unspecifically-stained band, marked by an asterisk, confirms equal loading of lysates. **B** Venus-LC3 is expressed at a higher level from the same construct than LRRK2-CFP. Protein lysates were from the same experiment as in (A) and were analysed with an anti-GFP antibody, which detects both CFP and Venus. Incubation time for signal detection was 30 min for the upper blot and 10 min for the lower blot. **C** A repeated experiment confirmed the different expression levels of effector proteins. Cell lysates of an independent transfection experiment were analysed with anti-LRRK2 (upper panel) or anti-GFP (middle panel) antibodies. The blot probed with an anti-beta actin antibody (lower panel) serves as loading control. Detection time for the ECL signal was 10 min for the anti-LRRK2 blot and 2 min each for the anti-GFP and anti-beta actin blot. Abbreviations: wt, wild-type; G>S, G2019S mutant; kd, kinase-dead; no, control pDest vector without LRRK2.

instance, compared to direct expression by the strong CMV promoter in the second case. Additionally, it seemed to be the case that the two expression units of the effector construct, both regulated by 4xUAS(shuffled) sites, were not expressed to the same level. CFP and Venus are both derived from GFP (Tsien, 1998; Nagai *et al.*, 2002) and can be detected with an anti-GFP antibody, see Figure 23B and C. However, if one compares the upper and lower panels of Fig. 23B, which were probed with the same anti-GFP antibody, it can be observed that the Venus-LC3 protein level is much higher than LRRK2-CFP. Of note, Venus-LC3, which has a calculated Mw of 42 kDa, was running below 35 kDa on Tris-glycine gels and is detectable at the very bottom of this blot. Compare also protein levels of LRRK2 and Venus-LC3 in Figure 23C. To conclude these expression analyses, it can be stated that the disease gene is expressed but at a low detectable protein level. And it was not clear from these experiments if the amount of LRRK2 would be sufficient to induce a detectable and potentially neuro-toxic phenotype *in vivo*.

The final destination plasmids were next tested *in vivo* by injection into fertilized eggs of a Gal4-expressing driver line, either *Tg(her3:KalTA4)* or the newly-established *Tg(NBT:H2B-TagBFP-T2A-KalTA3)*. Mosaic expression of the effector construct in individual hindbrain neurons of injected *Tg(her3:KalTA4)* larvae could be observed by confocal microscopy. As shown in Figure 24, a strong and homogeneous cytoplasmic Venus-LC3 signal was visible with few puncta corresponding to autophagosomes. At the same time the elaborate mitochondrial network was visualized by mito-TagRFP. Both fluorescent proteins were coexpressed and targeted to their respective subcellular structures in all transgene-expressing



neurons, indicating that the T2A-mediated self-processing of the nascent protein was efficient not only in cell culture but also *in vivo*. Although the absolute expression level did vary between neurons, the protein ratio between mito-TagRFP and Venus-LC3 was at a constant 1:1 ratio due to this mode of coexpression.

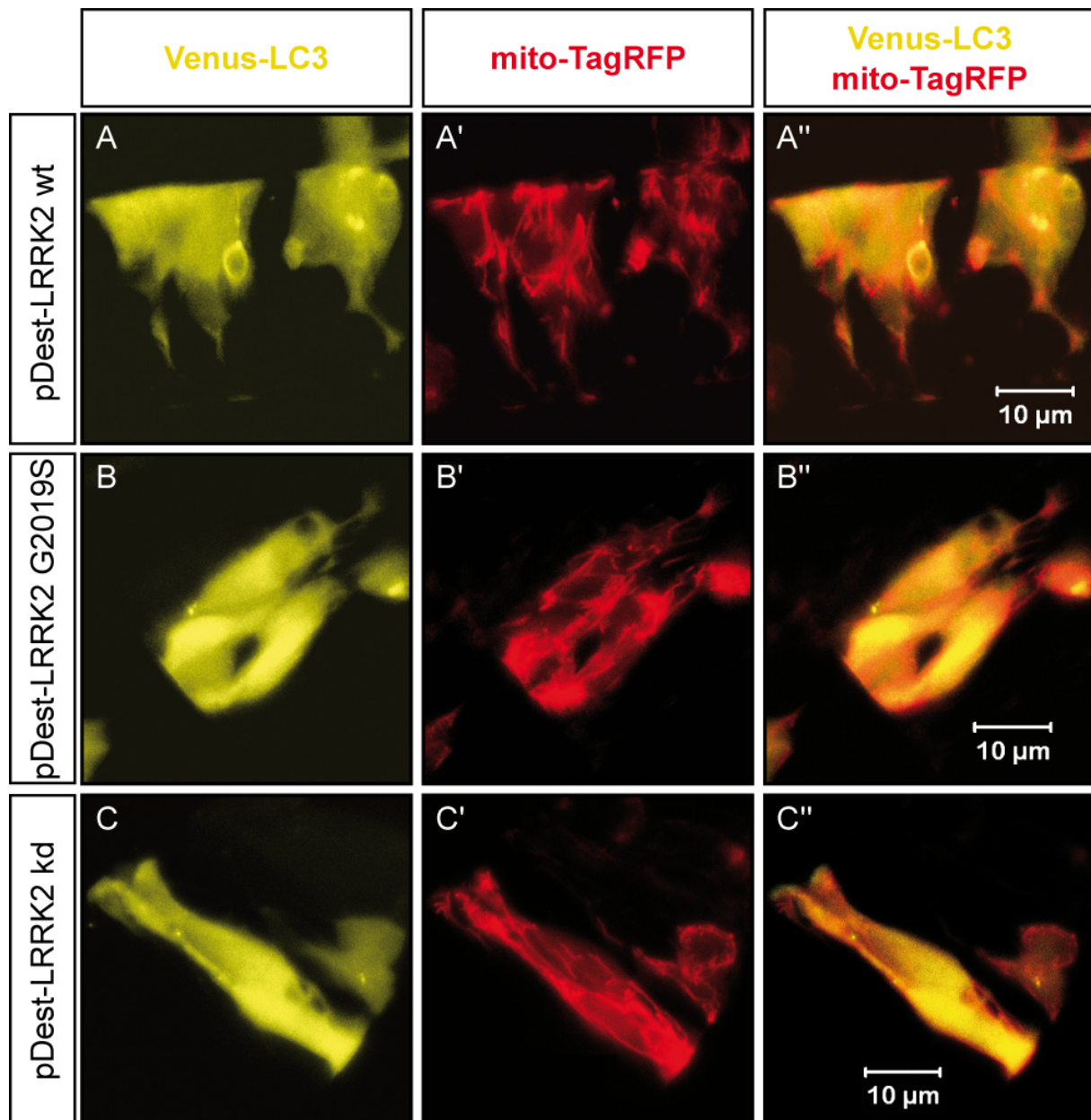


**Figure 24. Mito-TagRFP and Venus-LC3 label the respective subcellular structures in neurons *in vivo* when expressed from the effector constructs.** The LRRK2-containing destination plasmids were injected into one-cell stage embryos of *Tg(her3:KalTA4)*, as indicated. Zebrafish larvae at 32 hpf were observed by confocal microscopy. **A, B, C** A diffuse cytoplasmic Venus-LC3 staining with only few autophagic vesicles is visible in hindbrain neurons. **A', B', C'** The mitochondrial network is tagged by mito-TagRFP in the same neurons that express Venus-LC3. **A'' to C''** A merge of both fluorescence signals is shown.

### 3.2.2.6. Initiating the generation of transgenic effector lines

The four pDest effector constructs, which had been shown to be functional, were subsequently used to generate transgenic fish lines by coinjecting each of the plasmids together with mRNA encoding Tol2 transposase into one-cell stage wild-type embryos. As the FPs are only expressed in the presence of Gal4, adult injected fish (P or F0 generation) had to be crossed to a driver line, i.e. *Tg(her3:KalTA4)*, in order to detect transgene carriers. Within screening clutches only few double-transgenic larvae could be observed, and these exhibited a very weak TagRFP signal, which was difficult to detect by eye on a fluorescence stereo microscope (not shown). Because of the time-intensive screening and crossing procedure, effector lines could not be established in the course of this study.

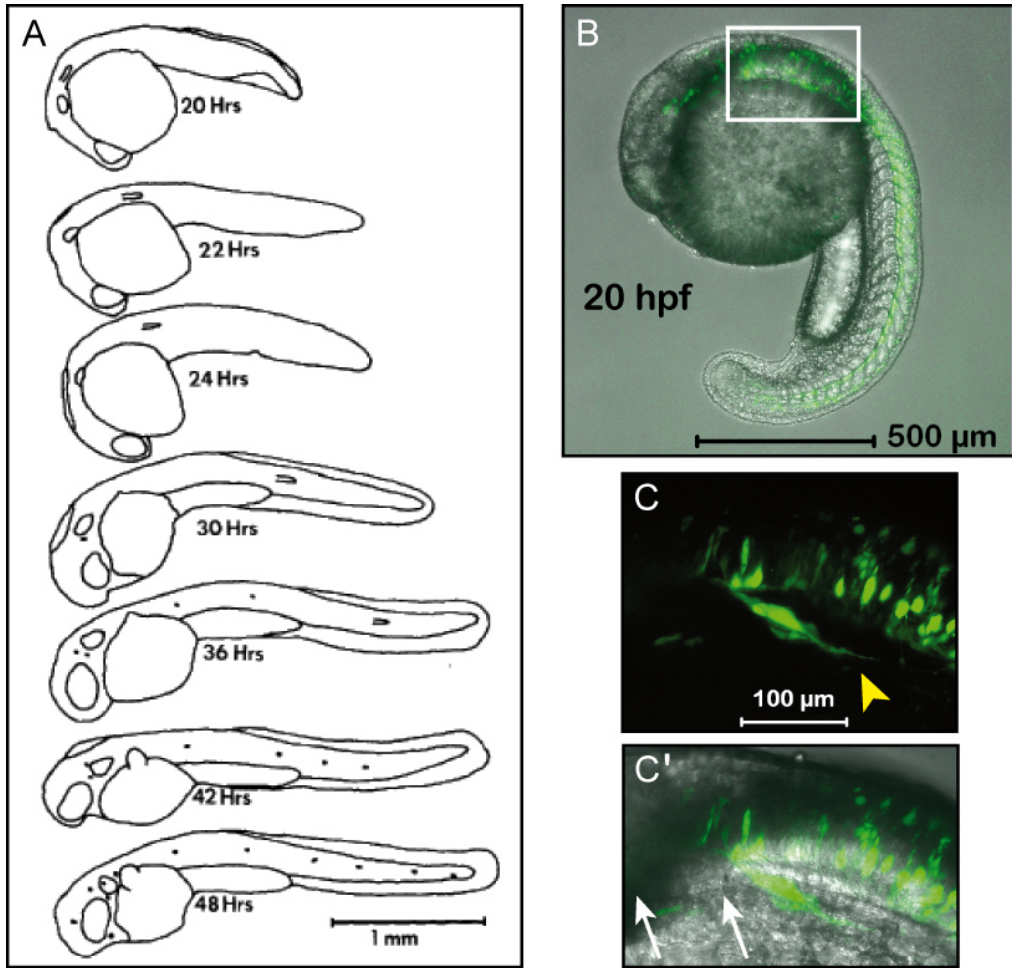
In the meantime, a transient transgenic experimental strategy could be established. Effector constructs were injected directly into eggs of the NBT promoter-containing neuronal driver line *Tg(NBT:H2B-TagBFP-T2A-KalTA3)* and larvae were analysed by confocal microscopy a few days post injection. These plasmid injection experiments have the advantage of a mosaic distribution and expression of the effector construct in a limited number and sparse distribution of neurons – which is ideally suited to image mitochondrial axonal transport in single or few labelled neurons.

### 3.3. Imaging Mitochondrial Axonal Transport *in vivo* in the Posterior Lateral Line Nerve

#### 3.3.1. Choosing a driver line to label suitable neurons for axonal imaging

As stable effector lines of our disease model were not readily available in the course of this project, we decided to follow a transient transgenic approach. We generated LRRK2-expressing larvae for *in vivo* imaging by injecting pDest constructs together with Tol2 mRNA into one-cell stage embryos of a suitable driver line. Two neuronal driver lines were available and had to be evaluated: *Tg(her3:KalTA4)* and the newly established line *Tg(NBT:H2B-TagBFP-T2A-KalTA3)*. In order to image mitochondrial axonal transport, a suitable neuronal type had to be identified, and the following criteria had to be fulfilled: (1) The effector construct had to be expressed in reproducibly labelled and identifiable neurons as the same neuronal type has to be used in several independent experiments. (2) The selected neuronal type should be differentiated, connected to its target cells and be functionally mature, and the developmental stage of the embryo had to be chosen accordingly. In the beginning, we focussed on motoneurons as these are one of the earliest differentiating neurons and they can be easily identified along the rostro-caudal body axis. They first appear at around 19-20 hpf. Differentiation of the three types of primary motoneurons is well documented in the literature (Eisen *et al.*, 1986; Myers *et al.*, 1986). They appear in a segmental pattern and can be unequivocally identified by location and axonal branching pattern. Motoneurons were labelled in both transgenic driver lines when crossed to the UAS-GFP reporter line. However, it became clear that the prominently visible axonal trees of motoneurons are strongly tangentially bent (i.e. from dorsal to lateral to ventral) so that it was not possible to bring a section of the axon into one imaging plane. Taking z-stacks during confocal recordings was not an option as image acquisition had to be fast (1-3 seconds between frames). Additionally, repeated recordings could induce photodamage of the tissue. (3) Therefore, another criterion for optimal imaging of axonal transport was the straightness of the axon.

A characteristic group of neurons that fulfill these criteria were stained in the NBT promotor-containing line – the posterior lateral line neurons (PLL). These afferent neurons deliver mechano-sensory input from clusters of hair cells, so-called neuromasts, for processing into the hindbrain. The PLL neurons had been identified previously, when the newly-generated driver line was characterized (see Chapter 3.2.1.4, Figures 13 and 14). When during embryonic development do these neurons differentiate and can be used for imaging? The primary posterior lateral line system consists of six to eight neuromasts which are positioned along the midline of the embryo and which are connected to the PLL nerve during the second



*Tg(NBT:H2B-TagBFP-T2A-KalTA3)* crossed to *Tg(UAS:GFP)*

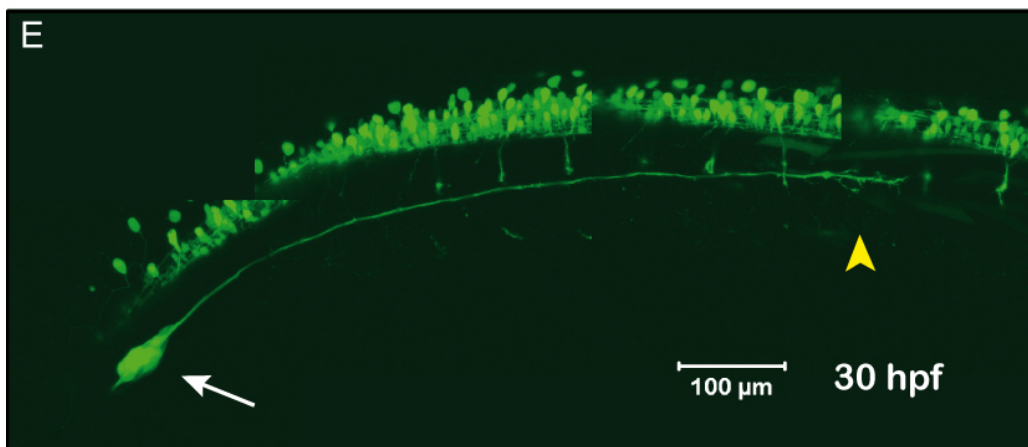
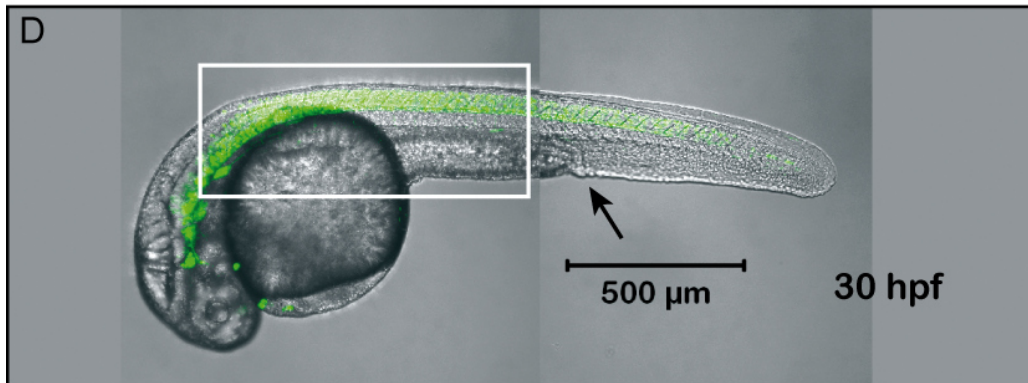


**Figure 25. Outgrowth and differentiation of the posterior lateral line nerve is taking place between 20 and 48 hpf.** **A** Leading axons of PLL neurons are growing together with the lateral line primordium, which is migrating caudally along the lateral side of the embryo between 20 and 36 hpf. The primordium deposits cell clusters along its path that will differentiate into neuromasts. These sensory organs contain hair cells for the detection of changes in water current as well as accessory cells. At the end of embryogenesis, 6 to 8 neuromasts are detectable and are depicted as small dots in this schematic drawing (adapted from Metcalfe, 1985). **B** An overview of an embryo from a cross between *Tg(NBT:H2B-TagBFP-T2A-KalTA3)* and *Tg(UAS:GFP)* is shown at 20 hpf, the time when the primordium has not started to migrate. **C, C'** An emerging axon of a PLL neuron is marked by a yellow arrowhead (enlarged view of the boxed area in image B). The position of the otic vesicle is indicated by white arrows. **D** An overview of an embryo at 30 hpf is depicted when the primordium has reached the location of the vent (black arrow). The primordium is not stained in this transgenic line. **E** The PLL nerve and its axonal growth cones (yellow arrowhead) at 30 hpf. Neuronal somata are located in the PLL ganglion (white arrow). This image corresponds to the boxed area in D.

day of embryonic development. The so-called PLL primordium, a cluster of dividing and differentiating cells, is migrating caudally along the midbody line of the embryo between 20 and 40 hpf. It deposits the cell clusters of the neuromasts during this migration (Ghysen and Dambly-Chaudière, 2007). PLL sensory neurons mature during the same period and the leading growth cones of peripheral axons comigrate with the primordium (Metcalfe, 1985; Gilmour *et al.*, 2004). The development of the PLL system could be observed in embryos and larvae of a cross between *Tg(NBT:H2B-TagBFP-T2A-KalTA3)* and the UAS-GFP effector line (Figure 25). At 20 hpf the primordium is visible for the first time in the postauditory region (Figure 25A) but its cells are not stained by the neuron-specific driver construct as they are non-neuronal. The first outgrowing axon of a PLL neuron is visible in a 20 hpf embryo, as shown in images 25B, C and C'. The axon grows together with the migrating primordium and at 30 hpf the most advanced growth cones are located close to the vent, while the somata of all neurons are positioned in the PLL ganglion close to the otic vesicle (Figure 25D and E). It has been reported by Metcalfe (1985) that by 42 hpf the primordium has reached the base of the caudal fin and is no longer visible. By 48 hpf the six primary neuromasts are differentiated and PLL axons are connected to their target hair cells. Thus imaging of axonal transport in mature neurons should be achieved after 48 hpf. It has been described in the literature that some remodeling of the PLL system (nerve and neuromasts) is taking place around this time of development, e.g. the nerve repositions from the epidermis across the basement membrane into the subepidermal space (Raphael *et al.*, 2010). Imaging mitochondria within PLL axons was, therefore, evaluated experimentally in transiently transgenic larvae after 2 days and 3 days of development. Individual axons within this nerve were found to be straighter at 2 dpf than at 3 dpf (data not shown) and could thus be better

recorded in one imaging plane. This phenomenon might be connected to myelination of individual axons by Schwann cells, which occurs around this time of development (Voas *et al.*, 2009; Raphael *et al.*, 2010).

Additionally, it was observed that in embryos, injected with the effector construct, usually only one or a few axons of the nerve were labelled, which was optimal for resolving individual mitochondria. In order to allow for reproducible data acquisition during repeated experiments, in a next step, parameters that could increase variability of the system had to be identified and standardized.

### 3.3.2. Optimizing parameters for reproducible image and data acquisition

We wanted to observe and quantitatively analyse the subcellular process of axonal mitochondrial transport in living zebrafish larvae under the influence of the expression of different alleles of the Parkinson's disease gene *LRRK2*. To minimize variability between experiments, critical parameters were identified and a standard imaging procedure was established:

- (1) The temperature during imaging was kept constant by preheating the imaging dish containing agarose-embedded embryos and a fixed volume of buffer at 28.5°C before imaging. Three embryos were embedded per dish to keep imaging times short and temperature changes at a minimum.
- (2) As mentioned in the previous paragraph, the optimal developmental stage for imaging axons of the PLL nerve was identified to be shortly after 48 hpf – a time point when individual axons run most straight.
- (3) To detect mitoTagRFP fluorescence in a single or few PLL neurons of injected larvae, these had to be screened by fluorescence microscopy. At the same time, larvae with morphological defects were observed, e.g. with mislocalized PLL axons or with defects in blood flow, and could be sorted out.
- (4) In order to discriminate between anterograde (from the soma to the synapse) and retrograde mitochondrial transport the embedding direction of the larvae had to be documented as directionality was not evident from time-lapse recordings, where a 56 µm stretch of the axon is visible.
- (5) The imaging position along the rostro-caudal axis of the nerve, which covers the whole distance from the ganglion in the head to the tip of the tail, should be kept constant. A good region, where the nerve runs straight and where larvae could be embedded in tight contact to

the bottom of the imaging chamber, was close to the vent. So, this position – shortly before, above, or shortly after the vent – was used for all time-lapse recordings.

(6) Next, the imaging settings on the confocal laser scanning microscope had to be optimized as photobleaching and phototoxicity caused by repeatedly exposing fluorescent proteins and cells to excitation light are main problems when observing mitochondria in living cells. Indeed, photobleaching of mitoTagRFP could be observed after repeated confocal scanning of transfected Pac2 cells (data not shown). Minimizing excitation light intensity and exposure time can reduce this photodamage. Laser intensity was reduced to 3% with still good mitochondrial fluorescence achieved for optimal detection. The scan time per frame was kept below 500 ms by scanning the sample once for each time point – no stack was recorded, no averaging over several scans could be done, and a limited area around the axon was captured. From observations of mitochondrial movement in the PLL nerve it was decided to record images every 2 s for a period of 10 min. These were 300 images per movie.

With these parameters a standardized experimental procedure was established, encompassing injection of pDest plasmids into fertilized eggs of *Tg(NBT:H2B-TagBFP-T2A-KalTA3)*, screening for labelled PLL axons in injected larvae at 48 hpf, subsequent embedding and time-lapse imaging with constant microscope settings (see Materials and Methods).

### **3.3.3. General observations about mitochondrial transport in PLL axons**

Repeated time-lapse recordings of mitochondrial transport were performed according to the standardized protocol described in the previous chapter. As summarized in Table 1, 26 recordings were captured from 18 control animals expressing the fluorescent reports only, and 16 movies were collected from 12 animals expressing human LRRK2(G2019S) in PLL neurons. Example movies for both conditions are available under Supplementary Material on a CD (Movie S1, S2 for the control condition and Movie S3, S4 of LRRK2(G2019S)-expressing neurons).

When directly observing the time-lapse recordings, it was evident that only few mitochondria were stationary, and most axonal mitochondria were engaged in active transport processes. Additionally, mitochondrial movement was not saltatory but quite constant and highly persistent in one direction, either anterograde or retrograde – with persistence of mitochondrial motility being defined as the period of ongoing transport in one direction without pausing or reversal of direction (De Vos and Sheetz, 2007). These observations are in contrast to what has been described in the literature mostly for cell culture experiments, where the majority

(60-85%) of mitochondria were stationary, and mitochondrial transport in axons was described as saltatory movement consisting of brief periods of rapid directed movement followed by longer stationary phases (Morris and Hollenbeck, 1995; De Vos *et al.*, 2003). Although transport velocities do vary between faster and slower tracks in our system, and transported mitochondria do pause, they usually resume their movement in the same direction. It could hardly ever be observed in any of the recordings that a moving mitochondrion was changing its transport direction within the axonal stretch in the field of view. However, this observation was not quantified in the course of this project.

no LRRK2			
	Number of animals	Designation of animals	Number of movies
Day 1	6	animal 1 to 6	6
Day 2	6	animal 7 to 12	9
Day 3	2	13, 14	4
Day 4	4	15 to 18	7
<b>Total numbers</b>	<b>18</b>	<b>animal 1 to 18</b>	<b>26</b>
LRRK2(G2019S)			
	Number of animals	Designation of animals	Number of movies
Day 1	3	animal 19, 20, 21	3
Day 2	3	animal 22, 23, 24	4
Day 3	3	animal 25, 26, 27	3
Day 4	2	animal 28, 29	4
Day 5	1	animal 30	2
<b>Total numbers</b>	<b>12</b>	<b>animal 19 to 30</b>	<b>16</b>

**Table 1. Available data sets of mitochondrial transport time-lapse recordings.** Time-lapse recordings were captured according to a standardized operating procedure in several independent experiments and for two experimental conditions: *Tg(NBT:H2B-TagBFP-T2A-KalTA3)* larvae at 2 dpf expressing either the injected control plasmid without *LRRK2*, pDest-mitoTagRFP-T2A-Venus-LC3, or the effector plasmid encoding human *LRRK2(G2019S)*. As can be deduced from the number of movies compared to the number of animals, in some cases the same PLL nerve has been imaged twice (in one case three times). For experiments highlighted in yellow the sizes of transported mitochondria were determined.

### 3.3.4. Establishing a method to quantify mitochondrial mobility

A commonly used method to extract mobility parameters out of time-lapse recordings is by generating kymographs (De Vos and Sheetz, 2007). A kymograph is a two-dimensional (x-position vs. time) representation of the three-dimensional data (x,y-position and time). Such a graph can be generated for axonal transport with the ImageJ software (created by W. Rasband, NIH, Bethesda, Maryland; <http://rsb.info.nih.gov/ij/>). Example kymographs for the two genetic experimental conditions are shown in Figure 26. Mitochondria moving in the anterograde direction are represented by a line with a negative slope, while a line with a positive slope represents mitochondria moving in the retrograde direction. Some mitochondria are stationary or show some back-and-forth flickering movement (vertical lines). No obvious differences are observable between kymographs from the two conditions. As a kymograph again is a graphic representation of mitochondrial mobility, further procedures have to be performed to extract quantitative and numerical data. Each line representing a moving mitochondrion has to be tracked with the ImageJ software. This was problematic. Especially retrogradely moving mitochondria were difficult to track as their movement was discontinuous with short periods of fast movement interrupted by slower phases and many pauses. In the same way their slopes in the kymograph are discontinuous (see Figure 26). Additionally, as soon as mitochondria moving in the same direction pass each other, it can no longer be determined which path on the kymograph belongs to which mitochondrion after the crossing. Short pauses and stops during movement, which might be only one pixel wide on the y-axis of the kymograph, will also be overlooked and included in the velocity calculations. Therefore, it was decided to determine mitochondrial velocities directly from the confocal time-lapse image files. All clearly identifiable transported mitochondria in movies for the two genetic conditions were tracked manually with tools from the microscope software (Figure 27). Velocities were calculated for periods of continuous movement only. Stops were not included. The distance travelled was determined and divided by the time elapsed during movement. In this way, velocities for 345 mitochondria moving in anterograde direction and 217 moving in retrograde direction were determined for the control condition. In case of embryos expressing LRRK2(G2019S), 204 mitochondria were evaluated moving anterogradely and 150 moving retrogradely. At a later stage during analysis, mitochondrial length measurements were included, and this data is available for about half of all movies (see Table 1).

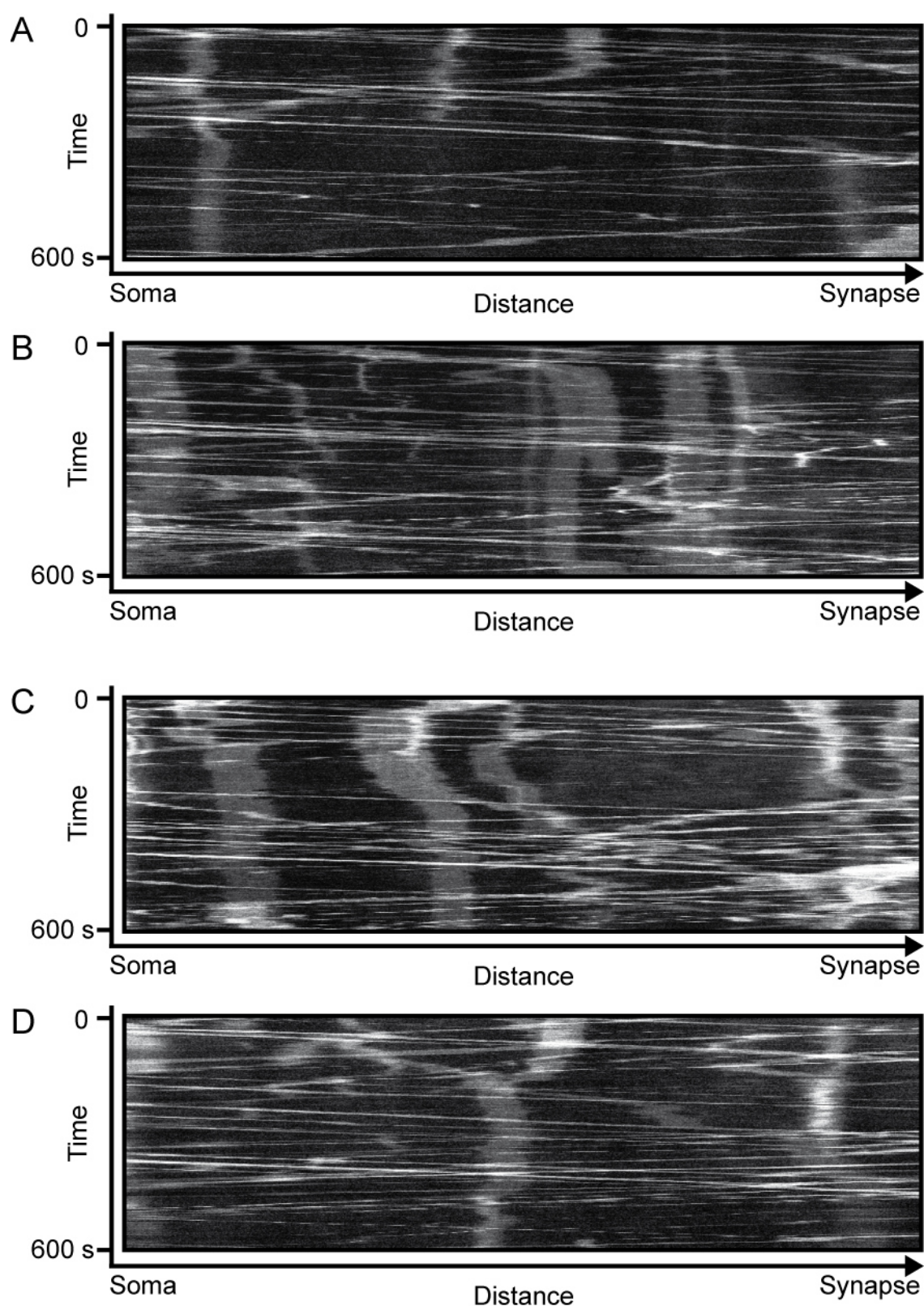


**Figure 26. Kymographs of mitochondrial axonal transport in the absence and presence of LRRK2(G2019S).** Kymographs were generated with the ImageJ software from 10 min time-lapse recordings of mitochondrial transport in PLL axons. **A, B** Kymographs are from embryos expressing the control effector plasmid (see Table 1; fish 10 and fish 16, respectively). **C, D** Kymographs are from larvae expressing LRRK2(G2019S) (see Table 1; fish 23 and fish 29, respectively). No gross differences between kymographs from the two different genetic conditions are evident.

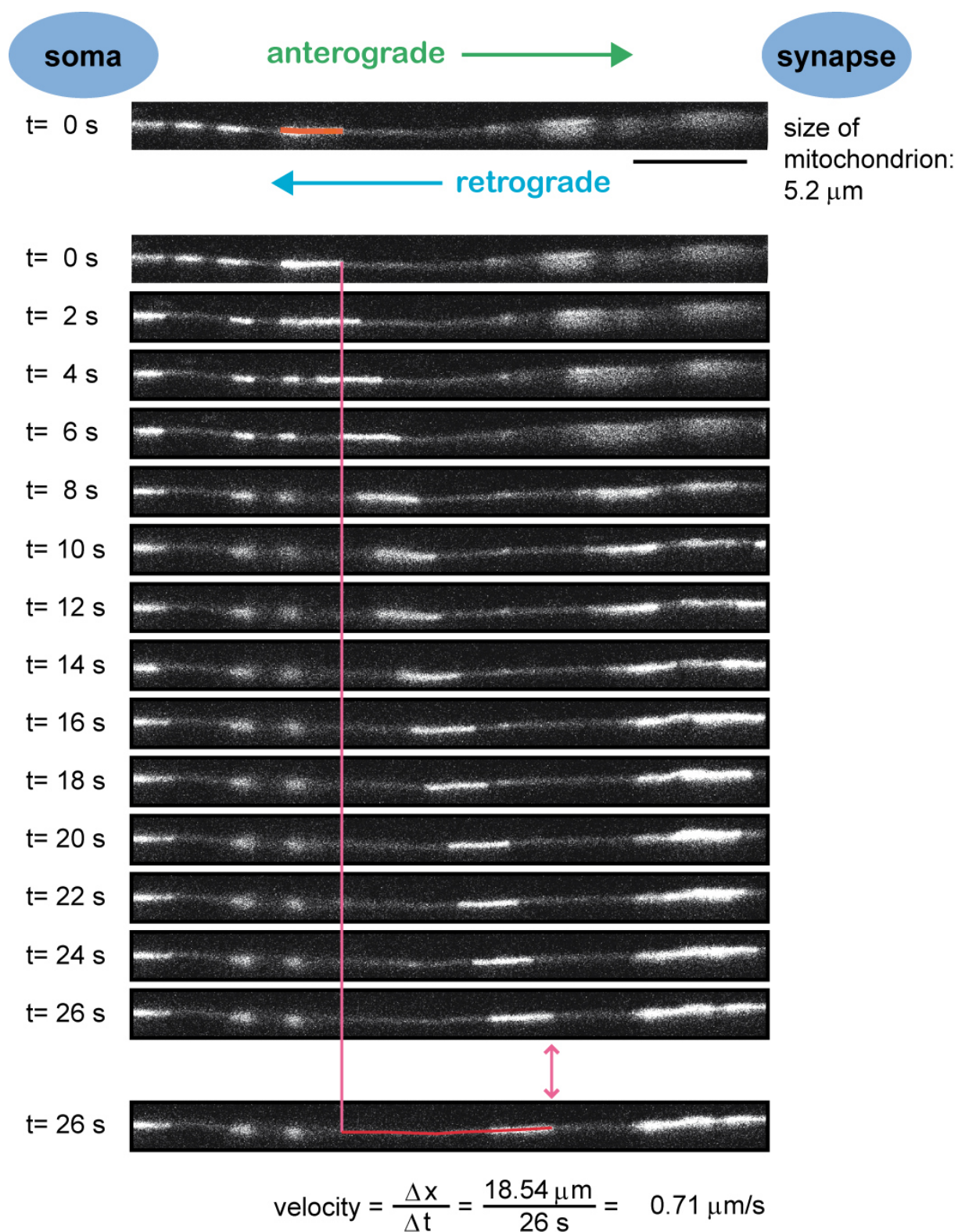


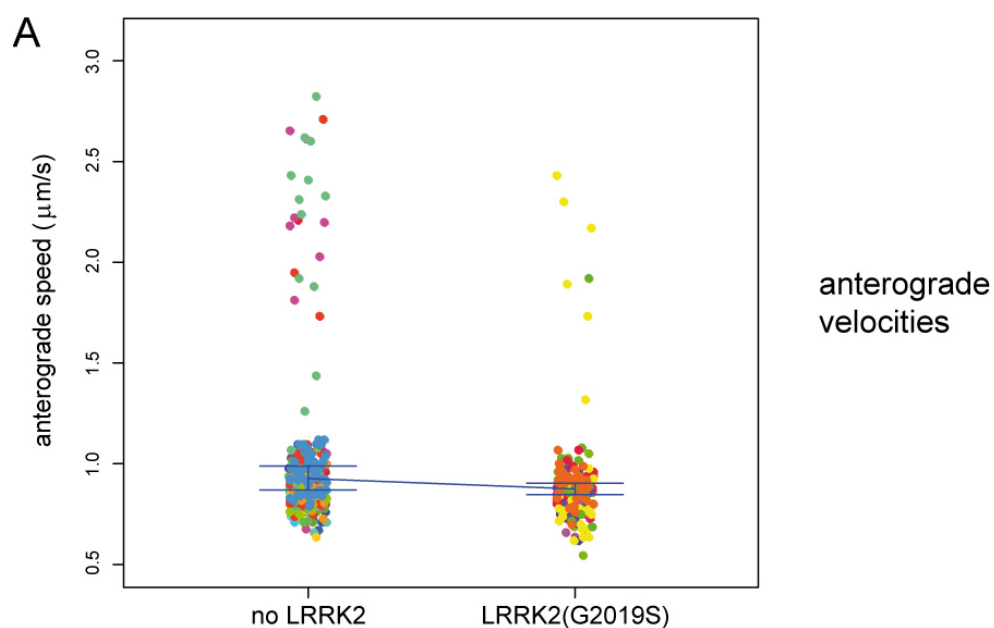
**Figure 27. Mitochondrial velocities were directly determined from time-lapse recordings.**

Each clearly identifiable moving mitochondrion was tracked within the confocal image series using LSM software tools. To determine velocity, a sequence of continuous movement without pausing was selected. Velocity was calculated as the distance travelled over a number of frames divided by the time elapsed. An example of an anterogradely transported mitochondrion is shown. The calculated velocity is 0.71  $\mu\text{m}$  per second. The distance travelled is tracked by a red line in the lower image and is 18.54  $\mu\text{m}$ . The length of this mitochondrion (marked in orange in the upper image) is 5.2  $\mu\text{m}$ . Black scale bar at t= 0, 10  $\mu\text{m}$ .

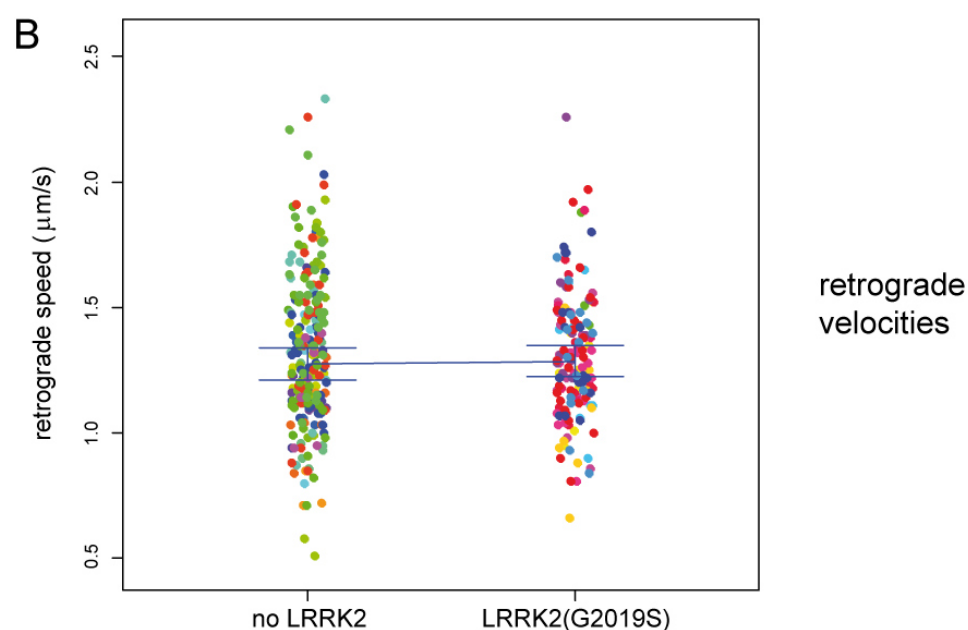
### 3.3.5. LRRK2(G2019S) does not affect mitochondrial transport *in vivo*

Transport velocities of mitochondria in the posterior lateral line nerve have been determined for several independent experiments and for the two experimental conditions: in the absence and presence of transient transgenic expression of the human disease gene *LRRK2(G2019S)*. Anterograde and retrograde transport have to be evaluated separately as they are mechanistically distinct processes regulated by different molecular machineries. For anterograde transport, velocity values in the range of 0.64 to 2.82  $\mu\text{m/s}$ , in the absence of human LRRK2 expression, and between 0.55 and 2.43  $\mu\text{m/s}$ , in the presence of LRRK2(G2019S) expression, could be detected (Figure 28A). Retrograde velocities were distributed between a minimal value of 0.51  $\mu\text{m/s}$  and a maximal value of 2.33  $\mu\text{m/s}$ , in the absence of the disease gene, and between 0.66 and 2.26  $\mu\text{m/s}$ , in axons expressing the LRRK2(G2019S) sequence (Figure 28B). It is evident that the range between minimal and maximal velocity values is very similar for both transport directions and for each of the two transgenic expression conditions. For a statistical evaluation of the data it has to be considered that velocities determined from the same time-lapse recording (i.e. from one animal) represent dependent or clustered data. Mixed-effects models constitute a suitable statistical tool to analyse such clustered data sets. Analysis was performed by T. Faus-Keßler (Helmholtz Zentrum; see Materials and Methods). For anterograde transport a geometric mean value of 0.929  $\mu\text{m/s}$  (95% confidence interval 0.871-0.989  $\mu\text{m/s}$ ; n= 345) was obtained in the absence of exogenous LRRK2 expression, as shown in Figure 28A. Mean velocity in the presence of LRRK2(G2019S) expression was 0.876  $\mu\text{m/s}$  (95% confidence interval 0.848-0.904  $\mu\text{m/s}$ ; n= 204). No significant difference between these values can be observed, indicating that LRRK2 expression had no effect on anterograde transport velocities. The same was true for retrograde transport. The geometric mean for retrograde transport velocities in the absence of exogenous LRRK2(G2019S) was 1.27  $\mu\text{m/s}$  (95% confidence interval 1.21-1.34  $\mu\text{m/s}$ ; n= 217), and in the presence of the LRRK2(G2019S) transgene the geometric mean was 1.28  $\mu\text{m/s}$  (95% confidence interval 1.22-1.35  $\mu\text{m/s}$ ; n= 150) (Figure 28B). Again, there is no difference of mean retrograde velocities between experiments, and LRRK2 expression had no effect on retrograde mitochondrial transport in our experimental set-up. Next, we wanted to evaluate if mutant LRRK2(G2019S) expression could have an effect on the size of transported mitochondria. Mitochondrial lengths were measured for the two experimental conditions, and data was separated by transport direction for statistical analysis. As can be seen in Figure 29A, sizes were spread over a wide but similar range for all four categories. The smallest possible size of a mitochondrion, for which transport

parameters could be determined, was 0.27  $\mu\text{m}$  (anterograde speed: 1.26  $\mu\text{m/s}$ ; no-LRRK2 control). While a length of 6.96  $\mu\text{m}$  was the largest dimension of any motile mitochondrion tracked (anterograde speed: 1.07  $\mu\text{m/s}$ ; LRRK2(G2019S) expressed). As evident from Figure 29B, a similar and wide size range of transported mitochondria was obtained for most individual experiments, and a more restricted size distribution is evident in few experiments. A narrow distribution, with length measures from 0.6 to 2.53  $\mu\text{m}$ , was obtained for one axon from an animal injected with the control vector without LRRK2 sequence (Figure 29B; animal 13, data plotted in red), while very wide size ranges were obtained for two axons: from 0.38  $\mu\text{m}$  up to 6.63  $\mu\text{m}$  in animal 26 and from 0.61  $\mu\text{m}$  up to 6.96  $\mu\text{m}$  in animal 27, both injected with the LRRK2(G2019S) expression construct. To evaluate an impact of the disease gene, geometric means of mitochondrial size distributions were calculated (Figure 29A). For anterograde transport the geometric mean in the absence of LRRK2 expression was 1.57  $\mu\text{m}$  (95% confidence interval 1.26-1.95  $\mu\text{m}$ ; n= 196), while the geometric mean size in the presence of LRRK2(G2019S) expression was 1.85  $\mu\text{m}$  (95% confidence interval 1.57-2.19  $\mu\text{m}$ ; n= 124), which was slightly larger. However, this value is within the confidence interval of the control experiment and represents no significant increase in size. For retrograde transport the geometric mean of mitochondrial sizes in the absence of mutant LRRK2 was 1.93  $\mu\text{m}$  (95% confidence interval 1.64-2.27  $\mu\text{m}$ ; n= 125) compared to 2.02  $\mu\text{m}$  (95% confidence interval 1.57-2.59  $\mu\text{m}$ ; n= 99) when LRRK2(G2019S) was expressed, and this value was again not significantly different. These results indicate that LRRK2(G2019S) expressed from our effector construct had no effect on the size of transported mitochondria in any of the trafficking directions. We also wanted to determine if a connection between transport speed and size of mitochondria could be detected. Additionally, a potential LRRK2(G2019S) effect might only be revealed by a more detailed analysis of anterograde and retrograde transport. Transported mitochondria were classified as small if they were up to 1  $\mu\text{m}$  in length, medium size if they were between 1 and 3  $\mu\text{m}$  and large if they were longer than 3  $\mu\text{m}$ . Anterograde and retrograde velocities were plotted against these size classes or against the full size range, as depicted in Figures 30 and 31. Geometric means of velocity values for the different size classes were calculated for anterograde transport. For small mitochondria ( $\leq 1 \mu\text{m}$ ) the value in the absence of disease gene expression was 1.165  $\mu\text{m/s}$  (95% confidence interval 0.909-1.492  $\mu\text{m/s}$ ; n= 50), and 1.056  $\mu\text{m/s}$  (95% confidence interval 0.811-1.374  $\mu\text{m/s}$ ; n= 20) was obtained for experiments conducted with the LRRK2(G2019S)-encoding plasmid. These geometric mean values were similar for the two transgene expression conditions. Comparisons in the medium size class yielded a similar



Anterograde velocities by genotype					
geometric means with 95%-confidence intervals					
	geometric mean	CI- lower	CI- upper	observations	groups
no LRRK2	0.929	0.871	0.989	345	18
LRRK2(G2019S)	0.876	0.848	0.904	204	12



Retrograde velocities by genotype					
geometric means with 95%-confidence intervals					
	geometric mean	CI- lower	CI- upper	observations	groups
no LRRK2	1.27	1.21	1.34	217	18
LRRK2(G2019S)	1.28	1.22	1.35	150	12

**Figure 28. LRRK2(G2019S) has no effect on mitochondrial transport velocities.** **A** Anterograde velocities are plotted by genotype with data sets from different animals and movies in different colours. Geometric mean values of velocities are indicated. **B** Retrograde velocities are on average higher than anterograde ones, and values are more widely and more symmetrically distributed. Values from different animals are plotted in different colours. An effect of the disease gene from the injected transgenic construct on anterograde or retrograde transport cannot be observed. Abbreviations are: CI, confidence interval; geomean, geometric mean.

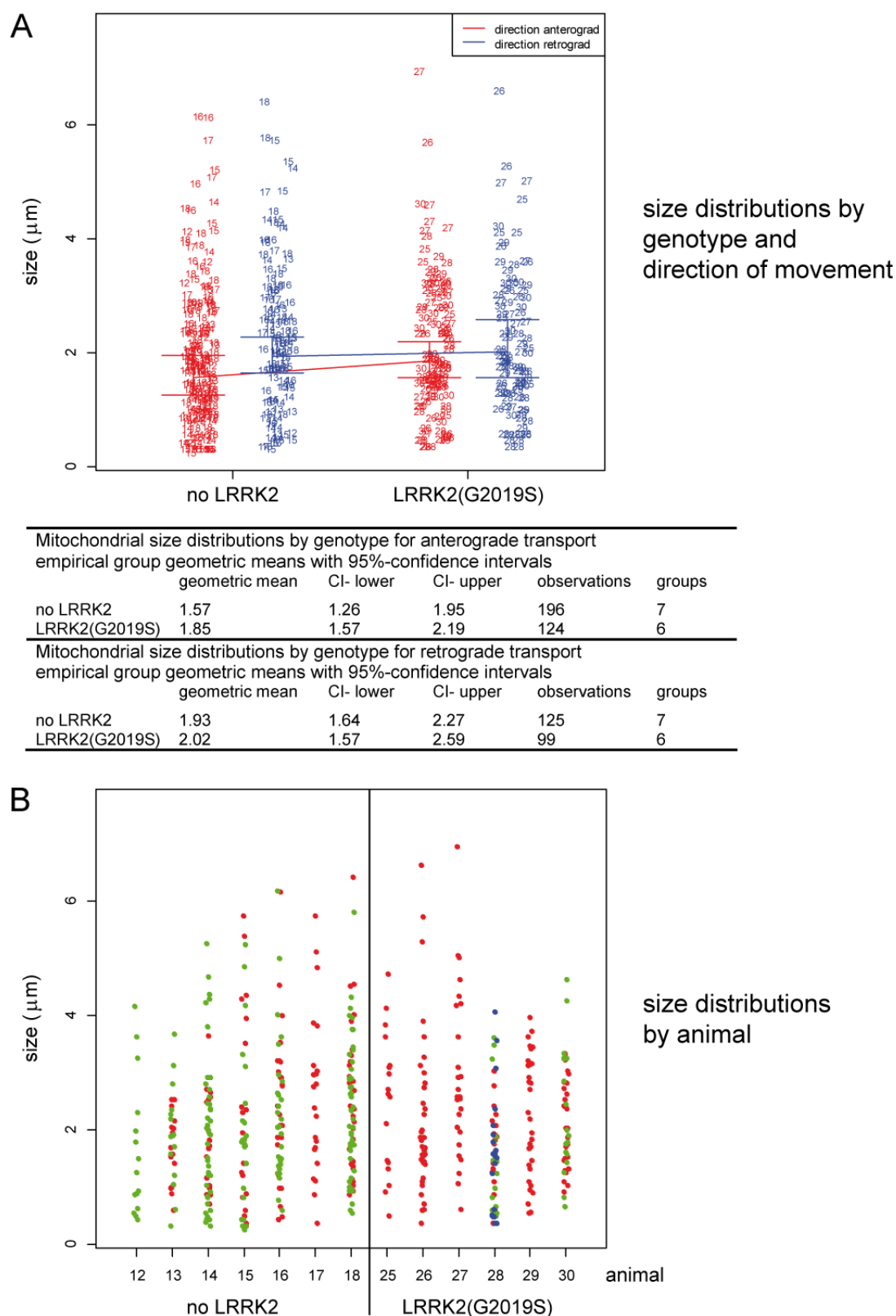
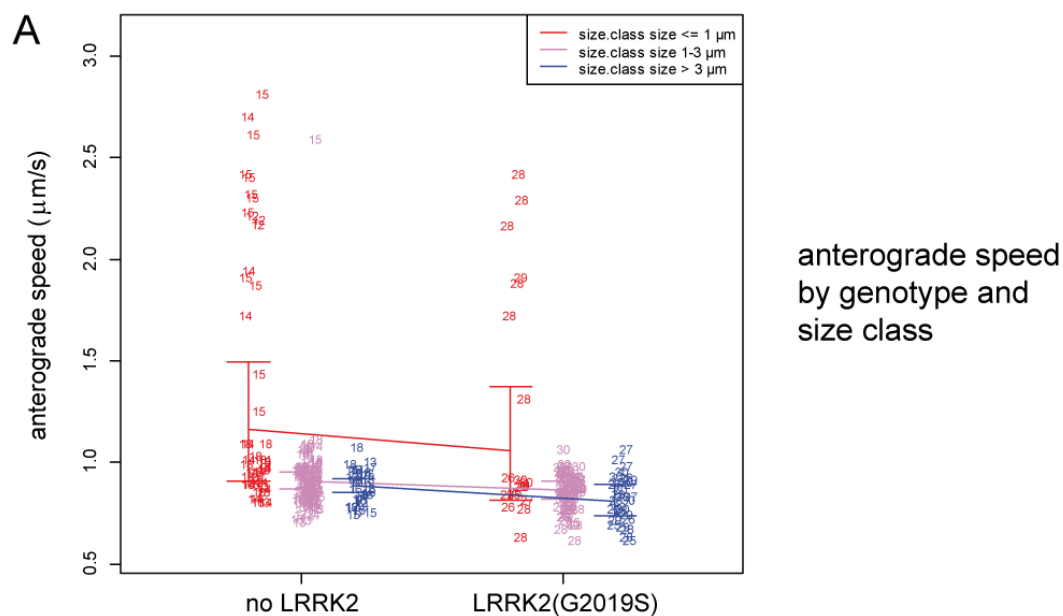


**Figure 29. Size distributions of motile mitochondria are similar between experiments.**

**A** LRRK2(G2019S) has no effect on the size of transported mitochondria. Mitochondrial lengths are plotted against genotype and transport direction. Numbers of data points refer to the designation of animals according to Table 1 (animals 12 to 18: without LRRK2; animals 25 to 30: LRRK2(G2019S)). Mitochondria moving retrogradely are on average by 0.278  $\mu\text{m}$  larger than anterogradely transported mitochondria (two-way ANOVA,  $p=0.0086$ ). **B** Sizes of anterogradely and retrogradely transported mitochondria are combined and plotted per animal, with different movies indicated in different colours.



Anterograde speed by genotype and size class  
empirical group geometric means and 95%-confidence intervals

	geometric mean	CI- lower	CI- upper	observations	groups
<i>size ≤ 1 µm</i>					
no LRRK2	1.165	0.909	1.492	50	6
LRRK2(G2019S)	1.056	0.811	1.374	20	6
<i>size 1- 3 µm</i>					
no LRRK2	0.907	0.867	0.950	114	7
LRRK2(G2019S)	0.862	0.819	0.907	75	6
<i>size &gt; 3 µm</i>					
no LRRK2	0.884	0.854	0.916	32	7
LRRK2(G2019S)	0.810	0.736	0.890	29	6

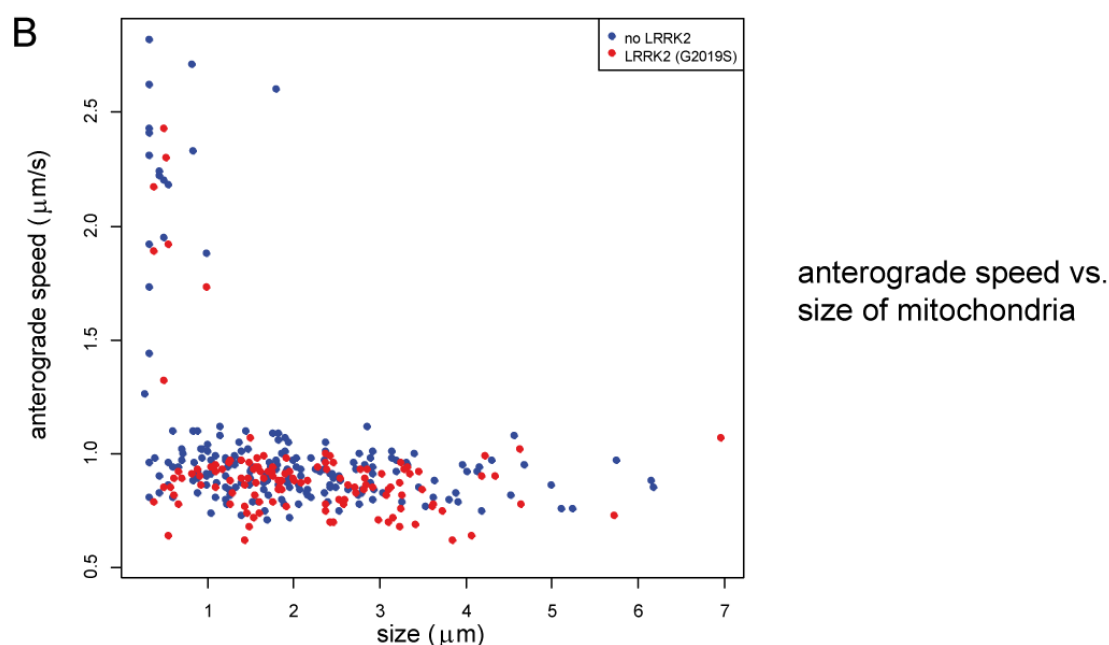


**Figure 30. Small mitochondria move faster in the anterograde direction only.** **A** Mitochondria were classified according to their size as small ( $\leq 1 \mu\text{m}$ ), medium ( $1-3 \mu\text{m}$ ) or large ( $>3 \mu\text{m}$ ) and size classes were plotted for the two indicated genotypes. The presence of LRRK2(G2019S) has no influence on anterograde velocities. A significant difference in velocities occurs between size classes, with small mitochondria moving significantly faster than medium or large mitochondria (ANOVA,  $p < 0.0001$ ). **B** Anterograde velocities are plotted against size. It is evident that some small mitochondria move fast while larger mitochondria have a more limited range of velocities.

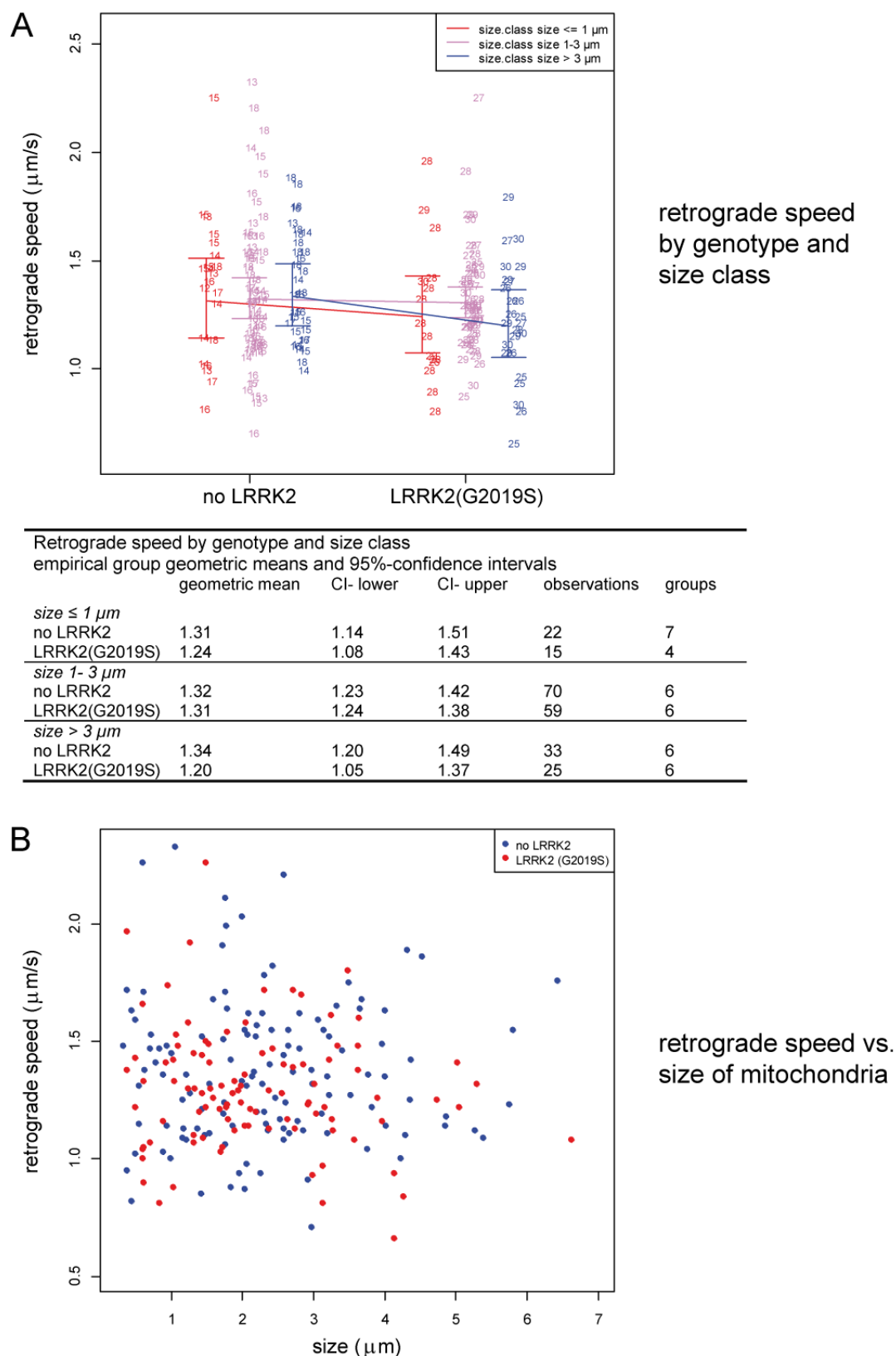


**Figure 31. Retrograde transport velocities are highly variable.**

**A** The disease gene *LRRK2(G2019S)* and mitochondrial size have no effect on retrograde transport velocities of mitochondria. Retrograde movement is more heterogeneous and covers a broader range of velocities than anterograde movement in all size classes. **B** Retrograde velocities are plotted against mitochondrial size, and a broad distribution of velocities is visible across all different sizes.

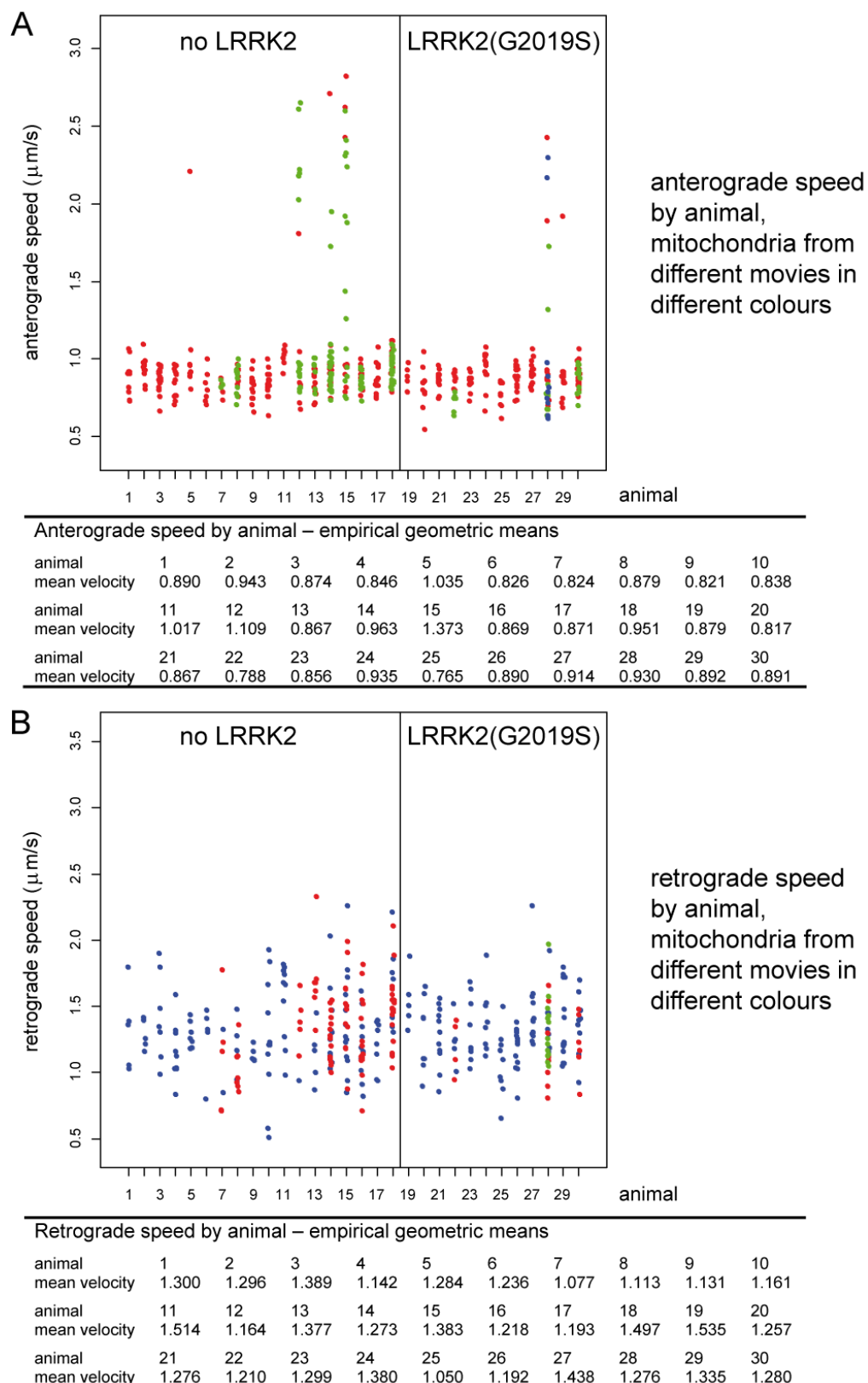


**Figure 32. Anterograde transport of mitochondria is more homogeneous than retrograde transport.** **A** and **B** Anterograde and retrograde velocities, respectively, are plotted for each animal and for two experimental conditions, with mitochondria from different movies depicted in different colours. Despite small mitochondria, which can move fast, velocity values of anterograde movement are clustered in between  $0.71 \mu\text{m/s}$  and  $1.12 \mu\text{m/s}$  for experiments without LRRK2 expression (**A**). Velocity distributions are more widespread for retrograde movement (**B**). Geometric mean values are provided for each animal and transport direction.

result: a mean velocity of 0.907  $\mu\text{m/s}$  (95% confidence interval 0.867-0.950  $\mu\text{m/s}$ ; n= 114) for experiments with the control plasmid was not significantly different from the 0.862  $\mu\text{m/s}$  (95% confidence interval 0.819-0.907  $\mu\text{m/s}$ ; n= 75), which was determined in the presence of LKRR2(G2019S) expression. Finally, geometric mean velocities in the large size class were 0.884  $\mu\text{m/s}$  (95% confidence interval 0.854-0.916  $\mu\text{m/s}$ ; n= 32) in experiments without *LRRK2* sequence compared to a similar value of 0.810  $\mu\text{m/s}$  (95% confidence interval 0.736-0.890  $\mu\text{m/s}$ ; n= 29) when LKRR2(G2019S) was expressed. In conclusion, there was no significant difference between mean velocities for the two transgenic conditions in any of the three size classes. A similar result was obtained for retrograde transport. Geometric mean velocity in the small size class ( $\leq 1 \mu\text{m}$ ) and in the absence of the disease gene was 1.31  $\mu\text{m/s}$  (95% confidence interval 1.14-1.51  $\mu\text{m/s}$ ; n= 22). A similar value of 1.24  $\mu\text{m/s}$  (95% confidence interval 1.08-1.43  $\mu\text{m/s}$ ; n= 15) was calculated for experiments with the LRRK2(G2019S) expression construct (Figure 31A). In the same way, mean transport velocities in the medium size class were nearly identical for the two experimental conditions: 1.32  $\mu\text{m/s}$  (95% confidence interval 1.23-1.42  $\mu\text{m/s}$ ; n= 70) without disease gene versus 1.31  $\mu\text{m/s}$  (95% confidence interval 1.24-1.38  $\mu\text{m/s}$ ; n= 59) for experiments with mutant LRRK2 expression. Finally, the geometric means in the large size class were: 1.34  $\mu\text{m/s}$  (95% confidence interval 1.20-1.49  $\mu\text{m/s}$ ; n= 33) with no exogenous LRRK2 and 1.20  $\mu\text{m/s}$  (95% confidence interval 1.05-1.37  $\mu\text{m/s}$ ; n= 25) in experiments with the LRRK2(G2019S) expression construct. Again, no significant differences in geometric mean transport velocities between the two experimental conditions could be observed for any of the three size classes. These results confirm the previously described more general observation that expression of mutant LRRK2(G2019S) from our effector construct does not affect mitochondrial velocities in any of the two transport directions (Figure 28).

In summary, the clear-cut result from this analysis is that a neuropathogenic effect from expression of LRRK2(G2019S) on axonal transport of mitochondria could not be revealed in our experimental set-up. Expression of the disease gene from the effector construct had no effect on velocities and size distributions of mitochondria engaged in either anterograde or retrograde transport. This negative result or lack of phenotype is problematic insofar as it could be due to low and insufficient expression of the disease gene from the transgenic construct, as will be outlined in the discussion (Chapters 4.3.3 and 4.4.3.).

Despite this lack of a LRRK2(G2019S)-associated phenotype some novel insights and unprecedented quantitative results for mitochondrial axonal transport within long nerve fibres

*in vivo* could be obtained from this study. As evident in Figure 30, few mitochondria engaged in anterograde transport did move faster than 1.5  $\mu\text{m/s}$ , and all but one of the fast mitochondria belong to the small size class, with sizes up to 1  $\mu\text{m}$  (one mitochondrion has a length of 1.8  $\mu\text{m}$  and is trafficking with 2.6  $\mu\text{m/s}$ ). Indeed, this correlation between size of mitochondria and transport velocity is of statistical significance for anterograde transport. Small size mitochondria moved with a mean velocity of 1.165  $\mu\text{m/s}$  (95% confidence interval 0.909-1.492  $\mu\text{m/s}$ ; n= 50), while medium size mitochondria moved with 0.907  $\mu\text{m/s}$  (95% confidence interval 0.867-0.950  $\mu\text{m/s}$ ; n= 114) and large size mitochondria had a mean velocity of 0.884  $\mu\text{m/s}$  (95% confidence interval 0.854-0.916  $\mu\text{m/s}$ ; n= 32) in experiments without LRRK2 expression (Figure 30A). Therefore, small size mitochondria move on average 1.3 fold faster in the anterograde direction than medium or large size mitochondria (ANOVA analysis,  $p < 0.0001$ ). At this point it should be mentioned that small and fast mitochondria are likely underrepresented in this analysis because they were difficult to track. These mitochondria could only be evaluated in few good-quality movies, as can be seen in Figure 32A. Another observation for anterograde transport is that transport velocities for medium and large size mitochondria ( $>1 \mu\text{m}$ ) were distributed within a limited range from between 0.71  $\mu\text{m/s}$  and 1.12  $\mu\text{m/s}$  for experiments without disease gene expression (compare data plots in Figures 32A and 30B). For retrograde transport, a correlation between mitochondrial size and speed could not be revealed (Figure 31). Here, mitochondria moving with velocities of 1.5  $\mu\text{m/s}$  or faster are not necessarily of a small size – e.g. a mitochondrion from an experiment with the control plasmid without LRRK2 sequence had a length of 6.43  $\mu\text{m}$  and was travelling at a speed of 1.76  $\mu\text{m/s}$ . Velocities were distributed over a wide range for mitochondria of all different sizes (Figure 31B). For example, large mitochondria, with sizes longer than 3  $\mu\text{m}$ , were detected with velocities up to 1.89  $\mu\text{m/s}$  (this mitochondrion has a length of 4.32  $\mu\text{m}$ ) in experiments without exogenous LRRK2 expression. This difference in the distribution of velocity data between anterograde and retrograde transport is also evident in Figure 32. Another novel finding of this study is that retrograde transport *in vivo* clearly is faster than anterograde transport. The geometric mean velocity for retrograde transport was 1.27  $\mu\text{m/s}$ , which is 37% higher than the mean anterograde velocity of 0.929  $\mu\text{m/s}$  (values obtained from control experiments without disease gene expression) (Figure 28). Finally, another important observation was that mitochondria on the retrograde track were on average by 0.278  $\mu\text{m}$  larger than mitochondria moving in anterograde direction (two-way ANOVA with factors genotype and direction,  $p = 0.0086$ ) – an observation that has not been previously recognized.

### 3.4. Characterization of a Pink1 deficiency zebrafish disease model

A stable loss of function zebrafish model for *pink1*-linked recessive Parkinson's disease was generated by the Bandmann group and is called in the following *pink1*<sup>-/-</sup> (Flinn *et al.*, 2013).. Through TILLING they identified a non-sense mutation in the *pink1* gene in one animal of a chemically mutagenized population, from which a stable line could be retrieved. The mutation would lead to a C-terminal truncation (Y431\*) within the kinase domain (full-length protein of 574 aa), and this deletion abrogates kinase activity of Pink1. Additional proof was provided that the defective mRNA is subject to nonsense-mediated decay and is partially degraded in *pink1* mutant animals. As loss of dopaminergic neurons is the pathological hallmark of PD, these neurons had been analysed in larval fish at 5 dpf. A reduction in the number of DA neurons in diencephalic Clusters 1, 2, 4 and 5 by approximately 25% had been observed in the mutant at this early developmental stage. Next, we wanted to know if DA neurons are also affected in adult Pink1-deficient animals. Therefore, the corresponding dopaminergic clusters had to be identified and analysed in adult brain tissue.

#### 3.4.1. DA neuron numbers are not altered in adult brain of *pink1* mutant animals

In order to observe and quantitatively analyse the dopaminergic system in adult zebrafish of the disease model, two brains each of 6-months-old wild-type and *pink1*<sup>-/-</sup> fish were processed for cryosectioning. Serial cross sections of the relevant forebrain regions were generated. DA neurons were identified by TH immunoreactivity followed by immunofluorescence detection. To reveal major anatomical landmarks, nuclei were stained with DAPI. Characteristic diencephalic dopaminergic cell populations as described by Wullimann and colleagues (Wullimann *et al.*, 1996; Rink and Wullimann, 2001, 2002a, 2002b) could be identified on consecutive tissue sections by confocal microscopy. Confocal image stacks were recorded and DA neurons were counted on image stacks. Cluster 1, 2 and 4, which contain ascending DA neurons, are located in the posterior tuberculum. Cluster 1 cells are small round unipolar cells and are of cytological Type 1 (see Introduction, Figure 9C). They are densely clustered in the periventricular nucleus of the posterior tuberculum (TPp), which is evident from the schematic drawings and confocal images in Figure 33A-C. In the first pair of wild-type and *pink1*<sup>-/-</sup> fish analysed, Cluster 1 could only be counted partially on 6 consecutive tissue sections. This was due to damaged and lost sections. A total of 234 DA neurons were counted in wild-type and 290 in *pink1*<sup>-/-</sup> tissue (Figure 33D). For the second pair of animals more tissue sections were available and could be evaluated. Cluster 1 was distributed over 14 consecutive sections. Unfortunately, two sections were lost for the

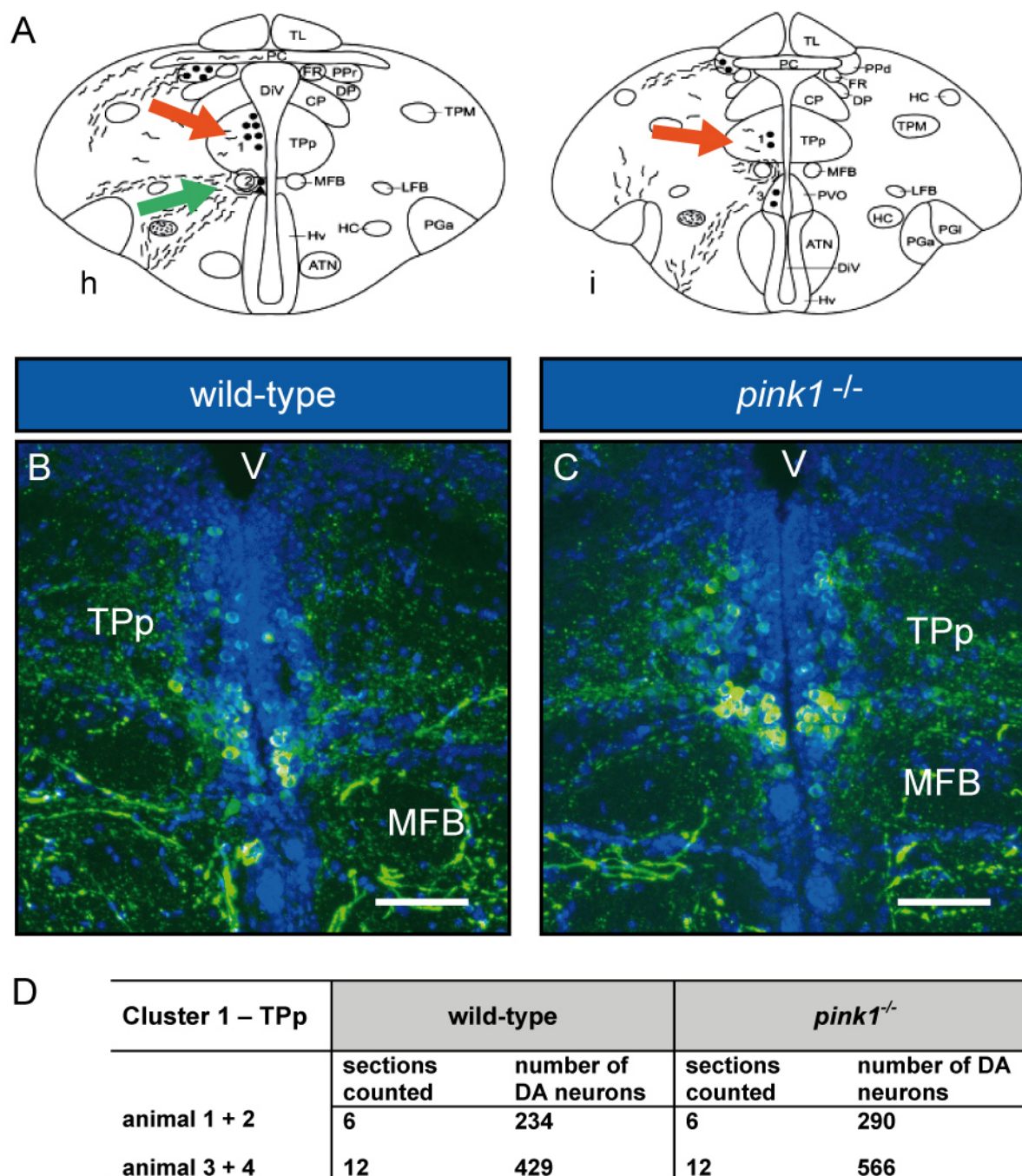


**Figure 33. Cluster 1 DA neurons in the periventricular nucleus of the posterior tuberculum are not altered in the brain of *pink1*<sup>-/-</sup> fish.** **A** Schematic drawings of TH-immunoreactive cell clusters in cross sections of adult brain. Levels of sections (h and i) are indicated in Figure 9A of the Introduction; drawings adapted from Rink and Wullimann, 2001; see therein for abbreviations of anatomical structures. Small round Type 1 cells located in the periventricular nucleus of the posterior tuberculum (TPp) comprise Cluster 1 and are indicated by red arrows. A green arrow indicates DA neurons with Type 2 morphology. **B** and **C** Dopaminergic neurons in the TPp are revealed by TH-immunofluorescence detection (green signal). Nuclei are DAPI stained (blue). Projections of confocal image stacks recorded from wild-type and *pink1* mutant tissue are shown, as indicated. A dense cluster of DA neurons in the TPp is visible in both animals. Abbreviations are: MFB, medial forebrain bundle; V, ventricle. Scale bar, 50  $\mu$ m. **D** Neurons in Cluster 1 were quantified for two wild-type and two *pink1*<sup>-/-</sup> fish. Six and twelve sections were counted and no loss of neurons could be observed in the mutant.

wild-type brain and therefore two corresponding slices were omitted from analysis of the mutant. In the wild-type 429 Cluster 1 cells were counted versus 566 cells in the *pink1*<sup>-/-</sup>. No reduction in cell number was evident in the mutant.

Cluster 2 and 4 cells were easily identified by their characteristic large size and pear-shaped morphology (see Introduction, Figure 9C), which has been designated Type 2 morphology. There were only few cells of this type per tissue section: a maximum of 5 Type 2 cells could be observed on one section. Type 2 cells were distributed over up to 19 serial sections under experimental conditions applied in this study. The first Cluster 2 cells appear in the posterior tuberculum (TP) ventral of Cluster 1. Their cell bodies are positioned close to the ventricle and medial to a characteristic tract of nerve fibres, the medial forebrain bundle (MFB). The prominent lateral processes of Type 2 cells were visible (Figure 34C). Cluster 4 is located posterior to and adjacent to Cluster 2. A clear distinction between Cluster 2 and 4 cells was not possible as they have the same morphology. Type 2 cells in more posterior tissue sections (i.e. Cluster 4) could be detected more distantly to the ventricle/midline, in more lateral positions (data not shown). For the first pair of wild-type and *pink1*<sup>-/-</sup> fish, Type 2 cells of Cluster 2+4 were observed on 19 and 16 consecutive tissue sections, respectively. However, due to damaged or lost tissue 17 sections could be evaluated for the wt, and 18 Type 2 cells were counted in total. 15 sections of *pink1*<sup>-/-</sup> tissue were analysed and these did contain 22 Type 2 cells. Again no reduction in DA cell number is evident in the mutant (Figure 34D). The analysis of a second pair of animals confirmed the observation that no loss of DA neurons in Cluster 2 and 4 could be detected in the mutant. This time, 16 consecutive tissue sections could be analysed per genotype, and a total of 26 versus 24 Type 2 cells were observed for wt and mutant animals, respectively.

For the analysis of DA neurons in 5 dpf larvae, cells of Cluster 5 had been quantified by the Bandmann group. In adult brain Cluster 5 cells are small bipolar cells of cytological Type 3 (see Introduction, Figure 9C). They are located in the dorsal zone of the periventricular hypothalamus (Hd, encircled in yellow in Figure 34A). These cells were small, densely packed and only weakly stained on the tissue sections generated here and could not be considered for quantification. Instead, Cluster 6 cells, which are of Type 1 morphology, were more strongly stained and could be unequivocally identified. They are located in the posterior tuberal nucleus (PTN) and extend into the dorsal part of the caudal zone of the periventricular hypothalamus (Hc, dorsal part, Figure 35). This cluster was covered by 14 serial sections in all four brains analysed. Due to damaged or lost tissue, three sections each were omitted from analysis of the first pair of animals, leaving 11 tissue sections for quantification. A total of

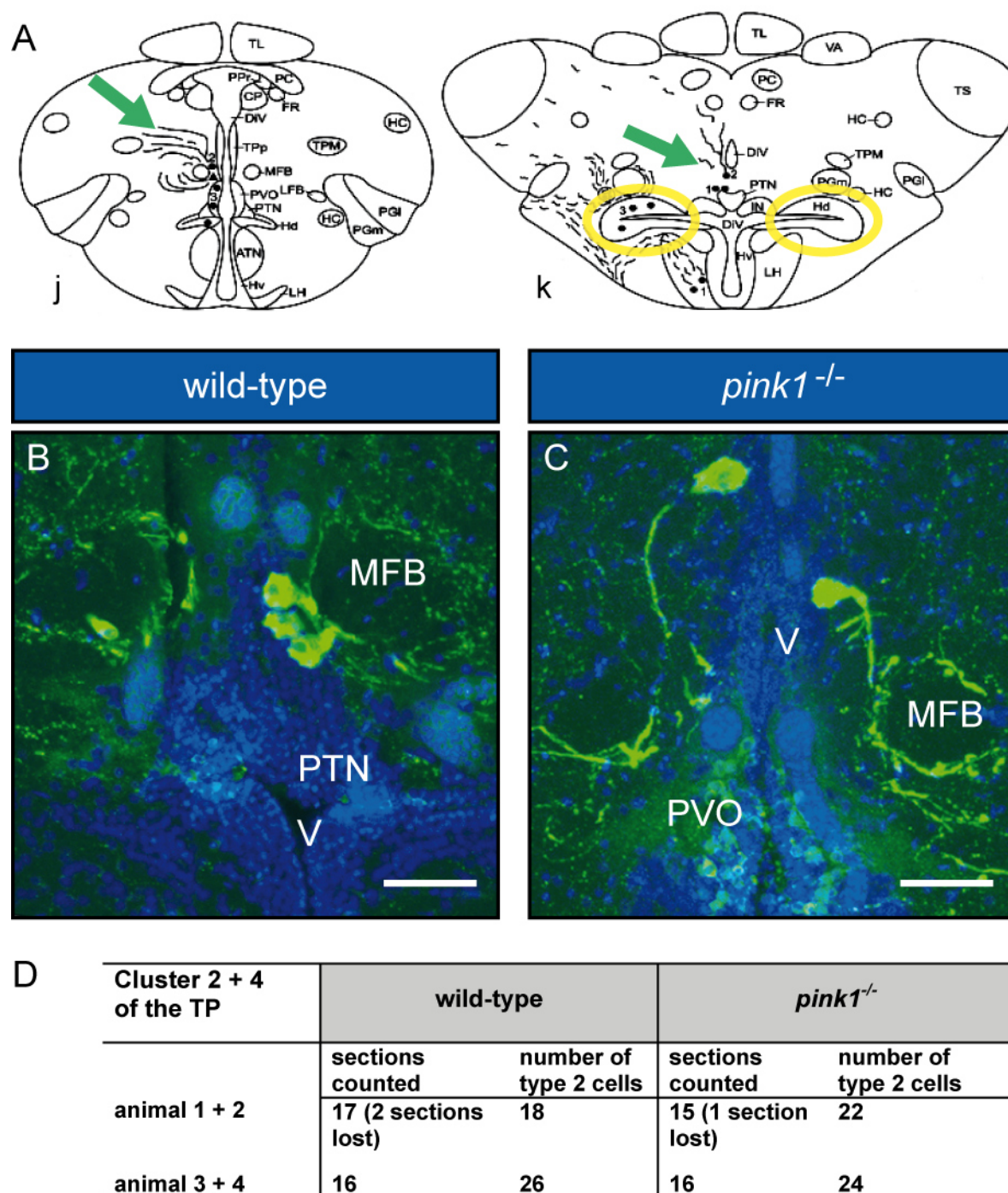


**Figure 34. The number and organization Cluster 2 and 4 DA neurons are not altered in the posterior tuberculum of *pink1*<sup>-/-</sup> fish.** **A** Schematic drawings of dopaminergic cell clusters in cross sections of adult brain. Levels of sections (j and k) are indicated in Figure 9A of the Introduction; drawings adapted from Rink and Wullimann, 2001; see therein for abbreviations of anatomical structures. Large Type 2 neurons are sparsely distributed over many consecutive tissue sections. They constitute Cluster 2 and 4, as indicated by green arrows. Neurons of Cluster 5 are encircled in yellow and are localized in the dorsal zone of the periventricular hypothalamus (Hd). **B** Three Type 2 neurons are revealed by TH-immunofluorescence detection (in green) in wt tissue. Nuclei are stained with DAPI. These neurons send prominent lateral processes around the medial forebrain bundle (MFB). **C** Two Type 2 cells are visible close to the midline in *pink1*<sup>-/-</sup> tissue. Their processes project ventrally. Abbreviations: PTN, posterior tuberal nucleus; PVO, paraventricular organ; V, ventricle. Scale bar, 50  $\mu$ m. **D** Cluster 2+4 neurons were quantified for two wt and two *pink1* mutant animals. No reduction in cell number was detectable in the mutant. Note, that some tissue sections were lost in animals 1 and 2.

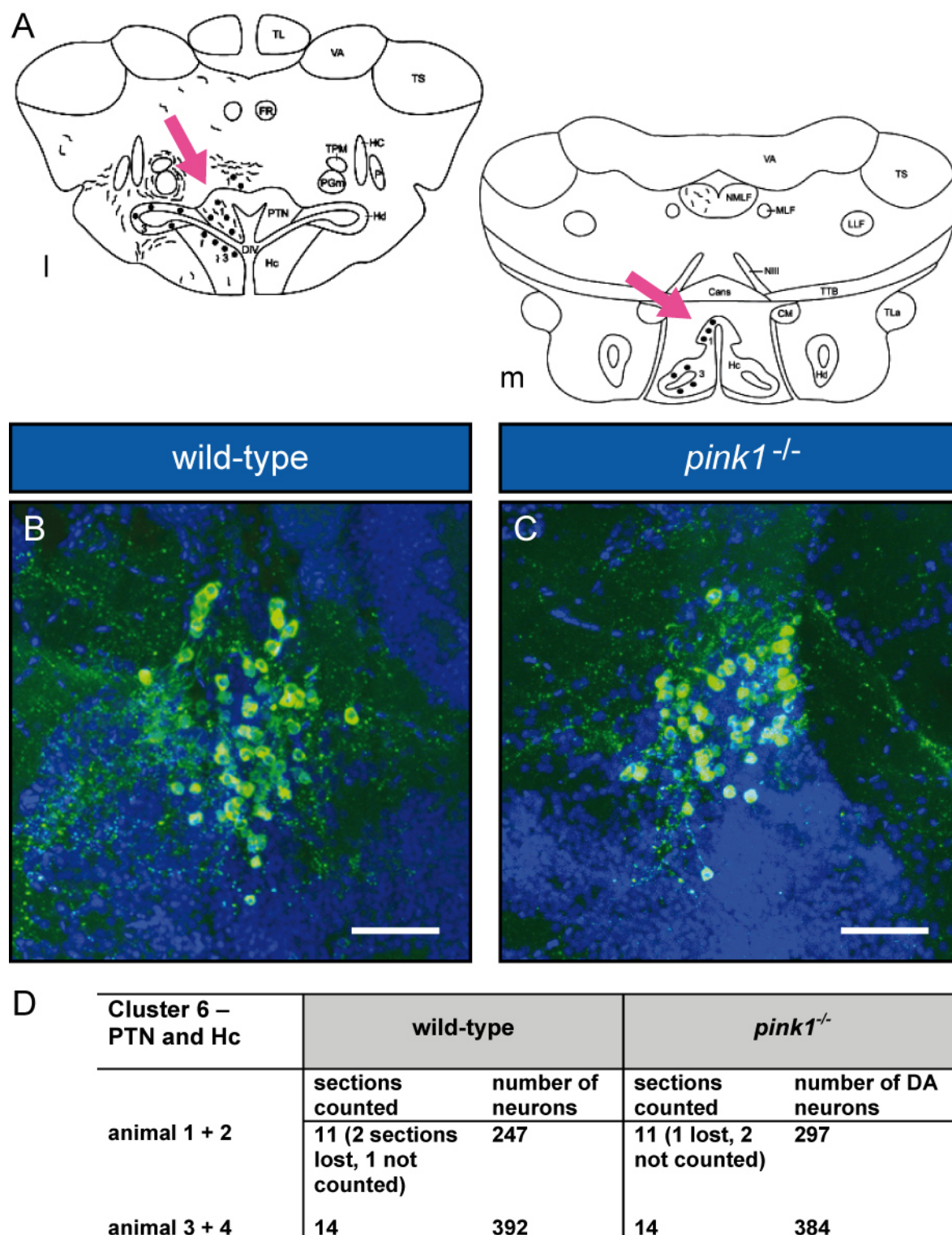


**Figure 35. Cluster 6 dopamine neurons in the posterior tuberal nucleus and the caudal zone of the periventricular hypothalamus are not altered in *Pink1*-deficient animals.** **A** Schematic drawings depict the locations of TH-immunoreactive cell clusters. Locations of cross sections (l and m) are indicated in Figure 9A of the Introduction; adapted from Rink and Wullimann, 2001; see therein for abbreviations. Pink arrows indicate DA neurons of cytological Type 1 in the posterior tuberal nucleus (PTN) and the caudal zone of the periventricular hypothalamus (Hc), which constitute Cluster 6. **B** and **C** Anti-TH immunoreactive cells in the hypothalamus of wild-type and *pink1*<sup>-/-</sup> brains, respectively, were detected by fluorescence (green). Nuclei were stained with DAPI. Projections of confocal image stacks are shown. Scale bar, 50  $\mu$ m. **D** Cluster 6 neurons were

quantified in two pairs of animals – one wild-type and one *pink1* mutant each. Note, that some tissue sections were lost in the first pair analysed. No reduction in DA cell numbers could be observed.

247 DA neurons were counted for wild-type and 297 for *pink1*<sup>-/-</sup> animals (see Figure 35D). For the second pair of animals all 14 sections could be evaluated, yielding a total of 392 cells for wt and 384 for the mutant. Again, no loss of DA neurons in Cluster 6 was evident in mutant compared to wt tissue.

In summary, there is no hint for specific dopaminergic neurodegeneration in brains of 6-months-old Pink1-deficient animals. No repeated reduction in DA neuron numbers in any of the four cell populations was obtained for the two pairs of wt and mutant animals. It has to be stated, however, that two animals of each genotype were not enough to allow for a statistical evaluation of the data, and further analyses could not be performed in the course of this study.

### **3.4.2. Mitochondrial ultrastructure is altered in muscle tissue of *pink1* mutants**

Striking ultrastructural abnormalities and dysfunction of mitochondria, as well as degeneration of muscle tissue have been reported for several *Drosophila PINK1* deletion strains (Clark *et al.*, 2006; Park *et al.*, 2006; Yang *et al.*, 2006). To investigate if similar mitochondrial defects would occur in our *pink1*<sup>-/-</sup> zebrafish model, we next examined mitochondrial ultrastructure in muscle tissue of 6-months-old animals. Sample preparation and transmission electron microscopy was performed by Mrs. Jennen (Institute of Pathology, Helmholtz Center Munich). Like neurons, muscle fibres have a high energy demand and are absolutely dependent on the functionality of their mitochondria. As seen in Figure 36, dense clusters of mitochondria could be observed close to the cell membrane of muscle fibres in wild-type tissue. Mitochondria are also interspersed in between myofibrils of muscle fibres (Figure 37). Mitochondria in wild-type tissue had a homogeneous appearance. They had a similar electron density of the matrix and of intracristal luminal spaces. They also showed a homogeneous organization of internal cristae membranes. These membranes were densely stacked, as can be seen in the higher magnification images of Figures 36 and 37. When inspecting mitochondrial ultrastructure in muscle tissue of 6-months-old *pink1*<sup>-/-</sup> animals, a first qualitative observation was that there seem to be fewer mitochondria compared to wild-type tissue, especially in regions close to the cell membrane, as evident in Figure 38. Such densely-packed mitochondria as seen in the wild-type (Figure 36A) could hardly be identified in the *pink1* mutant. Another characteristic of Pink1-deficient tissue was the heterogeneity of

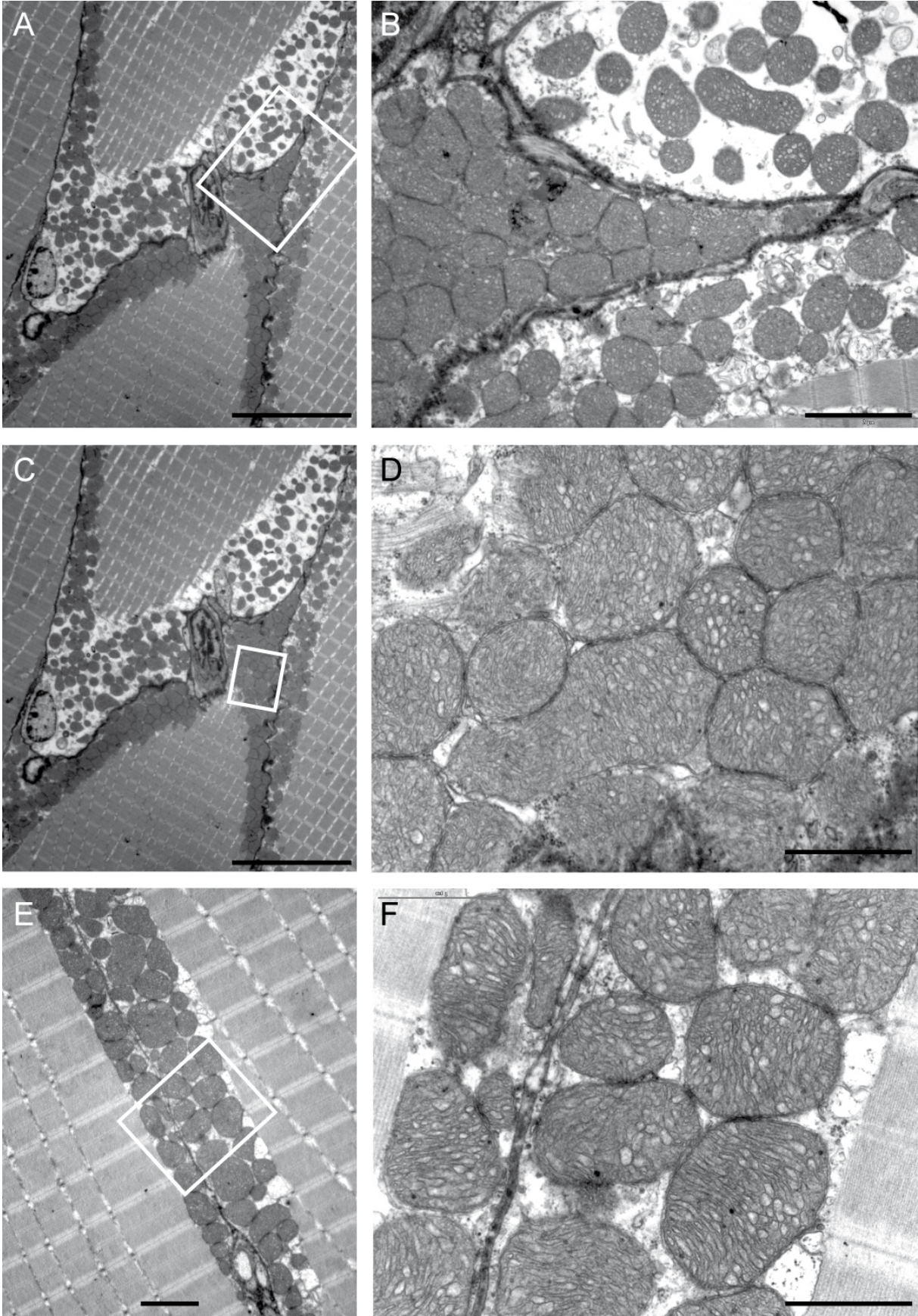


**Figure 36. Mitochondria are densely clustered close to the cell membrane of muscle cells in wild-type tissue.** Muscle tissue from 6-months-old wild-type animals was analysed by electron microscopy. **A to F** Mitochondria located close to the cell membrane of muscle cells are shown. Note

that all mitochondria have a homogeneous appearance. B, D and F are enlarged views of A, C and E, respectively, as indicated by the white boxed areas. Scale bars in A and C, 10  $\mu\text{m}$ ; in B and E, 2  $\mu\text{m}$  and in D and F, 1  $\mu\text{m}$ .

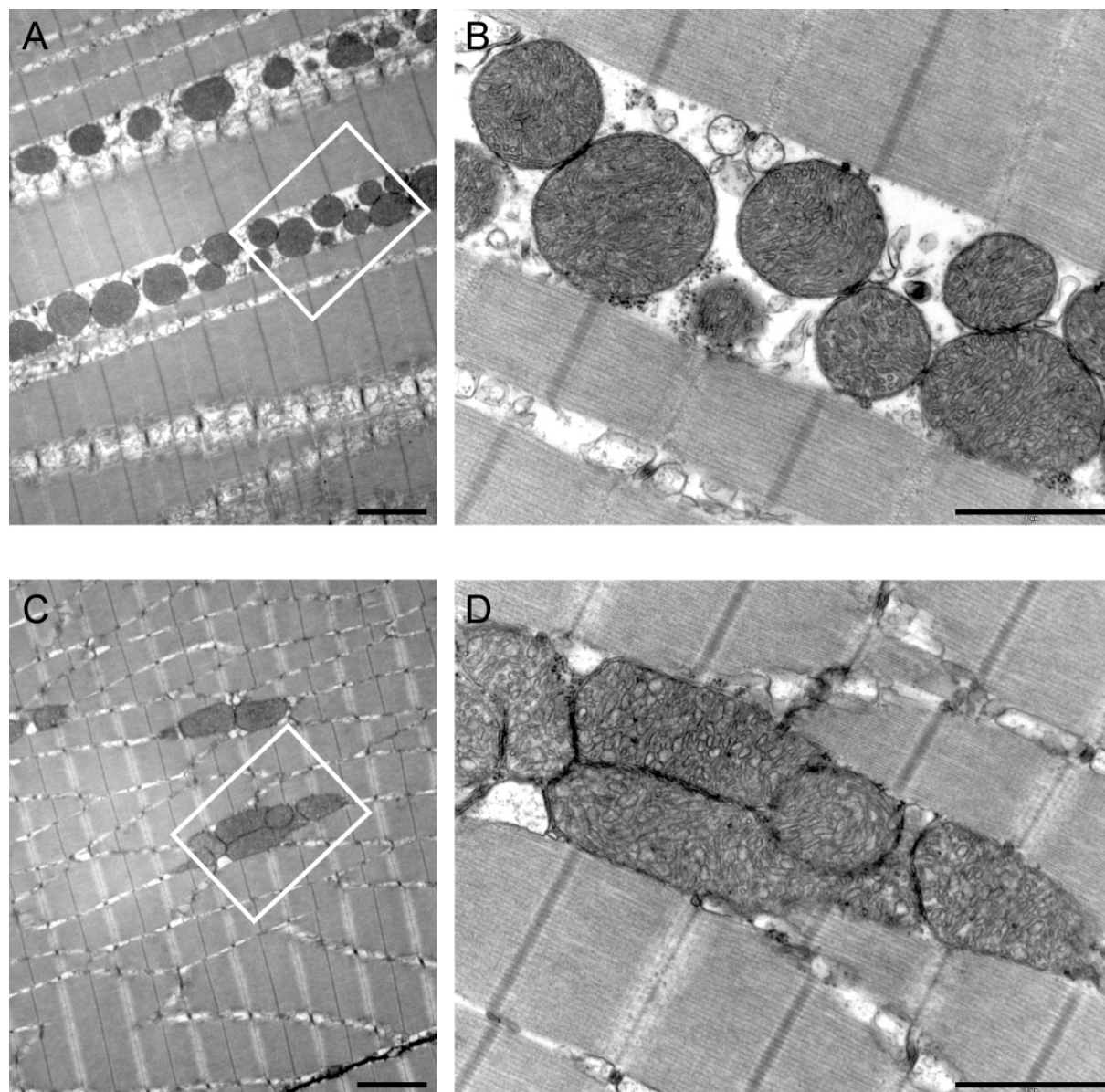


**Figure 37. Mitochondria are located between myofibrils inside of muscle cells.** Tissue was prepared from 6-months-old wild-type animals. **A to D** Electron micrographs of mitochondria located inside of muscle cells are shown. A homogeneous appearance of mitochondria is evident. Images B and D are enlarged views of A and C, respectively, as indicated by the white boxed areas. Scale bars in A and C, 2  $\mu\text{m}$ , and in B and D, 1  $\mu\text{m}$ .

mitochondrial ultrastructure. In particular, the amount of electron-dense material in the matrix and the amount of cristae membranes appeared to be reduced in some mitochondria, but not in all (Figure 39C to F). These “brighter” and “darker” mitochondria with differences in cristae morphology and a different amount of electron-dense material in the matrix could

be observed in the same electron micrograph, thereby excluding an artefact from electron microscopy. Finally, some mitochondria in the mutant seemed to have a larger diameter than in wild-type. A quantitative analysis was required to verify these observations, and this was performed by Prof. Andreas Reichert (Frankfurt, Germany). He analysed mitochondria located in between myofibrils and did not consider those at the cell membrane. Using a stereology approach (Griffiths, 1993) he could quantify the density of mitochondria, defined as mitochondrial area per area of “free space” in between myofibrils. This parameter was similar between the *pink1* mutant (ratio  $0.55 \pm 0.14$ ;  $n=16$ ) and wild-type muscle (ratio  $0.58 \pm 0.19$ ;  $n=12$ ). Thus, there seems to be no reduction in the number of mitochondria – at least not of mitochondria inside of muscle fibres. However, an increase in mitochondrial size by

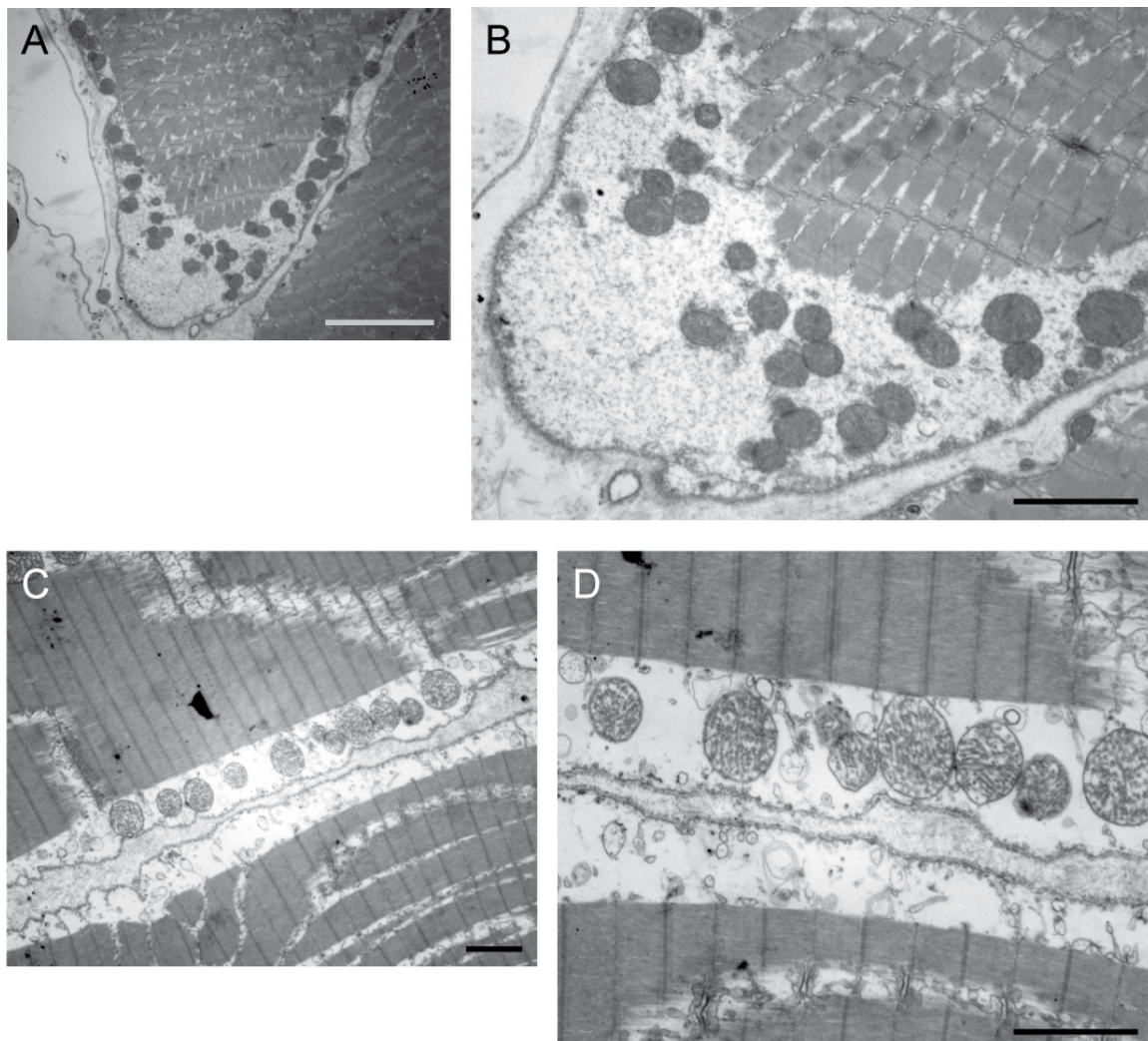


**Figure 38. There seem to be fewer mitochondria in muscle tissue from *pink1* mutant animals.** Tissue was prepared from 6-months-old animals. **A to D** Electron micrographs depict mitochondria located close to the cell membrane of muscle fibres. As a qualitative observation there seem to be fewer mitochondria in mutant than in wild-type tissue (compare to Figure 45). Scale bar in A, 5  $\mu\text{m}$ , and in B, C and D, 2  $\mu\text{m}$  (B and D, same scale).

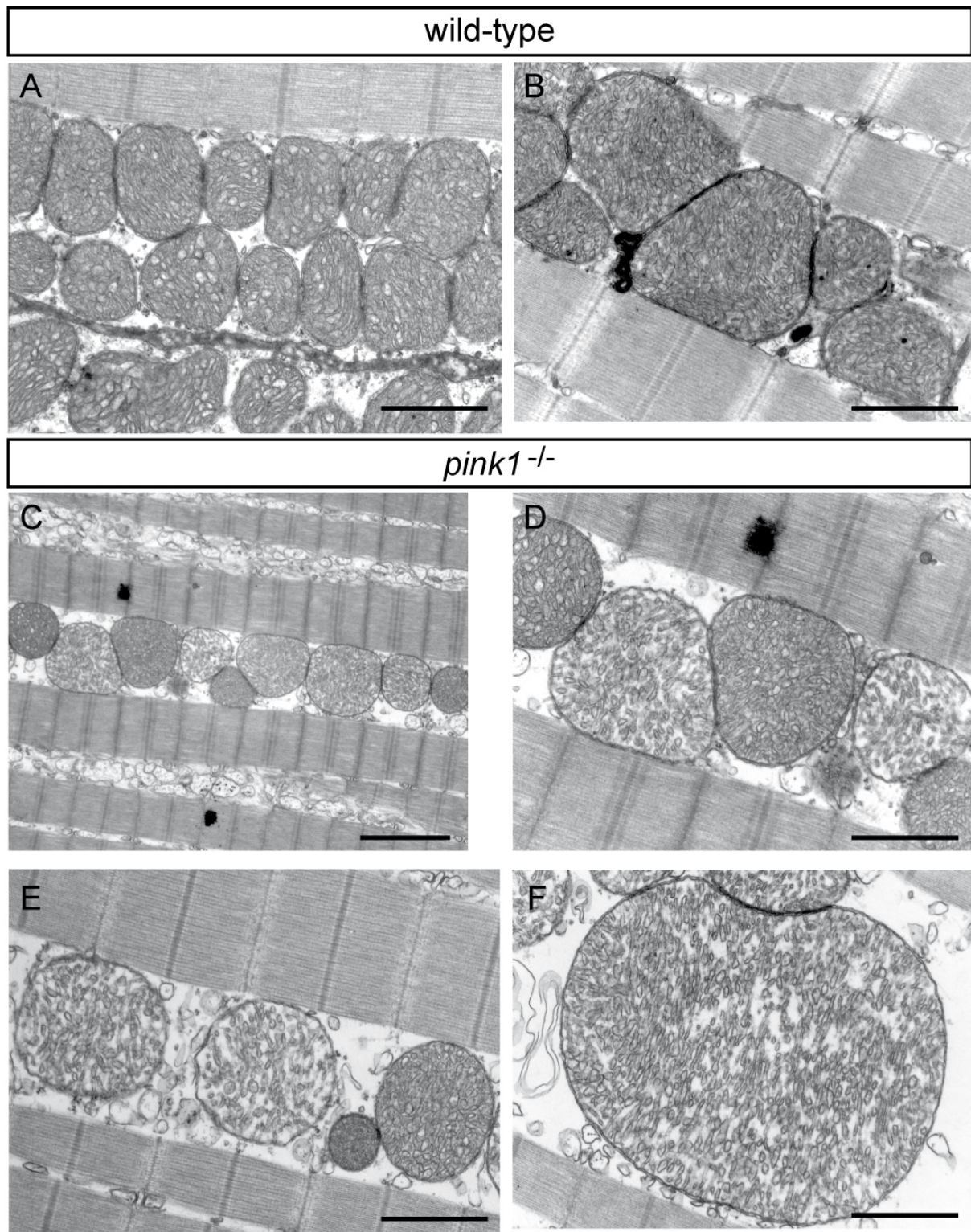


**Figure 39. Mitochondria in muscle tissue from adult *pink1*<sup>-/-</sup> animals have a heterogeneous ultrastructure.** A and B Mitochondria in muscle tissue from wild-type animals have a homogeneous appearance and similar electron density. Cristae membranes are densely packed. Scale bar, 1 μm. C to F The ultrastructure of mitochondria in *pink1*<sup>-/-</sup> animals is heterogeneous. The amount of electron-dense material in the matrix and the amount of cristae membranes are reduced in some mitochondria but not in all (brighter versus darker mitochondria). The size of some mitochondria clearly is increased in mutant compared to wild-type. Image D is an enlarged view of C. D, E and F are to the same scale. Scale bar in C, 2 μm; in D, E and F, 1 μm.

47% was detected in the mutant – the average mitochondrial area per section was  $1.37 \mu\text{m}^2$  for *pink1*<sup>-/-</sup> tissue (n=228) compared to  $0.93 \mu\text{m}^2$  in the wild-type (n=231). The internal heterogeneity of mitochondrial cristae in the *pink1* mutant was not quantified. But this heterogeneity clearly is evident from the images and is in contrast to wild-type tissue.

Next, we analysed the ultrastructure of mitochondria in muscle tissue of 5 dpf larval zebrafish by electron microscopy to determine if the observed alterations in adult tissue were already apparent early in development. Mitochondria in muscle tissue of 5 dpf *pink1*<sup>-/-</sup> animals were quite homogeneous and largely resembled mitochondria from wild-type (Figure 40). Cristae membranes were densely packed and the electron density of the matrix was similar between mutant and wild-type. Few mitochondria in Pink1-deficient muscle had swollen intracristal luminal spaces (Figure 40F, H). However, some enlargements of cristae could also be seen in the wild-type (Figure 40D). A quantitative analysis by Prof. Reichert confirmed that the density of mitochondria between myofibrils did not differ between the two genotypes: mitochondrial area per total area was  $0.52 \pm 0.13$  for *pink1*<sup>-/-</sup> tissue (n=11) and  $0.58 \pm 0.09$  for wild-type tissue (n=10). But again an increase in mitochondrial size by about 40% was measurable when Pink1 function was lost. The average mitochondrial area per section for the *pink1* mutant was  $0.69 \mu\text{m}^2$  (n=175) versus  $0.49 \mu\text{m}^2$  for wild-type (n=174). It is also evident that the absolute values of ‘average mitochondrial area per section’ are lower for 5 dpf larvae compared to the values for adult animals (reported before), which must be due to differences in the number, distribution and/or size of mitochondria during tissue development.

Taken together, it can be concluded that loss of Pink1 function in zebrafish is linked to moderate but significant alterations in mitochondrial ultrastructure. An increase in mitochondrial size is already detectable during larval development, indicating that Pink1 is required for mitochondrial integrity from early developmental stages onwards. Furthermore, the internal mitochondrial structure is quite heterogeneous in adult mutant tissue. Compensatory mechanisms seem to be effective and must ensure that not all mitochondria are defective. In line with this conclusion, myofibrils within muscle fibres in the mutant had a normal arrangement. As well, the overall appearance and behaviour of adult *pink1* mutant zebrafish were inconspicuous, with no obvious defects in swimming behaviour, fertility or viability (observations by the Bandmann group).

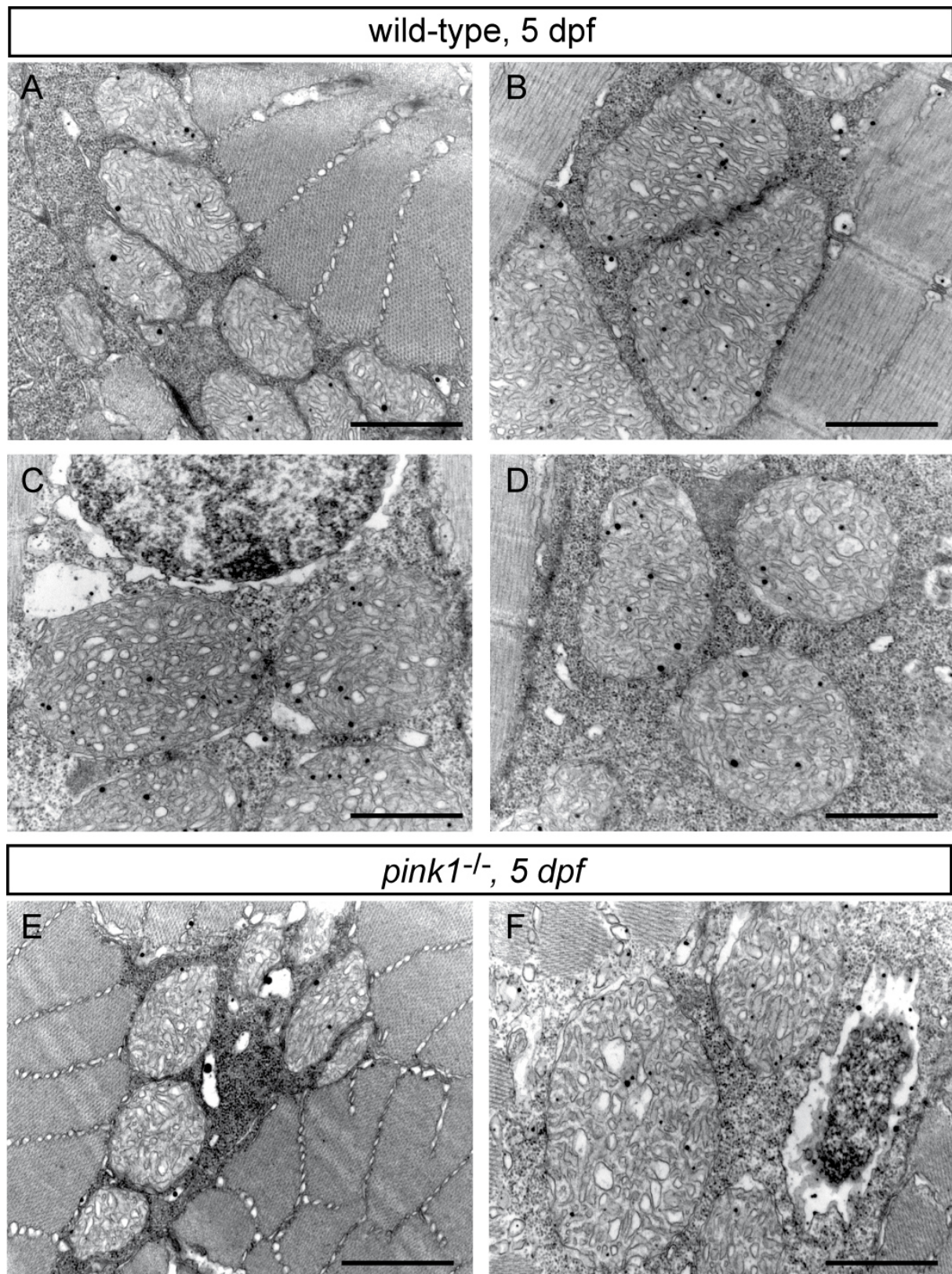
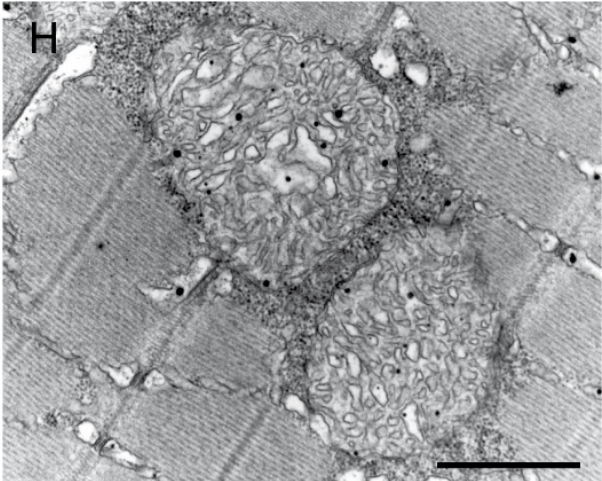
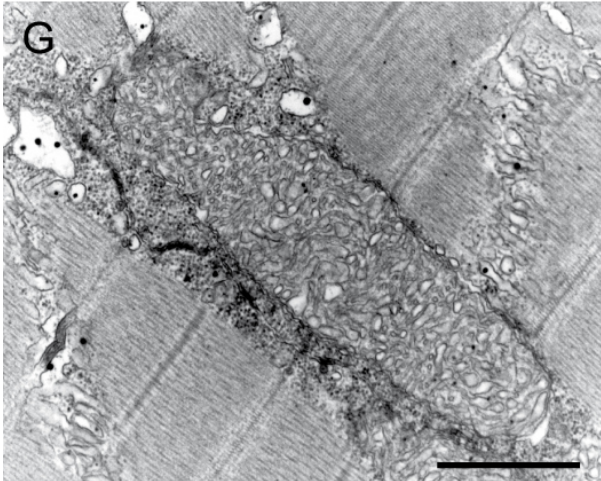


**Figure 40. Mitochondrial ultrastructure in muscle tissue of *pink1*<sup>-/-</sup> larvae resembles that of wild-type mitochondria.** A to D Electron micrographs depict mitochondria in muscle tissue of 5-days-old wild-type larvae. Mitochondria have a homogeneous appearance. E to H Mitochondria within muscle tissue of 5 dpf *pink1* mutant larvae also appear homogeneous. Few mitochondria show swollen intracristal luminal spaces (F and H, but also in D). Scale bars, 1  $\mu$ m.

*pink1*<sup>-/-</sup>, 5 dpf



## 4 Discussion

### 4.1. Zebrafish Swims into Focus as a New Parkinson's Disease Model

*Danio rerio* has orthologs for more than 80% of all annotated human disease genes (Howe *et al.*, 2013), and it is now increasingly being used as a vertebrate model to decipher the cellular and molecular processes of diverse human pathologies, including cancer, cardiovascular diseases, infectious diseases and inflammation, neurologic and neurodegenerative diseases and many more (Sager *et al.*, 2010; Meijer and Spaink, 2011; Xi *et al.*, 2011; Goldsmith and Jobin, 2012; Santoriello and Zon, 2012; Norton, 2013; Schmid and Haass, 2013; Asnani and Peterson, 2014; Phillips and Westerfield, 2014).

In this study, an effort was made to generate a transgenic neurodegeneration model in zebrafish based on expression of the Parkinson's disease-linked dominant mutant allele *LRRK2(G2019S)*. We wanted to make use of the Gal4/UAS system and generate two independent transgenic lines. A novel neuron-specific driver line could be established, which expresses KalTA3, an improved version of Gal4, in many central and peripheral neurons. Additionally, a trifunctional effector construct was assembled, which induces UAS-regulated expression of two subcellular fluorescent markers to visualize mitochondria and autophagosomes. At the same time, expression of the mutant disease gene (or a control allele) could be achieved. By combining these genetic tools, an *in vivo* time-lapse imaging procedure in transiently transgenic larval zebrafish was established, to be able to observe an effect of the disease gene on mitochondrial transport in long axons of the posterior lateral line nerve. A negative influence of *LRRK2(G2019S)* expression on transport velocities was not evident under the experimental conditions used. At the same time, new insights into this fast intracellular logistics process in axons could be gained. With few adjustments our experimental system can be employed in future experiments to analyse the influence of different genetic or environmental factors on mitochondrial axonal transport *in vivo*.

A second zebrafish disease model with a loss-of-function mutation in the *pink1* gene was analysed in this study and provided ultrastructural indications that mitochondria are adversely affected in this recessive form of PD. The characteristic neurodegeneration of dopaminergic neuronal circuits required for motor regulation, however, could not be observed in the course of this thesis.

## 4.2. Mapping *LRRK2* Gene Expression

What is known about *LRRK2* expression in humans and in rodent tissue? In humans, *LRRK2* mRNA is expressed in all adult tissues analysed by Northern blotting and RT-PCR, with stronger expression in lung and kidney. The transcript is detectable with variable expression levels in many brain regions, albeit at lower levels than in other organs analysed (Paisán-Ruíz *et al.*, 2004; Zimprich *et al.*, 2004). Human brain regions with strong *LRRK2* expression are striatum and cerebral cortex. Lower expression could be detected in the *substantia nigra pars compacta* (Biskup *et al.*, 2006). In the mouse, distinct expression was detectable in adult animals in many different organs, including the brain. Expression levels are highest in adult kidney and lung, which is in accordance to the human results. *Lrrk2* protein could clearly be visualized by Western blot analysis in rat kidney, whereas protein levels were lower in other tissues (Biskup *et al.*, 2006 and 2007). In adult mouse and rat brain, highest *Lrrk2* expression was present in regions of the forebrain, namely striatum, cortex and hippocampus, as well as in the cerebellum of the hindbrain, as detected by ISH and IHC (Biskup *et al.*, 2006; Giesert *et al.*, 2013). Similar to humans, the SNpc showed only comparable low level of expression. During mouse embryonic development *Lrrk2* mRNA expression was first detectable after embryonic day 15, when measured by whole-embryo Northern blotting (Biskup *et al.*, 2007). *Lrrk2* transcripts were detected by ISH in the developing kidney, lung, liver and heart. Of note, Giesert *et al.*, 2013, could not detect *Lrrk2* expression in the developing brain by high-sensitive radioactive *in situ* hybridization on tissue sections. Others, too, were unable to detect *Lrrk2* protein in the brain before embryonic day 17, as observed on Western blots of whole-brain lysates (Biskup *et al.*, 2007). *Lrrk2* therefore does not seem to play a major role during early brain development. In fact, *Lrrk2* knockout mice develop normally and without any conspicuous phenotype; and they show normal growth and survival (Tong *et al.*, 2010; Hinkle *et al.*, 2012). In summary, the authors of the human and rodent studies state that *LRRK2* is widely expressed throughout the adult brain and in peripheral tissues, albeit at low expression levels. During embryogenesis detection is restricted to non-neuronal tissues.

As shown in this study, zebrafish expresses the *lrrk2* ortholog from early developmental stages onwards. Low expression levels could be detected in embryos and larvae in our hands, which is similar to the rodent and human situation. In contrast to our results, the strong *lrrk2* mRNA signal in the developing zebrafish brain documented by Sheng *et al.*, 2010, requires further proof. A repeated *in situ* hybridization analysis with a different antisense probe should be performed to clarify the issue. To enhance signal intensity two or three antisense probes from different regions of the transcript can be used in the same hybridization reaction.

Sheng and coworkers also detected *lrrk2* mRNA and protein in adult zebrafish brain, gut, muscle and ovary – albeit at varying levels depending on the detection mode (Sheng *et al.*, 2010). Due to time limitations, such analyses of adult tissue have not been done in this study, but the results will be interesting in the future. *In situ* hybridization of adult brain could provide more precise information on the expression of this gene than RT-PCR and Northern blotting – especially as long as a good antibody to detect zebrafish Lrrk2 is still missing. The recently available and now well-established monoclonal antibody MJFF#2 (developed with support of The Michael J. Fox Foundation for Parkinson’s Research) detects human, mouse and rat LRRK2, and has to be tested for its crossreactivity with the zebrafish protein.

In summary, due to the high degree of conservation between human and zebrafish *LRRK2*, concerning genomic organisation, coding sequence (between 53% and 71% amino acid identity in the catalytic domains; Sheng *et al.*, 2010) and expression, it can be presumed that zebrafish Lrrk2 is an integral part of signalling pathways that are very similar between human and zebrafish.

### **4.3. Setting the Stage for *in vivo* Imaging of Mitochondrial Axonal Transport**

#### **4.3.1. A novel neuronal driver line with advantages and handicaps**

In this study, we were able to generate the neuronal driver line, *Tg(NBT:H2B-TagBFP-T2A-KalTA3)*; and all necessary components – NBT promoter, H2B-TagBFP and KalTA3 – had been established and were available in our laboratory. A subsequent detailed analysis confirmed that this line was suitable to drive neuronal expression of UAS-regulated target genes. On the other hand, several weaknesses of the line emerged, setting it aside from being an ideal and stable neuronal driver line. A main drawback is that the *neuronal beta tubulin* promoter seems to activate only weak expression of its direct target gene. This weak activity was unforeseeable at the beginning of the project, as the same promoter induces a strong pan-neuronal red fluorescent protein signal from early developmental stages onwards in *Tg(NBT:DsRed)* line (Peri and Nüsslein-Volhard, 2008). The discrepancy can be explained by multiple concatemeric transgene insertions at a single genomic site in the latter line – a phenomenon observed in the past, when transgenic zebrafish were generated by stable integration of injected plasmid DNA (Stuart *et al.*, 1990). The first hint for a weak promoter activity in this study was already observed in the course of establishing the transgenic line. Expression of the blue fluorescent reporter was too weak to allow direct screening and selection of transgene-carrying larvae using a fluorescence stereo microscope. This is in

contrast to the fact that TagBFP is one of the best monomeric blue fluorescent proteins reported to date, with a brightness similar to that of commonly used EGFP (Subach *et al.*, 2008). Its targeting to the nucleus should further enhance signal intensity. A second indication and consequence of the weak NBT promoter emerged when we characterized the transgenic line by crossing it to UAS-GFP reporter fish. It became evident that selected F2 animals of *Tg(NBT:H2B-TagBFP-T2A-KalTA3)* did contain several copies of the transgene, integrated at different genomic loci to allow free segregation. The consequence is that this transgenic line is not stable, and will require permanent selection to maintain the desired expression level, which is only achieved in the presence of several transgenes.

It is also not clear why the Gal4/UAS system did not considerably amplify expression in double-transgenic offspring from a cross between the driver line and the UAS-GFP reporter. Concerning this, it was observed in our lab that the Gal4/UAS system is not always reliable (e.g. a Purkinje neuron-specific promoter regulated specific expression of a direct fluorescent reporter, whereas cell-type specific expression was not achieved, when the same promoter was used indirectly, via expression of KalTA4 and UAS sites; K. Namikawa, personal communication). So, it should be kept in mind to empirically test this expression system for each transgenic strategy. Additionally, it is known that position effects, mediated by the genomic context at the site of transgene integration, can affect the specificity and level of expression.

Nevertheless, our newly established *Tg(NBT:H2B-TagBFP-T2A-KalTA3)* line was useful to target neuronal expression of UAS-regulated effector genes. Although a complete pan-neuronal transgene expression could not be achieved, many central and peripheral neurons were reliably expressing the transactivator KalTA3. Such a mosaic transgene expression is quite common for transgenic animals, and it can be explained by position effects at the integration site. Due to their characteristic location and branching pattern, neurons of the peripheral nervous system could be reproducibly and unequivocally identified by NBT promoter-driven reporter expression. These were primary motoneurons, sensory neurons of the cranial ganglia, Rohon-Beard sensory neurons of the spinal cord, as well as neurons of the posterior lateral line (PLL). Concerning the expression level in the context of our disease model, a strong overexpression of mutant LRRK2 might induce unspecific, cytotoxic phenotypes. Lower, more physiologically relevant doses of the transgenic product were therefore appreciated, and our transgenic line seemed to drive expression in this range.

### 4.3.2. Alternative zebrafish lines for neuron-specific gene expression

To generate a novel transgenic driver line is a time consuming and laborious task and, as encountered in this study, the result might not always be satisfying. So, why not using one already established neuronal driver line? Many neuron-specific promoters have been characterized and employed in the past. One of the first driver lines to visualize neurons was established by Scheer *et al.*, in 2001, by using the a 6 kb promoter fragment from the *deltaD* gene, *Tg(dld:Gal4)*. This line encodes the full-length yeast Gal4 protein, which turned out to be a weak transcriptional activator in zebrafish. Because of this, none of the original Gal4 driver lines generated by Nico Scheer are used anymore. Other neuronal lines, either direct fluorescent reporter lines or a driver line, have been generated with the 3.2 kb fragment of the HuC promoter, including the transcriptional start site: *Tg(elavl3:GFP)*, *Tg(elavl3:Kaede)*, *Tg(elavl3:Gal4-VP16)* (Park *et al.*, 2000; Higashijima *et al.*, 2003; Sato *et al.*, 2006; Kimura *et al.*, 2008; Paquet *et al.*, 2009). This promoter is activating strong pan-neuronal expression from early differentiation onwards, and it has been successfully employed by many laboratories. The HuC:Gal4-VP16 driver line has recently been used to establish live imaging of cellular and subcellular neuro-pathogenic processes in a zebrafish tauopathy disease model (Paquet *et al.*, 2009; Plucińska *et al.*, 2012). However, it was observed by others that the full VP16 transactivation domain fused to the Gal4 DNA-binding domain produces a very strong transactivator. Gal4-VP16 might induce artificially high target gene expression, which can be detrimental to the organism (Distel *et al.*, 2009). Therefore, attenuated versions of the VP16 transactivation domain were generated (called TA2, TA3 and TA4), which are better tolerated by the organism. With these, a full collection of cell-type specific KalTA4-expressing driver lines has been provided by our laboratory through enhancer trapping, and several of the lines show expression in subsets of neurons (Distel *et al.*, 2009). However, these lines prohibit the use of a red fluorescent subcellular marker as they report their expression pattern with mCherry. Another point is that, if a suitable neuronal type for mitochondrial imaging had been identified in the beginning of the project, a corresponding neuron-specific promoter could have been identified and used. Plucińska and Paquet, for example, imaged Rohon-Beard sensory neurons innervating the tail fin to analyse mitochondrial transport recently (Plucińska *et al.*, 2012). These neurons can be labelled by expression from a pan-neuronal promoter, like the HuC or NBT promoter. Additionally, the *islet2b* promoter (Pittman *et al.*, 2008) or the somatosensory neuron-specific CREST3 enhancer from the *islet 1* gene (Uemura *et al.*, 2005) have been used to label these neurons. In this study, we identified the posterior lateral line nerve as an ideal system to study mitochondrial trafficking within long straight

axons. Development, function, degeneration and regeneration of PLL neurons has been extensively investigated with HuC promoter-driven fluorescent reporter constructs and transgenic lines (Sato *et al.*, 2006; Faucherre *et al.*, 2009; Villegas *et al.*, 2012). Single-cell resolution in the PLL could be achieved with these constructs, as well as labelling of subcellular structures, like, for example, mitochondria, as mentioned before (Sato *et al.*, 2010; Paquet *et al.*, 2009; Plucińska *et al.*, 2012). Another transgenic enhancer trap line, *hspGFF53A*, has been described, which expresses the Gal4FF variant of the transcriptional activator and which can drive expression of UAS-regulated target genes in PLL neurons (Pujol-Martí *et al.*, 2010).

Concluding, it can be stated that many promoter and enhancer elements are now available to activate target genes in subsets of neurons. However, a suitable pan-neuronal driver line with adjusted transactivation potential was not available at the beginning of this project. As LRRK2 is expressed in many brain regions and in different types of neurons in humans and other model organisms, we wanted to achieve a similar broad expression in our disease model. Such a pan-neuronal expression is also important in order to be able to observe any neurotoxic phenotype, as it is uncertain which neurons will be mainly affected by mutant LRRK2 in zebrafish. Our NBT-KalTA3 driver line was useful in this regard, but it also had its drawbacks. In the end, a different promoter, e.g. the HuC promoter, shall be tested in future attempts.

#### **4.3.3. Reaching the limit with tri-functional effector constructs**

Combination of two UAS-regulated expression cassettes through Gateway cloning yielded four different trifunctional effector plasmids. Owing to the T2A peptide the two reporter proteins, mitoTagRFP and Venus-LC3, were efficiently coexpressed from the first transcription unit. And they were targeted to their correct subcellular locations: mitoTagRFP to the mitochondrial network and Venus-LC3 to the cytoplasm, with subsequent transfer to autophagosomes upon autophagy induction. However, problems did occur with fluorescence imaging of the LRRK2-CFP variants expressed from the second transcription unit. Their signal was obscured by Venus-LC3 fluorescence bleaching into the CFP detection channel. A homogeneous cytoplasmic CFP signal could be detected in cell culture, when LRRK2-CFP fusion proteins were encoded by eukaryotic, CMV promoter-regulated expression plasmids. Studies by Biskup *et al.*, 2006, and Higashi *et al.*, 2007, reported a punctate cytoplasmic staining of endogenous LRRK2 as detected by anti-LRRK2 antibody staining in rat primary cortical neuronal cultures, and in brain tissue from rodents and humans. The authors

demonstrated that LRRK2-containing puncta partly represent mitochondria and lysosomes, as well as other unidentified intracellular structures. Such a mitochondrial staining was not observed with the overexpressed LRRK2 fusion proteins in our experiments. However, a careful characterization of the subcellular localization and staining pattern of LRRK2-Strep-CFP was not intended. Other studies documented that LRRK2 mainly is a cytosolic protein (~75%) with a smaller amount (~25%) localized at membranes (Biskup *et al.*, 2007; Berger *et al.*, 2010). Indeed, we could detect LRRK2 protein expressed from the effector constructs by Western blotting in cell-lysates prepared with standard low-salt extraction buffers, which is another indication that LRRK2-CFP is a soluble protein. Another observation on Western blots was that LRRK2 expression levels were drastically reduced compared to reporter protein levels encoded by the same construct. This was an indication that expression from the first transcription unit of the effector construct was more efficient than from the second unit. The low expression of LRRK2 might be due to the fact that the two transcription cassettes were positioned very close to each other on the same construct. Although the reporter protein cassette contains a 3' globin intron sequence to enhance expression as well as a polyadenylation sequence to terminate transcription, it can be assumed that its transcription will interfere with transcription initiation of the disease gene at the second UAS enhancer site by mechanical or sterical hindrance of initiation complex assembly. Hasegawa and Nakatsuji, 2002, describe that two transcription units in a single construct were expressed in an independent manner only, if insulator sequences are put at both ends of each expression unit. On the other hand, Köster and Fraser, 2001, did show that Gal4-VP16 efficiently activated coexpression of two UAS-dependent transgenes, when both expression cassettes were arranged in close proximity, and one after the other, on the same construct. Another more likely explanation for the low expression of LRRK2-CFP is that this fusion protein is encoded by a very long transcription unit of over 9 kb. It has been observed that the transcription and translation efficiency of long transgenes clearly is reduced compared to shorter sequences. Finally, we have hints from transgenic integration and expression studies that the 4xUAS(shuffled) sequence used in our constructs is a suboptimal transcriptional activation sequence. A similar observation was reported by colleagues in this lab for a different construct. With the 4xUAS(shuffled) sequence we had intended to avoid possible epigenetic inactivation of the transgene known to be induced by repetitive DNA sequences (Halpern *et al.*, 2008). The variable middle positions of the Gal4-binding consensus sequence (5' CGG-N<sub>11</sub>-CCG 3') were shuffled to have four different UAS sites arrayed. These sequences deviated from the optimized Gal4-binding 17-mer (5' CGG-AGTACTGTCCT-CCG 3'). Thus,

the combination of the shuffled sequences generates a weaker Gal4-activating sequence than the 4xUAS tandem array of identical, optimized Gal4-binding sites.

In the end, it was not clear if expression of the disease gene in our system would be sufficiently high to interfere with signalling pathways in zebrafish neurons. On the other hand, it is known from the literature that endogenous LRRK2 expression is very low in the brain compared to reference proteins (Biskup *et al.*, 2007).

For the subsequent establishment of mitochondrial transport imaging we followed a transient transgenic approach, as the effector constructs were suitable to label and observe mitochondria when injected into eggs of the newly-established NBT-KalTA3 driver line.

#### **4.3.4. Simplify your cloning and start with a transient transgenic approach first**

We extensively modified the Tol2kit vector system in this study to meet our needs, but the main advantage of the system was not exploited. The Tol2kit offers a quick-and-easy exchange and combination of many sequences cloned into different entry vectors (Kwan *et al.*, 2007). For example, a variety of promoter sequences (cloned in the first entry vector) can be quickly combined with different target genes (cloned in the second vector) and these can again be fused to different 3'-tags or fluorescent reporters (cloned into the third vector). The effector constructs compiled here could have been assembled in a more economical way by conventional cloning into a general Tol2 transposon vector (Kawakami, 2007). Next our strategy to assemble three effector functions into one construct was very ambitious, but seems to be feasible. However, the inefficient expression of the long LRRK2 transcription unit was problematic. This should have been considered by using a stronger upstream activating sequence composed of a tandem array of four or five optimized Gal4-binding sites. Finally, one of the advantages of zebrafish is that experimental results can be obtained quickly by using transient expression methods. This approach should be taken in the first place to test the feasibility of the experimental concept and the functionality of the constructs. Genomic integration of constructs can be achieved in this case (but is not necessarily required) by coinjection of transposon vectors together with Tol2 mRNA. If expression is regulated by a specific promoter from early developmental stages onwards, live imaging of injected embryos and larvae is feasible. An additional advantage of this system is a mosaic transgene expression in a limited number of cells. This DNA injection technique has been applied by many labs to resolve individual cells for structural or functional analyses (Nagiel *et al.*, 2008; Faucherre *et al.*, 2009; Pujol-Martí *et al.*, 2010). Such single-neuron imaging in an otherwise unstained background is preferred, when intricate structures (e.g. axonal and dendritic

projections) and/or motile cellular and subcellular events have to be analysed, as, for example, mitochondrial dynamics or autophagic degradation (Misgeld and Kerschensteiner, 2006; Misgeld *et al.*, 2007; Plucińska *et al.*, 2012). In the context of a stable transgenic line, where the disease gene is expressed in many cell types, an alternative method to enhance resolution and allow single cargo transport imaging is by using photoconvertible fluorescent proteins, like the green-to-red convertible protein Kaede or Dendra2 (Ando *et al.*, 2002; Gurskaya *et al.*, 2006). Indeed, mitochondria-targeted MitoKaede and MitoDendra have been used to analyse mitochondrial dynamics in animal disease models, with rat neuronal cultures and in tissue explants from transgenic mice (Magrané *et al.*, 2012; Marinković *et al.*, 2012).

The final aim when generating a disease model is, of course, to generate stable transgenic driver and effector lines; and this was the approach of this thesis. By crossing these lines an unlimited number of offspring can be generated, which will express the disease gene in a reproducible manner, and in many cells or throughout the body – depending on the driver line. This allows a wide spectrum of analyses to carefully characterize the phenotype, including histological and bioimaging studies, behavioural experiments and different omics profiling approaches. As soon as a suitable readout has been identified, an assay for high-throughput screening can be developed to allow identification of novel disease-modifying substances.

#### **4.4. Mitochondrial Speed Dating in the Posterior Lateral Line Nerve**

##### **4.4.1. Our standard operating procedure for mitochondrial transport imaging**

We performed transient expression experiments by injecting effector plasmids into eggs of the neuronal driver line, *Tg(NBT:H2B-TagBFP-T2A-KalTA3)*, to analyse the influence of mutant LRRK2 on mitochondrial axonal transport. This method generated a sparse transgene expression in one or a few neurons of injected animals. Which neuronal type could be used to establish axonal transport imaging? Imaging high-speed subcellular processes, like mitochondrial axonal transport, within elaborate 3D structures and with high resolution requires sophisticated 3D microscopic techniques for fast acquisition rates, like spinning disc confocal microscopy, single plane illumination microscopy, and their latest improvements (Gao *et al.*, 2012; Stehbens *et al.*, 2012; Wolenski and Julich, 2014). Alternatively, mitochondrial dynamics in two dimensional neuronal processes, for example when grown in tissue culture, are commonly recorded by wide-field fluorescence microscopy with a high speed video camera. Recently, the laboratory of Thomas Misgeld established mitochondrial transport imaging in Rohon-Beard (RB) sensory neurons in a transgenic reporter fish (Plucińska *et al.*, 2012). RB neurons innervating the skin of the tail fin have a superficial

location and a wide two-dimensional axonal field. However, their peripheral axonal processes are highly ramified and mitochondrial movement is very interrupted and discontinuous in the short axonal segments. In this study, axons of the posterior lateral line (PLL) nerve were identified as running straight and in a superficial position along both flanks of the larvae to allow recording in one imaging plane with a confocal laser scanning microscope. We established a reproducible time-lapse imaging procedure for mitochondrial axonal transport in PLL axons of larval zebrafish at 50-60 hpf, on the third day of development. Was this developmental time point chosen wisely concerning maturation of the nerve and functionality of the mechanosensory circuitry? Outgrowth and development of the PLL nerve takes place between 20 and 42 hpf, concomitantly with the migration of the PLL primordium. This cell cluster deposits 5 lateral and 2-3 caudal pro-neuromast sensory organs along its rostro-caudal migratory route (Metcalf, 1985; Gilmour *et al.*, 2004; Ghysen and Dambly-Chaudière, 2007). Sensory hair cell differentiation and ribbon synapse formation onto PLL afferent specifications proceeds within few hours after proneuromast deposition in an anterior-to-posterior chronological pattern. At the same time, myelination of PLL axons by Schwann cells takes place (Brösamle and Halpern, 2002; López-Schier *et al.*, 2004; Lyons *et al.*, 2005; López-Schier and Hudspeth, 2006; Sarrazin *et al.*, 2006; Nagiel *et al.*, 2008; Raphael *et al.*, 2010; Langworthy and Appel, 2012). At the end of embryonic development first hair cell afferent synapses have been established, and are potentially competent for neurotransmitter release. Treating larvae with one of the vital fluorescent dyes 4-Di-2-ASP or FM4-64, which are selectively taken up by mature hair cells, can be used to probe the maturity of the system (Sarrazin *et al.*, 2006; Nagiel *et al.*, 2008). Although our experimental time point was chosen early, and it has to be assumed that not all axons of the nerve were functionally connected to their target cells, it is known that larvae respond well to vibration-induced swimming tests at this developmental time point. And this is an indication that the PLL system works well and is functional. Another aspect of PLL neurons and axons is that they do not represent an absolutely homogeneous cell group. Instead, structural and functional heterogeneity has been reported, and the system is constantly upgraded throughout embryonic and larval development, and into adulthood, regarding the number of neurons and neuromasts (Ghysen and Dambly-Chaudière, 2007; Nagiel *et al.*, 2008; Faucherre *et al.*, 2009; Haehnel *et al.*, 2012; Liao and Haehnel, 2012). Each PLL neuron innervates many hair cells of the same polarity in either one or multiple neuromasts; PLL cell bodies and axonal diameters display a continuum of sizes, and they show different spontaneous spiking activities. The latter observation might also be linked to different degrees of axonal myelination. This

physiological heterogeneity of PLL neurons was not considered in this analysis. But our experimental system can be used to reveal the detailed mechanisms and fine tuning of mitochondrial transport dynamics depending on cell physiology and in response to neuronal activity, in future experiments.

#### **4.4.2. Obtaining the bigger picture with extensive data collection and evaluation**

For quantitative evaluation of mitochondrial motility we decided to concentrate on determining absolute velocities during phases of continuous movement (excluding pauses) and to generate values directly from confocal image files. With the focus on one transport parameter, only a limited view of the complex logistics process could be given, and subtle effects of the disease gene, affecting other parameters, could have been missed. As seen in studies presented by others, a plethora of transport parameters – always separated for anterograde and retrograde direction – can be collected: (1) % mobile mitochondria (% anterograde moving and % retrograde moving); (2) mitochondrial flux, also called transport rate, which is mitochondria passing a certain point per axon per time interval (e.g. mitochondria per min); (3) persistence of movement (time in seconds of continuous movement between pauses); (4) run length or distance travelled during continuous movement (in  $\mu\text{m}$ ); (5) stop frequency, as the number of stops during an observation period divided by the duration of that period; (6) average duration of stops between movements or total time spent pausing during an observation period (in seconds); (7) size distribution histograms of mobile mitochondria; (8) velocity distribution histograms of mobile mitochondria; (9) density of mitochondria per axonal stretch (e.g. number of mitochondria per 100  $\mu\text{m}$ ) (De Vos *et al.*, 2003; De Vos and Sheetz, 2007; Llorens-Martín *et al.*, 2011; Magrané *et al.*, 2012; Mórotz *et al.*, 2012; Shahpasand *et al.*, 2012). – Of course, data acquisition remains a laborious and time-intensive process. Therefore, best knowledge and handling of state-of-the-art assistant software programs (e.g. ImageJ by W. Rasband, NIH, Bethesda, USA; Object Image by N.Visscher, University of Amsterdam, The Netherlands; MetaMorph, Molecular Devices, Sunnyvale, USA) is required and an automated or semi-automated tracking routine would be preferred.

#### **4.4.3. The lack of a phenotype**

Expression of the disease gene from the effector construct had no effect on the velocity of mitochondria in any of the transport directions. This negative result or lack of a phenotype is problematic insofar, as it can be the case that the expression level of the disease gene was

insufficiently low. In fact, as described before, studies in cell culture had provided evidence that the two transcription units of the effector construct – reporter genes and disease gene – were not expressed to the same level. We performed *in situ* hybridization experiments with up to three probes per reaction to detect human *LRRK2(G2019S)* mRNA in injected embryos (data not shown) – but without success. This can be due to the fact that only single neurons were expressing the construct, which were probably too few to be visualized by standard whole-mount *in situ* hybridization.

Concluding, it has to be said that a final statement about an impact of *LRRK2(G2019S)* on axonal transport of mitochondria cannot be made from the experiments reported here. Further analyses with higher expression levels will be required to elucidate the neurotoxic mechanisms of this mutant protein.

#### **4.4.4. Moving our understanding of mitochondrial trafficking forward**

Mitochondrial transport analyses conducted in the past have mainly been performed with cell culture systems *in vitro*, for example, with differentiated neuronal cell lines (e.g. PC12, N2A cells) or with primary neuronal cultures from several different brain regions of embryonic or postnatal mouse or rat tissue, which have been induced to differentiate *in vitro*. The majority (60-80%) of mitochondria in neuronal processes are stationary in these systems. And the remaining motility has been characterized as bidirectional and saltatory movement, with short stretches of directed movement interrupted by longer pauses, and with frequent changes in transport direction (Morris and Hollenbeck, 1995; Hollenbeck and Saxton, 2005). This description of mitochondrial transport is perpetuated in the current literature (Sheng and Cai, 2012; Sheng, 2014). Evidence to the contrary was observed in our experiments. We found that the majority of mitochondria were mobile in the long axon tracts of the PLL nerve. At the same time, mitochondrial movement is quite continuous and persistent in one direction, either anterograde or retrograde. A reversal of transport direction of a moving mitochondrion within the axonal stretch in the field of view could hardly ever be observed. Although transport velocities do vary with faster and slower tracks, and occasional pausing can be observed, mitochondria usually resume their movement in the same direction. Unfortunately, these results were not quantified here, but other groups report a similar directional bias of moving mitochondria (Pilling *et al.*, 2006). So far, documented mean transport velocities were highly variable due to the different experimental systems used, and were in the range of 0.10 – 1.0  $\mu\text{m/s}$  (Morris and Hollenbeck, 1995; De Vos *et al.*, 2003; Frederick and Shaw, 2007; Falzone *et al.*, 2009; Kiryu-Seo *et al.*, 2010; Chang *et al.*, 2011; Llorens-Martín *et al.*,

2011; Ohno *et al.*, 2011; Kim *et al.*, 2012; Magrané *et al.*, 2012; Mórotz *et al.*, 2012; Shahpasand *et al.*, 2012). At the same time, differences between anterograde and retrograde transport have not been recognized, or might have been overlooked in these studies. Some authors even reported a slower retrograde transport velocity compared to the anterograde one (Falzone *et al.*, 2009; Kim-Han *et al.*, 2011; Ohno *et al.*, 2011). However, the picture is getting clearer with recent analyses in mature neurons of an intact nervous system. Several groups imaged and tracked mitochondria in motor neurons immediately after dissection of the *Drosophila* larval neuro-muscular system. Although velocity values were low in these experimental set-ups, with 0.13  $\mu\text{m/s}$  for anterograde and 0.3  $\mu\text{m/s}$  for retrograde transport, as reported by Liu *et al.*, 2012; or a mean anterograde velocity of 0.26  $\mu\text{m/s}$  and a mean retrograde velocity of 0.45  $\mu\text{m/s}$ , as published by Pilling *et al.*, 2006, evidence was provided that anterograde and retrograde transport have different characteristics. Retrograde movement is faster than anterograde movement and has a more irregular and discontinuous pattern. This fits to our data from posterior lateral line axons in zebrafish. We determined a mean anterograde transport speed of 0.93  $\mu\text{m/s}$  (95% confidence interval: 0.87-0.99  $\mu\text{m/s}$ ), while retrograde velocities were higher, with a mean value of 1.27  $\mu\text{m/s}$  (95% confidence interval: 1.21-1.34  $\mu\text{m/s}$ ). Additionally, we did characterize retrograde transport as discontinuous and “jumpy” – although these observations were not quantified. Retrograde transport shows a high variability in speed during short stretches of movement, and these are often interrupted by brief stops or pauses. Anterograde transport is more homogeneous; velocities lie within a smaller range and are contained over longer distances. This difference in mobility pattern is directly obvious on kymographs shown in this study and by other researchers (Pilling *et al.*, 2006; De Vos and Sheetz, 2007; Magrané *et al.*, 2012; Mórotz *et al.*, 2012). It is interesting to note that these differences in mitochondrial transport characteristics between anterograde and retrograde movement are in accordance with recent descriptions about the biochemical properties of the respective motor proteins – kinesins in charge of anterograde transport and dyneins managing retrograde transport. Kinesins have been described to move with a coordinated hand-over-hand stepping pattern along their microtubule tracts, while dyneins’ stepping pattern shows variable step sizes and is more uncoordinated, at least in reconstituted biochemical assays *in vitro* (Yildiz *et al.*, 2004; Yildiz *et al.*, 2008; DeWitt *et al.*, 2012; Walter and Diez, 2012).

On the other hand, we measured a broad range of velocities in our system for both transport directions: 0.64-2.82  $\mu\text{m/s}$  for anterograde transport, and 0.51-2.33  $\mu\text{m/s}$  for retrograde transport. Similar broad velocity distributions have been mentioned by other groups (De Vos

*et al.*, 2003; Shahpasand *et al.*, 2012). Pilling *et al.*, 2006, determined an anterograde speed range of 0.1-1.79  $\mu\text{m/s}$  and a retrograde range of 0.1-2.86  $\mu\text{m/s}$  for the *Drosophila* motor neuron system. An explanation for these results can be that multiple motor proteins with different intrinsic mechano-chemical properties contribute to the transport mechanism – and many of these proteins have yet to be identified.

How does our data fit to recent descriptions of other physiologically more relevant experimental set-ups? Misgeld and Kerschensteiner developed imaging techniques in transgenic mitoCFP or mitoYFP-expressing mice, using either acute intercostal nerve-muscle explants or imaging in living mice (Misgeld *et al.*, 2007; Kerschensteiner *et al.*, 2008). Although they report a high percentage of immobile axonal mitochondria (87%), an observation that is not true for mitochondria in the PLL nerve in zebrafish larvae, their velocity values are very similar to ours (anterograde velocity in tissue explants:  $1.02 \pm 0.02$   $\mu\text{m/s}$ , retrograde velocity:  $1.41 \pm 0.03$   $\mu\text{m/s}$ ). They also document that retrogradely moving mitochondria are a bit larger ( $1.69 \pm 0.03$   $\mu\text{m}$ ) than anterogradely moving ones ( $1.47 \pm 0.03$   $\mu\text{m}$ ). To this, we found that mitochondria on the retrograde track were on average by 0.278  $\mu\text{m}$  larger than mitochondria moving in anterograde direction. These results can contribute to the ongoing discussion about an imbalance between a higher mitochondrial flux (number per time interval) towards the synapse than the return rate, which has been reported for several systems (Pilling *et al.*, 2006; Misgeld *et al.*, 2007; Plucińska *et al.*, 2012). It also highlights the fact that precise size measurements are required to understand and elucidate mitochondrial turnover in neurons.

Plucińska and coworkers established tools to study the life cycle and motility of mitochondria in sensory neurons in transgenic mitoCFP-expressing zebrafish larvae (Plucińska *et al.*, 2012). They also showed results for mitochondrial movement disorders in a tauopathy disease model. When analyzing mitochondrial transport in the stem axon of Rohon-Beard sensory neurons, they provide quantitative evidence that retrograde transport is faster ( $0.92 \pm 0.02$   $\mu\text{m/s}$ ) than anterograde transport ( $0.77 \pm 0.01$   $\mu\text{m/s}$ ), and at the same time it is more discontinuous, with more frequent and longer pauses. Later they imaged mitochondria in distal parts of RB axonal arbors, and here they determined a higher velocity value of around 1.25  $\mu\text{m/s}$  (exact numbers were not provided) for the combined antero- and retrograde movement. The drawbacks when observing mitochondria in distal parts of sensory neurons is that they are hardly moving within the high-order axonal branches (percentage of moving mitochondria:  $1.03 \pm 0.12\%$ ). Additionally, run-lengths are short and no continuous movement can be evaluated. In the end, a word of caution shall be raised not to pool velocity data for

anterograde and retrograde mitochondrial movement, as these are mechanistically distinct processes with fundamentally different characteristics, as described here.

Concluding remarks about our experimental system follow, as it provides a sea of options for future experiments. Long neuronal processes are ideally suited to characterize mitochondrial mobility parameters, such as direction, duration and persistence of movement. PLL axons of larval zebrafish are integrated into functional neuronal circuits and networks *in vivo*, and can be observed in their entirety from postsynaptic specializations onto hair cells to central synapses in the hindbrain. At the same time, they can easily be manipulated by a huge repertoire of experimental strategies, e.g. diverse genetic manipulations, drug application to the rearing medium, mechanical stimulation of upstream sensory hair cells or electrical stimulation, laser ablation and many more. Mitochondrial motility can be studied in different parts of the axon – from the axon initial segment and the proximal part, to more distal parts and into the dendritic specializations. The influence of myelination, de- and re-myelination can be analysed as zebrafish is known for its high regenerative potential. Finally, more subtle effects of neuronal physiology on mitochondrial trafficking could be studied. PLL neurons with a range of different cell and axonal diameters exist; they show different degrees of myelination and different neuronal firing rates.

## **4.5. The Pink1 Loss-of-function Mutant**

### **4.5.1. Mitochondrial form follows function in homeostasis and disease**

The first genetic animal models for PINK1 loss of function were generated in *Drosophila*. In 2006, three research groups reported severe degenerative pathologies and PD-associated behavioural changes in adult PINK1 null mutant flies (Clark *et al.*, 2006; Park *et al.*, 2006; Yang *et al.*, 2006). As revealed by electron microscopy, mitochondria within the indirect flight muscle were grossly enlarged; they had a “brighter”, hollow appearance due to the disintegration of internal cristae membranes and larger inter-cristae luminal spaces. These structural defects coincided with severely compromised mitochondrial function and a resultant energy deficiency. In contrast to this severe phenotype in flies, mitochondria in tissues from *PINK1* knockout mice do not show overt morphological and ultrastructural abnormalities, although different functional defects have been described (Kitada *et al.*, 2007; Gautier *et al.*, 2008). In addition, PINK1-deficient mice do not recapitulate major motor dysfunctions, as well as the underlying dopaminergic neurodegeneration in the SNpc characteristic for the human condition (Kitada *et al.*, 2007; Zhou *et al.*, 2007; Gispert *et al.*, 2009; Glasl *et al.*, 2012). Specifically to elucidate pathological changes at the level of the

mitochondria, a more suitable vertebrate model would be required. In this study, we provide evidence that mitochondria in muscle tissue of Pink1 loss-of-function mutant zebrafish exhibit clear ultrastructural abnormalities that worsen with age. While an increase in mitochondrial size was already observable in larval fish – and persists in adult tissue – the internal organisation of cristae membranes is not affected at the early developmental stage. This phenotype changes at the age of six months, when mitochondria with a “brighter”, less electron dense internal structure can be detected in the mutant. These mitochondria contain enlarged inter-cristae luminal spaces, similar to but not as severe as what has been described for the *Drosophila* model, and they are intermingled with normal looking mitochondria. At the same time, mitochondrial functional deficits, namely reduced respiratory complex I and complex III activity, were reported by Flinn *et al.*, 2013, for this *pink1* mutant zebrafish line at the larval stage and in adults. These defects are a clear indication that Pink1 is involved in maintaining mitochondrial homeostasis from early developmental stages onwards. In this regard, it can be assumed that homeostasis is different in the growing larval muscle, where it is tilted towards mitochondrial biogenesis, compared to adult muscle, where anabolic and catabolic processes must be more balanced. This might explain why Pink1 deficiency is likely to have different effects for the two physiological conditions. Pink1 could possibly affect many aspects of mitochondrial function; these are mitochondrial biogenesis, respiratory chain function and ATP synthesis, calcium homeostasis, mitochondrial dynamics (the fission-fusion balance), active transport processes, mitochondrial autophagy and, finally, a role in apoptosis. Can the observed mitochondrial ultrastructural abnormalities in PINK1 loss-of-function mutants provide any clues to the precise role of PINK1? Or is it a more general ‘mitochondrial dysfunction’ phenotype? In this regard it is interesting to note that similar ultrastructural abnormalities such as enlarged mitochondria lacking organized cristae have been reported for cells defective in the autophagy regulator Atg7 (Jung *et al.*, 2008; Wu *et al.*, 2009) and for neurons lacking the GTPase Mitofusin 2, which is required for mitochondrial outer membrane fusion (Chen *et al.*, 2007). These two processes are intimately intertwined as mitochondrial fission is required for mitophagy, and PINK1 has been shown to affect and regulate both of them. Actually, it has recently been revealed that PINK1-phosphorylated Mfn2 is a Parkin receptor for removing damaged mitochondria (Chen and Dorn, 2013), and that mitofusins (Mfn1 and Mfn2) are degraded during mitophagy (reviewed by Pilsl and Winklhofer, 2012; de Vries and Przedborski, 2013). On the other hand, molecular redundancies for PINK1 function and compensatory mechanisms must be operative in tissues from *PINK1* knockout mice and in human PD patients, which preclude any mitochondrial

morphological phenotype. These fail-safe mechanisms could be tricked by acute disruption of PINK1 protein levels. Such an acute knockdown of PINK1, for example by RNA interference in cultured human and mouse cells, induced a fragmented mitochondrial morphology and ultrastructural abnormalities similar to the ones described before, namely occasional enlarged organelle profiles with a diminished number of cristae membranes (Exner *et al.*, 2007; Dagda *et al.*, 2009; Lutz *et al.*, 2009). These morphological alterations were accompanied by functional impairments. A loss of mitochondrial transmembrane potential, a decrease in cellular ATP production and an increase in reactive oxygen species (ROS) were observed in the *in vitro* cell culture experiments. Similarly, in primary fibroblasts from patients with homozygous *PINK1* mutations oxidative stress markers were found upregulated, and, as a putative cause, a mild decrease in complex I activity could be detected (Hoepken *et al.*, 2007). Again, these results are in accordance with data from post-mortem tissue of PD patients (Schapira *et al.*, 1989; Giordano *et al.*, 2014).

Despite the obvious mitochondrial defects in Pink1-deficient zebrafish, compensatory mechanisms must be active here, too, as the overall arrangement of myofibrils and the integrity of muscle tissue were not affected. However, it might still be the case that other cells types and tissues are more susceptible to loss of Pink1 function, like, for example, dopaminergic neurons with their high endogenous burden of oxidative stress.

#### **4.5.2. Are DA neurons in zebrafish brain in the pink?**

Results concerning this question were conflicting in our *pink1*<sup>-/-</sup> zebrafish model. While scientists from the collaborating Bandmann group reported a 25% reduction of diencephalic DA neurons in Cluster 1, 2, 4 and 5 in larval *pink1*<sup>-/-</sup> zebrafish at 5 dpf, we found no reduced cell numbers after counting four characteristic diencephalic DA clusters (Cluster 1, 2, 4 and 6) in adult zebrafish at 6 months of age. However, it has to be stated that the results presented in this study are not supported by statistical analysis, as only two animals were analysed per genotype. Then again, quantification of two small DA cell groups (Cluster 3 and 4), of only 20 to 30 neurons each, by a colleague in this lab yielded results for a specific cell loss in older mutant animals at 18 months of age (Flinn *et al.*, 2013). Cells of Cluster 4, thought to be homologous to the mammalian midbrain dopaminergic system of the SNpc, were reduced in number by 45% in the mutant and this data reached statistical significance. Cluster 3 DA neuron counts were also found reduced in the mutant. It would be interesting to know, if the neuronal loss, especially in larvae, is linked to any motor behaviour phenotype. So far, the escape response of larvae after tactile stimulation or the spontaneous swimming activity of

larvae or aged adult fish with loss of Pink1 was not investigated. Impairments of locomotor function were observed in Morpholino-mediated Pink1 knockdown experiments by two groups. Anichtchik *et al.*, 2008, also reported a reduction of DA neurons by 37% in Morpholino-injected larvae at 2 dpf, while Xi *et al.*, 2010, did observe a small neuronal loss, affecting Cluster 1 cells only. Instead, the latter group presented a patterning defect, with mislocated DA neurons and shortened or lost axonal processes, as the presumptive cause of the locomotor dysfunctions. Interestingly, Anichtchik and coworkers, too, reported loss of axonal tracts distributed over the brain and spinal cord as a characteristic phenotype in the Morpholino-treated Pink1-knockdown larvae. Even for our stable genetic disease model it cannot be completely ruled out that the observed reduction in DA cell counts in 5 dpf larvae is due to retarded DA neuron development or defective neuronal growth and patterning. Concerning the quantification of tyrosine hydroxylase-expressing neurons in whole-mount larval specimen, immuno-fluorescence detection in combination with confocal microscopy is recommended over colorimetric *in situ* hybridization analyses (Fett *et al.*, 2010). For a more refined histological resolution in larvae, tissue sections of larval brain will be required (Rink and Wullmann, 2002b). Such an inspection of serial sections is the only way to count neurons in adult zebrafish brain. For mice and humans unbiased stereological methods have been established and computer-aided image analysis systems are available to determine neuron numbers in large brain volumes (Schmitz and Hof, 2005; Hou *et al.*, 2012). With such a system, defined samples of the total cell population (e.g. brain region) have to be counted, and subsequent extrapolation provides the total cell number. However, stereological estimation of cell number is not established for zebrafish. To quantify DA neurons in characteristic diencephalic clusters of adult brain, we counted TH-immunoreactive cells on all available serial cross sections covering each cluster. Some bias (systematic error) was likely introduced in the quantification as, for example, neuron fragments located at the upper and lower surface of a section might have been counted twice on consecutive sections. But this was not problematic, as obtaining exact total cell numbers was not the specific goal. For qualitative pathological comparisons it is adequate, if samples from wild-type and mutant are treated and analyzed identically. In this regard, problems did occur in our study due to lost and damaged tissue sections. The resultant cell counts for animals at 6 months of age were too variable, and not enough brains have been analysed to be able to draw a final conclusion. In summary, DA neuron counts in larvae and aged adults, as provided by our collaborators and by a colleague in this lab, point towards a specific dopaminergic neurodegeneration in *pink1* mutant zebrafish. Recently developed recessive gene knockout rat models also

recapitulate the major dopaminergic neuron loss in the SNpc characteristic for the human disease. And this is in contrast to the more convenient mouse models, which do not recapitulate this degenerative phenotype (Kitada *et al.*, 2007; Glasl *et al.*, 2012; Dave *et al.*, 2014). With our stable zebrafish line an experimentally amenable vertebrate is now available to further elucidate cellular and molecular disease mechanisms.

#### **4.6. A Final Glance at Pink1 and Lrrk2, and future perspectives**

By screening NCBI's PubMed in October 2014, the latest trends concerning PINK1 and LRRK2 functions are summarized here briefly. Mitophagy stays at the center of the PINK1 (and Parkin) universe. The list of regulators and interaction partners in the PINK1/Parkin mitophagy pathway is constantly growing, and the exact details of the process are refined. For example, the anti- and pro-apoptotic mitochondrial regulators of the Bcl-2 family can interfere in mitophagy. Prosurvival members of the Bcl-2 family (e.g. Bcl-xL and Mcl-1) inhibited Parkin translocation to damaged mitochondria, while BH3-only proteins enhanced Parkin recruitment (Hollville *et al.*, 2014). Essential E2 ubiquitin-conjugating enzymes upstream of Parkin have been identified (Geisler *et al.*, 2014), and the mitochondrial deubiquitinase USP30 acts as a major opponent for Parkin-mediated ubiquitination (Bingol *et al.*, 2014). Another hot story uncovered by different groups is that PINK1 not only phosphorylates Parkin at its N-terminal ubiquitin-like domain, but PINK1 is the first described ubiquitin kinase. Phosphorylated ubiquitin in turn is required for full activation of Parkin E3 ubiquitin ligase activity and for Parkin translocation to damaged mitochondria (Kane *et al.*, 2014; Kazlauskaitė *et al.*, 2014; Koyano *et al.*, 2014). On the other hand, the relevance of PINK1/Parkin-mediated mitophagy in neurons remains controversial, and defective mitophagy may not be the sole cause leading to dopaminergic neurodegeneration in PD (Scarffe *et al.*, 2014). All aspects of mitochondrial function and quality control have to be considered. The regulation of oxidative phosphorylation, the fission-fusion balance, transport, biogenesis and degradation are mechanistically interwoven, and they are all affected by loss of PINK1 function. With our Pink1 deficient zebrafish line and the live fluorescent staining tools established in this thesis, several aspects of mitochondrial homeostasis in the context of PD can now be addressed *in vivo*.

The multidomain protein LRRK2 continues to be involved in diverse cellular pathways and may have multiple functions. Repeatedly, a role in intracellular vesicle trafficking is supported, in which – depending on the experimental strategy – all different kinds of vesicles have been involved: from ER-Golgi transport, Golgi-derived vesicles and protein sorting, to

the endo-lysosomal system and autophagic vesicles (Beilina *et al.*, 2014; Cho *et al.*, 2014; Gómez-Suaga *et al.*, 2014). In neurons, synaptic vesicle exo- and endocytosis were affected by LRRK2 dysfunction (Matta *et al.*, 2012; Cîrnaru *et al.*, 2014), and LRRK2 binds to synaptic vesicle-associated proteins via its WD40 domain (Piccoli *et al.*, 2014). Then again, a direct interaction with three  $\beta$ -tubulin isoforms mediated by the Roc domain and modulation of dynamic microtubules within growth cones was reported by Law *et al.*, 2014. Within growth cones and during synaptogenesis the actin cytoskeleton, too, is indirectly affected by LRRK2 malfunction via dysregulation of tropomyosin 4 and/or protein kinase A activity (Häbig *et al.*, 2013; Parisiadou *et al.*, 2014). In one recent study published in *Cell* by Martin *et al.*, 2014, pathogenic LRRK2(G2019S) induced an aberrant increase in mRNA translation by phosphorylating ribosomal protein s15, and this bulk protein synthesis was linked to neurodegeneration. LRRK2, which is widely expressed throughout the body, might have different functions in different cell types due to different interaction partners. For example, many of the aforementioned intracellular vesicular and cytoskeletal dynamics have to be tightly orchestrated in cells of the immune system, and a role of LRRK2 in these cells and in inflammatory processes has been repeatedly described (reviewed by Russo *et al.*, 2014). Additionally, autophagy and autophagic abnormalities are a constant observation in LRRK2 functional analyses *in vitro* and *in vivo* (Manzoni *et al.*, 2013; Schapansky *et al.*, 2014). Here an intersection with PINK1-regulated pathways is evident. However, it remains to be determined, which of the many LRRK2 functions is mainly affected in dopaminergic neurons in the context of Parkinson's disease. Especially to observe dynamic intracellular pathogenic processes, a good vertebrate LRRK2 model is still urgently required. And the transgenic zebrafish line and genetic tools established in this thesis have paved the way to reach this goal.

## **5 Supplementary Movies**

In order to document the confocal time-lapse recordings of mitochondrial axonal transport within the posterior lateral line nerve, four movies are provided as supplementary material on a CD. Each movie shows an axonal stretch of 56  $\mu\text{m}$ . Anterior is always to the left. Therefore, anterograde transport proceeds from left to right and retrograde transport is from right to left. The total time interval for each recording was 10 min and frames were captured every 2 seconds. All files are in Apple QuickTime format.

**Movie S1 and S2** were recorded from PLL axons of larvae injected with the control effector plasmid, which contains no LRRK2 sequence (fish 15 and 16, respectively).

**Movie S3 and S4** were recorded from animals injected with the LRRK2(G2019S)-expressing effector plasmid (animal 23 and 24, respectively).

## 6 References

- Alegre-Abarrategui, J., Christian, H., Lufino, M.M., Mutihac, R., Venda, L.L., Ansorge, O., and Wade-Martins, R. (2009). LRRK2 regulates autophagic activity and localizes to specific membrane microdomains in a novel human genomic reporter cellular model. *Hum. Mol. Genet.* *18*, 4022-4034.
- Amores, A., Force, A., Yan, Y.L., Joly, L., Amemiya, C., Fritz, A., Ho, R.K., Langeland, J., Prince, V., Wang, Y.L., Westerfield, M., Ekker, M., and Postlethwait, J.H. (1998). Zebrafish hox clusters and vertebrate genome evolution. *Science* *282*, 1711-1714.
- Anand, V.S., Reichling, L.J., Lipinski, K., Stochaj, W., Duan, W., Kelleher, K., Pungaliya, P., Brown, E.L., Reinhart, P.H., Somberg, R., Hirst, W.D., Riddle, S.M., and Braithwaite, S.P. (2009). Investigation of leucine-rich repeat kinase 2 : enzymological properties and novel assays. *FEBS J.* *276*, 466-478.
- Ando, R., Hama, H., Yamamoto-Hino, M., Mizuno, H., and Miyawaki, A. (2002). An optical marker based on the UV-induced green-to-red photoconversion of a fluorescent protein. *Proc. Natl. Acad. Sci. USA* *99*, 12651-12656.
- Andres-Mateos, E., Perier, C., Zhang, L., Blanchard-Fillion, B., Greco, T.M., Thomas, B., Ko, H.S., Sasaki, M., Ischiropoulos, H., Przedborski, S., Dawson, T.M., and Dawson, V.L. (2007). DJ-1 gene deletion reveals that DJ-1 is an atypical peroxiredoxin-like peroxidase. *Proc. Natl. Acad. Sci. USA* *104*, 14807-14812.
- Anichtchik, O., Diekmann, H., Fleming, A., Roach, A., Goldsmith, P., and Rubinsztein, D.C. (2008). Loss of PINK1 function affects development and results in neurodegeneration in zebrafish. *J. Neurosci.* *28*, 8199-8207.
- Asakawa, K., and Kawakami, K. (2008). Targeted gene expression by the Gal4-UAS system in zebrafish. *Dev. Growth Differ.* *50*, 391-399.
- Ascherio, A., Zhang, S.M., Hernán, M.A., Kawachi, I., Colditz, G.A., Speizer, F.E., and Willett, W.C. (2001). Prospective study of caffeine consumption and risk of Parkinson's disease in men and women. *Ann. Neurol.* *50*, 56-63.
- Asnani, A., and Peterson, R.T. (2014). The zebrafish as a tool to identify novel therapies for human cardiovascular disease. *Dis. Model Mech.* *7*, 763-767.
- Balgi, A.D., Fonseca, B.D., Donohue, E., Tsang, T.C., Lajoie, P., Proud, C.G., Nabi, I.R., and Roberge, M. (2009). Screen for chemical modulators of autophagy reveals novel therapeutic inhibitors of mTORC1 signaling. *PLoS One* *4*, e7124.
- Bampton, E.T., Goemans, C.G., Niranjana, D., Mizushima, N., and Tolkovsky A.M. (2005). The dynamics of autophagy visualized in live cells: from autophagosome formation to fusion with endo/lysosomes. *Autophagy* *1*, 23-36.
- Baron, U., Gossen, M., and Bujard, H. (1997). Tetracycline-controlled transcription in eukaryotes: novel transactivators with graded transactivation potential. *Nucleic Acids Res.* *25*, 2723-2729.
- Beilina, A., Rudenko, I.N., Kaganovich, A., Civiero, L., Chau, H., Kalia, S.K., Kalia, L.V., Lobbstaël, E., Chia, R., Ndukwe, K., Ding, J., Nalls, M.A.; International Parkinson's Disease Genomics Consortium, North American Brain Expression Consortium et al. (2014). Unbiased screen for interactors of leucine-rich repeat kinase 2 supports a common pathway for sporadic and familial Parkinson disease. *Proc. Natl. Acad. Sci. USA* *111*, 2626-2631.
- Berger, Z., Smith, K.A., and LaVoie, M.J. (2010). Membrane localization of LRRK2 is associated with increased formation of the highly active LRRK2 dimer and changes in its phosphorylation. *Biochemistry* *49*, 5511-5523.
- Berry, C., La Vecchia, C., and Nicotera, P. (2010). Paraquat and Parkinson's disease. *Cell Death Differ.* *17*, 1115-1125.

- Betarbet, R., Sherer, T.B., MacKenzie, G., Garcia-Osuna, M., Panov, A.V., and Greenamyre, J.T. (2000). Chronic systemic pesticide exposure reproduces features of Parkinson's disease. *Nat. Neurosci.* *3*, 1301-1306.
- Bill, B.R., Petzold, A.M., Clark, K.J., Schimmenti, L.A., and Ekker, S.C. (2009). A primer for morpholino use in zebrafish. *Zebrafish* *6*, 69-77.
- Bingol, B., Tea, J.S., Phu, L., Reichelt, M., Bakalarski, C.E., Song, Q., Foreman, O., Kirkpatrick, D.S., and Sheng, M. (2014). The mitochondrial deubiquitinase USP30 opposes parkin-mediated mitophagy. *Nature* *510*, 370-375.
- Biskup, S., Moore, D.J., Celsi, F., Higashi, S., West, A.B., Andrabi, S.A., Kurkinen, K., Yu, S.W., Savitt, J.M., Waldvogel, H.J., Faull, R.L., Emson, P.C., Torp, R., Ottersen, O.P., Dawson, T.M., and Dawson, V.L. (2006). Localization of LRRK2 to membranous and vesicular structures in mammalian brain. *Ann. Neurol.* *60*, 557-569.
- Biskup, S., Moore, D.J., Rea, A., Lorenz-Deperieux, B., Coombes, C.E., Dawson, V.L., Dawson, T.M., and West, A.B. (2007). Dynamic and redundant regulation of LRRK2 and LRRK1 expression. *BMC Neurosci.* *8*: 102.
- Biskup, S., and West, A.B. (2009). Zeroing in on LRRK2-linked pathogenic mechanisms in Parkinson's disease. *Biochim. Biophys. Acta* *1792*, 625-633.
- Bové, J., and Perier, C. (2012). Neurotoxin-based models of Parkinson's disease. *Neuroscience* *211*, 51-76.
- Braak, H., Del Tredici, K., Rüb, U., de Vos, R.A., Jansen Steur E.N., and Braak, E. (2003). Staging of brain pathology related to sporadic Parkinson's disease. *Neurobiol. Aging* *24*, 197-211.
- Braak, H., Ghebremedhin, E., Rüb, U., Bratzke, H., and Del Tredici, K. (2004). Stages in the development of Parkinson's disease-related pathology. *Cell Tissue Res.* *318*, 121-134.
- Brand, A.H., and Perrimon, N. (1993). Targeted gene expression as a means of altering cell fates and generating dominant phenotypes. *Development* *118*, 401-415.
- Bretaud, S., Allen, C., Ingham, P.W., and Bandmann, O. (2007). p53-dependent neuronal cell death in a DJ-1-deficient zebrafish model of Parkinson's disease. *J. Neurochem.* *100*, 1626-1635.
- Brösamle, C., and Halpern, M.E. (2002). Characterization of myelination in the developing zebrafish. *Glia* *39*, 47-57.
- Cai, Q., Davis, M.L., and Sheng, Z.-H. (2011). Regulation of axonal mitochondrial transport and its impact on synaptic transmission. *Neurosci Res.* *70*, 9-15.
- Campello, S., and Scorrano, L. (2010). Mitochondrial shape changes: orchestrating cell pathophysiology. *EMBO Rep.* *11*, 678-684.
- Carvey, P.M., Punati, A., and Newman, M.B. (2006). Progressive dopamine neuron loss in Parkinson's disease: the multiple hit hypothesis. *Cell Transplant.* *15*, 239-250.
- Carlsson, A., Lindqvist, M., and Magnusson, T. (1957). 3,4-Dihydroxyphenylalanine and 5-hydroxytryptophan as reserpine antagonists. *Nature* *180*, 1200.
- Chan, N.C., Salazar, A.M., Pham, A.H., Sweredoski, M.J., Kolawa, N.J., Graham, R.L., Hess, S., and Chan, D.C. (2011). Broad activation of the ubiquitin-proteasome system by Parkin is critical for mitophagy. *Hum. Mol. Genet.* *20*, 1726-1737.
- Chang, K.T., Niescier, R.F., and Min, K.T. (2011). Mitochondrial matrix Ca<sup>2+</sup> as an intrinsic signal regulating mitochondrial motility in axons. *Proc. Natl. Acad. Sci. USA* *108*, 15456-15461.
- Chartier-Harlin, M.C., Dachsel, J.C., Vilariño-Güell, C., Lincoln, S.J., Leprêtre, F., Hulihan, M.M., Kachergus, J., Milnerwood, A.J., Tapia, L., Song, M.S., Le Rhun, E., Mutez, E. et al. (2011). Translation initiator EIF4G1 mutations in familial Parkinson disease. *Am. J. Hum. Genet.* *89*, 398-406.
- Chen, H., McCaffery, J.M., and Chan, D.C. (2007). Mitochondrial fusion protects against neurodegeneration in the cerebellum. *Cell* *130*, 548-562.

- Chen, Y., and Dorn, G.W. 2nd. (2013). PINK1-phosphorylated mitofusin 2 is a Parkin receptor for culling damaged mitochondria. *Science* 340, 471-475.
- Cho, H.J., Yu, J., Xie, C., Rudrabhatla, P., Chen, X., Wu, J., Parisiadou, L., Liu, G., Sun, L., Ma, B., Ding, J., Liu, Z., and Cai, H. (2014). Leucine-rich repeat kinase 2 regulates Sec16A at ER exit sites to allow ER-Golgi export. *EMBO J. Sep 8*. pii: e201487807. [Epub ahead of print]
- Chu, Y., Senghaas, N., Köster, R.W., Wurst, W., and Kühn, R. (2008). Novel caspase-suicide proteins for tamoxifen-inducible apoptosis. *Genesis* 46, 530-536.
- Cirnaru, M.D., Marte, A., Belluzzi, E., Russo, I., Gabrielli, M., Longo, F., Arcuri, L., Murru, L., Bubacco, L., Matteoli, M., Fedele, E., Sala, C., Passafaro, M., Morari, M., Greggio, E., et al. (2014). LRRK2 kinase activity regulates synaptic vesicle trafficking and neurotransmitter release through modulation of LRRK2 macro-molecular complex. *Front. Mol. Neurosci.* 7, Article 49, 1-12.
- Clark, I.E., Dodson, M.W., Jiang, C., Cao, J.H., Huh, J.R., Seol, J.H., Yoo, S.J., Hay, B.A., and Guo, M. (2006). *Drosophila pink1* is required for mitochondrial function and interacts genetically with parkin. *Nature* 441, 1162-1166.
- Collier, T.J., Kanaan, N.M., and Kordower, J.H. (2011). Ageing as a primary risk factor for Parkinson's disease: evidence from studies of non-human primates. *Nat. Rev. Neurosci.* 12, 359-366.
- Cookson, M.R. (2010). The role of leucine-rich repeat kinase 2 (LRRK2) in Parkinson's disease. *Nat. Rev. Neurosci.* 11, 791-797.
- Corti, O., Lesage, S., and Brice, A. (2011). What genetics tells us about the causes and mechanisms of Parkinson's disease. *Physiol. Rev.* 91, 1161-1218.
- Cotzias, G.C., Van Woert, M.H., and Schiffer, L.M. (1967). Aromatic amino acids and modification of parkinsonism. *New Engl. J. Med.* 276, 374-379.
- Covy, J.P., and Giasson, B.I. (2009). Identification of compounds that inhibit the kinase activity of leucine-rich repeat kinase 2. *Biochem. Biophys. Res. Commun.* 378, 473-477. Erratum in: (2009) *Biochem. Biophys. Res. Commun.* 387, 419-420.
- Criollo, A., Senovilla, L., Authier, H., Maiuri, M.C., Morselli, E., Vitale, I., Kepp, O., Tasmir, E., Galluzzi, L., Shen, S., Tailler, M., Delahaye, N., Tesniere, A. et al. (2010). The IKK complex contributes to the induction of autophagy. *EMBO J.* 29, 619-631.
- Culp, P., Nüsslein-Volhard, C., and Hopkins, N. (1991). High-frequency germ-line transmission of plasmid DNA sequences injected into fertilized zebrafish eggs. *Proc. Natl. Acad. Sci. USA* 88, 7953-7957.
- Culp, P. (1994). Random DNA integrations as an approach to insertional mutagenesis in the zebrafish (*Brachydanio rerio*). PhD thesis. Massachusetts Institute of Technology, Cambridge, MA.  
<https://dspace.mit.edu/bitstream/handle/1721.1/33505/31053562.pdf>
- Dagda, R.K., Cherra, S.J. 3rd, Kulich, S.M., Tandon, A., Park, D., and Chu, C.T. (2009). Loss of PINK1 function promotes mitophagy through effects on oxidative stress and mitochondrial fission. *J. Biol. Chem.* 284, 13843-13855.
- Daher, J.P., Pletnikova, O., Biskup, S., Musso, A., Gellhaar, S., Galter, D., Troncoso, J.C., Lee, M.K., Dawson, T.M., Dawson, V.L., and Moore, D.J. (2012). Neurodegenerative phenotypes in an A53T  $\alpha$ -synuclein transgenic mouse model are independent of LRRK2. *Hum. Mol. Genet.* 21, 2420-2431.
- Dave, K.D., De Silva, S., Sheth, N.P., Ramboz, S., Beck, M.J., Quang, C., Switzer, R.C. 3rd, Ahmad, S.O., Sunkin, S.M., Walker, D., Cui, X., Fisher, D.A., McCoy, A.M., et al. (2014). Phenotypic characterization of recessive gene knockout rat models of Parkinson's disease. *Neurobiol. Dis.* 70, 190-203.

- Davidson, M.W., and Campbell, R.E. (2009). Engineered fluorescent proteins: innovations and applications. *Nat. Methods* 6, 713-717.
- Dawson, T.M., Ko, H.S., and Dawson, V.L. (2010). Genetic animal models of Parkinson's disease. *Neuron* 66, 646-661.
- Day, R.N., and Davidson, M.W. (2009). The fluorescent protein palette: tools for cellular imaging. *Chem. Soc. Rev.* 38, 2887-2921.
- Deas, E., Plun-Favreau, H., and Wood, N.W. (2009). PINK1 function in health and disease. *EMBO Mol. Med.* 1, 152-165.
- Deas, E., Plun-Favreau, H., Gandhi, S., Desmond, H., Kjaer, S., Loh, S.H., Renton, A.E., Harvey, R.J., Whitworth, A.J., Martins, L.M., Abramov, A.Y., and Wood, N.W. (2011). PINK1 cleavage at position A103 by the mitochondrial protease PARL. *Hum. Mol. Genet.* 20, 867-879.
- de Felipe, P., Luke, G.A., Hughes, L.E., Gani, D., Halpin, C., and Ryan, M.D. (2006). E unum pluribus: multiple proteins from a self-processing polyprotein. *Trends Biotechnol.* 24, 68-75.
- Deng, J., Lewis, P.A., Greggio, E., Sluch, E., Beilina, A., and Cookson, M.R. (2008). Structure of the ROC domain from the Parkinson's disease-associated leucine-rich repeat kinase 2 reveals a dimeric GTPase. *Proc. Natl. Acad. Sci. USA* 105, 1499-1504.
- Deng, X., Dzamko, N., Prescott, A., Davies, P., Liu, Q., Yang, Q., Lee, J.D., Patricelli, M.P., Nomanbhoy, T.K., Alessi, D.R., and Gray, N.S. (2011). Characterization of a selective inhibitor of the Parkinson's disease kinase LRRK2. *Nat. Chem. Biol.* 7, 203-205.
- De Vos, K.J., Sable, J., Miller, K.E., and Sheetz, M.P. (2003). Expression of phosphatidylinositol (4,5) bisphosphate-specific pleckstrin homology domains alters direction but not the level of axonal transport of mitochondria. *Mol. Biol. Cell* 14, 3636-3649.
- De Vos, K.J., and Sheetz, M.P. (2007). Visualization and quantification of mitochondrial dynamics in living animal cells. *Methods Cell Biol.* 80, 627-682.
- de Vries, R.L., and Przedborski, S. (2013). Mitophagy and Parkinson's disease: be eaten to stay healthy. *Mol. Cell. Neurosci.* 55, 37-43.
- DeWitt, M.A., Chang, A.Y., Combs, P.A., and Yildiz, A. (2012). Cytoplasmic dynein moves through uncoordinated stepping of the AAA+ ring domains. *Science* 335, 221-225.
- Distel, M., Wullimann, M.F., and Köster, R.W. (2009). Optimized Gal4 genetics for permanent gene expression mapping in zebrafish. *Proc. Natl. Acad. Sci. USA* 106, 13365-13370.
- Doronina, V.A., Wu, C., de Felipe, P., Sachs, M.S., Ryan, M.D., and Brown, J.D. (2008). Site-specific release of nascent chains from ribosomes at a sense codon. *Mol. Cell. Biol.* 28, 4227-4239.
- Doyon, Y., McCammon, J.M., Miller, J.C., Faraji, F., Ngo, C., Katibah, G.E., Amora, R., Hocking, T.D., Zhang, L., Rebar, E.J., Gregory, P.D., Urnov, F.D., and Amacher, S.L. (2008). Heritable targeted gene disruption in zebrafish using designed zinc-finger nucleases. *Nat. Biotechnol.* 26, 702-708.
- Drechsel, D.A., and Patel, M. (2008). Role of reactive oxygen species in the neurotoxicity of environmental agents implicated in Parkinson's disease. *Free Radic. Biol. Med.* 44, 1873-1886. Erratum in: *Free Radic. Biol. Med.* (2008) 45, 1045.
- Dusonchet, J., Kochubey, O., Stafa, K., Young, S.M. Jr., Zufferey, R., Moore, D.J., Schneider, B.L., and Aebischer, P. (2011). A rat model of progressive nigral neurodegeneration induced by the Parkinson's disease-associated G2019S mutation in LRRK2. *J. Neurosci.* 31, 907-912.
- Ehringer, H., and Hornykiewicz, O. (1960). Distribution of noradrenaline and dopamine (3-hydroxytyramine) in the human brain and their behavior in diseases of the extrapyramidal system. *Klin. Wochenschr.* 38, 1236-1239.

- Eisen, J.S., Myers, P.Z., and Westerfield, M. (1986). Pathway selection by growth cones of identified motoneurons in live zebra fish embryos. *Nature* 320, 269-271.
- Exner, N., Treske, B., Paquet, D., Holmström, K., Schiesling, C., Gispert, S., Carballo-Carbajal, I., Berg, D., Hoepken, H.H., Gasser, T., Krüger, R., Winklhofer, K.F., Vogel, F., Reichert, A.S., Auburger, G., Kahle, P.J., Schmid, B., and Haass, C. (2007). Loss-of-function of human PINK1 results in mitochondrial pathology and can be rescued by parkin. *J. Neurosci.* 27, 12413-12418.
- Exner, N., Lutz, A.K., Haass, C., and Winklhofer, K.F. (2012). Mitochondrial dysfunction in Parkinson's disease: molecular mechanisms and pathophysiological consequences. *EMBO J.* 31, 3038-3062.
- Fahn, S. (2003). Description of Parkinson's disease as a clinical syndrome. *Ann. N.Y. Acad. Sci.* 991, 1-14.
- Fahn, S. (2010). Parkinson's disease: 10 years of progress, 1997-2007. *Mov. Disord.* 25, Suppl. 1, S2-S14.
- Falzone, T.L., Stokin, G.B., Lillo, C., Rodrigues, E.M., Westerman, E.L., Williams, D.S., and Goldstein, L.S. (2009) Axonal stress kinase activation and tau misbehavior induced by kinesin-1 transport defects. *J. Neurosci.* 29, 5758-5767.
- Faucherre, A., Pujol-Martí, J., Kawakami, K., and López-Schier, H. (2009). Afferent neurons of the zebrafish lateral line are strict selectors of hair-cell orientation. *PLoS One* 4, e4477. doi: 10.1371/journal.pone.0004477.
- Feil, R., Wagner, J., Metzger, D., and Chambon, P. (1997). Regulation of Cre recombinase activity by mutated estrogen receptor ligand-binding domains. *Biochem. Biophys. Res. Commun.* 237, 752-757.
- Fett, M.E., Pilsl, A., Paquet, D., van Bebber, F., Haass, C., Tatzelt, J., Schmid, B., and Winklhofer, K.F. (2010). Parkin is protective against proteotoxic stress in a transgenic zebrafish model. *PLoS One* 5, e11783.
- Fleming, A., and Rubinsztein, D.C. (2011). Zebrafish as a model to understand autophagy and its role in neurological disease. *Biochim. Biophys. Acta* 1812, 520-526.
- Flinn, L., Mortiboys, H., Volkmann, K., Köster, R.W., Ingham, P.W., and Bandmann, O. (2009). Complex I deficiency and dopaminergic neuronal cell loss in parkin-deficient zebrafish (*Danio rerio*). *Brain* 132, 1613-1623.
- Flinn, L.J., Keatinge, M., Bretaud, S., Mortiboys, H., Matsui, H., De Felice, E., Woodroof, H.I., Brown, L., McTighe, A., Soellner, R., Allen, C.E., Heath, P.R., Milo, M., Muqit, M.M., Reichert, A.S., Köster, R.W., Ingham, P.W., and Bandmann, O. (2013). TigarB causes mitochondrial dysfunction and neuronal loss in PINK1 deficiency. *Ann. Neurol.* 74, 837-847.
- Florey, O., and Overholtzer, M. (2012). Autophagy proteins in macroendocytic engulfment. *Trends Cell Biol.* 22, 374-380.
- Fong, A.P., Yao, Z., Zhong, J.W., Cao, Y., Ruzzo, W.L., Gentleman, R.C., and Tapscott, S.J. (2012). Genetic and epigenetic determinants of neurogenesis and myogenesis. *Dev. Cell* 22, 721-735.
- Frederick, R.L., and Shaw, J.M. (2007) Moving mitochondria: establishing distribution of an essential organelle. *Traffic* 8, 1668-1675.
- Gandhi, P.N., Wang, X., Zhu, X., Chen, S.G., and Wilson-Delfosse, A.L. (2008). The Roc domain of leucine-rich repeat kinase 2 is sufficient for interaction with microtubules. *J. Neurosci. Res.* 86, 1711-1720.
- Gao, L., Shao, L., Higgins, C.D., Poulton, J.S., Peifer, M., Davidson, M.W., Wu, X., Goldstein, B., and Betzig, E. (2012). Noninvasive imaging beyond the diffraction limit of 3D dynamics in thickly fluorescent specimens. *Cell* 151, 1370-1385.
- Gasser, T. (2009). Molecular pathogenesis of Parkinson disease: insights from genetic studies. *Expert Rev. Mol. Med.* 11, e22.

- Gautier, C.A., Kitada, T., and Shen, J. (2008). Loss of PINK1 causes mitochondrial functional defects and increased sensitivity to oxidative stress. *Proc. Natl. Acad. Sci. USA* *105*, 11364-11369.
- Geisler, S., Holmström, K.M., Skujat, D., Fiesel, F.C., Rothfuss, O.C., Kahle, P.J., and Springer, W. (2010). PINK1/Parkin-mediated mitophagy is dependent on VDAC1 and p62/SQSTM1. *Nat. Cell Biol.* *12*, 119-131.
- Geisler, S., Vollmer, S., Golombek, S., and Kahle, P.J. (2014). The ubiquitin-conjugating enzymes UBE2N, UBE2L3 and UBE2D2/3 are essential for Parkin-dependent mitophagy. *J. Cell Sci.* *127*, 3280-3293.
- Ghysen, A., and Dambly-Chaudière, C. (2007). The lateral line microcosmos. *Genes Dev.* *21*, 2118-2130.
- Giesert, F., Hofmann, A., Bürger, A., Zerle, J., Kloos, K., Hafen, U., Ernst, L., Zhang, J., Vogt-Weisenhorn, D.M., and Wurst, W. (2013). Expression analysis of *Lrrk1*, *Lrrk2* and *Lrrk2* splice variants in mice. *PLoS One* *8*:e63778.
- Gillardot, F. (2009). Leucine-rich repeat kinase 2 phosphorylates brain tubulin-beta isoforms and modulates microtubule stability--a point of convergence in parkinsonian neurodegeneration? *J. Neurochem.* *110*, 1514-1522.
- Gillies, A., Willshaw, D., and Li, Z. (2002). Subthalamic-pallidal interactions are critical in determining normal and abnormal functioning of the basal ganglia. *Proc. Biol. Sci.* *269*, 545-551.
- Gilmour, D., Knaut, H., Maischein, H.M., and Nüsslein-Volhard, C. (2004). Towing of sensory axons by their migrating target cells in vivo. *Nat. Neurosci.* *7*, 491-492.
- Giordano, S., Darley-Usmar, V., and Zhang, J. (2014). Autophagy as an essential cellular antioxidant pathway in neurodegenerative disease. *Redox Biol.* *2*, 82-90.
- Gispert, S., Ricciardi, F., Kurz, A., Azizov, M., Hoepken, H.H., Becker, D., Voos, W., Leuner, K., Müller, W.E., Kudin, A.P., Kunz, W.S., Zimmermann, A., Roeper, J., Wenzel, D. et al. (2009). Parkinson phenotype in aged PINK1-deficient mice is accompanied by progressive mitochondrial dysfunction in absence of neurodegeneration. *PLoS One* *4*:e5777.
- Glasl, L., Kloos, K., Giesert, F., Roethig, A., Di Benedetto, B., Kühn, R., Zhang, J., Hafen, U., Zerle, J., Hofmann, A., de Angelis, M.H., Winklhofer, K.F., Höltter, S.M., Vogt Weisenhorn, D.M., and Wurst, W. (2012). Pink1-deficiency in mice impairs gait, olfaction and serotonergic innervation of the olfactory bulb. *Exp. Neurol.* *235*, 214-227.
- Gloeckner, C.J., Kinkl, N., Schumacher, A., Braun, R.J., O'Neill, E., Meitinger, T., Kolch, W., Prokisch, H., and Ueffing, M. (2006). The Parkinson disease causing LRRK2 mutation I2020T is associated with increased kinase activity. *Hum. Mol. Genet.* *15*, 223-232.
- Gloeckner, C.J., Schumacher, A., Boldt, K., and Ueffing, M. (2009). The Parkinson disease-associated protein kinase LRRK2 exhibits MAPKKK activity and phosphorylates MKK3/6 and MKK4/7, in vitro. *J. Neurochem.* *109*, 959-968.
- Gloeckner, C.J., Boldt, K., von Zweyendorf, F., Helm, S., Wiesent, L., Sarioglu, H., and Ueffing, M. (2010). Phosphopeptide analysis reveals two discrete clusters of phosphorylation in the N-terminus and the Roc domain of the Parkinson-disease associated protein kinase LRRK2. *J. Proteome Res.* *9*, 1738-1745.
- Goldsmith, J.R., and Jobin, C. (2012). Think small: zebrafish as a model system of human pathology. *J. Biomed. Biotechnol.* *2012*:817341. doi: 10.1155/2012/817341.
- Gómez-Suaga, P., Rivero-Ríos, P., Fdez, E., Blanca Ramírez, M., Ferrer, I., Aiastui, A., López De Munain, A., and Hilfiker, S. (2014). LRRK2 delays degradative receptor trafficking by impeding late endosomal budding through decreasing Rab7 activity. *Hum. Mol. Genet.* Jul 30. pii: ddu395.

- Graham, F.L., Smiley, J., Russell, W.C., and Nairn, R. (1977). Characteristics of a human cell line transformed by DNA from human adenovirus type 5. *J. Gen Virol.* 36, 59-74.
- Green, D.R., Galluzzi, L., and Kroemer, G. (2011). Mitochondria and the autophagy-inflammation-cell death axis in organismal aging. *Science* 333, 1109-1112.
- Greggio, E., Jain, S., Kingsbury, A., Bandopadhyay, R., Lewis, P., Kaganovich, A., van der Brug, M.P., Beilina, A., Blackinton, J., Thomas, K.J., Ahmad, R., Miller, D.W. et al. (2006). Kinase activity is required for the toxic effects of mutant LRRK2/dardarin. *Neurobiol. Dis.* 23, 329-341.
- Greggio, E., Zambrano, I., Kaganovich, A., Beilina, A., Taymans, J.M., Daniëls, V., Lewis, P., Jain, S., Ding, J., Syed, A., Thomas, K.J., Baekelandt, V., and Cookson, M.R. (2008). The Parkinson disease-associated leucine-rich repeat kinase 2 (LRRK2) is a dimer that undergoes intramolecular autophosphorylation. *J. Biol. Chem.* 283, 16906-16914.
- Greggio, E., Taymans, J.M., Zhen, E.Y., Ryder, J., Vancraenenbroeck, R., Beilina, A., Sun, P., Deng, J., Jaffe, H., Baekelandt, V., Merchant, K., and Cookson, M.R. (2009). The Parkinson's disease kinase LRRK2 autophosphorylates its GTPase domain at multiple sites. *Biochem. Biophys. Res. Commun.* 389, 449-454.
- Greggio, E., Civiero, L., Bisaglia, M., and Bubacco, L. (2012). Parkinson's disease and immune system: is the culprit LRRK in the periphery? *J. Neuroinflammation* 9:94. doi: 10.1186/1742-2094-9-94.
- Griffiths, G. (1993). *Fine Structure Immunocytochemistry*. Springer-Verlag, Heidelberg, Berlin.
- Guo, S., Wilson, S.W., Cooke, S., Chitnis, A.B., Driever, W., and Rosenthal, A. (1999). Mutations in the zebrafish unmask shared regulatory pathways controlling the development of catecholaminergic neurons. *Dev. Biol.* 208, 473-487.
- Guo, L., Gandhi, P.N., Wang, W., Petersen, R.B., Wilson-Delfosse, A.L., and Chen, S.G. (2007). The Parkinson's disease-associated protein, leucine-rich repeat kinase 2 (LRRK2), is an authentic GTPase that stimulates kinase activity. *Exp. Cell Res.* 313, 3658-3670.
- Gurskaya, N.G., Verkhusha, V.V., Shcheglov, A.S., Staroverov, D.B., Chepurnykh, T.V., Fradkov, A.F., Lukyanov, S., and Lukyanov, K.A. (2006). Engineering of a monomeric green-to-red photoactivatable fluorescent protein induced by blue light. *Nat. Biotechnol.* 24, 461-465.
- Häbig, K., Gellhaar, S., Heim, B., Djuric, V., Giesert, F., Wurst, W., Walter, C., Hentrich, T., Riess, O., and Bonin, M. (2013). LRRK2 guides the actin cytoskeleton at growth cones together with ARHGEF7 and Tropomyosin 4. *Biochim. Biophys. Acta.* 1832, 2352-2367.
- Haehnel, M., Taguchi, M., and Liao, J.C. (2012). Heterogeneity and dynamics of lateral line afferent innervation during development in zebrafish (*Danio rerio*). *J. Comp. Neurol.* 520, 1376-1386.
- Halpern, M.E., Rhee, J., Goll, M.G., Akitake, C.M., Parsons, M., and Leach, S.D. (2008). Gal4/UAS transgenic tools and their application to zebrafish. *Zebrafish* 5, 97-110.
- Hanneman, E., Trevarrow, B., Metcalfe, W.K., Kimmel, C.B., and Westerfield, M. (1988). Segmental pattern of development of the hindbrain and spinal cord of the zebrafish embryo. *Development* 103, 49-58.
- Hasegawa, K., and Nakatsuji, N. (2002). Insulators prevent transcriptional interference between two promoters in a double gene construct for transgenesis. *FEBS Lett.* 520, 47-52.
- Hatano, T., Kubo, S., Imai, S., Maeda, M., Ishikawa, K., Mizuno, Y., and Hattori, N. (2007). Leucine-rich repeat kinase 2 associates with lipid rafts. *Hum. Mol. Genet.* 16, 678-690.

- He, C., Bartholomew, C.R., Zhou, W., and Klionsky, D.J. (2009). Assaying autophagic activity in transgenic GFP-Lc3 and GFP-Gabarap zebrafish embryos. *Autophagy* 5, 520-526.
- He, C., and Klionsky, D.J. (2009). Regulation mechanisms and signaling pathways of autophagy. *Annu. Rev. Genet.* 43, 67-93.
- Hernán, M.A., Zhang, S.M., Rueda-deCastro, A.M., Colditz, G.A., Speizer, F.E., and Ascherio, A. (2001). Cigarette smoking and the incidence of Parkinson's disease in two prospective studies. *Ann. Neurol.* 50, 780-786.
- Higashi, S., Moore, D.J., Colebrooke, R.E., Biskup, S., Dawson, V.L., Arai, H., Dawson, T. M., and Emson, P.C. (2007). Expression and localization of Parkinson's disease associated leucine-rich repeat kinase 2 in the mouse brain. *J. Neurochem.* 100, 368-381.
- Higashijima, S., Masino, M.A., Mandel, G., and Fetcho, J.R. (2003). Imaging neuronal activity during zebrafish behavior with a genetically encoded calcium indicator. *J. Neurophysiol.* 90, 3986-3997.
- Hinkle, K.M., Yue, M., Behrouz, B., Dächsel, J.C., Lincoln, S.J., Bowles, E.E., Beevers, J.E., Dugger, B., Winner, B., Prots, I., Kent, C.B., Nishioka, K., Lin, W.L., Dickson, D.W., Janus, C.J., Farrer, M.J., and Melrose, H.L. (2012). LRRK2 knockout mice have an intact dopaminergic system but display alterations in exploratory and motor coordination behaviors. *Mol. Neurodegener.* 7, doi: 10.1186/1750-1326-7-25.
- Hirokawa, N., Niwa, S., and Tanaka, Y. (2010). Molecular motors in neurons: transport mechanisms and roles in brain function, development, and disease. *Neuron* 68, 610-638.
- Hoepken, H.H., Gispert, S., Morales, B., Wingerter, O., Del Turco, D., Mülsch, A., Nussbaum, R.L., Müller, K., Dröse, S., Brandt, U., Deller, T., Wirth, B., Kudin, A.P., Kunz, W.S., and Auburger, G. (2007). Mitochondrial dysfunction, peroxidation damage and changes in glutathione metabolism in PARK6. *Neurobiol. Dis.* 25, 401-411.
- Hollenbeck, P.J., and Saxton, W.M. (2005). The axonal transport of mitochondria. *J. Cell Sci.* 118, 5411-5419.
- Hollville, E., Carroll, R.G., Cullen, S.P., and Martin, S.J. (2014). Bcl-2 family proteins participate in mitochondrial quality control by regulating Parkin/PINK1-dependent mitophagy. *Mol. Cell* 55, 451-466.
- Holzschuh, J., Ryu, S., Aberger, F., and Driever, W. (2001). Dopamine transporter expression distinguishes dopaminergic neurons from other catecholaminergic neurons in the developing zebrafish embryo. *Mech. Dev.* 101, 237-243.
- Hong, M., Fitzgerald, M.X., Harper, S., Luo, C., Speicher, D.W., and Marmorstein, R. (2008). Structural basis for dimerization in DNA recognition by Gal4. *Structure* 16, 1019-1026.
- Hou, J., Riise, J., and Pakkenberg, B. (2012). Application of immunohistochemistry in stereology for quantitative assessment of neural cell populations illustrated in the Göttingen minipig. *PLoS One* 7:e43556.
- Howe, K., Clark, M.D., Torroja, C.F., Torrance, J., Berthelot, C., Muffato, M., Collins, J.E., Humphray, S., McLaren, K., Matthews, L., McLaren, S., Sealy, I., Caccamo, M., Churcher, C., et al. (2013). The zebrafish reference genome sequence and its relationship to the human genome. *Nature* 496, 498-503.
- Huang, P., Xiao, A., Zhou, M., Zhu, Z., Lin, S., and Zhang, B. (2011). Heritable gene targeting in zebrafish using customized TALENs. *Nat. Biotechnol.* 29, 699-700.
- Hwang, W.Y., Fu, Y., Reyon, D., Maeder, M.L., Tsai, S.Q., Sander, J.D., Peterson, R.T., Yeh, J.R., and Joung J.K. (2013). Efficient genome editing in zebrafish using a CRISPR-Cas system. *Nat. Biotechnol.* 31, 227-229.

- Imai, Y., Gehrke, S., Wang, H.Q., Takahashi, R., Hasegawa, K., Oota, E., and Lu B. (2008). Phosphorylation of 4E-BP by LRRK2 affects the maintenance of dopaminergic neurons in *Drosophila*. *EMBO J.* 27, 2432-2443.
- Jaleel, M., Nichols, R.J., Deak, M., Campbell, D.G., Gillardon, F., Knebel, A., and Alessi, D.R. (2007). LRRK2 phosphorylates moesin at threonine-558: characterization of how Parkinson's disease mutants affect kinase activity. *Biochem. J.* 405, 307-317.
- Jankovic, J. (2008). Parkinson's disease: clinical features and diagnosis. *J. Neurol. Neurosurg. Psychiatry* 79, 368-376.
- Jin, S.M., Lazarou, M., Wang, C., Kane, L.A., Narendra, D.P., and Youle, R.J. (2010). Mitochondrial membrane potential regulates PINK1 import and proteolytic destabilization by PARL. *J. Cell Biol.* 191, 933-942.
- Jin, S.M., and Youle, R.J. (2012). PINK1- and Parkin-mediated mitophagy at a glance. *J. Cell Sci.* 125, 795-799.
- Jung, H.S., Chung, K.W., Won Kim, J., Kim, J., Komatsu, M., Tanaka, K., Nguyen, Y.H., Kang, T.M., Yoon, K.H., Kim, J.W., Jeong, Y.T., Han, M.S., Lee, M.K., Kim, K.W., Shin, J., and Lee, M.S. (2008). Loss of autophagy diminishes pancreatic beta cell mass and function with resultant hyperglycemia. *Cell Metab.* 8, 318-324.
- Kabeya, Y., Mizushima, N., Ueno, T., Yamamoto, A., Kirisako, T., Noda, T., Kominami, E., Ohsumi, Y., and Yoshimori, T. (2000). LC3, a mammalian homologue of yeast Apg8p, is localized in autophagosome membranes after processing. *EMBO J.* 19, 5720-5728. Erratum in: (2003) *EMBO J.* 22, 4577.
- Kamikawaji, S., Ito, G., and Iwatsubo, T. (2009). Identification of the autophosphorylation sites of LRRK2. *Biochemistry* 48, 10963-10975.
- Kanda, T., Sullivan, K.F., and Wahl, G.M. (1998). Histone-GFP fusion protein enables sensitive analysis of chromosome dynamics in living mammalian cells. *Curr. Biol.* 8, 377-385.
- Kane, L.A., Lazarou, M., Fogel, A.I., Li, Y., Yamano, K., Sarraf, S.A., Banerjee, S., and Youle, R.J. (2014). PINK1 phosphorylates ubiquitin to activate Parkin E3 ubiquitin ligase activity. *J. Cell Biol.* 205, 143-153.
- Kawakami, K., Koga, A., Hori, H., and Shima, A. (1998). Excision of the tol2 transposable element of the medaka fish, *Oryzias latipes*, in zebrafish, *Danio rerio*. *Gene* 225, 17-22.
- Kawakami, K., Shima, A., and Kawakami, N. (2000). Identification of a functional transposase of the Tol2 element, an Ac-like element from the Japanese medaka fish, and its transposition in the zebrafish germ lineage. *Proc. Natl. Acad. Sci. USA* 97, 11403-11408.
- Kawakami K. (2007). Tol2: a versatile gene transfer vector in vertebrates. *Genome Biol.* 8 (Suppl 1), S7.
- Kawakami, F., Yabata, T., Ohta, E., Maekawa, T., Shimada, N., Suzuki, M., Maruyama, H., Ichikawa, T., and Obata, F. (2012). LRRK2 phosphorylates tubulin-associated tau but not the free molecule: LRRK2-mediated regulation of the tau-tubulin association and neurite outgrowth. *PLoS One* 7, e30834.
- Kazlauskaite, A., Kondapalli, C., Gourlay, R., Campbell, D.G., Ritorto, M.S., Hofmann, K., Alessi, D.R., Knebel, A., Trost, M., and Muqit, M.M. (2014). Parkin is activated by PINK1-dependent phosphorylation of ubiquitin at Ser65. *Biochem. J.* 460, 127-139.
- Kerschensteiner, M., Reuter, M.S., Lichtman, J.W., and Misgeld, T. (2008). Ex vivo imaging of motor axon dynamics in murine triangularis sterni explants. *Nat. Protoc.* 3, 1645-1653.
- Kett, L.R., Boassa, D., Ho, C.C., Rideout, H.J., Hu, J., Terada, M., Ellisman, M., and Dauer, W.T. (2012). LRRK2 Parkinson disease mutations enhance its microtubule association. *Hum. Mol. Genet.* 21, 890-899.

- Kim, J.H., Lee, S.R., Li, L.H., Park, H.J., Park, J.H., Lee, K.Y., Kim, M.K., Shin, B.A., and Choi, S.Y. (2011). High cleavage efficiency of a 2A peptide derived from porcine teschovirus-1 in human cell lines, zebrafish and mice. *PLoS One* 6, e18556.
- Kim, C., Choi, H., Jung, E.S., Lee, W., Oh, S., Jeon, N.L., and Mook-Jung, I. (2012) HDAC6 inhibitor blocks amyloid beta-induced impairment of mitochondrial transport in hippocampal neurons. *PLoS One* 7, e42983.
- Kim-Han, J.S., Antenor-Dorsey, J.A., and O'Malley, K.L. (2011). The parkinsonian mimetic, MPP+, specifically impairs mitochondrial transport in dopamine axons. *J. Neurosci.* 31, 7212-7221.
- Kimmel, C.B. (1972). Mauthner axons in living fish larvae. *Dev. Biol.* 27, 272-275.
- Kimmel, C.B. (1993). Patterning the brain of the zebrafish embryo. *Annu. Rev. Neurosci.* 16, 707-732.
- Kimmel, C.B., Ballard, W.W., Kimmel, S.R., Ullmann, B., Schilling, T.F. (1995). Stages of embryonic development of the zebrafish. *Dev. Dyn.* 203, 253-310.
- Kimura, Y., Satou, C., and Higashijima, S. (2008). V2a and V2b neurons are generated by the final divisions of pair-producing progenitors in the zebrafish spinal cord. *Development* 135, 3001-3005.
- Kiryu-Seo, S., Ohno, N., Kidd, G.J., Komuro, H., and Trapp, B.D. (2010). Demyelination increases axonal stationary mitochondrial size and the speed of axonal mitochondrial transport. *J. Neurosci.* 30, 6658-6666.
- Kitada, T., Pisani, A., Porter, D.R., Yamaguchi, H., Tscherter, A., Martella, G., Bonsi, P., Zhang, C., Pothos, E.N., and Shen, J. (2007). Impaired dopamine release and synaptic plasticity in the striatum of PINK1-deficient mice. *Proc. Natl. Acad. Sci. USA* 104, 11441-11446.
- Klein, C., and Westenberger, A. (2012). Genetics of Parkinson's disease. *Cold Spring Harb. Perspect. Med.* 2, a008888.
- Klionsky, D.J., Abeliovich, H., Agostinis, P., Agrawal, D.K., Aliev, G., Askew, D.S., Baba, M., Baehrecke, E.H., Bahr, B.A., Ballabio, A., Bamber, B.A., Bassham, D.C., Bergamini, E., Bi, X., Biard-Piechaczyk, M., Blum, J.S. et al. (2008). Guidelines for the use and interpretation of assays for monitoring autophagy in higher eukaryotes. *Autophagy* 4, 151-175.
- Koga, A., Suzuki, M., Inagaki, H., Bessho, Y., and Hori, H. (1996). Transposable element in fish. *Nature* 383, 30.
- Köster, R.W., and Fraser, S.E. (2001). Tracing transgene expression in living zebrafish embryos. *Dev. Biol.* 233, 329-346.
- Koyano, F., Okatsu, K., Kosako, H., Tamura, Y., Go, E., Kimura, M., Kimura, Y., Tsuchiya, H., Yoshihara, H., Hirokawa, T., Endo, T., Fon, E.A., Trempe, J.F., Saeki, Y., Tanaka, K., and Matsuda, N. (2014). Ubiquitin is phosphorylated by PINK1 to activate parkin. *Nature* 510, 162-166.
- Kwan, K.M., Fujimoto, E., Grabher, C., Mangum, B.D., Hardy, M.E., Campbell, D.S., Parant, J.M., Yost, H.J., Kanki, J.P., and Chien, C.-B. (2007). The Tol2kit: A multisite gateway based construction kit for *Tol2* transposon transgenesis constructs. *Dev. Dyn.* 236, 3088-3099.
- Langston, J.W., Ballard, P., Tetrud, J.W., and Irwin, I. (1983). Chronic Parkinsonism in humans due to a product of meperidine-analog synthesis. *Science* 219, 979-980.
- Langworthy, M.M., and Appel, B. (2012). Schwann cell myelination requires Dynein function. *Neural Dev.* 7:37, doi: 10.1186/1749-8104-7-37.
- Law, B.M., Spain, V.A., Leinster, V.H., Chia, R., Beilina, A., Cho, H.J., Taymans, J.M., Urban, M.K., Sancho, R.M., Ramírez, M.B., Biskup, S., Baekelandt, V., Cai, H., Cookson, M.R. et al. (2014). A direct interaction between leucine-rich repeat kinase 2

- and specific  $\beta$ -tubulin isoforms regulates tubulin acetylation. *J. Biol. Chem.* 289, 895-908.
- Lawson, N.D., and Wolfe, S.A. (2011). Forward and reverse genetic approaches for the analysis of vertebrate development in the zebrafish. *Dev. Cell* 21, 48-64.
- Lazarou, M., Jin, S.M., Kane, L.A., and Youle, R.J. (2012). Role of PINK1 binding to the TOM complex and alternate intracellular membranes in recruitment and activation of the E3 ligase Parkin. *Dev. Cell* 22, 320-333.
- Lee, B.D., Shin, J.H., VanKampen, J., Petrucelli, L., West, A.B., Ko, H.S., Lee, Y.I., Maguire-Zeiss, K.A., Bowers, W.J., Federoff, H.J., Dawson, V.L., and Dawson, T.M. (2010a). Inhibitors of leucine-rich repeat kinase-2 protect against models of Parkinson's disease. *Nat. Med.* 16, 998-1000.
- Lee, J.Y., Nagano, Y., Taylor, J.P., Lim, K.L., and Yao, T.P. (2010b). Disease-causing mutations in parkin impair mitochondrial ubiquitination, aggregation, and HDAC6 dependent mitophagy. *J. Cell Biol.* 189, 671-679.
- Lee, S., Liu, H.P., Lin, W.Y., Guo, H., and Lu, B. (2010c). LRRK2 kinase regulates synaptic morphology through distinct substrates at the presynaptic and postsynaptic compartments of the *Drosophila* neuromuscular junction. *J. Neurosci.* 30, 16959-16969.
- Lees, A.J., Hardy, J., and Revesz, T. (2009). Parkinson's disease. *Lancet* 373, 2055-2066. Erratum in: *Lancet* 374, 684.
- Lesage, S., and Brice, A. (2009). Parkinson's disease: from monogenic forms to genetic susceptibility factors. *Hum. Mol. Genet.* 18, R48-59.
- Lewis, P.A., Greggio, E., Beilina, A., Jain, S., Baker, A., and Cookson, M.R. (2007). The R1441C mutation of LRRK2 disrupts GTP hydrolysis. *Biochem. Biophys. Res. Commun.* 357, 668-671.
- Lewis, P.A., and Manzoni, C. (2012). LRRK2 and human disease: a complicated question or a question of complexes. *Science Signal.* 5, pe2.
- Liao, J.C., and Haehnel, M. (2012). Physiology of afferent neurons in larval zebrafish provides a functional framework for lateral line somatotopy. *J. Neurophysiol.* 107, 2615-2623.
- Li, X., Tan, Y.C., Poulouse, S., Olanow, C.W., Huang, X.Y., and Yue, Z. (2007). Leucine-rich repeat kinase 2 (LRRK2)/PARK8 possesses GTPase activity that is altered in familial Parkinson's disease R1441C/G mutants. *J. Neurochem.* 103, 238-247.
- Li, X., Moore, D.J., Xiong, Y., Dawson, T.M., and Dawson, V.L. (2010). Reevaluation of phosphorylation sites in the Parkinson disease-associated leucine-rich repeat kinase 2. *J. Biol. Chem.* 285, 29569-29576.
- Lin, X., Parisiadou, L., Gu, X.L., Wang, L., Shim, H., Sun, L., Xie, C., Long, C.X., Yang, W.J., Ding, J., Chen, Z.Z., Gallant, P.E., Tao-Cheng, J.H., Rudow, G., Troncoso, J.C., Liu, Z., Li, Z., and Cai, H. (2009). Leucine-rich repeat kinase 2 regulates the progression of neuropathology induced by Parkinson's-disease-related mutant alpha synuclein. *Neuron* 64, 807-827.
- Lin, C.H., Tsai, P.I., Wu, R.M., and Chien, C.T. (2010). LRRK2 G2019S mutation induces dendrite degeneration through mislocalization and phosphorylation of tau by recruiting autoactivated GSK3 $\beta$ . *J. Neurosci.* 30, 13138-13149.
- Lin, C.H., Tsai, P.I., Wu, R.M., and Chien, C.T. (2011). LRRK2 Parkinson's disease: from animal models to cellular mechanisms. *Rev. Neurosci.* 22, 411-418.
- Liu, S., Sawada, T., Lee, S., Yu, W., Silverio, G., Alapatt, P., Millan, I., Shen, A., Saxton, W., Kanao, T., Takahashi, R., Hattori, N., Imai, Y., and Lu, B. (2012). Parkinson's disease associated kinase PINK1 regulates Miro protein level and axonal transport of mitochondria. *PLoS Genet.* 8, e1002537.

- Llorens-Martín, M., López-Doménech, G., Soriano, E., and Avila, J. (2011). GSK3 $\beta$  is involved in the relief of mitochondria pausing in a Tau-dependent manner. *PLoS One* 6, e27686.
- López-Schier, H., Starr, C.J., Kappler, J.A., Kollmar, R., and Hudspeth, A.J. (2004). Directional cell migration establishes the axes of planar polarity in the posterior lateral-line organ of the zebrafish. *Dev. Cell* 7, 401-412.
- López-Schier, H., and Hudspeth, A.J. (2006). A two-step mechanism underlies the planar polarization of regenerating sensory hair cells. *Proc. Natl. Acad. Sci. USA* 103, 18615-18620.
- Lutz, A.K., Exner, N., Fett, M.E., Schlehe, J.S., Kloos, K., Lämmermann, K., Brunner, B., Kurz-Drexler, A., Vogel, F., Reichert, A.S., Bouman, L., Vogt-Weisenhorn, D., Wurst, W., Tatzelt, J., Haass, C., and Winklhofer, K.F. (2009). Loss of parkin or PINK1 function increases Drp1-dependent mitochondrial fragmentation. *J. Biol. Chem.* 284, 22938-22951.
- Lynch-Day, M.A., Mao, K., Wang, K., Zhao, M., and Klionsky, D.J. (2012). The role of autophagy in Parkinson's disease. *Cold Spring Harb. Perspect. Med.* 2, a009357.
- Lyons, D.A., Pogoda, H.M., Voas, M.G., Woods, I.G., Diamond, B., Nix, R., Arana, N., Jacobs, J., and Talbot, W.S. (2005). *erbb3* and *erbb2* are essential for schwann cell migration and myelination in zebrafish. *Curr. Biol.* 15, 513-524.
- Ma, P.M. (2003). Catecholaminergic systems in the zebrafish.IV. Organization and projection pattern of dopaminergic neurons in the diencephalon. *J. Comp. Neurol.* 460, 13-37.
- MacLeod, D., Dowman, J., Hammond, R., Leete, T., Inoue, K., and Abeliovich, A. (2006). The familial Parkinsonism gene LRRK2 regulates neurite process morphology. *Neuron* 52, 587-593.
- Magrané, J., Sahawneh, M.A., Przedborski, S., Estévez, Á.G., and Manfredi, G. (2012) Mitochondrial dynamics and bioenergetic dysfunction is associated with synaptic alterations in mutant SOD1 motor neurons. *J. Neurosci.* 32, 229-242.
- Manzoni, C., Mamais, A., Dihanich, S., McGoldrick, P., Devine, M.J., Zerle, J., Kara, E., Taanman, J.W., Healy, D.G., Marti-Masso, J.F., Schapira, A.H., Plun-Favreau, H., Tooze, S. et al. (2013). Pathogenic Parkinson's disease mutations across the functional domains of LRRK2 alter the autophagic/lysosomal response to starvation. *Biochem. Biophys. Res. Commun.* 441, 862-866.
- Marín, I. (2006). The Parkinson disease gene LRRK2: evolutionary and structural insights. *Mol. Biol. Evol.* 23, 2423-2433.
- Marín, I. (2008). Ancient origin of the Parkinson disease gene LRRK2. *J. Mol. Evol.* 67, 41-50.
- Marinković, P., Reuter, M.S., Brill, M.S., Godinho, L., Kerschensteiner, M., and Misgeld, T. (2012). Axonal transport deficits and degeneration can evolve independently in mouse models of amyotrophic lateral sclerosis. *Proc. Natl. Acad. Sci. USA* 109, 4296-4301.
- Martin, I., Dawson, V.L., and Dawson, T.M. (2011). Recent advances in the genetics of Parkinson's disease. *Annu. Rev. Genomics Hum. Genet.* 12, 301-325.
- Martin, I., Kim, J.W., Lee, B.D., Kang, H.C., Xu, J.C., Jia, H., Stankowski, J., Kim, M.S., Zhong, J., Kumar, M., Andrabi, S.A., Xiong, Y., Dickson, D.W., Wszolek, Z.K., Pandey, A. et al. (2014). Ribosomal protein s15 phosphorylation mediates LRRK2 neurodegeneration in Parkinson's disease. *Cell* 157, 472-485.
- Mata, I.F., Wedemeyer, W.J., Farrer, M.J., Taylor, J.P., and Gallo, K.A. (2006). LRRK2 in Parkinson's disease: protein domains and functional insights. *Trends Neurosci.* 29, 286-293.
- Matsuda, N., Sato, S., Shiba, K., Okatsu, K., Saisho, K., Gautier, C.A., Sou, Y.S., Saiki, S., Kawajiri, S., Sato, F., Kimura, M., Komatsu, M., Hattori, N., and Tanaka, K. (2010). PINK1 stabilized by mitochondrial depolarization recruits Parkin to damaged mitochondria and activates latent Parkin for mitophagy. *J. Cell Biol.* 189, 211-221.

- Matta, S., Van Kolen, K., da Cunha, R., van den Bogaart, G., Mandemakers, W., Miskiewicz, K., De Bock, P.J., Morais, V.A., Vilain, S., Haddad, D., Delbroek, L., Swerts, J., et al. (2012). LRRK2 controls an EndoA phosphorylation cycle in synaptic endocytosis. *Neuron* 75, 1008-1021.
- Meijer, A.H., and Spaink, H.P. (2011). Host-pathogen interactions made transparent with the zebrafish model. *Curr. Drug Targets* 12, 1000-1017.
- Meissner, C., Lorenz, H., Weihofen, A., Selkoe, D.J., and Lemberg, M.K. (2011). The mitochondrial intramembrane protease PARL cleaves human Pink1 to regulate Pink1 trafficking. *J. Neurochem.* 117, 856-867.
- Melrose, H.L., Dächsel, J.C., Behrouz, B., Lincoln, S.J., Yue, M., Hinkle, K.M., Kent, C.B., Korvatska, E., Taylor, J.P., Witten, L., Liang, Y.Q., Beevers, J.E., Boules, M. et al. (2010). Impaired dopaminergic neurotransmission and microtubule-associated protein tau alterations in human LRRK2 transgenic mice. *Neurobiol. Dis.* 40, 503-517.
- Meng, X., Noyes, M.B., Zhu, L.J., Lawson, N.D., and Wolfe, S.A. (2008). Targeted gene inactivation in zebrafish using engineered zinc-finger nucleases. *Nat. Biotechnol.* 26, 695-701.
- Merzlyak, E.M., Goedhart, J., Shcherbo, D., Bulina, M.E., Shcheglov, A.S., Fradkov, A.F., Gaintzeva, A., Lukyanov, K.A., Lukyanov, S., Gadella, T.W., and Chudakov, D.M. (2007). Bright monomeric red fluorescent protein with an extended fluorescence lifetime. *Nat. Methods* 4, 555-557.
- Metcalf, W.K. (1985). Sensory neuron growth cones comigrate with posterior lateral line primordial cells in zebrafish. *J. Comp. Neurol.* 238, 218-224.
- Metzger, D., Clifford, J., Chiba, H., and Chambon, P. (1995). Conditional site-specific recombination in mammalian cells using a ligand-dependent chimeric Cre recombinase. *Proc. Natl. Acad. Sci. U S A* 92, 6991-6995.
- Milanese, C., Sager, J.J., Bai, Q., Farrell, T.C., Cannon, J.R., Greenamyre, J.T., and Burton, E.A. (2012). Hypokinesia and reduced dopamine levels in zebrafish lacking  $\beta$ - and  $\gamma$ 1-synucleins. *J. Biol. Chem.* 287, 2971-2983.
- Misgeld, T., and Kerschensteiner, M. (2006). In vivo imaging of the diseased nervous system. *Nat. Rev. Neurosci.* 7, 449-463.
- Misgeld, T., Kerschensteiner, M., Bareyre, F.M., Burgess, R.W., and Lichtman, J.W. (2007). Imaging axonal transport of mitochondria in vivo. *Nat. Methods* 4, 559-561.
- Mizushima, N., Levine, B., Cuervo, A.M., and Klionsky, D.J. (2008). Autophagy fights disease through cellular self-digestion. *Nature* 451, 1069-1075.
- Mizushima, N., and Komatsu, M. (2011). Autophagy: renovation of cells and tissues. *Cell* 147, 728-741.
- Morais, V.A., Verstreken, P., Roethig, A., Smet, J., Snellinx, A., Vanbrabant, M., Haddad, D., Frezza, C., Mandemakers, W., Vogt-Weisenhorn, D., Van Coster, R., Wurst, W., Scorrano, L., and De Strooper, B. (2009). Parkinson's disease mutations in PINK1 result in decreased Complex I activity and deficient synaptic function. *EMBO Mol. Med.* 1, 99-111.
- Mórotz, G.M., De Vos, K.J., Vagnoni, A., Ackerley, S., Shaw, C.E., and Miller, C.C. (2012). Amyotrophic lateral sclerosis-associated mutant VAPBP56S perturbs calcium homeostasis to disrupt axonal transport of mitochondria. *Hum. Mol. Genet.* 21, 1979-1988.
- Morris, R.L., and Hollenbeck, P.J. (1995). Axonal transport of mitochondria along microtubules and F-actin in living vertebrate neurons. *J. Cell Biol.* 131, 1315-1326.
- Myers, P.Z., Eisen, J.S., and Westerfield, M. (1986). Development and axonal outgrowth of identified motoneurons in the zebrafish. *J. Neurosci.* 6, 2278-2289.
- Nagai, T., Ibata, K., Park, E.S., Kubota, M., Mikoshiba, K., and Miyawaki, A. (2002). A variant of yellow fluorescent protein with fast and efficient maturation for cell-

- biological applications. *Nat. Biotechnol.* 20, 87-90.
- Nagiel, A., Andor-Ardó, D., and Hudspeth, A.J. (2008). Specificity of afferent synapses onto plane-polarized hair cells in the posterior lateral line of the zebrafish. *J. Neurosci.* 28, 8442-8453.
- Narendra, D., Tanaka, A., Suen, D.F., and Youle R.J. (2008). Parkin is recruited selectively to impaired mitochondria and promotes their autophagy. *J. Cell Biol.* 183, 795-803.
- Narendra, D.P., Jin, S.M., Tanaka, A., Suen, D.F., Gautier, C.A., Shen, J., Cookson, M.R., and Youle, R.J. (2010). PINK1 is selectively stabilized on impaired mitochondria to activate Parkin. *PLoS Biol.* 8, e1000298.
- Nasevicius, A., and Ekker, S.C. (2000). Effective targeted gene 'knockdown' in zebrafish. *Nat. Genet.* 26, 216-220.
- Norton, W.H. (2013). Toward developmental models of psychiatric disorders in zebrafish. *Front. Neural Circuits* 7:79. doi: 10.3389/fncir.2013.00079.
- Ohno, N., Kidd, G.J., Mahad, D., Kiryu-Seo, S., Avishai, A., Komuro, H., and Trapp, B.D. (2011). Myelination and axonal electrical activity modulate the distribution and motility of mitochondria at CNS nodes of Ranvier. *J. Neurosci.* 31, 7249-7258.
- Olanow, C.W., Perl, D.P., DeMartino, G.N., and McNaught, K.S. (2004). Lewy-body formation is an aggregates-related process: a hypothesis. *Lancet Neurol.* 3, 496-503.
- Orenstein, S.J., Kuo, S.H., Tasset, I., Arias, E., Koga, H., Fernandez-Carasa, I., Cortes, E., Honig, L.S., Dauer, W., Consiglio, A., Raya, A., Sulzer, D., and Cuervo, A.M. (2013). Interplay of LRRK2 with chaperone-mediated autophagy. *Nat. Neurosci.* 16, 394-406.
- Paisán-Ruíz, C., Jain, S., Evans, E.W., Gilks, W.P., Simón, J., van der Brug, M., López de Munain, A., Aparicio, S., Gil, A.M., Khan, N., Johnson, J., Martinez, J.R., Nicholl, D., Carrera, I.M., Pena, A.S., de Silva, R., Lees, A., Martí-Massó, J.F., Pérez-Tur, J., Wood, N.W., and Singleton, A.B. (2004). Cloning of the gene containing mutations that cause PARK8-linked Parkinson's disease. *Neuron* 44, 595-600.
- Palmer, C.S., Osellame, L.D., Stojanovski, D., and Ryan, M.T. (2011). The regulation of mitochondrial morphology: intricate mechanisms and dynamic machinery. *Cell Signal.* 23, 1534-1545.
- Paquet, D., Bhat, R., Sydow, A., Mandelkow, E.M., Berg, S., Hellberg, S., Fälting, J., Distel, M., Köster, R.W., Schmid, B., and Haass, C. (2009). A zebrafish model of tauopathy allows in vivo imaging of neuronal cell death and drug evaluation. *J. Clin. Invest.* 119, 1382-1395.
- Parisiadou, L., Xie, C., Cho, H.J., Lin, X., Gu, X.L., Long, C.X., Lobbstaël, E., Baekelandt, V., Taymans, J.M., Sun, L., and Cai, H. (2009). Phosphorylation of ezrin/radixin/moesin proteins by LRRK2 promotes the rearrangement of actin cytoskeleton in neuronal morphogenesis. *J. Neurosci.* 29, 13971-13980.
- Parisiadou, L., Yu, J., Sgobio, C., Xie, C., Liu, G., Sun, L., Gu, X.L., Lin, X., Crowley, N.A., Lovinger, D.M., and Cai, H. (2014). LRRK2 regulates synaptogenesis and dopamine receptor activation through modulation of PKA activity. *Nat. Neurosci.* 17, 367-376.
- Park, H.C., Kim, C.H., Bae, Y.K., Yeo, S.Y., Kim, S.H., Hong, S.K., Shin, J., Yoo, K.W., Hibi, M., Hirano, T., Miki, N., Chitnis, A.B., and Huh, T.L. (2000). Analysis of upstream elements in the HuC promoter leads to the establishment of transgenic zebrafish with fluorescent neurons. *Dev. Biol.* 227, 279-293.
- Park, J., Lee, S.B., Lee, S., Kim, Y., Song, S., Kim, S., Bae, E., Kim, J., Shong, M., Kim, J.M., and Chung, J. (2006). Mitochondrial dysfunction in *Drosophila* PINK1 mutants is complemented by parkin. *Nature* 441, 1157-1161.
- Peri, F., and Nüsslein-Volhard, C. (2008). Live imaging of neuronal degradation by microglia reveals a role for v0-ATPase a1 in phagosomal fusion in vivo. *Cell* 133, 916-927.
- Pedrosa, D.J., and Timmermann, L. (2013). Review: management of Parkinson's disease. *Neuropsychiatr. Dis. Treat.* 9, 321-340.

- Phillips, J.B., and Westerfield, M. (2014). Zebrafish models in translational research: tipping the scales toward advancements in human health. *Dis. Model Mech.* 7, 739-743.
- Picard, D. (1994). Regulation of protein function through expression of chimaeric proteins. *Curr. Opin. Biotechnol.* 5, 511-515.
- Piccoli, G., Onofri, F., Cîrnaru, M.D., Kaiser, C.J., Jagtap, P., Kastenmüller, A., Pischedda, F., Marte, A., von Zweyendorf, F., Vogt, A., Giesert, F., Pan, L., Antonucci, F., Kiel, C., Zhang, M., et al., (2014). Leucine-rich repeat kinase 2 binds to neuronal vesicles through protein interactions mediated by its C-terminal WD40 domain. *Mol. Cell Biol.* 34, 2147-2161.
- Pilling, A.D., Horiuchi, D., Lively, C.M., and Saxton, W.M. (2006). Kinesin-1 and Dynein are the primary motors for fast transport of mitochondria in *Drosophila* motor axons. *Mol. Biol. Cell* 17, 2057-2068.
- Pisls, A., and Winklhofer, K.F. (2012). Parkin, PINK1 and mitochondrial integrity: emerging concepts of mitochondrial dysfunction in Parkinson's disease. *Acta Neuropathol.* 123, 173-188.
- Pittman, A.J., Law, M.Y., and Chien, C.B. (2008). Pathfinding in a large vertebrate axon tract: isotypic interactions guide retinotectal axons at multiple choice points. *Development* 135, 2865-2871.
- Plowey, E.D., Cherra, S.J., Liu, Y.J., and Chu, C.T. (2008). Role of autophagy in G2019S LRRK2-associated neurite shortening in differentiated SH-SY5Y cells. *J. Neurochem.* 105, 1048-1056.
- Plucińska, G., Paquet, D., Hruscha, A., Godinho, L., Haass, C., Schmid, B., and Misgeld, T. (2012). In vivo imaging of disease-related mitochondrial dynamics in a vertebrate model system. *J. Neurosci.* 32, 16203-16212.
- Polymeropoulos, M.H., Lavedan, C., Leroy, E., Ide, S.E., Dehejia, A., Dutra, A., Pike, B., Root, H., Rubenstein, J., Boyer, R., Stenroos, E.S., Chandrasekharappa, S., Athanassiadou, A. et al. (1997). Mutation in the alpha-synuclein gene identified in families with Parkinson's disease. *Science* 276, 2045-2047.
- Postlethwait, J., Amores, A., Cresko, W., Singer, A., and Yan, Y.L. (2004). Subfunction partitioning, the teleost radiation and the annotation of the human genome. *Trends Genet.* 20, 481-490.
- Postlethwait, J.H. (2007). The zebrafish genome in context: ohnologs gone missing. *J. Exp. Zool. (Mol. Dev. Evol.)* 308B, 563-577.
- Pujol-Martí, J., Baudoin, J.P., Faucherre, A., Kawakami, K., and López-Schier, H. (2010). Progressive neurogenesis defines lateralis somatotopy. *Dev. Dyn.* 239, 1919-1930.
- Pungaliya, P.P., Bai, Y., Lipinski, K., Anand, V.S., Sen, S., Brown, E.L., Bates, B., Reinhart, P.H., West, A.B., Hirst, W.D., and Braithwaite, S.P. (2010). Identification and characterization of a leucine-rich repeat kinase 2 (LRRK2) consensus phosphorylation motif. *PLoS One* 5, e13672.
- Raphael, A.R., Perlin, J.R., and Talbot, W.S. (2010) Schwann cells reposition a peripheral nerve to isolate it from postembryonic remodeling of its targets. *Development* 137, 3643-3649.
- Ravikumar, B., Sarkar, S., Davies, J.E., Futter, M., Garcia-Arencibia, M., Green-Thompson, Z.W., Jimenez-Sanchez, M., Korolchuk, V.I., Lichtenberg, M., Luo, S., Massey, D.C. et al. (2010). Regulation of mammalian autophagy in physiology and pathophysiology. *Physiol. Rev.* 90, 1383-1435.
- Rink, E., and Wullimann, M.F. (2001). The teleostean (zebrafish) dopaminergic system ascending to the subpallium (striatum) is located in the basal diencephalon (posterior tuberculum). *Brain Res.* 889, 316-330.

- Rink, E., and Wullimann, M.F. (2002a). Connections of the ventral telencephalon and tyrosine hydroxylase distribution in the zebrafish brain (*Danio rerio*) lead to identification of an ascending dopaminergic system in a teleost. *Brain Res. Bull.* *57*, 385-387.
- Rink, E., and Wullimann, M.F. (2002b). Development of the catecholaminergic system in the early zebrafish brain: an immunohistochemical study. *Dev. Brain Res.* *137*, 89-100.
- Ross, L.S., Parrett, T., and Easter, S.S., Jr. (1992). Axonogenesis and morphogenesis in the embryonic zebrafish brain. *J. Neurosci.* *12*, 467-482.
- Ross, G.W., Abbott, R.D., Petrovitch, H., Morens, D.M., Grandinetti, A., Tung, K.H., Tanner, C.M., Masaki, K.H., Blanchette, P.L., Curb, J.D., Popper, J.S., and White, L.R. (2000). Association of coffee and caffeine intake with the risk of Parkinson disease. *JAMA* *283*, 2674-2679.
- Rubinsztein, D.C., Shpilka, T., and Elazar, Z. (2012). Mechanisms of autophagosome biogenesis. *Curr. Biol.* *22*, 29-34.
- Russo, I., Bubacco, L., and Greggio, E. (2014). LRRK2 and neuroinflammation: partners in crime in Parkinson's disease? *J. Neuroinflammation* *11*:52, 1-9.
- Ryan, M.D., and Drew, J. (1994). Foot-and-mouth disease virus 2A oligopeptide mediated cleavage of an artificial polyprotein. *EMBO J.* *13*, 928-933.
- Sager, J.J., Bai, Q., and Burton, E.A. (2010). Transgenic zebrafish models of neurodegenerative diseases. *Brain Struct. Funct.* *214*, 285-302.
- Saiki, S., Sato, S., and Hattori, N. (2012). Molecular pathogenesis of Parkinson's disease: update. *J. Neurol. Neurosurg. Psychiatry* *83*, 430-436.
- Samii, A., Nutt, J.G., and Ransom, B.R. (2004). Parkinson's disease. *Lancet* *363*, 1783-1793.
- Sander, J.D., Cade, L., Khayter, C., Reyon, D., Peterson, R.T., Joung, J.K., and Yeh J.R. (2011). Targeted gene disruption in somatic zebrafish cells using engineered TALENs. *Nat. Biotechnol.* *29*, 697-698.
- Santoriello, C., and Zon, L.I. (2012). Hooked! Modeling human disease in zebrafish. *J. Clin. Invest.* *122*, 2337-2343.
- Sarkar, S., Floto, R.A., Berger, Z., Imarisio, S., Cordenier, A., Pasco, M., Cook, L.J., and Rubinsztein, D.C. (2005). Lithium induces autophagy by inhibiting inositol monophosphatase. *J. Cell Biol.* *170*, 1101-1111.
- Sarraf, S.A., Raman, M., Guarani-Pereira, V., Sowa, M.E., Huttlin, E.L., Gygi, S.P., and Harper, J.W. (2013). Landscape of the PARKIN-dependent ubiquitylome in response to mitochondrial depolarization. *Nature* *496*, 372-376.
- Sarrazin, A.F., Villablanca, E.J., Nuñez, V.A., Sandoval, P.C., Ghysen, A., and Allende, M.L. (2006). Proneural gene requirement for hair cell differentiation in the zebrafish lateral line. *Dev. Biol.* *295*, 534-545.
- Satake, W., Nakabayashi, Y., Mizuta, I., Hirota, Y., Ito, C., Kubo, M., Kawaguchi, T., Tsunoda, T., Watanabe, M., Takeda, A., Tomiyama, H., Nakashima, K. et al. (2009). Genome-wide association study identifies common variants at four loci as genetic risk factors for Parkinson's disease. *Nat. Genet.* *41*, 1303-1307.
- Sato, T., Takahoko, M., and Okamoto, H. (2006). HuC:Kaede, a useful tool to label neural morphologies in networks in vivo. *Genesis* *44*, 136-142.
- Sato, A., Koshida, S., and Takeda, H. (2010). Single-cell analysis of somatotopic map formation in the zebrafish lateral line system. *Dev. Dyn.* *239*, 2058-2065.
- Saxton, W.M., and Hollenbeck, P.J. (2012). The axonal transport of mitochondria. *J. Cell Sci.* *125*, 2095-2104.
- Scarffe, L.A., Stevens, D.A., Dawson, V.L., and Dawson, T.M. (2014). Parkin and PINK1: much more than mitophagy. *Trends Neurosci.* *37*, 315-324.
- Schapansky, J., Nardozzi, J.D., Felizia, F., and LaVoie, M.J. (2014). Membrane recruitment of endogenous LRRK2 precedes its potent regulation of autophagy. *Hum. Mol. Genet.* *23*, 4201-4214.

- Schapira, A.H., Cooper, J.M., Dexter, D., Jenner, P., Clark, J.B., and Marsden, C.D. (1989). Mitochondrial complex I deficiency in Parkinson's disease. *Lancet* *1*, 1269.
- Scheer, N., and Campos-Ortega, J.A. (1999). Use of the Gal4-UAS technique for targeted gene expression in the zebrafish. *Mech. Dev.* *80*, 153-158.
- Scheer, N., Groth, A., Hans, S., and Campos-Ortega, J.A. (2001). An instructive function for Notch in promoting gliogenesis in the zebrafish retina. *Development* *128*, 1099-1107.
- Schmid, B., and Haass, C. (2013). Genomic editing opens new avenues for zebrafish as a model for neurodegeneration. *J. Neurochem.* *127*, 461-470.
- Schmitz, C., and Hof, P.R. (2005). Design-based stereology in neuroscience. *Neuroscience* *130*, 813-831.
- Seibler, P., Graziotto, J., Jeong, H., Simunovic, F., Klein, C., and Krainc, D. (2011). Mitochondrial Parkin recruitment is impaired in neurons derived from mutant PINK1 induced pluripotent stem cells. *J. Neurosci.* *31*, 5970-5976.
- Seglen, P.O., and Gordon, P.B. (1980). Effects of lysosomotropic monoamines, diamines, amino alcohols, and other amino compounds on protein degradation and protein synthesis in isolated rat hepatocytes. *Mol. Pharmacol.* *18*, 468-475.
- Sen, S., Webber, P.J., and West, A.B. (2009). Dependence of leucine-rich repeat kinase 2 (LRRK2) kinase activity on dimerization. *J. Biol. Chem.* *284*, 36346-36356.
- Senghaas, N., and Köster, R.W. (2009). Culturing and transfecting zebrafish PAC2 fibroblast cells. *Cold Spring Harb. Protoc.* *6*, pdb.prot5235.
- Shahpasand, K., Uemura, I., Saito, T., Asano, T., Hata, K., Shibata, K., Toyoshima, Y., Hasegawa, M., and Hisanaga, S. (2012). Regulation of mitochondrial transport and inter-microtubule spacing by tau phosphorylation at the sites hyperphosphorylated in Alzheimer's disease. *J. Neurosci.* *32*, 2430-2441.
- Shaner N.C., Patterson G.H., and Davidson, M.W. (2007). Advances in fluorescent protein technology. *J. Cell Sci.* *120*, 4247-4260.
- Sheng, D., Qu, D., Kwok, K.H., Ng, S.S., Lim, A.Y., Aw, S.S., Lee, C.W., Sung, W.K., Tan, E.K., Lufkin, T., Jesuthasan, S., Sinnakaruppan, M., and Liu, J. (2010). Deletion of the WD40 domain of LRRK2 in zebrafish causes Parkinsonism-like loss of neurons and locomotive defect. *PLoS Genetics* *6*, e1000914.
- Sheng, Z.H., and Cai, Q. (2012). Mitochondrial transport in neurons: impact on synaptic homeostasis and neurodegeneration. *Nat. Rev. Neurosci.* *13*, 77-93.
- Sheng, Z.-H. (2014). Mitochondrial trafficking and anchoring in neurons: New insight and implications. *J. Cell Biol.* *204*, 1087-1098.
- Shults, C.W. (2006). Lewy bodies. *Proc. Natl. Acad. Sci. USA* *103*, 1661-1668.
- Simón-Sánchez, J., Schulte, C., Bras, J.M., Sharma, M., Gibbs, J.R., Berg, D., Paisan-Ruiz, C., Lichtner, P., Scholz, S.W., Hernandez, D.G., Krüger, R., Federoff, M. et al. (2009) Genome-wide association study reveals genetic risk underlying Parkinson's disease. *Nat. Genet.* *41*, 1308-1312.
- Skerra, A. (2003). Das Strep-tag als molekulares Werkzeug zur Hochdurchsatz-Proteinreinigung in der Proteomforschung. *BIOspectrum* *2*, 189-192.
- Smith, W.W., Pei, Z., Jiang, H., Dawson, V.L., Dawson, T.M., and Ross, C.A. (2006). Kinase activity of mutant LRRK2 mediates neuronal toxicity. *Nat. Neurosci.* *9*, 1231-1233.
- Son, O.L., Kim, H.T., Ji, M.H., Yoo, K.W., Rhee, M., and Kim, C.H. (2003). Cloning and expression analysis of a Parkinson's disease gene, uch-L1, and its promoter in zebrafish. *Biochem. Biophys. Res. Commun.* *312*, 601-607.
- Sood, R., English, M.A., Jones, M., Mullikin, J., Wang, D.M., Anderson, M., Wu, D., Chandrasekharappa, S.C., Yu, J., Zhang, J., and Liu, P P. (2006). Methods for reverse genetic screening in zebrafish by resequencing and TILLING. *Methods* *39*, 220-227.
- Soulard, A., and Hall, M.N. (2007). SnapShot: mTOR signaling. *Cell* *129*, 434.

- Stehbens, S., Pemble, H., Murrow, L., and Wittmann, T. (2012). Imaging intracellular protein dynamics by spinning disk confocal microscopy. *Methods Enzymol.* *504*, 293-313.
- Stepanenko, O.V., Stepanenko, O.V., Shcherbakova, D.M., Kuznetsova, I.M., Turoverov, K.K., Verkhusha, V.V. (2011). Modern fluorescent proteins: from chromophore formation to novel intracellular applications. *Biotechniques* *51*, 313-327.
- Streisinger, G., Walker, C., Dower, N., Knauber, D., and Singer, F. (1981). Production of clones of homozygous diploid zebra fish (*Brachydanio rerio*). *Nature* *291*, 293-296.
- Stuart, G.W., Vielkind, J.R., McMurray, J.V., and Westerfield, M. (1990). Stable lines of transgenic zebrafish exhibit reproducible patterns of transgene expression. *Development* *109*, 577-584.
- Subach, O.M., Gundorov, I.S., Yoshimura, M., Subach, F.V., Zhang, J., Grünwald, D., Souslova, E.A., Chudakov, D.M., and Verkhusha, V.V. (2008). Conversion of red fluorescent protein into a bright blue probe. *Chem. Biol.* *15*, 1116-1124.
- Sulzer, D. (2007). Multiple hit hypotheses for dopamine neuron loss in Parkinson's disease. *Trends Neurosci.* *30*, 244-250.
- Sun, Z., and Gitler, A.D. (2008). Discovery and characterization of three novel synuclein genes in zebrafish. *Dev. Dyn.* *237*, 2490-2495.
- Tanaka, M., Kim, Y.M., Lee, G., Junn, E., Iwatsubo, T., and Mouradian, M.M. (2004). Aggregates formed by alpha-synuclein and synphilin-1 are cytoprotective. *J. Biol. Chem.* *279*, 4625-4631.
- Thacker, E.L., O'Reilly, E.J., Weisskopf, M.G., Chen, H., Schwarzschild, M.A., McCullough, M.L., Calle, E.E., Thun, M.J., and Ascherio, A. (2007). Temporal relationship between cigarette smoking and risk of Parkinson disease. *Neurology* *68*, 764-768.
- Todde, V., Veenhuis, M., and van der Klei, I.J. (2009). Autophagy: principles and significance in health and disease. *Biochim. Biophys. Acta* *1792*, 3-13.
- Tong, Y., Yamaguchi, H., Giaime, E., Boyle, S., Kopan, R., Kelleher, R.J. 3rd, and Shen, J. (2010). Loss of leucine-rich repeat kinase 2 causes impairment of protein degradation pathways, accumulation of alpha-synuclein, and apoptotic cell death in aged mice. *Proc. Natl. Acad. Sci. U S A* *107*, 9879-9884.
- Tong, Y., Giaime, E., Yamaguchi, H., Ichimura, T., Liu, Y., Si, H., Cai, H., Bonventre, J.V., and Shen, J. (2012). Loss of leucine-rich repeat kinase 2 causes age-dependent biphasic alterations of the autophagy pathway. *Mol. Neurodegener.* *7*:2, doi:10.1186/1750-1326-7-2
- Tsien, R.Y. (1998). The green fluorescent protein. *Annu. Rev. Biochem.* *67*, 509-544.
- Tsika, E., and Moore, D.J. (2012). Mechanisms of LRRK2-mediated neurodegeneration. *Curr. Neurol. Neurosci. Rep.* *12*, 251-260.
- Tsunaka, Y., Kajimura, N., Tate, S., and Morikawa, K. (2005). Alteration of the nucleosomal DNA path in the crystal structure of a human nucleosome core particle. *Nucleic Acids Res.* *33*, 3424-3434.
- Uemura, O., Okada, Y., Ando, H., Guedj, M., Higashijima, S., Shimazaki, T., Chino, N., Okano, H., and Okamoto, H. (2005). Comparative functional genomics revealed conservation and diversification of three enhancers of the *isl1* gene for motor and sensory neuron-specific expression. *Dev. Biol.* *278*, 587-606.
- Valente, E.M., Abou-Sleiman, P.M., Caputo, V., Muqit, M.M., Harvey, K., Gispert, S., Ali, Z., Del Turco, D., Bentivoglio, A.R., Healy, D.G., Albanese, A., Nussbaum, R. et al. (2004). Hereditary early-onset Parkinson's disease caused by mutations in *PINK1*. *Science* *304*, 1158-1160.
- Vilain, S., Esposito, G., Haddad, D., Schaap, O., Dobрева, M.P., Vos, M., Van Meensel, S., Morais, V.A., De Strooper, B., and Verstreken, P. (2012). The yeast complex I equivalent NADH dehydrogenase rescues *pink1* mutants. *PLoS Genet.* *8*, e1002456.

- Vilariño-Güell, C., Wider, C., Ross, O.A., Dachsel, J.C., Kachergus, J.M., Lincoln, S.J., Soto-Ortolaza, A.I., Cobb, S.A., Wilhoite, G.J., Bacon, J.A., Behrouz, B., Melrose, H.L. et al. (2011). VPS35 mutations in Parkinson disease. *Am. J. Hum. Genet.* *89*, 162-167.
- Villegas, R., Martin, S.M., O'Donnell, K.C, Carrillo, S.A., Sagasti, A., and Allende, M.L. (2012). Dynamics of degeneration and regeneration in developing zebrafish peripheral axons reveals a requirement for extrinsic cell types. *Neural. Dev.* *7*, doi: 10.1186/1749-8104-7-19.
- Vives-Bauza, C., Zhou, C., Huang, Y., Cui, M., de Vries, R.L., Kim, J., May, J., Tocilescu, M.A., Liu, W., Ko, H.S., Magrané, J., Moore, D.J., Dawson, V.L., Grailhe, R., Dawson, T.M., Li, C., Tieu, K., and Przedborski, S. (2010). PINK1-dependent recruitment of Parkin to mitochondria in mitophagy. *Proc. Natl. Acad. Sci. USA* *107*, 378-383.
- Voas, M.G., Glenn, T.D., Raphael, A.R., and Talbot, W.S. (2009). Schwann cells inhibit ectopic clustering of axonal sodium channels. *J. Neurosci.* *29*, 14408-14414.
- Vos, M., Esposito, G., Edirisinghe, J.N., Vilain, S., Haddad, D.M., Slabbaert, J.R., Van Meensel, S., Schaap, O., De Strooper, B., Meganathan, R., Morais, V.A., and Verstreken, P. (2012). Vitamin K2 is a mitochondrial electron carrier that rescues pink1 deficiency. *Science* *336*, 1306-1310.
- Wakabayashi, K., Tanji, K., Odagiri, S., Miki, Y., Mori, F., and Takahashi, H. (2013). The Lewy body in Parkinson's disease and related neurodegenerative disorders. *Mol. Neurobiol.* *47*, 495-508.
- Walter, W.J., and Diez, S. (2012). Molecular motors: A staggering giant. *Nature* *482*, 44-45.
- Wang, X., Winter, D., Ashrafi, G., Schlehe, J., Wong, Y.L., Selkoe, D., Rice, S., Steen, J., LaVoie, M.J., and Schwarz, T.L. (2011). PINK1 and Parkin target Miro for phosphorylation and degradation to arrest mitochondrial motility. *Cell* *147*, 893-906.
- Webber, P.J., Smith, A.D., Sen, S., Renfrow, M.B., Mobley, J.A., and West, A.B. (2011). Autophosphorylation in the leucine-rich repeat kinase 2 (LRRK2) GTPase domain modifies kinase and GTP-binding activities. *J. Mol. Biol.* *412*, 94-110.
- Weber, T., and Köster, R. (2013). Genetic tools for multicolor imaging in zebrafish larvae. *Methods.* *62*, 279-291.
- Weihofen, A., Thomas, K.J., Ostaszewski, B.L., Cookson, M.R., and Selkoe, D.J. (2009). Pink1 forms a multiprotein complex with Miro and Milton, linking Pink1 function to mitochondrial trafficking. *Biochemistry* *48*, 2045-2052.
- West, A.B., Moore, D.J., Biskup, S., Bugayenko, A., Smith, W.W., Ross, C.A., Dawson, V.L., and Dawson, T.M. (2005). Parkinson's disease-associated mutations in leucine-rich repeat kinase 2 augment kinase activity. *Proc. Natl. Acad. Sci. USA* *102*, 16842-16847.
- West, A.B., Moore, D.J., Choi, C., Andrabi, S.A., Li, X., Dikeman, D., Biskup, S., Zhang, Z., Lim, K.L., Dawson, V.L., and Dawson, T.M. (2007). Parkinson's disease-associated mutations in LRRK2 link enhanced GTP-binding and kinase activities to neuronal toxicity. *Hum. Mol. Genet.* *16*, 223-232.
- Westerfield, M. (2000). *The zebrafish book. A guide for the laboratory use of zebrafish (Danio rerio)*. 4th ed., Univ. of Oregon Press, Eugene, available at [www.zfin.org](http://www.zfin.org)
- Westerlund, M., Belin, A.C., Anvret, A., Bickford, P., Olson, L., and Galter, D. (2008). Developmental regulation of leucine-rich repeat kinase 1 and 2 expression in the brain and other rodent and human organs: Implications for Parkinson's disease. *Neuroscience* *152*, 429-436.
- Wienholds, E., van Eeden, F., Kosters, M., Mudde, J., Plasterk, R.H., and Cuppen, E. (2003). Efficient target-selected mutagenesis in zebrafish. *Genome Res.* *13*, 2700-2707.
- Wirdefeldt, K., Adami, H.O., Cole, P., Trichopoulos, D., and Mandel, J. (2011). Epidemiology and etiology of Parkinson's disease: a review of the evidence.

- Eur. J. Epidemiol. 26, S1-S58.
- Wolenski, J.S., and Julich, D. (2014). Fluorescence microscopy gets faster and clearer: roles of photochemistry and selective illumination. *Yale J. Biol. Med.* 87, 21-32.
- Wong, E., and Cuervo, A.M. (2010). Integration of clearance mechanisms: the proteasome and autophagy. *Cold Spring Harb. Perspect. Biol.* 2, a006734.
- Wood-Kaczmar, A., Gandhi, S., and Wood, N.W. (2006). Understanding the molecular causes of Parkinson's disease. *Trends Mol. Med.* 12, 521-528.
- Wu, J.J., Quijano, C., Chen, E., Liu, H., Cao, L., Fergusson, M.M., Rovira, I.I., Gutkind, S., Daniels, M.P., Komatsu, M., and Finkel, T. (2009). Mitochondrial dysfunction and oxidative stress mediate the physiological impairment induced by the disruption of autophagy. *Aging* 1, 425-437.
- Wullimann, M.F., Rupp, B., and Reichert, H. (1996). Neuroanatomy of the zebrafish brain. A topological atlas. Birkhäuser Verlag, Basel. ISBN 3-7643-5120-9.
- Xi, Y., Ryan, J., Noble, S., Yu, M., Yilbas, A.E., and Ekker, M. (2010). Impaired dopaminergic neuron development and locomotor function in zebrafish with loss of pink1 function. *Eur. J. Neurosci.* 31, 623-633.
- Xi, Y., Noble, S., and Ekker, M. (2011). Modeling neurodegeneration in zebrafish. *Curr. Neurol. Neurosci. Rep.* 11, 274-282.
- Xie, Z., and Klionsky, D.J. (2007). Autophagosome formation: core machinery and adaptations. *Nat. Cell Biol.* 9, 1102-1109.
- Yamamoto, K., Ruuskanen, J.O., Wullimann, M.F., and Vernier, P. (2010). Two tyrosine hydroxylase genes in vertebrates. New dopaminergic territories revealed in the zebrafish brain. *Mol. Cell. Neurosci.* 43, 394-402.
- Yang, Y., Gehrke, S., Imai, Y., Huang, Z., Ouyang, Y., Wang, J.W., Yang, L., Beal, M.F., Vogel, H., and Lu, B. (2006). Mitochondrial pathology and muscle and dopaminergic neuron degeneration caused by inactivation of *Drosophila* Pink1 is rescued by Parkin. *Proc. Natl. Acad. Sci. USA* 103, 10793-10798.
- Yang, Z., and Klionsky, D.J. (2010). Mammalian autophagy: core molecular machinery and signaling regulation. *Curr. Opin. Cell Biol.* 22, 124-131.
- Yildiz, A., Tomishige, M., Vale, R.D., and Selvin, P.R. (2004). Kinesin walks hand-over-hand. *Science* 303, 676-678.
- Yildiz, A., Tomishige, M., Gennerich, A., and Vale, R.D. (2008). Intramolecular strain coordinates kinesin stepping behavior along microtubules. *Cell* 134, 1030-1041.
- Zhou, H., Falkenburger, B.H., Schulz, J.B., Tieu, K., Xu, Z., and Xia, X.G. (2007). Silencing of the Pink1 gene expression by conditional RNAi does not induce dopaminergic neuron death in mice. *Int. J. Biol. Sci.* 3, 242-250.
- Zimprich, A., Biskup, S., Leitner, P., Lichtner, P., Farrer, M., Lincoln, S., Kachergus, J., Hulihan, M., Uitti, R.J., Calne, D.B., Stoessl, A.J., Pfeiffer, R.F., Patenge, N., Carbajal, I.C., Vieregge, P., Asmus, F., Müller-Myhok, B., Dickson, D.W., Meitinger, T., Strom, T.M., Wszolek, Z.K., and Gasser, T. (2004). Mutations in LRRK2 cause autosomal-dominant parkinsonism with pleomorphic pathology. *Neuron* 44, 601-607.
- Zimprich, A., Benet-Pagès, A., Struhal, W., Graf, E., Eck, S.H., Offman, M.N., Haubenberger, D., Spielberger, S., Schulte, E.C., Lichtner, P., Rossle, S.C., Klopp, N., et al. (2011). A mutation in VPS35, encoding a subunit of the retromer complex, causes late-onset Parkinson disease. *Am. J. Hum. Genet.* 89, 168-175.

Additional information material:

MultiSite Gateway Three-Fragment Vector Construction Kit, user manual from Invitrogen at [http://tools.invitrogen.com/content/sfs/manuals/multisite\\_gateway\\_man.pdf](http://tools.invitrogen.com/content/sfs/manuals/multisite_gateway_man.pdf)

Webcast deposited at [www.youtube.com](http://www.youtube.com):

Wood, N. (28/05/2012). The genetics of LRRK2: A role in the sporadic form of Parkinson's disease, presented at the Biochemical Society Focused Meeting on LRRK2: function and dysfunction, held in March 2012

## **7 Appendix**

### **7.1. Eidesstattliche Erklärung**

Ich erkläre hiermit an Eides statt, dass ich die vorliegende Arbeit gemäß der Promotionsordnung der Technischen Universität München selbständig und ohne unzulässige fremde Hilfe und unerlaubte Hilfsmittel angefertigt habe. Alle verwendeten Literaturquellen sind im Literaturverzeichnis vollständig aufgeführt.

München, den

---

Rosemarie Söllner

## 7.2. Publications

Results reported in Chapter 3.4.2. have been made public recently.

Flinn, L.J., Keatinge, M., Bretaud, S., Mortiboys, H., Matsui, H., De Felice, E., Woodroof, H.I., Brown, L., McTighe, A., Soellner, R., Allen, C.E., Heath, P.R., Milo, M., Muqit, M.M., Reichert, A.S., Köster, R.W., Ingham, P.W., and Bandmann, O. (2013). TigarB causes mitochondrial dysfunction and neuronal loss in PINK1 deficiency. *Ann. Neurol.* 74, 837-847.

### 7.3. Curriculum Vitae

#### Persönliche Daten

---

Geburtsdaten 17.10.1971, München

Familienstand ledig

#### Berufs- und Forschungserfahrung

---

07/2013 – 11/2013 *Vier-monatige Fachqualifikation 'Life Science Management' bei der ATV Ausbildung Training Vernetzung GmbH München*

[www.atv-seminare.de](http://www.atv-seminare.de)

- Aktuelle gesetzliche und gesundheitspolitische Grundlagen
- Projektmanagement
- Qualitätsmanagement, Qualitätssicherung
- Betriebswirtschaftliche Grundlagen
- Rhetorik und Präsentation
- Team- und Führungstraining

01/2009 – 07/2012 *Wissenschaftliche Mitarbeiterin zur Promotion am Helmholtz Zentrum München, Institut für Entwicklungs-genetik*

Arbeitsgruppe von Prof. Reinhard Köster – Zebrafish Neuroimaging  
Forschungsschwerpunkt: Molekulare Mechanismen der Neurodegeneration am Modellorganismus Zebrafisch (*Danio rerio*)

Titel der Doktorarbeit: Establishment and cell biological analysis of neurodegeneration models in zebrafish based on Parkinson's disease-linked genes LRRK2 and PINK1

- Einarbeitung in das Forschungsgebiet Neurodegeneration und Morbus Parkinson
- Präsentation von Forschungsergebnissen vor Fachpublikum
- Kollaboration mit Laboren in Frankfurt und in Sheffield, England
- Aufbau und Pflege von Netzwerken zum Wissensaustausch

09/2003 – 08/2008 *Wissenschaftliche Mitarbeiterin am Trinity College, University of Dublin, Irland*

2006 – 2008 Institute of Neuroscience

Arbeitsgruppe von Prof. Mani Ramaswami – Analyse neuronaler Funktion und Plastizität am Modellorganismus Fruchtfliege (*Drosophila melanogaster*)

- Einarbeitung in das Forschungsgebiet der molekularen Mechanismen von Nervenzellfunktion und Gedächtnis
- Labormanagement (Bestellung und Bereitstellung von Labor- und Verbrauchsmaterial)
- Experimentelle Forschungstätigkeit

2003 – 2006 Institute of Genetics

Arbeitsgruppe von Prof. Seamus Martin – Molekulare Kontrolle des programmierten Zelltodes und von Immunreaktionen durch Caspasen

Anfertigung einer Abschlußarbeit für den Master of Science by Research

Titel der Masterarbeit: Identification and characterization of novel substrates for inflammatory caspases

- Einarbeitung in das Forschungsgebiet der molekularen Regulation immunologischer Entzündungsprozesse
- Konferenzteilnahme und Präsentationen

07/1999 – 06/2003 *Bench-Scientist bei Aventis Pharma Deutschland GmbH, Aventis Center for Functional Genomics, Martinsried, ehemalige Zweigstelle der Sanofi-Aventis Deutschland GmbH, Frankfurt*

- Durchführung von Three-hybrid Screening Assays in Hefe zur Identifizierung von Drug Targets
- Assay Development für das High-Throughput Screening von Kinaseinhibitoren in vivo, mit der Bäckerhefe (*Saccharomyces cerevisiae*)
- Labormanagement (Bereitstellung von Labor- und Verbrauchsmaterial)
- Konferenzteilnahmen
- Regelmäßiges Reporting

## Studium und Schulbildung

---

11/1991 – 02/1999 *Biologie an der Ludwig-Maximilians-Universität, München*

Studienschwerpunkte: Genetik, Immunologie, Biochemie, Zoologie  
Abschluss: Diplom-Biologin, Note: 1,6

Diplomarbeit am Institut für Mikrobiologie und Genetik, Arbeitsgruppe von Prof. Christian Koch – Transkriptionale Regulation des Zellzyklus der Bäckerhefe

Titel der Diplomarbeit: Identification of START-specific transcriptional regulators in the cell cycle of baker's yeast *Saccharomyces cerevisiae*

07/1991 Abitur am Louise-Schröder-Gymnasium, München